

Contents

1	Introduction	1
1.1	Evidence for Dark Matter	1
1.1.1	Astrophysical Observations	1
1.1.2	Cosmological Evidence	3
1.2	Potential Models of Dark Matter	6
1.2.1	Dark Matter in an Effective Field Theory Framework	11
1.2.2	Overview of Effective Field Theory	11
1.2.3	Dimension 6 EFT Operators for Dirac Fermion Dark Matter	13
1.2.4	From DM-Quark to DM-Nucleon Interactions	14
1.3	Current Status of Dark Matter Constraints	16
1.3.1	Collider Bounds	16
1.3.2	Direct Detection Searches	17
1.3.3	Indirect Detection	20
1.4	Dark Matter Signals from the Sun	21
1.5	Compact Objects as Dark Matter Probes	25
1.6	Thesis Outline	27
2	A Primer on Compact Objects	29
2.1	Structure Equations from General Relativity	30
2.2	White Dwarfs	33
2.2.1	The FMT Equation of State	33
2.2.2	Observational Status	39
2.3	Neutron Stars	41
2.3.1	Observational Status	43
2.3.2	Neutron Star Equations of State	46
3	Improved Treatment of Dark Matter Capture in Compact Objects	51
3.1	Dark Matter Capture in the Sun	51
3.2	Capture in Compact Objects	55
3.2.1	General Relativistic Corrections to the Capture Rate	55
3.2.2	Geometric Limit and Threshold Cross-Section	57

3.2.3	Interaction Rate for Relativistic Energies and Degenerate Targets	58
3.3	The Differential Interaction Rate	61
3.3.1	Pauli Blocking	65
3.4	Capture in the Low, Intermediate and High Mass Regimes	66
3.4.1	Low and intermediate DM mass range	69
3.4.2	Large Mass Regime: Multiple Scattering	72
3.5	Results	78
3.6	Summary	81
4	Capture from Leptonic Species	83
4.1	Capture from Leptons in Neutron Stars	83
4.1.1	Capture Rate	84
4.1.2	Finite Temperature Effects and Evaporation	89
4.1.3	Results	92
4.2	Capture from Electrons in White Dwarfs	96
4.2.1	Capture Rates	96
4.2.2	Finite Temperature Effects and Evaporation	100
4.2.3	DM Induced Heating of WDs in GC M4	101
4.3	Summary	106
5	Capture on Baryonics in Neutron Stars	109
5.1	Baryon Structure and Strong Interactions	109
5.1.1	Baryon Effective Masses	109
5.1.2	Momentum Dependence of Hadronic Form Factors	111
5.1.3	Modifications to the Capture Rate	117
5.2	Capture Rate Results	121
5.2.1	Nucleons	122
5.3	Threshold Cross-Sections for Nucleon Scattering	126
Appendix A	Dark Matter Interaction Rates	129
A.1	General Interaction Rates for Scattering within a Degenerate Media	129
A.2	Elastic Scattering	135
A.2.1	Down-scattering Rate	135
A.2.2	Up-scattering Rate	137
A.3	Non-degenerate weak field limit	140
A.4	Intermediate DM mass range	140
A.5	Kinematic phase space for DM-electron scattering	143
A.6	Interaction Rate for Low Energies	145

Appendix B Hadronic matrix elements for scattering operators	149
B.1 Nucleons	149
B.2 Hyperons	150

1

Introduction

1.1 Evidence for Dark Matter

Today, the amount of evidence in support of dark matter's existence is overwhelming. This evidence comes from astrophysical and cosmological observations that are inconsistent with a universe composed entirely of visible matter. This section reviews this evidence.

1.1.1 Astrophysical Observations

Galaxy Clusters

Some of the first hints for the existence of dark matter came from observations of galaxy clusters. Perhaps the most famous analysis was performed by Fritz Zwicky [1], who was puzzled by the high rotational velocities of galaxies within the Coma Cluster. By applying the virial theorem, equating the cluster's kinetic and gravitational potential energies, he found that the cluster would need to contain a much more significant amount of *dunkle materie* (dark matter) than visible matter to accommodate these high velocities.

Rotation Curves of Spiral Galaxies

The anomalous rotational velocities observed in galaxy clusters can also be observed at the galactic scale. The rotation curves of spiral galaxies, which relate

the rotational velocities of stars to their distance from the galactic centre, were observed to be flat at large distances. From the observed distribution of visible matter, Newtonian mechanics predicts that the orbital velocity of a star a distance r from the galactic centre, $v_*(r)$, is related to the mass contained within a radius r , $M(r)$, through

$$v_*(r) = \sqrt{\frac{GM(r)}{r}}, \quad (1.1)$$

indicating that the velocity should fall off as $1/\sqrt{r}$ at the outer regions of the galaxy where $M(r)$ is constant. Instead, observations of many spiral galaxies indicate that this velocity remains constant out to the galaxy's edge.

A simple way to produce such a rotation curve is to introduce a spherically symmetric distribution of dark matter surrounding the galaxy,

$$\rho_{\text{DM}}(r) = \frac{v_0^2}{4\pi G r^2}, \quad (1.2)$$

which results in a constant rotational velocity of v_0 out to the galaxy edge. Detailed simulations of structure formation in a Cold Dark Matter (CDM) Universe indicate that the true distribution is better represented by distribution functions such as the Navaro-Frenk-White (NFW) profile [2, 3] or Einasto [4] profiles, which are commonly used in the literature.

An example rotation curve for galaxy NGC 6503 is presented in Fig. 1.1, with the contributions from each of the matter components to the rotational velocity shown [5, 6]. As can be seen, the visible matter constituting disk and gas components does not explain the observed rotational velocity.

Gravitational Lensing

As described by General Relativity, the curvature of space-time around massive entities causes light to travel along curved paths. As such, the mass of astrophysical structures can be deduced from the extent to which they distort the images of objects in the background. The extent of the distortions depends on how massive the foreground object is, ranging from the shearing of the background image (weak lensing), to multiple copies of the background object appearing (strong lensing) [7]. The disparity between the mass obtained from gravitational lensing and the mass of visible matter in the system is further evidence of dark matter's existence [8, 9].

The Bullet Cluster

Galaxy cluster 1E 0657-56, commonly referred to as the “bullet cluster”, was formed by the collision of two separate galaxy clusters. The baryonic matter in these

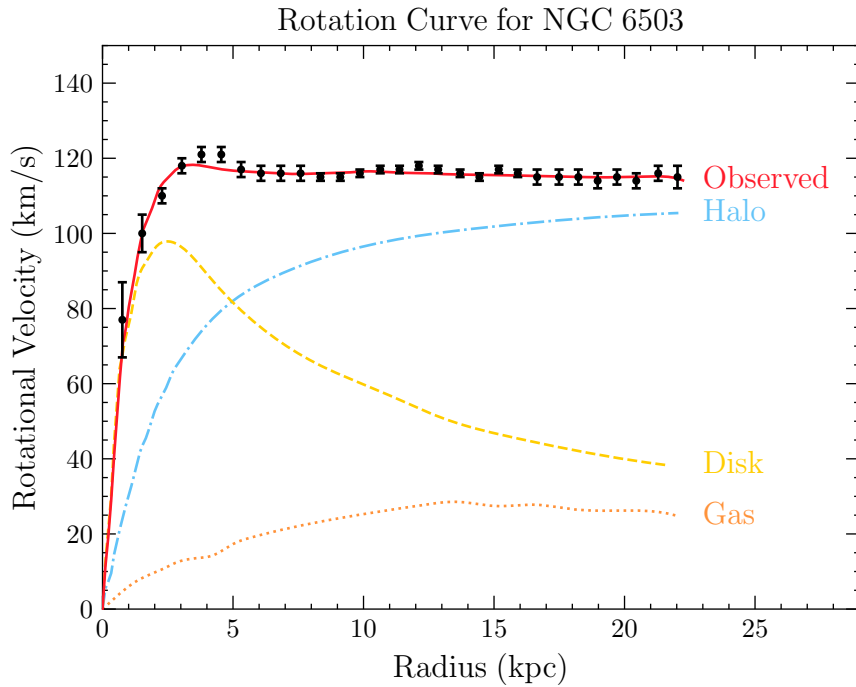


Figure 1.1: Galaxy rotation curve for NGC 6503, showing the contributions to the total velocity (red) from the DM halo (blue), disk (yellow), and gas components. Data used in making this plot was obtained from [5, 6].

clusters is mostly composed of a strongly interacting gas and, as expected, produced a significant amount of X-rays during the collision. These X-rays were imaged by the Chandra X-Ray telescope [10], providing information on the resulting distribution of the visible matter. This is shown by the red regions of Fig. 1.2, where it can be seen how the visible matter has been smeared due to the collision. However, when the gravitational potential was mapped using gravitational lensing, it was clear that the majority of the mass was displaced relative to the visible matter. This mass is attributed to the dark matter components of the original clusters. As indicated by the purple regions in Fig. 1.2, the dark matter halos seem to have passed through each other mostly unperturbed. This tells us that not only is the majority of the mass comprised of dark matter, but that the dark matter has extremely weak interactions with both the visible matter and itself.

1.1.2 Cosmological Evidence

The current best cosmological model is the Λ -Cold Dark Matter model (Λ CDM), in which Λ refers to the cosmological constant associated with dark energy, and



Figure 1.2: Image of the Bullet Cluster with contours of the gravitational potential superposed. The red regions indicate the baryonic matter after the collision, while the purple regions are the expected DM components deduced from gravitational lensing. [10, 11]

as the name suggests, cold (i.e. non-relativistic) dark matter plays a prominent role. The key components of this model are the aforementioned dark energy and dark matter, along with baryonic matter, and it assumes that gravity is described by Einstein's General Relativity. The total energy density of the universe, $\rho_{\text{Univ.}}$, can be broken down into three components based on how their density redshifts with the expansion of the Universe. In the Λ CDM model, these components are matter, radiation, and the vacuum energy Λ . The cosmological abundances of each component, (Ω_m , Ω_r , Ω_Λ respectively), are expressed as a fraction of the critical density, ρ_{crit} ,

$$\rho_{\text{crit}} = \frac{H^2}{8\pi G_N}, \quad (1.3)$$

$$\Omega_i = \frac{\rho_i}{\rho_{\text{crit}}}, \quad (1.4)$$

where H is the Hubble parameter, such that the total energy density of the Universe satisfies

$$\Omega_m + \Omega_r + \Omega_\Lambda = \frac{\rho_{\text{Univ.}}}{\rho_{\text{crit}}}. \quad (1.5)$$

The ratio $\rho_{\text{Univ.}}/\rho_{\text{crit}}$ determines the curvature of the universe, with values greater than 1 corresponding to a closed universe, less than 1 to an open universe, and

equal to 1 to a spatially flat universe. Current observations are consistent with a spatially flat universe, and so we have $\sum_i \Omega_i = 1$.

The Λ CDM model has seen huge success as it provides explanations for observed the power spectrum of the Cosmic Microwave Background (CMB), the large-scale structure of the Universe, the abundances of light elements (hydrogen, deuterium, helium, and lithium), and the accelerated expansion rate of the Universe. These observations constrain the parameters of the model and hence provide a complementary probe of the properties of dark matter to the astronomical observations discussed above.

The Cosmic Microwave Background

One of the strongest probes of cosmological models is the Cosmic Microwave Background (CMB), relic photons from the time epoch of last scattering. This occurred after recombination, at a temperature of around ~ 3000 K, once the photons had decoupled from the baryonic matter and could freely propagate through the universe. The photons observed today have been redshifted by the expansion of the Universe and are well described by a blackbody spectrum with a temperature of $T_{\text{CMB}} = 2.73 \pm 0.0006$ K. Observations of the CMB temperature reveal that it is not exactly isotropic, with anisotropies at the level of $\delta T_{\text{CMB}}/T_{\text{CMB}} \sim 10^{-5} - 10^{-6}$ seen on a range of angular scales in the sky. These anisotropies were seeded by the primordial density perturbations that arise during inflation. These perturbations evolve due to the acoustic oscillations of the photon-baryon plasma driven by the interplay between the pressure from the photons and the gravitational attraction of the matter. The oscillations cease once the photons decouple, freezing in their temporal phases that are observed as peaks in the angular power spectrum of the temperature anisotropies.

Measurements of the CMB power spectrum provide information on many of the cosmological parameters. The locations of the acoustic peaks depend on the spatial geometry of the Universe and hence constrains Ω_{tot} . The total matter density, Ω_m , affects how the CMB spectrum is gravitationally lensed. The relative amplitudes of the peaks probe the baryon-to-photon ratio and hence the baryon density, Ω_b . Finally, the density of dark matter, Ω_{DM} , is obtained by fitting the cosmological parameters to the exact shape of the spectrum [5, 12].

The Planck collaboration most recently performed a precise measurement of the CMB power spectrum in 2018, obtaining best-fit parameters [12, 13]

$$\Omega_m = 0.311 \pm 0.006, \quad \Omega_\Lambda = 0.689 \pm 0.006, \quad (1.6)$$

for the matter and dark energy densities. They obtained a total energy density of $\Omega_{\text{tot}} = 1.011 \pm 0.006$ at 68% confidence level, providing strong evidence for

a spatially flat Universe. The breakdown of the matter density into the dark and baryonic components is determined by combining the CMB results with constraints from Big Bang Nucleosynthesis (BBN)¹ giving

$$\Omega_{\text{DM}} h^2 = 0.1193 \pm 0.0009, \quad \Omega_b h^2 = 0.02242 \pm 0.00014, \quad (1.7)$$

where h is the dimensionless Hubble constant such that the Hubble parameter today is $H_0 = 100 h \text{ km s}^{-1} \text{ Mpc}$.

Large Scale Structure

After recombination, the pressure on the baryonic matter from photons began to decrease, eventually allowing the small density perturbations to grow. This led to the growth of stars, galaxies, and the large-scale structure we observe today [14]. N-body simulations of the Universe's evolution require a cold dark matter component for this structure to form. While a small component of the dark matter can be warm, hot dark matter would wash out small-scale structures [15].

1.2 Potential Models of Dark Matter

Given that baryonic matter is composed of particles described by the Standard Model (SM) of particle physics, it is a fair assumption that dark matter will also have a particle nature. Therefore, models of particle dark matter are built by extending the SM in a way consistent with its symmetries. Such models may be as simple as introducing a single new field into the SM, or there may be a more extensive hidden sector with a complicated symmetry structure. Additionally, there are compelling theories in which dark matter is not a fundamental particle, such as primordial black holes (PBHs) formed in the early universe. Given the few details we know about dark matter, there exists an enormous library of viable dark matter candidates. However, there are generic properties a good dark matter candidate must satisfy, namely:

- **Stable on Cosmological Timescales:** Dark matter must either be stable or have a lifetime significantly longer than the age of the Universe to be present in its current abundance.

¹BBN is the process that produced the light elements (D , ${}^3\text{He}$, ${}^4\text{He}$, and ${}^7\text{Li}$) were produced in the early universe. This process is highly sensitive to the physical condition of the universe at that time, allowing for strong constraints to be placed on physics beyond the Standard Model.

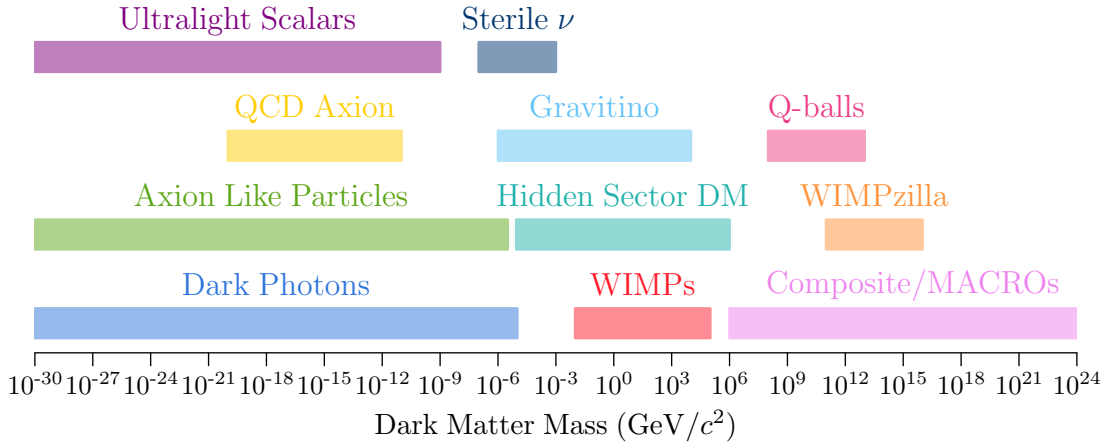


Figure 1.3: Illustrative landscape of dark matter models and the mass range for which they predict a valid candidate. Details can be found in the Dark Matter chapter of the PDG [20].

- **Neutral or milli-charged under Electromagnetism:** Dark matter, as its name suggests, does not significantly interact with light. Requiring that dark matter be completely decoupled from the Standard Model plasma by the time of recombination yields an upper bound on the electric charge of dark matter [16]

$$q_{\text{DM}}/e < \begin{cases} 3.5 \times 10^{-7} \left(\frac{m_{\text{DM}}}{1 \text{ GeV}}\right)^{0.58}, & m_{\text{DM}} > 1 \text{ GeV} \\ 4.0 \times 10^{-7} \left(\frac{m_{\text{DM}}}{1 \text{ GeV}}\right)^{0.35}, & m_{\text{DM}} < 1 \text{ GeV} \end{cases} \quad (1.8)$$

- **Small Self-Interactions:** The standard Λ CDM cosmology assumes that the dark matter is collisionless. However, small dark matter self-interactions can help resolve existing small-scale structure issues [17, 18]. Current limits on the self-interaction cross-section are $\sigma_{\text{DM-DM}}/m_{\text{DM}} < 0.48 \text{ cm}^2/\text{g}$ come from merging galaxy clusters [11] and the ellipticity of galaxies obtained from X-ray observations [19].
- **Cold:** Dark matter is required to be non-relativistic at the time of structure formation. At most, a small component of the dark matter can be warm (semi-relativistic).

A selection of the more prominent dark matter candidates is shown in Fig. 1.3. The key features of a few of these models are discussed below.

WIMPs

Weakly Interacting Massive Particles (WIMPs) are a class of dark matter candidates that generically have masses and interaction strengths around the weak scale. Many extensions of the SM naturally predict the existence of such a particle, with famous examples being the lightest supersymmetric particle in supersymmetric theories [21], or the lightest stable Kaluza-Klein mode in theories with extra dimensions [22].

Nowadays, WIMP dark matter is used almost synonymously to mean thermal relic, referring to a species whose relic abundance is produced thermally in the early universe through the freeze-out mechanism [23]. In this paradigm, the WIMP is initially in thermal equilibrium with the Standard Model bath. This equilibrium is maintained as long as the interaction rates of the WIMP with the bath, denoted Γ , remain faster than the Hubble expansion of the universe, H . As the universe continues to expand, the temperature of the bath drops, slowing down the interaction rates. Eventually, the expansion rate overtakes the interaction rates, $\Gamma/H \lesssim 1$, and the interactions “freeze out” causing the WIMP to fall out of equilibrium with the bath. At this point, the WIMPs can no longer efficiently annihilate, and their abundance gets “frozen-in” to the value it had at freeze-out, leading to the abundance observed today.

A cold thermal relic, such as dark matter, will freeze out after it has become non-relativistic. In this scenario, the interaction rates become Boltzmann suppressed², and the species rapidly freezes out. The relic density is therefore sensitive to the annihilation cross-section of the species, $\langle\sigma_{\text{ann}}v\rangle$. More efficient annihilations correspond to larger cross-sections, resulting in the species remaining in equilibrium for longer times. This allows the number density to continue following the exponentially decreasing Boltzmann distribution and yield a smaller relic abundance. The evolution of the abundance of a Majorana fermion WIMP of mass $m_{\text{WIMP}} = 100 \text{ GeV}$ is shown in Fig. 1.4 for three values of the annihilation cross-section. A simple expression relating the annihilation cross-section and the abundance that is correct to $\sim 5\%$ can be obtained [24]

$$\Omega_{\text{DM}} h^2 = \frac{10^{-27} \text{ cm}^3 \text{ s}^{-1}}{\langle\sigma_{\text{ann}}v_\chi\rangle} \frac{x_*}{g_*^{1/2}} \quad (1.9)$$

$$\sim 0.12 \left(\frac{2.2 \times 10^{-26} \text{ cm}^3 \text{ s}^{-1}}{\langle\sigma v\rangle} \right), \quad m_\chi \gtrsim 10 \text{ GeV}, \quad (1.10)$$

where $x_* = m_{\text{WIMP}}/T_*$ is evaluated at an intermediate temperature between equilib-

²The number density of a non-relativistic species in thermal equilibrium with the bath will follow $n \propto (m T_{\text{bath}})^{3/2} \exp(-m/T_{\text{bath}})$. Once the temperature falls below the mass of the species, the number density becomes exponentially suppressed. This is what is known as “Boltzmann suppression”.

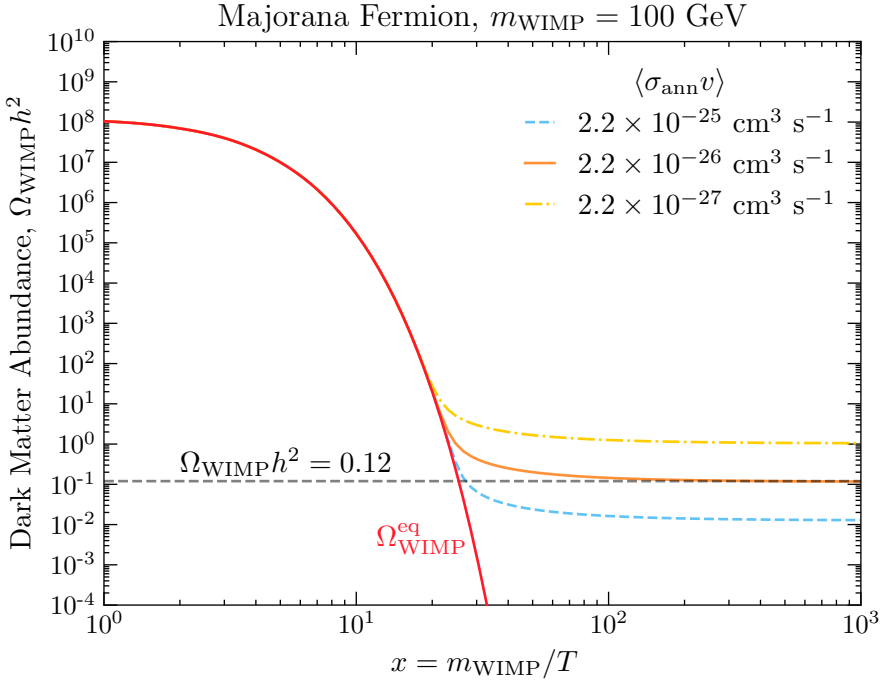


Figure 1.4: Evolution of the DM abundance as a function of $x = m_{\text{DM}}/T$. The red line tracks the abundance of the WIMP if it remains in equilibrium with the bath. The relic abundance for three different annihilation cross-sections is shown in blue, orange, and yellow for $\langle \sigma_{\text{ann}} v \rangle = 2.2 \times 10^{-25}, 2.2 \times 10^{-26},$ and $2.2 \times 10^{-27} \text{ cm}^3 \text{ s}^{-1}$ respectively.

rium and freeze-out, with g_* the effective number of relativistic degrees of freedom present at this time.

The allowed mass range for a thermal WIMP is between $10 \text{ MeV} \lesssim m_{\text{WIMP}} \lesssim 100 \text{ TeV}$. Lighter WIMPs will make non-negligible contributions to the effective number of neutrinos at the time of Big Bang Nucleosynthesis, measured to be $N_{\text{eff}}^{\text{BBN}} = 3.044$ [25], altering the observed abundances of the light elements. The CMB offers an additional probe of N_{eff} at the later time of recombination and can be combined with the BBN result leading to the value $N_{\text{eff}} = 2.99 \pm 0.17$ [12]. Given the Standard Model predicts a value of $N_{\text{eff}} = 3.044$, contributions from additional relativistic degrees of freedom must be less than $\Delta N_{\text{eff}} < 0.28$ [25]. At the high end of this range, masses larger than $\sim 100 \text{ TeV}$ are excluded from partial wave unitarity [26].

Axions

The axion originally arose from the Pecci-Quinn solution to the Strong CP problem. This refers to the lack of observed CP-violation in the QCD sector of the Standard Model that arises from the topological term in the Lagrangian

$$\mathcal{L}_{\theta_{\text{QCD}}} = \frac{g_s^2}{32\pi} \theta_{\text{QCD}} G_{\mu\nu} \tilde{G}^{\mu\nu}, \quad (1.11)$$

where g_s is the QCD coupling constant, $G_{\mu\nu}$ is the gluon field strength tensor and $\tilde{G}^{\mu\nu}$ is its dual. This term generates an electric dipole moment for the neutron (nEDM) that has yet to be observed experimentally. The current upper bound on the nEDM is $|d_n| < 0.18 \times 10^{-26} e \text{ cm}$ [27] and can be translated to an upper bound on the CP-violating QCD θ -parameter such that $|\theta_{QCD}| \lesssim 10^{-10}$, raising questions as to why this value seems to be fine-tuned to such a small value.

The Peccei-Quinn solution to this problem introduces a new, anomalous, global $U(1)_{\text{PQ}}$ symmetry and promotes θ_{QCD} to be a dynamical field. Wilczek [28] and Weinberg [29] showed that the axion emerges as the pseudo-Goldstone boson associated with the breaking of $U(1)_{\text{PQ}}$. Though the original axion was quickly out, many modern extensions of the SM predict the existence of a QCD axion. Two of the most prominent UV completions of the axion are the KSVZ [30, 31] and DFSZ [32, 33] models. In these models, the axion produced in the early Universe can serve the role of cold dark matter today. This makes it a very compelling dark matter candidate, as it solves two of the biggest mysteries of physics in one neat package.

However, solving the Strong CP problem can be rather restrictive on the model parameters. For example, the QCD axion's coupling to the photon, $g_{a\gamma\gamma}$, is not a free parameter and depends on the scale at which the PQ symmetry is broken. Many models introduce a light pseudoscalar particle, say a , that couples to the photon in the same way as the QCD axion,

$$\mathcal{L}_{a\gamma\gamma} = -\frac{g_{a\gamma\gamma}}{4} a F_{\mu\nu} \tilde{F}^{\mu\nu}, \quad (1.12)$$

but is not associated with a solution to the Strong CP problem. Such pseudoscalars are known as “Axion Like Particles” (ALPs) and can make a good dark matter candidate.

Primordial Black Holes

Primordial black holes (PBHs) are formed during the early Universe through various mechanisms. The simplest mechanism predicts that PBHs are produced from

the gravitational collapse of superhorizon density fluctuations seeded during inflation [34–36]. Unlike black holes that originate from stellar collapse, which have masses $\gtrsim 3M_\odot$, the mass of a PBH can be arbitrary. PBHs can also make a good dark matter candidate, satisfying all the criteria points outlined above. In fact, PBHs with a mass between $\sim (10^{-17} - 10^{-12}) M_\odot$, dubbed “asteroid mass PBHs”, can account for 100% of the dark matter content in the Universe [37]. Outside this range, PBHs can still make up a small fraction of dark matter [38].

1.2.1 Dark Matter in an Effective Field Theory Framework

For a dark matter candidate to be truly compelling, it should be able to be embedded into an ultraviolet (UV) complete theory. Such theories are renormalisable³ and gauge invariant under the SM gauge group $SU(3)_{\text{colour}} \otimes SU(2)_L \otimes U(1)_Y$. This allows them to be predictive up to arbitrarily high energies. These theories are typically quite complex, requiring the introduction of multiple new fields and many more free parameters. As an example, consider the phenomenological Minimal Supersymmetric Standard Model (pMSSM) [38] in which the lightest neutralino⁴ can be a thermal WIMP dark matter candidate. In this theory, 19 free parameters are introduced on top of the free parameters in the SM, requiring 38 independent experimental observations to fully constrain the model. Given that at this time, all good dark matter candidates are equally likely to be the correct one, a model-independent approach to interpreting experimental results is desirable. This is achieved by describing the interactions of dark matter with the SM through an effective field theory (EFT).

1.2.2 Overview of Effective Field Theory

Modern physics can be thought of as a ladder of theories that are designed to describe the physics present at a given energy (or length) scale. For example, Newtonian mechanics is a sufficient description of the physics experienced in our everyday lives. However, in situations where the energy is comparable to the mass of the system, Newtonian mechanics breaks down, and Special Relativity must be used to describe the physics. In particle physics, the Standard Model provides an excellent description of particle interactions up to the energies reached at LHC, 13.6 TeV, and perhaps even further beyond. However, even it is expected to break

³In a renormalisable theory, the infinities that arise from UV divergences can be absorbed by fixing a finite number of parameters to experimentally observed values.

⁴The neutralinos are the mass eigenstates of the supersymmetric partners of the neutral gauge bosons and the higgsino.

down at higher energy scales, in particular at the Planck scale, where a quantum theory of gravity is required. Hence, both Newtonian mechanics and the SM are low-energy, effective descriptions of a more complete theory.

This philosophy based on only describing the physics relevant below some energy scale, Λ , is the core principle of EFTs. The Lagrangian for the effective theory only contains the degrees of freedom that can be produced below the scale Λ , i.e. fields that have masses less than this scale. This low-energy regime described by the EFT is often called the infrared (IR) regime.

In general, the EFT Lagrangian will contain renormalizable terms, $\mathcal{L}_{\text{renorm.}}$, built out of operators that have mass dimension ≤ 4 , as well as operators with mass dimension $n > 4$, $\mathcal{O}_i^{(n)}$, that encapsulate the contributions from the UV physics. Each of these higher dimensional operators will be suppressed by the scale of new physics, Λ^{4-n} . The effective Lagrangian can then be written as

$$\mathcal{L}_{\text{EFT}} = \mathcal{L}_{\text{renorm.}} + \sum_{n>4} \sum_{i=1}^{j_n} \frac{C_i^{(n)}(\tilde{\mu})}{\Lambda^{n-4}} \mathcal{O}_i^{(n)}, \quad (1.13)$$

where we sum over all j_n operators present at mass dimension n . The expansion coefficients, $C_i^{(n)}$, are the Wilson coefficients that contain the effects of the UV physics. In general, the Wilson coefficients run with the energy scale they are evaluated at, $\tilde{\mu}$, described by the renormalisation group equations (RGEs). The sum over the mass dimension of the operators is typically terminated at some sensible value, as higher dimensional operators get increasingly suppressed by the cutoff scale Λ .

The series of operators in Eq. 1.13 can be constructed in two different ways. First, we assume some prior knowledge of the underlying UV theory. Then, for a given energy scale Λ , the heavy degrees of freedom are known, and can be explicitly integrated out. There are various methods for performing this process, the simplest being expanding the propagator of the heavy fields in powers of the momenta over the heavy mass, $(p/M)^2$. For the simple case of a heavy scalar, this corresponds to

$$\frac{i}{p^2 - M^2} = \frac{-i}{M^2} \left(\frac{1}{1 - (p/M)^2} \right) \approx \frac{-i}{M^2} \left(1 + \left(\frac{p}{M} \right)^2 + \mathcal{O} \left(\left(\frac{p}{M} \right)^4 \right) \right). \quad (1.14)$$

An alternate method is to replace the heavy fields in the Lagrangian with their classical equations of motion. The resulting effective Lagrangian will contain all the operators generated by the UV theory at tree level. Constructing an EFT in this way is called the *top-down* method.

The second method of constructing an EFT is to be agnostic to the UV physics and write down all possible operators that can be constructed from the IR degrees of freedom. These operators must obey the symmetries of the IR theory, as well as

any other constraints one wishes to impose⁵. This is the *bottom-up* approach, offering a more model-independent approach than the top-down method. The Wilson coefficients, in this case, will be arbitrary functions of the energy scale determined by solving the RGEs.

In general, the parameter space of the EFT will be lower dimensional than those of the corresponding UV models. This allows for an easier comparison with experimental results, as fewer parameters need to be fit to the data. Once the Wilson coefficients have been constrained at the low energy scale of the experiments, they can be matched to the coefficients generated by some UV theory at another scale, thereby constraining the UV parameters.

1.2.3 Dimension 6 EFT Operators for Dirac Fermion Dark Matter

This work will focus on dimension 6 EFT operators that describe the interactions of Dirac fermion dark matter with standard model fermions. These operators will have a structure

$$\mathcal{L}_{\text{EFT}}^{(6)} \sim \frac{1}{\Lambda^2} (\bar{\chi} \Gamma_{\text{DM}} \chi) (\bar{f} \Gamma_{\text{SM}} f), \quad (1.15)$$

where the Γ_i determines the Lorentz structure of the interaction by taking appropriate combinations from the set

$$\Gamma_i \in \{1, i\gamma_5, \gamma^\mu, i\gamma^\mu\gamma^5, \sigma^{\mu\nu}, i\sigma^{\mu\nu}\gamma^5\}. \quad (1.16)$$

For example, the case of $\Gamma_\chi = \Gamma_{\text{SM}} = 1$ yields scalar currents for both the DM and SM fermions and would correspond to integrating out a heavy scalar mediator in the UV theory. Under the assumption of minimal flavour violation (MFV)⁶ are ten such operators at dimension six that form a linearly independent basis. These are given in Table 1.1, along with spin-averaged squared matrix element for dark matter scattering with a fermion. The operators are classified based on the Lorentz nature of the SM fermion bilinear; D1-2: Scalar (S), D3-4: Pseudoscalar (P), D5-6: Vector (V), D7-8: Axial-vector (A), and D9-10: tensor (T). The coupling constant, g_f , for operators that involve the S and P fermion bilinears (operators D1-4) are normalised by the corresponding Yukawa couplings. This is because, in a UV complete theory, these bilinears would couple to the new scalar/pseudoscalar field that mediates the interactions with the dark matter. In many models, this new

⁵For example, one might require that no flavour changing processes are present at dimension 5, despite such operator being allowed by the symmetries.

⁶MFV is the assumption that the only source of flavour violation in the quark sector comes from the SM Yukawa matrices and not from any new physics introduced at a higher scale.

Name	Operator	g_f	$ \overline{M}(s, t, m_i) ^2$
D1	$\bar{\chi}\chi \bar{f}f$	$\frac{y_f}{\Lambda_f^2}$	$g_f^2 \frac{(4m_\chi^2 - t)(4m_\chi^2 - \mu^2 t)}{\mu^2}$
D2	$\bar{\chi}\gamma^5\chi \bar{f}f$	$i \frac{y_f}{\Lambda_f^2}$	$g_f^2 \frac{t(\mu^2 t - 4m_\chi^2)}{\mu^2}$
D3	$\bar{\chi}\chi \bar{f}\gamma^5 f$	$i \frac{y_f}{\Lambda_f^2}$	$g_f^2 t (t - 4m_\chi^2)$
D4	$\bar{\chi}\gamma^5\chi \bar{f}\gamma^5 f$	$\frac{y_f}{\Lambda_f^2}$	$g_f^2 t^2$
D5	$\bar{\chi}\gamma_\mu\chi \bar{f}\gamma^\mu f$	$\frac{1}{\Lambda_f^2}$	$2g_f^2 \frac{2(\mu^2 + 1)^2 m_\chi^4 - 4(\mu^2 + 1)\mu^2 s m_\chi^2 + \mu^4(2s^2 + 2st + t^2)}{\mu^4}$
D6	$\bar{\chi}\gamma_\mu\gamma^5\chi \bar{f}\gamma^\mu f$	$\frac{1}{\Lambda_f^2}$	$2g_f^2 \frac{2(\mu^2 - 1)^2 m_\chi^4 - 4\mu^2 m_\chi^2 (\mu^2 s + s + \mu^2 t) + \mu^4(2s^2 + 2st + t^2)}{\mu^4}$
D7	$\bar{\chi}\gamma_\mu\chi \bar{f}\gamma^\mu\gamma^5 f$	$\frac{1}{\Lambda_f^2}$	$2g_f^2 \frac{2(\mu^2 - 1)^2 m_\chi^4 - 4\mu^2 m_\chi^2 (\mu^2 s + s + t) + \mu^4(2s^2 + 2st + t^2)}{\mu^4}$
D8	$\bar{\chi}\gamma_\mu\gamma^5\chi \bar{f}\gamma^\mu\gamma^5 f$	$\frac{1}{\Lambda_f^2}$	$2g_f^2 \frac{2(\mu^4 + 10\mu^2 + 1)m_\chi^4 - 4(\mu^2 + 1)\mu^2 m_\chi^2 (s + t) + \mu^4(2s^2 + 2st + t^2)}{\mu^4}$
D9	$\bar{\chi}\sigma_{\mu\nu}\chi \bar{f}\sigma^{\mu\nu} f$	$\frac{1}{\Lambda_f^2}$	$8g_f^2 \frac{4(\mu^4 + 4\mu^2 + 1)m_\chi^4 - 2(\mu^2 + 1)\mu^2 m_\chi^2 (4s + t) + \mu^4(2s + t)^2}{\mu^4}$
D10	$\bar{\chi}\sigma_{\mu\nu}\gamma^5\chi \bar{f}\sigma^{\mu\nu} f$	$\frac{i}{\Lambda_f^2}$	$8g_f^2 \frac{4(\mu^2 - 1)^2 m_\chi^4 - 2(\mu^2 + 1)\mu^2 m_\chi^2 (4s + t) + \mu^4(2s + t)^2}{\mu^4}$

Table 1.1: Dimension 6 EFT operators [39] for the coupling of Dirac DM to fermions (column 2), together with the squared matrix elements DM-fermion scattering (column 5), where s and t are Mandelstam variables, $\mu = m_\chi/m_T$, and m_T is the target mass.

field will mix with the SM Higgs field, leading to couplings that depend on the fermion masses. The remaining bilinears have coupling constants that depend only on the cutoff scale, Λ_f .

1.2.4 From DM-Quark to DM-Nucleon Interactions

The operators in Table 1.1 describe dark matter interactions at the quark level, as these are the degrees of freedom most models are formulated with. However, we will primarily be interested in dark matter scattering with baryons, which requires taking the matrix element of the quark operators between baryon states, i.e. $\langle \mathcal{B} | \bar{q} \Gamma_q q | \mathcal{B} \rangle$. These matrix elements can be calculated through the application of Chiral Perturbation Theory (ChPT), giving a baryon level EFT. The operators of this EFT will have the same form as those in Table 1.1, with the obvious replacement of $f \rightarrow \mathcal{B}$, as well as additional form factors that take into account the structure of the baryons.

The required form factors for each operator have been calculated at zero mo-

momentum transfer in Ref. [40] and are given by

$$c_{\mathcal{B}}^S(0) = \frac{2m_{\mathcal{B}}^2}{v^2} \left[\sum_{q=u,d,s} f_{T_q}^{(\mathcal{B})} + \frac{2}{9} f_{T_G}^{(\mathcal{B})} \right]^2, \quad (1.17)$$

$$c_{\mathcal{B}}^P(0) = \frac{2m_{\mathcal{B}}^2}{v^2} \left[\sum_{q=u,d,s} \left(1 - 3 \frac{\bar{m}}{m_q} \right) \Delta_q^{(\mathcal{B})} \right]^2, \quad (1.18)$$

$$c_{\mathcal{B}}^V(0) = 9, \quad (1.19)$$

$$c_{\mathcal{B}}^A(0) = \left[\sum_{q=u,d,s} \Delta_q^{(\mathcal{B})} \right]^2, \quad (1.20)$$

$$c_{\mathcal{B}}^T(0) = \left[\sum_{q=u,d,s} \delta_q^{(\mathcal{B})} \right]^2, \quad (1.21)$$

where $v = 246$ GeV is the vacuum expectation value of the SM Higgs field, \mathcal{B} is the baryonic species, $\bar{m} \equiv (1/m_u + 1/m_d + 1/m_s)^{-1}$ and $f_{T_q}^{(\mathcal{B})}$, $f_{T_G}^{(\mathcal{B})} = 1 - \sum_{q=u,d,s} f_{T_q}^{(\mathcal{B})}$, $\Delta_q^{(\mathcal{B})}$ and $\delta_q^{(\mathcal{B})}$ are the hadronic matrix elements, determined either experimentally or by lattice QCD simulations. The specific values of these matrix elements for various baryons are provided in Appendix B.

The assumption of zero-momentum transfer is valid when considering interactions with momentum transfers $\lesssim 1$ GeV, such as in direct detection experiments. Once the momentum transfer exceeds this, the internal structure of the baryon begins to be resolved, and an additional momentum-dependent form factor is required to account for this [41],

$$F_{\mathcal{B}}(t) = \frac{1}{(1 - t/Q_0^2)^2}, \quad (1.22)$$

where t is the Mandelstam variable, and Q_0 is an energy scale that depends on the hadronic form factor. For simplicity, we will conservatively take $Q_0 = 1$ GeV for all operators. Putting everything together, the squared coupling constants for dark matter-baryon interactions are obtained by making the replacement

$$g_f^2 \rightarrow \frac{c_{\mathcal{B}}^I(t)}{\Lambda_q^4} \equiv \frac{1}{\Lambda_q^4} c_{\mathcal{B}}^I(0) F_{\mathcal{B}}^2(t), \quad I \in S, P, V, A, T, \quad (1.23)$$

in the matrix elements in the final column of Table 1.1.

1.3 Current Status of Dark Matter Constraints

In broad terms, there are three main ways that we can search for evidence of dark matter, often termed “make it, shake it, or break it”. “Make it” refers to the production of dark matter at colliders; “break it” to dark matter annihilation signals; and “shake it” to dark matter scattering. This section discusses the current status of these detection methods.

1.3.1 Collider Bounds

If dark matter is produced in a collider, it will simply leave the detector without depositing any energy. To determine if such an invisible particle was produced, conservation of energy-momentum is used to determine if any events are missing energy. In practice, what is searched for is missing momentum that is transverse to the beamline.

Currently, dark matter has not been observed to be produced in particle colliders. This non-observation has instead been used to constrain the dark matter mass and production cross-sections or couplings of various models. These limits are typically interpreted in a model-dependent manner, as different dark matter - Standard model couplings can significantly alter the production rates.

The ATLAS and CMS experiments at the LHC have performed analyses on various dark matter production mechanisms, including the exchange of a Z/Z' or Higgs, EFTs and heavy mediators, and mono-jet searches [42]⁷. Collider searches also offer complimentary probes of the dark matter-nucleon scattering cross-Section [43] as they probe the same underlying coupling of dark matter to quarks.

It is important to note that an observation of an invisible massive particle at a collider is not enough to infer that it is dark matter. Such an observation will only tell us that such a particle exists. On its own, it does not determine the abundance of the species or if it is stable in cosmological times. As such, it could be just a sub-component of a larger dark sector. To measure enough of the model parameters and determine these important properties, complimentary observations from direct or indirect detectors are often required.

⁷These searches refer to a single jet being produced alongside a pair of dark matter particles. This jet could be of Standard Model or dark sector origin, with the latter commonly referred to as “mono-X” searches.

1.3.2 Direct Detection Searches

In colliders, dark matter with mass below the collision energy can be produced as long as it couples to the electroweak or colour sectors of the SM. Direct detection experiments, on the other hand, must employ different experimental techniques to probe different mass ranges. For ALP dark matter that is wavelike, haloscope experiments such as ADMX [44] and MADMAX [45] attempt to convert ALPs to photons via the Primakoff effect. Searches for WIMP-like dark matter look for the dark matter scattering with some detector material, causing it to recoil and deposit energy into the detector. Given that our focus is on WIMP-like dark matter, this section will review the status of these experiments.

The differential rate at which the incoming flux of dark matter will scatter within a detector with N_T targets, as a function of the recoil energy, E_R , is given by

$$\frac{dR(E_R, t)}{dE_R} = N_T \frac{\rho_{\text{DM}}}{m_{\text{DM}}} \int_{v > v_{\min}}^{v_{\text{esc}}} v f(\vec{v} + \vec{v}_E) \frac{d\sigma}{dE_R} d^3v, \quad (1.24)$$

and depends on the quantities:

- v_{\min} is the minimum dark matter velocity required by kinematics for a scattering event to occur;
- $v_{\text{esc}} = 528 \text{ km s}^{-1}$ is the Milky Way escape velocity;
- \vec{v}_E is the velocity of the Earth through the dark matter halo⁸;
- $f(\vec{v} - \vec{v}_E)$ is the dark matter velocity distribution in the Earth's frame;
- $d\sigma/dE_R$ is the differential scattering cross-section.

Given the low interaction rate of dark matter, the expected event rate in detectors is very low, around one event per day, per kilogram of target material, per kiloelectronvolt deposited. To contend with such a low event rate, as much of the background noise needs to be reduced as possible. This is achieved by placing the detectors deep underground in laboratories that are naturally shielded from the majority of the cosmic rays incident on the surface.

The particle physics input into the scattering rate is encapsulated within the differential cross-section, $d\sigma/dE_R$. It is common to separate the cross-section into contributions from spin-dependent (SD) and spin-independent (SI) interactions such

⁸This accounts for the orbit of the Earth around the Sun, which induces an annual modulation in the flux of DM.

that

$$\frac{d\sigma}{dE_R} = \frac{(m_{\text{DM}} + m_T)^2}{m_T m_{\text{DM}}^2 v^2} (\sigma^{\text{SI}} |F_{\text{SI}}(E_R)|^2 + \sigma^{\text{SD}} |F_{\text{SD}}(E_R)|^2), \quad (1.25)$$

$$\sigma^{\text{SI}} \approx \sigma_0^{\text{SI}} A_T^2 \left(\frac{m_T}{m_p} \right)^2 \left(\frac{m_{\text{DM}} + m_p}{m_{\text{DM}} + m_T} \right)^2, \quad (1.26)$$

$$\sigma^{\text{SD}} \approx \sigma_0^{\text{SD}} \left(\frac{4(J_T + 1)}{3J_T} |\langle S_p \rangle + \langle S_n \rangle|^2 \right) \left(\frac{m_T}{m_p} \right)^2 \left(\frac{m_{\text{DM}} + m_p}{m_{\text{DM}} + m_T} \right)^2, \quad (1.27)$$

where m_T , A_T , J_T are the target mass, atomic mass number, and atomic spin, m_p is the mass of the proton, $\langle S_{p,n} \rangle$ are the expectation values of the protons and neutrons in the nucleus. The $\sigma_{p,0}^{\text{SI/SD}}$ are reference DM-proton scattering cross-sections evaluated in the zero-momentum transfer limit, with the form factors $F_{\text{SI/SD}}(E_R)$ depending on the recoil energy accounting for the finite size of the nucleus being probed at high momentum transfer. We have assumed that dark matter interacts the same with neutrons and protons for simplicity.

The SI interactions do not couple to the spin of the target and as such the nuclear cross-section is a coherent sum over all the nucleons. This results in an A_T^2 enhancement compared to the dark matter-nucleon cross-section. Experiments searching for SI interactions take advantage of this by using heavy noble gases as the target material, such as Xenon and Argon. On the other hand, the SD interactions do couple to the spin of the target. As the total cross-section is the sum of all the nucleon contributions, the result is expected to average out to zero unless there is an unpaired nucleon present. Chemicals that contain ^{19}F are the favourable targets as it contains an unpaired proton.

The current leading constraints on the dark matter-nucleon scattering cross-section are shown in Fig. 1.5, with SI in the top panel and SD in the bottom. The SI limits are set by liquid noble gas experiments (LZ [46], XENON-1T [47], PandaX-II [48], and DarkSide-50 [49]), solid-state cryogenic detectors (CRESST-III [50], CDMSlite [51], with projected DARWIN sensitivities [52]), and room temperature crystals (DAMA/LIBRA [53], and COSINE-100 [54]).

The constraints on the SD dark matter-proton scattering cross-section are shown in the bottom panel of Fig 1.5. Superheated liquid experiments such as the PICO-60 [55] as well as PICASSO [56] provide the leading constraints. These interactions are also constrained by many of the same experiments that focus on SI interactions, as they will inevitably contain isotopes with non-zero spin, such as ^{129}Xe and ^{131}Xe in XENONnT.

The orange dashed line represents the neutrino floor⁹, providing a lower limit on the cross-section that can be probed by conventional direct detection experiments. Below this line, detectors will become sensitive to the irreducible background from

⁹Calling this the “neutrino fog” rather than floor has been gaining traction in recent years [57]

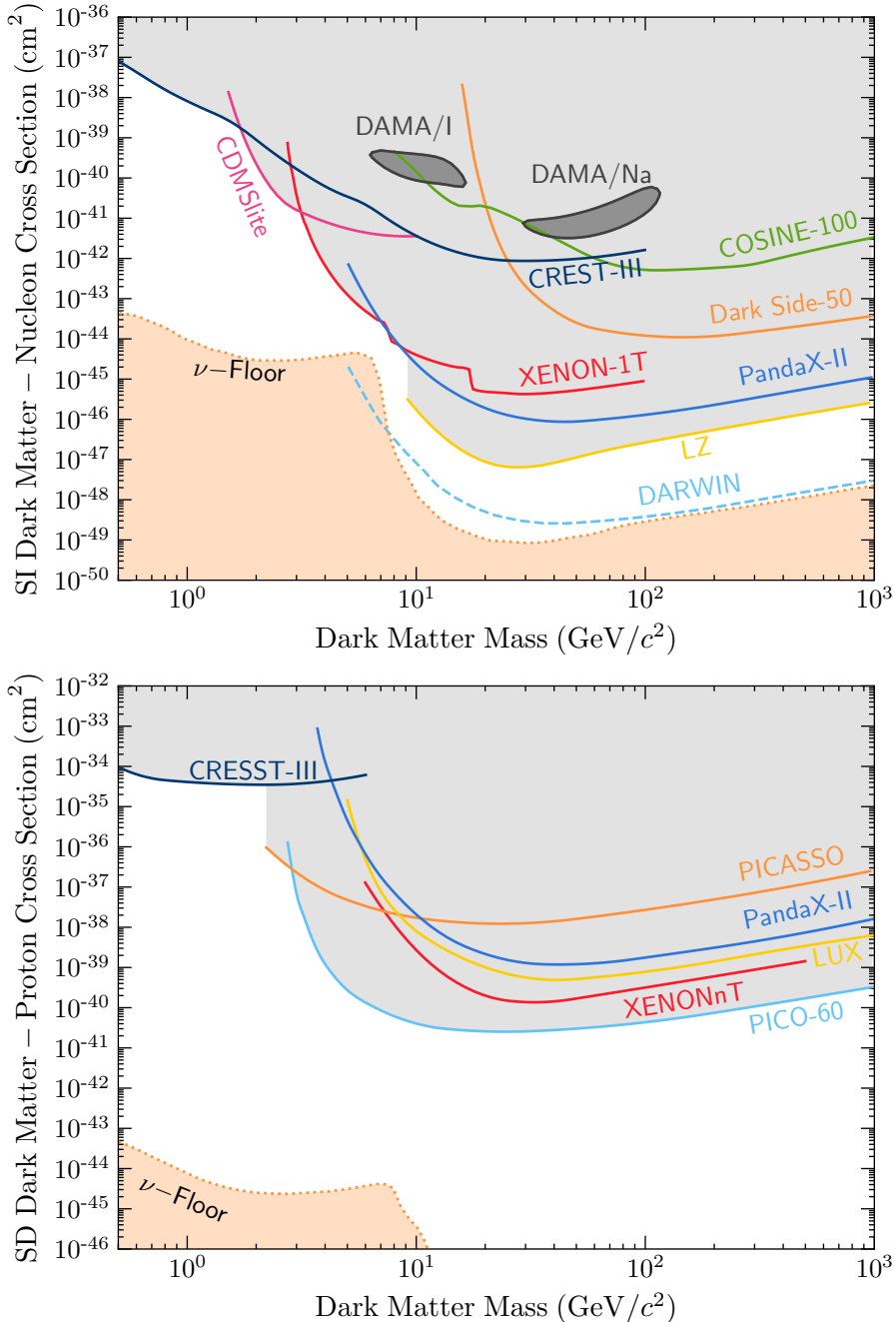


Figure 1.5: Current status of direct detection searches for dark matter. **Top:** Spin-independent dark matter-nucleon scattering. **Bottom:** Spin-dependent dark matter-proton scattering. Shaded regions above the coloured lines are excluded. Data was taken from the sources cited in the text.

Coherent Elastic Neutrino-Nucleus Scattering (CE ν NS). For dark matter masses $\lesssim 10\text{ GeV}$ the solar neutrino flux is the main background source, while the atmospheric neutrino flux becomes the dominant background for masses $\gtrsim 20\text{ GeV}$. A significant amount of effort is being put toward overcoming this limitation, with the main strategy being to take advantage of the directionality of dark matter flux [58]. Such experiments attempt to resolve the direction of the nuclear recoil event, giving information about the direction the incident particle came from. This could allow discrimination between dark matter events, that are expected to be from the direction of the Cygnus constellation, and the background solar and atmospheric neutrinos coming from the Sun and sky respectively.

Many experiments begin to lose sensitivity to low-mass dark matter ($m_{\text{DM}} \lesssim 10\text{ GeV}$) as the recoil energy of the targets falls below the threshold energy resolution of the detector. Current detectors can reach thresholds as low as $\sim \mathcal{O}(100\text{ eV})$, which is on the same order of magnitude as the recoil energy due to a 1 GeV dark matter collision.

On the other hand, above $\sim 10\text{ GeV}$ the sensitivities of the experiments all decrease at a rate inversely proportional to the dark matter mass. This is due to the interaction rate in Eq. 1.24 being proportional to the number of dark matter particles that pass through the detector, $N_{\text{DM}} = \rho_{\text{DM}}/m_{\text{DM}}$. As the local dark matter density is observed to be $\rho_{\text{DM}} = 0.4\text{ GeV cm}^{-3}$, N_{DM} decreases as the dark matter mass increases, and hence so do the detector sensitivities.

Direct detection limits also assume that the scattering cross-section is independent of the dark matter velocity and momentum transfer in the interaction. Given that the local dark matter dispersion velocity is predicted to be $v_d = 270\text{ km s}^{-1} \approx 10^{-3}c$, a back-of-the-envelope estimation for the momentum transfer gives $q_{\text{tr}} \lesssim 100\text{ MeV}$. Therefore, cross-sections proportional to v_{DM} or q_{tr} will result in significantly lower event rates and hence much weaker limits than the unsuppressed interactions.

1.3.3 Indirect Detection

This leads us to indirect detection methods, which can provide complementary probes to direct detection while also exploring interactions that are difficult, if not impossible, for terrestrial-based detectors to observe. Indirect detection experiments aim to infer the presence of dark matter through its annihilation or decay into Standard Model states. These searches look for dark matter annihilation products from astrophysical sources, including:

- Gamma-rays at terrestrial-based telescopes such as HESS [59–61], VERITAS [62–64], MAGIC [65, 66] and HAWC [67–70] as well as the Fermi-LAT [71–75] satellite;

- Neutrino signals at IceCube [76, 77], ANTARES [78–80], Super-K [81–83], and will be searched for at the upcoming Hyper-K [84–86], JUNO [87] experiments.
- Cosmic-Ray antimatter excess observed by the AMS-02 experiment [88, 89]

Signals from dark matter annihilation are best searched for by looking at regions where the dark matter density is expected to be high, boosting the annihilation rate. Natural places to look include the Galactic Centre [90, 91], dwarf-spheroidal galaxies [92], and celestial bodies where dark matter can accumulate over time. The latter scenario is central to this work and was pioneered by considering the effects of dark matter being captured within the Sun.

1.4 Dark Matter Signals from the Sun

Stars have a rich history of being used as astrophysical laboratories to help in the search for dark matter. Depending on the type of dark matter being searched for, there are various signals one can look for. Light bosonic dark matter, such as ALPs and dark photons, can be produced within the plasma of stars, altering the energy transport properties within them. This can ultimately lead to deviations in the evolution of the star, which can be used to place some of the strongest constraints on these models [93–95]. WIMP-like dark matter in the halo that couples to visible matter can scatter within the stars as they pass through. If the dark matter loses enough energy in these interactions, it can become gravitationally bound to the object and a population of dark matter will be accumulated within the star over time [23, 96–99].

This idea of WIMPs accumulating within the cores of stars has been applied extensively to the star closest to us, the Sun. The formalism for stellar capture of dark matter was set up by Gould [97, 98, 100] in the late 80’s, and has remained quite successful to this day, with many authors continuing to build upon these foundations over time [99, 101, 102].

Once the dark matter is captured, it will continue to scatter with the stellar constituents until it thermalises within the core of the Sun, collecting with an isothermal sphere. The radius of this sphere can be found by applying the virial theorem, with the gravitational potential given by

$$\Phi(r) = - \int_r^\infty \frac{GM_\odot(r')}{r'^2} dt', \quad (1.28)$$

$$\approx \frac{2}{3}\pi G\rho_{\odot,c}r^2, \quad (1.29)$$

assuming the density of the Sun within this region is constant, $\rho_{\odot,c}$. The resulting radius is

$$r_{\text{iso}}^2 = \frac{3T_{\odot}}{2\pi G m_{\text{DM}} \rho_{\odot}}. \quad (1.30)$$

The dark matter number density will follow a Gaussian profile,

$$n_{\text{iso}}(r) = n_0 \exp\left(-\frac{m_{\text{DM}}\Phi(r)}{T_{\odot}}\right), \quad (1.31)$$

$$= n_0 \exp(-r^2/r_{\text{iso}}^2), \quad (1.32)$$

where n_0 is a normalisation constant fixed by requiring that the total number of dark matter particles is

$$N_{\text{DM}} = \int d^3r n_{\text{iso}}(r). \quad (1.33)$$

In addition, dark matter velocity will follow a Maxwell-Boltzmann distribution,

$$f_{\text{MB}}(v) = 4\pi \left(\frac{m_{\text{DM}}}{4\pi T_{\odot}}\right)^{3/2} v^2 \exp\left[-\frac{m_{\text{DM}}v^2}{4T_{\odot}}\right]. \quad (1.34)$$

The time evolution of the total number of dark matter particles within the Sun is governed by three processes. Capture acts to increase the number over time, while annihilation and evaporation will reduce this number over time. This is described by the differential equation

$$\frac{dN_{\text{DM}}}{dt} = C - EN_{\text{DM}} - AN_{\text{DM}}^2, \quad (1.35)$$

where C and E are the capture and evaporation rates respectively, with A being related to the annihilation rate, Γ_{ann} through

$$\Gamma_{\text{ann}} = \frac{1}{2} \int dr^3 n_{\text{iso}}^2(r) \langle \sigma_{\text{ann}} v \rangle \quad (1.36)$$

$$\equiv \frac{1}{2} A N_{\text{DM}}^2, \quad (1.37)$$

where the factor of 1/2 accounts for each annihilation removing two dark matter particles from the Sun.

In this context, evaporation refers to the process in which dark matter can be ejected back out of the Sun by up-scattering¹⁰ off an energetic constituent. This

¹⁰Up-scattering refers to the interactions in which the dark matter gains rather than loses energy.

becomes increasingly important for lighter dark matter masses, as less energy will be required to boost the dark matter above the local escape velocity. Below a certain mass, the capture and evaporation come into equilibrium, and a net-zero amount of dark matter is contained within the Sun. This critical mass places a lower bound on the dark matter mass that can be probed through stellar capture and is named the evaporation mass, m_{evap} .

There are three regimes we are interested in solving this equation for. The simplest case is when evaporation and annihilation are both negligible, then the solution is simply,

$$N_{\text{DM}}(t) = Ct, \quad (1.38)$$

indicating that the dark matter will simply continue to grow over time.

Next, assume that annihilations are negligible ($A = 0$), while capture and evaporation are present. The result is

$$N_{\text{DM}}(t) = Ct \left(\frac{1 - e^{-Et}}{Et} \right), \quad (1.39)$$

where the first factor is the number of captured dark matter if evaporation is negligible. From this, we can estimate the evaporation mass by asking when the evaporation rate is large enough to cause a significant reduction in the number of captured dark matter particles relative to the $E = 0$ case. This can be expressed formally as [101]

$$\frac{1}{N_{\text{DM}}(m_{\text{evap}})} \left| N_{\text{DM}}(m_{\text{evap}}) - \frac{C(m_{\text{evap}})}{E(m_{\text{evap}})} \right| = \alpha, \quad (1.40)$$

where α is the fraction of evaporated dark matter, taken to be $\sim 10\%$.

Finally, consider the case in which evaporation can be neglected, $m_{\text{DM}} \gtrsim m_{\text{evap}}$. The solution in this regime is

$$N_{\text{DM}}(t) = \sqrt{\frac{C}{A}} \tanh(\sqrt{CA}t) \xrightarrow{t \rightarrow \infty} \sqrt{\frac{C}{A}}, \quad (1.41)$$

that reaches an equilibrium state between capture and annihilation for times longer than the characteristic scale, $t_{\text{eq}} = 1/\sqrt{CA}$. This state is known as capture-annihilation equilibrium.

The signals searched for depend on whether the dark matter can annihilate or not. If the dark matter is asymmetric, it cannot annihilate, and we can set $A = 0$ in Eq. 1.35. This leads to the population continuing to grow over time, with $N_{\text{DM}}(t) = Ct$ if evaporation is negligible. A large enough population of captured dark matter can alter the energy transport within the Sun, leading to the modifications of the solar neutrino flux, or even the solar structure itself [87, 103–105].

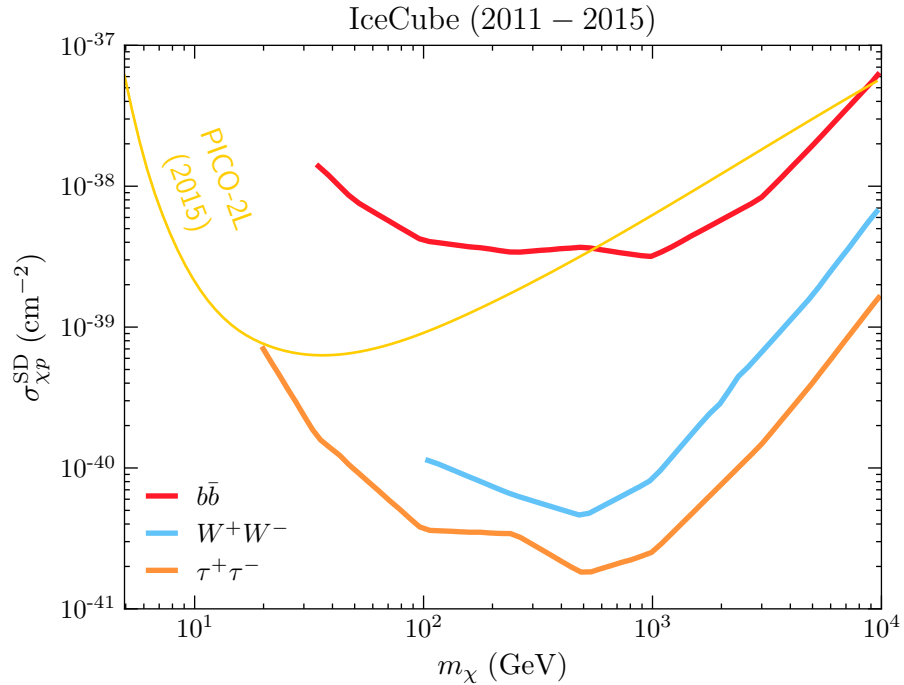


Figure 1.6: Limits on the SD dark matter-proton cross-section from the IceCube collaboration assuming 100% branching fraction to $b\bar{b}$ (red), W^+W^- (blue) or $\tau^+\tau^-$ (orange) final states. Also shown is the result from the PICO-2L DD experiment. This plot was recreated with data taken from Ref. [76].

Instead, if the dark matter can annihilate an equilibrium will eventually be reached between the capture and annihilation rates, and the total number of dark matter particles will be constant. If the annihilation products can escape the Sun, they can be searched for by various experiments depending on the nature of the final states. These could be neutrinos produced from the decays of other charged annihilation products [79–81, 106, 107], or to some other long-lived state that can escape the Sun and decay into visible states [108–112].

In comparison to DD searches, interpretation of indirect detection data will require additional model-dependent assumptions, namely the relevant annihilation channels of the dark matter. The most general limits can be placed by assuming that the dark matter only has a single annihilation channel, i.e. annihilation to a $\tau^+\tau^-$ final state 100% of the time. Under these assumptions, limits on the SD dark matter-proton cross-section have been placed that exceed current DD constraints, due to the rather large abundance of Hydrogen within the Sun. Constraints from the IceCube collaboration are shown in Fig. 1.6.

As stated above, the range of dark matter masses that can be probed by Solar capture is limited by the evaporation mass of ~ 3 GeV. Additionally, as with direct

detection, interactions that are suppressed by the momentum transfer/velocity of the dark matter will result in a significantly smaller capture rate and hence a smaller flux of annihilation products, resulting in weaker limits. These constraints also rely on the annihilation rate being sufficiently fast such that capture-annihilation equilibrium is reached within the lifetime of the Sun. If the annihilation cross-section is p -wave suppressed by the velocity of the annihilating dark matter, then this equilibrium may not be achieved. Should this be the case, then no limits can be placed as no flux of annihilation products to detect.

Overcoming the first of these issues requires either a colder star or one that is much heavier to decrease the evaporation mass. The second requires dark matter to scatter with the constituent material at relativistic energies to overcome the suppression in the cross-sections. Finally, the p -wave suppression can be alleviated if the dark matter annihilates within a very small volume in the core of the star, boosting the annihilation rate. Fortunately, there exist objects that can achieve all of these requirements, allowing for a wider variety of dark matter models to be explored than direct detection or traditional indirect detection experiments. These objects are known as compact objects, namely neutron stars and white dwarfs.

1.5 Compact Objects as Dark Matter Probes

The main goal behind this work is to explore how compact objects can be used to probe a wide variety of dark matter interactions that terrestrial direct detection experiments are insensitive to. By compact objects, we are referring to Neutron Stars (NSs) and White Dwarfs (WDs), and not Black Holes that also fall into this category.

Compact objects offer a unique laboratory for studying dark matter and its interactions with the Standard Model in environments unachievable anywhere else in the Universe. They generate strong gravitational fields and are composed of incredibly dense matter, with NSs reaching super-nuclear densities in their central cores. The capture rate within these objects is therefore enhanced due to these properties, with benefits over solar capture including:

- **Gravitational focusing of the DM flux:** The strong gravitational field will increase the impact parameter of the infalling dark matter. This increases the effective size of the capturing body, increasing the flux of dark matter passing through it.
- **Relativistic Interaction Energies:** In general, the infalling dark matter will be accelerated to (semi-)relativistic velocities ($\sim 0.2 - 0.7c$). Moreover,

the stellar constituents will also have relativistic energies. As such, interactions that are momentum/velocity dependent will suffer far less suppression than in DD experiments.

- **Large Number of Targets:** The extremely high densities of these objects correspond to a considerable number of targets for scattering to occur. This allows these objects to probe very small scattering cross-sections, with NSs in particular expected to reach as low as $\sim 10^{-45} \text{ cm}^2$.
- **Low Evaporation Masses:** Relative to the Sun, the evaporation mass in compact objects can be quite low, on the order of keV in some cases. This is due in part to the increased gravitational strength, but mainly to the significantly lower temperatures in old compact objects.

In the past, capture in NSs has been applied primarily in the context of seeding gravitational collapse into black holes [113–119], and the modifications of NS merger rates as well as the gravitational wave signatures of these mergers [120–123]. Capture in WDs has also been considered, with a variety of different applications of the capture process [124–129].

In recent years, dark matter induced heating of NSs has reemerged as a potential detection frontier [130–137]. It was shown that dark matter could reheat old, isolated NSs in our local neighbourhood¹¹ back up to temperatures that would cause them to radiate as blackbody peaked in the near-infrared. The aim is to locate the NSs with radio telescopes such as the Square-Kilometer-Array (SKA), and determine their age through their spin-down rate. Once located, the star's temperature can be determined through observations from infrared telescopes such as the James Webb Space Telescope (JWST). Knowing the age of the star allows us to compare its observed temperature to that predicted by models of neutron star cooling. A discrepancy between these two temperatures can indicate whether an additional heating source is present within the star.

This heating occurs in two stages. The dark matter will first kinetically heat the star through the scattering events that result in both its capture and thermalisation. We define *kinetic heating* to have been achieved once the dark matter has deposited 99% of its initial kinetic energy into the star. If the dark matter can annihilate, and assuming these annihilation products remain trapped within the star, its mass energy will be transferred to the star, further increasing the temperature of the star. In order for this *annihilation heating* to be efficient, capture-annihilation equilibrium must be achieved on a timescale shorter than the age of the star. These processes are illustrated in Fig. 1.7, with the temperatures shown assuming a NS in our local neighbourhood.

¹¹Local neighbourhood refers to the region within $\sim 1 \text{ kpc}$ of the Sun.

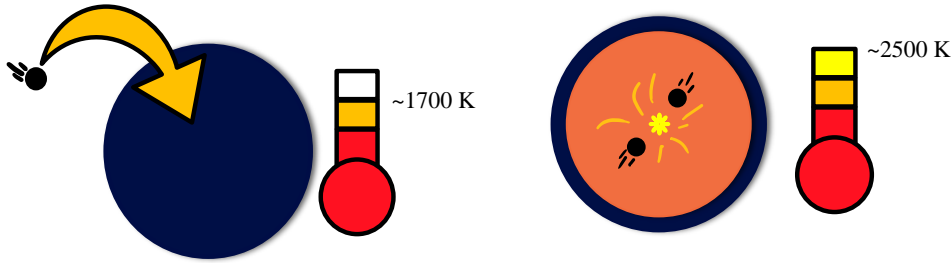


Figure 1.7: Illustration of DM-induced heating of compact objects. **Left:** kinetic heating due to DM scattering, raising the temperature to $\sim 1700\text{ K}$. **Right:** Annihilation heating contributes an additional $\sim 800\text{ K}$. This image is inspired by Ref. [130].

It is important to keep track of all the timescales involved in the heating process so that we can accurately determine the full extent of dark matter-induced heating. These timescales are the age of the star, t_* , the kinetic heating time, t_{kin} , and the capture-annihilation heating timescale, t_{eq} . In order for maximal heating to be achieved, we require $t_{\text{kin}} + t_{\text{eq}} < t_*$.

To accurately project how sensitive neutron star heating to dark matter interactions, one first requires an accurate calculation of the capture rate. However, existing calculations have relied on the formalism set up by Gould for capture in the Sun without fully accounting for the extreme physics present in these objects. Developing a consistent formalism for dark matter capture in compact objects, based on the Gould formalism, and applying this to dark matter induced heating is at the heart of this thesis.

1.6 Thesis Outline

Following this introduction, Chapter 2 covers the prerequisite knowledge of compact objects required for the remainder of this work. This includes a detailed overview of the general structure equations of relativistic stars, followed by details of the internal structure of both white dwarfs and neutron stars.

Chapters ?? and ?? of this thesis are devoted to reformulating Gould’s capture formalism to account for the physics specific to compact objects in a self-consistent manner. These include a relativistic treatment of the kinematics, using General Relativity to calculate the correct dark matter flux passing through the star, and accounting for Pauli blocking of the final state target using Fermi-Dirac statistics for the stellar constituents. In addition, we incorporate the internal structure of these objects by calculating the radial profiles for the relevant microscopic quantities (e.g.,

chemical potentials and number densities) via the adoption of a realistic equation of state.

Further considerations are required when considering dark matter interactions with the baryonic matter inside NSs. Due to the high density of the NS interior, the baryons undergo strong self-interactions and should not be treated as a free Fermi gas. Instead, adopting an equation of state that accounts for these interactions is required. These interactions modify the mass of the baryons, leading them to obtain an effective mass smaller than their value in vacuum. Furthermore, as we will see, the dark matter may interact with the baryons with momentum transfers on the order of 10 GeV. This is high enough that the dark matter will begin to resolve the internal structure of the baryon. To account for this, the momentum dependence of the baryon form factors that are typically neglected in direct detection and solar capture must be reintroduced.

This formalism is made in preparation for a thorough analysis of the timescales involved in the dark matter heating of compact objects, covered in Chapter ???. The energy deposited in both the kinetic and annihilation heating stages does not occur instantaneously, and the timescales involved in them need to be compared to the age of the star in question. We will define kinetic heating timescale as the time required for dark matter to deposit 99% of its initial kinetic energy into the star. For annihilation heating to occur, the dark matter must reach a state of capture-annihilation equilibrium within the stellar core. In standard calculations of this timescale, the dark matter must first become thermalised with the star. Only then can annihilations occur efficiently enough to heat the star.

We will work with the EFT operators in Table 1.1 that describe Dirac fermion dark matter interacting with Standard Model fermions. Each operator will be studied in isolation, i.e., by considering a Lagrangian that contains only one of the operators rather than a linear superposition of multiple. This way, we can analyse specific types of interactions independently, allowing us to take as model-independent an approach to the phenomenology as possible.

We present our concluding remarks on this thesis in Chapter ??.

2

A Primer on Compact Objects

Within the cores of stars, there exists a delicate balance between the gravitational forces pulling the matter inward, and the outward pressure generated by the thermonuclear fusion of light elements. This process begins as hydrogen is fused to form helium. Eventually, the hydrogen is depleted, allowing gravity to temporarily overcome the outward pressure, leading to the core to begin contracting. As this occurs, the gravitational potential energy is converted to thermal energy and the core eventually becomes hot enough to facilitate helium burning.

This cycle can continue as heavier and heavier elements are formed within the ever-increasingly hot stellar core. Lighter stars cannot reach the temperatures required to fuse light elements such as helium and carbon. If the star is heavy enough, iron will eventually be formed from the burning of silicon. As the fusion of iron nuclei is an endothermic process, it will not occur spontaneously, ending the cycle in heavy stars. Without a fuel source, the core will collapse under its gravity, leading to the death of the star.

What comes after this collapse depends on the mass of the progenitor star. Very light stars, $\lesssim 0.5M_{\odot}$, have lifetimes much longer than the age of the universe, and so are uninteresting to our current discussion. Moderately heavy stars, $1M_{\odot} \lesssim M_{\star} \lesssim 8M_{\odot}$, will continue burning fuel until the outer layers of the star are dispersed as it expands, leaving a core comprised of helium, carbon, and oxygen with small abundance of heavier elements. In this case, the core will begin to collapse until the Fermi degeneracy of the ultrarelativistic electrons is great enough to reestablish equilibrium, resulting in a White Dwarf (WD) [138].

Heavy stars, $\gtrsim 8M_{\odot}$, spectacularly end their lives in a type-II supernova event. This occurs when the core of the star exceeds the Chandrasekhar mass of $1.4M_{\odot}$, which cannot be supported by electron degeneracy pressure. The core itself will then collapse, leading to a shockwave that ejects the majority of the mass of the

star. All that will remain is an extremely dense core supported by neutron degeneracy pressure: a Neutron Star (NS) [139]. If the star was so massive that the gravitational forces overcome even the neutron degeneracy pressure, then the core collapses into a black hole.

These stellar corpses, white dwarfs, neutron stars, and black holes, are collectively known as compact objects. They have masses similar to or larger than the Sun, which is compressed into much smaller bodies with significantly larger surface gravities. These objects do not have a source of fuel, and spend the rest of their lives cooling through the emission of photons and neutrinos. For the remainder of this thesis, we will only be interested in white dwarfs and neutron stars and will collectively refer to these as compact objects, excluding black holes from this term.

This chapter is dedicated to discussing the aspects of the structure, composition, and observational status of compact objects relevant to this work

2.1 Structure Equations from General Relativity

Being comprised of matter in a highly dense state, the gravitational fields produced by neutron stars and white dwarfs are extremely strong. As such, modeling the structure of these objects falls into the domain of General Relativity (GR). Here we review the structure of static, spherically symmetric, compact objects, adapting the discussions in Refs. [140–142].

First, the static nature of the star means that the components of the metric are functions only of the spatial coordinates and not of time. Together with the assumption that the mass distribution of the star is spherically symmetric, this leads to a Schwarzschild-like metric of the form

$$ds^2 = -d\tau^2 = -B(r)dt^2 + A(r)dr^2 + r^2d\Omega^2, \quad (2.1)$$

with $d\tau$ the proper time interval. The functions $A(r)$, $B(r)$ depend only on the radial coordinate, and are often written as

$$A(r) = e^{2\Lambda(r)}, \quad B(r) = e^{2\Phi(r)}. \quad (2.2)$$

These functions are subject to the condition that at distances far from the star, $r \rightarrow \infty$, space-time must become flat, which translates to the boundary conditions

$$\lim_{r \rightarrow \infty} A(r) = \lim_{r \rightarrow \infty} B(r) = 1. \quad (2.3)$$

The matter within the star can be modeled as a perfect fluid, meaning we are neglecting any shear stresses and energy transport within the star. Such a fluid is

described by its pressure $P(r)$, density $\rho(r)$, and baryonic number density, $n_b(r)$, as well as the 4-velocity of the fluid $u^\mu(r)$. Being static, the only non-zero component of this velocity is the $\mu = 0$ component, which is fixed by the normalisation condition $g_{\mu\nu}u^\mu u^\nu = -1$ to be $u^0 = 1/\sqrt{B(r)}$. These quantities are used to construct the stress-energy tensor of the star, which takes the form

$$T^{\mu\nu} = (\rho + P)u^\mu u^\nu + Pg^{\mu\nu}. \quad (2.4)$$

The physics describing the underlying microscopic interactions within matter are encoded in an equation of state (EoS) that describes the relationship between the various thermodynamic quantities. This is typically expressed by providing the pressure as a function of the density, $P(\rho)$. It is often more convenient to parameterise the EoS by the number density of baryons n_b , and the entropy per baryon s , such that

$$P = P(n_b, s), \quad \rho = \rho(n_b, s). \quad (2.5)$$

The dependence on s turns out to be trivial in most scenarios involving compact objects, such as those considered throughout this work. The pressure in these stars arises from the degeneracy of the nucleons in NSs or the electrons in WDs, rather than from the thermal motion of the constituents as in main sequence stars. These thermal degrees of freedom will be frozen out at temperatures lower than the Fermi energy of the system, which is typically around $E_F \sim 10$ MeV in NSs or ~ 1 MeV in WDs, and correspond to temperatures of $T_* \sim 10^{11}$ K and $\sim 10^{10}$ K respectively. As these objects are expected to cool well below these temperatures quickly after formation [143–145], the entropy can be taken to be zero throughout the star. This allows us to reduce the two-parameter EoS to a simpler one-parameter one,

$$P = P(n_b, s = 0) = P(n_b), \quad \rho = \rho(n_b, s = 0) = \rho(n_b). \quad (2.6)$$

The structure of the star is therefore dictated by the quantities $A(r)$, $B(r)$, $P(r)$, $\rho(r)$, and $n_b(r)$. This system is determined by applying the Einstein field equations, $G^{\mu\nu} = 8\pi T^{\mu\nu}$, together with the energy-momentum conservation, $T^{\mu\nu}_{;\nu} = 0$, the EoS relations Eqs. 2.6, and the appropriate boundary conditions. The structure equations that come out of this analysis were first discovered concurrently by Tolman [146] and by Oppenheimer and Volkoff [147], and so are known as the TOV equations. They take the form

$$\frac{dP}{dr} = -\rho(r)c^2 \left[1 + \frac{P(r)}{\rho(r)c^2} \right] \frac{d\Phi}{dr}, \quad (2.7)$$

$$\frac{d\Phi}{dr} = \frac{GM(r)}{c^2 r^2} \left[1 + \frac{4\pi r^3 P(r)}{M(r)c^2} \right] \left[1 - \frac{2GM(r)}{c^2 r} \right]^{-1}, \quad (2.8)$$

$$\frac{dB}{dr} = 2B(r) \frac{d\Phi}{dr}, \quad (2.9)$$

where $M(r)$ is related to the metric factor $A(r)$ through

$$A(r) = \left[1 - \frac{GM(r)}{c^2 r} \right]^{-1}, \quad (2.10)$$

and is interpreted as the mass contained within a radius r . It obeys the mass equation

$$\frac{dM}{dr} = 4\pi r^2 \rho(r), \quad M(0) = 0, \quad (2.11)$$

which arises from the $\mu = \nu = 0$ component of the Einstein field equations. These equations are the general relativistic versions of the hydrostatic equilibrium equations of regular stellar structure, with Eq. 2.7 reducing to the familiar

$$\frac{dP}{dr} = -\frac{GM(r)}{r^2} \rho(r), \quad (2.12)$$

in the Newtonian limit, $GM(r)/c^2 r \ll 1$.

The radius of the star, R_\star , is identified as the point at which the pressure and density vanish, $P(R_\star) = \rho(R_\star) = 0$. In the region outside the star, $r > R_\star$, the total mass remains constant at the total mass of the star, $M(r \geq R_\star) = M_\star$, and so the only non-trivial structure functions in this region are the metric factors. Solving Eq. 2.9 for $B(r)$ with $P(r) = 0$ and constant $M(r) = M_\star$ leaves us with

$$A(r) = \left[1 - \frac{GM_\star}{c^2 r} \right]^{-1}, \quad B(r) = 1 - \frac{GM_\star}{c^2 r}, \quad \text{for } r > R_\star, \quad (2.13)$$

and the metric reduces to the familiar Schwarzschild metric outside the star. Continuity of the metric at $r = R_\star$ enforces a second boundary condition for $B(r)$,

$$B(R_\star) = 1 - \frac{GM_\star}{c^2 R_\star}. \quad (2.14)$$

The final boundary condition required is the central pressure $P(0) = P_c$ or, equivalently the central density/baryon number density. This is the only free parameter in the system and hence, for a given EoS, uniquely determines the stellar structure. Therefore, all the stars that are predicted by solving the coupled TOV + EoS system can be represented by a one-parameter sequence, represented by the mass-radius relation for the EoS model.

Given all the above, we can write a simple recipe for constructing a model of a compact object:

1. Model the constituent matter with an appropriate EoS.

2. Specify the central pressure of the star, P_c .
3. Integrate the coupled system of differential equations 2.7, 2.8, 2.11 from the centre of the star outward until the pressure vanishes.
4. Use the boundary condition Eq. 2.14 to normalise the metric function $B(r)$.

In general, additional quantities will be present in the EoS, such as chemical potentials and the speed of sound, which may be subject to additional constraints. These quantities will need to be calculated at each step of the integration alongside the other structure functions.

2.2 White Dwarfs

The fate of main sequence stars of mass below $M_\star \lesssim 8M_\odot$ is to end their lives as a white dwarf. Consequently, these compact stellar remnants, which are supported against gravitational collapse by electron degeneracy pressure, are the most abundant stars in the Galaxy ($\gtrsim 90\%$). They are born at very high temperatures and cool down over billions of years. Observations of the coldest WDs therefore contain information about the star formation history of the Galaxy.

The vast majority of observed WDs are composed primarily of carbon and oxygen, plus small traces of elements heavier than helium. At the extremely high densities found in WDs, $\rho_\star \sim 10^6 - 10^{10} \text{ g cm}^{-3}$, electrons are strongly degenerate and determine the WD equation of state (EoS) and internal structure. The stellar core resembles a Coulomb lattice of ions surrounded by the degenerate electron gas, implying that the WD core is isothermal and a very good thermal conductor. The degenerate core is enclosed by a thin envelope that accounts for $\lesssim 1\%$ of the total mass [148].

The outer layers form an atmosphere that is rich in lighter elements such as hydrogen or helium, where the exact composition depends on the evolution of the WD progenitor and changes as the WD cools. This atmosphere is non-degenerate and extremely opaque to radiation, with an EoS that is subject to finite temperature effects. We limit our discussion to the core region of the WD, which accounts for the vast majority of its mass.

2.2.1 The FMT Equation of State

In the limit of zero temperature, the simplest way to obtain the WD EoS is to assume an ideal Fermi gas of degenerate electrons, for a WD that is primarily composed of a single element. Corrections to the non-interacting electron picture

were introduced early by Salpeter [149]. By introducing the Wigner-Seitz (WS) cell approximation and assuming point-like nuclei, Salpeter obtained an analytical EoS that accounts for interactions between electrons and ions as well as other Coulomb corrections. These corrections, in general, depend on the chemical composition of the star.

More recently, it has been shown that the treatment of matter at high pressures presented by Feynman, Metropolis and Teller [150] can be extended to consistently take into account weak interactions and relativistic effects [151, 152], and incorporates Coulomb corrections in a more natural manner than the Salpeter EoS. The resulting Feynman-Metropolis-Teller (FMT) EoS is obtained by considering a relativistic Thomas-Fermi model within Wigner-Seitz cells of radius R_{WS} . For degenerate, relativistic, electrons, the equilibrium condition is that the Fermi energy, E_e^F , is constant within the cell,

$$E_e^F = \sqrt{(p_e^F)^2 + m_e^2} - m_e - eV(r) = \text{constant}, \quad (2.15)$$

where $V(r)$ is the Coulomb potential inside the cell, p_e^F is the electron Fermi momentum, m_e is the electron mass and e is the electric charge. To obtain an integrable solution for the energy density near the origin, it is necessary to introduce a finite size for the nucleus, with radius $R_c = \Delta\lambda_\pi Z^{1/3}$, where λ_π is the pion Compton wavelength, $\Delta \approx (r_0/\lambda_\pi)(A/Z)^{1/3}$, Z is the proton number, A is the atomic mass, and r_0 is an empirical constant ~ 1.2 fm. The proton and electron number densities inside the cell are then given by

$$n_p = \frac{(p_p^F)^3}{3\pi^2} = \frac{3Z}{4\pi R_c^3} \theta(R_c - r) = \frac{3}{4\pi} \left(\frac{1}{\Delta\lambda_\pi} \right)^3 \theta(R_c - r), \quad (2.16)$$

$$n_e = \frac{(p_e^F)^3}{3\pi^2} = \frac{1}{3\pi^2} \left[\hat{V}^2(r) + 2m_e \hat{V}(r) \right]^{3/2}, \quad (2.17)$$

$$\hat{V}(r) = eV(r) + E_e^F. \quad (2.18)$$

The Coulomb potential satisfies the Poisson equation

$$\nabla^2 V(r) = -4\pi e[n_p(r) - n_e(r)], \quad (2.19)$$

with the requirement of global charge neutrality of the cell enforcing the boundary conditions

$$\left. \frac{dV}{dr} \right|_{r=R_{\text{WS}}} = V(R_{\text{WS}}) = 0. \quad (2.20)$$

In practice, it is beneficial to work with dimensionless quantities, and so we define $x = r/\lambda_\pi$ and $\chi(r) = r\hat{V}(r)$, such that $x_c = R_c/\lambda_\pi$ and $x_{\text{WS}} = R_{\text{WS}}/\lambda_\pi$. Using

these expressions results in the relativistic Thomas-Fermi equation

$$\frac{1}{3x} \frac{d^2\chi}{dx^2} = -\frac{\alpha_{\text{EM}}}{\Delta^3} \theta(x_c - x) + \frac{4\alpha_{\text{EM}}}{9\pi} \left[\frac{\chi^2(x)}{x^2} + 2 \frac{m_e}{m_\pi} \frac{\chi(x)}{x} \right]^{3/2}, \quad (2.21)$$

with the boundary conditions

$$\chi(0) = 0, \quad \left. \frac{d\chi}{dx} \right|_{x_{\text{WS}}} = \frac{\chi(x_{\text{WS}})}{x_{\text{WS}}}. \quad (2.22)$$

By solving these equations, we can obtain the relevant thermodynamic quantities, namely the electron and proton number densities, electron chemical potential, and the energy and pressure of the cell. The electron chemical potential is obtained by evaluating Eq. 2.15 at the cell radius, noting that the Coulomb potential must vanish there, which results in the usual expression¹

$$\varepsilon_{F,e} = \sqrt{(p_e^F)^2 + m_e^2} - m_e. \quad (2.23)$$

The energy and pressure of the cell can then be obtained following the analysis presented in ref. [152]. The cell energy gains contributions from the nuclear mass, electron kinetic energy, and Coulomb interactions, such that

$$E_{\text{tot}} = M_N + E_k + E_C, \quad (2.24)$$

$$E_k = \int_0^{R_{\text{WS}}} 4\pi r^2 [\mathcal{E}_e(r) - m_e n_e(r)] dr, \quad (2.25)$$

$$E_C = \frac{1}{2} \int_{R_c}^{R_{\text{WS}}} 4\pi r^2 e [n_p(r) - n_e(r)] V(r) dr, \quad (2.26)$$

where

$$\mathcal{E}_e(r) = \frac{1}{\pi^2} \int_0^{p_e^F} p^2 \sqrt{p^2 + m_e^2} dp, \quad (2.27)$$

is the electron energy density, and M_N is the mass of the nucleus. The energy density of the cell is then simply

$$\rho_{\text{WS}} = \frac{E_{\text{tot}}}{V_{\text{WS}}}, \quad (2.28)$$

where $V_{\text{WS}} = 4\pi R_{\text{WS}}/3$ is the volume of the WS cell. The only contribution to the internal cell pressure comes from the electrons,

$$P_e(r) = \frac{1}{3\pi^2} \int_0^{p_e^F} \frac{p^4}{\sqrt{p^2 + m_e^2}} dp, \quad (2.29)$$

¹We use the symbol $\varepsilon_{F,i}$ to represent the chemical potential minus the mass of a particle species i , reserving $\mu_{F,i}$ for the full chemical potential.

EoS	WD₁	WD₂	WD₃	WD₄
ρ_c [g cm ⁻³]	1.47×10^6	3.84×10^7	3.13×10^8	2.31×10^{10}
M_\star [M_\odot]	0.440	1.000	1.252	1.384
R_\star [km]	9.39×10^3	5.38×10^3	3.29×10^3	1.25×10^3
$v_{\text{esc}}(R_\star)$ [km/s]	3.72×10^3	7.03×10^3	1.01×10^4	1.71×10^4

Table 2.1: Four configurations for white dwarfs composed of carbon, with an FMT EoS. Shown are the central densities, ρ_c , stellar mass M_\star and radius R_\star , and escape velocity at the edge of the WD, v_{esc} .

with the total pressure of the cell being $P_{\text{tot}} = P_e(R_{\text{WS}})$. Finally, the EoS is then obtained by solving Eq. 2.21 for various cell radii, yielding a relation between $E_{\text{tot}}(R_{\text{WS}})$ and $P_{\text{tot}}(R_{\text{WS}})$ parameterised by the radius of the Wigner-Seitz cell.

Different WD configurations can be obtained, assuming a non-rotating spherically symmetric star, by solving the Tolman-Oppenheimer-Volkoff (TOV) equations [146, 147] coupled to the FMT EoS with different initial conditions for the pressure at the centre of the star. In Fig. 2.1 we show radial profiles for n_e (top left), $\varepsilon_{F,e}$ (top right), and escape velocity v_{esc} (bottom) for the carbon WDs in Table 2.1. Note that the difference in radius between the lightest and heaviest WD in Table 2.1 spans almost one order of magnitude, while the electron number densities in the core can vary up to 4 orders of magnitude (see top left panel). As expected, electrons are more degenerate in more compact WDs and become relativistic (see top right panel). The escape velocity can reach $\mathcal{O}(0.1 c)$ at the interior of the most compact WDs, while for very low mass WDs it can be as low as $\sim 0.003 c$.

The mass-radius relations obtained from a zero-temperature EoS begin to deviate from observations for low-mass WDs. To address this discrepancy, finite temperature effects can be introduced to the EoS [153]. The extension to finite temperatures is made by reintroducing the temperature dependence in the Fermi-Dirac distributions. Now, the electron chemical potential is no longer simply the Fermi energy of the system due to thermal corrections. Define the finite temperature Fermi-Dirac integrals of degree s as

$$F_s(\eta, \beta) = \int_0^\infty \frac{t^s \sqrt{1 + (\beta/2)t}}{1 + e^{t-\eta}} dt, \quad (2.30)$$

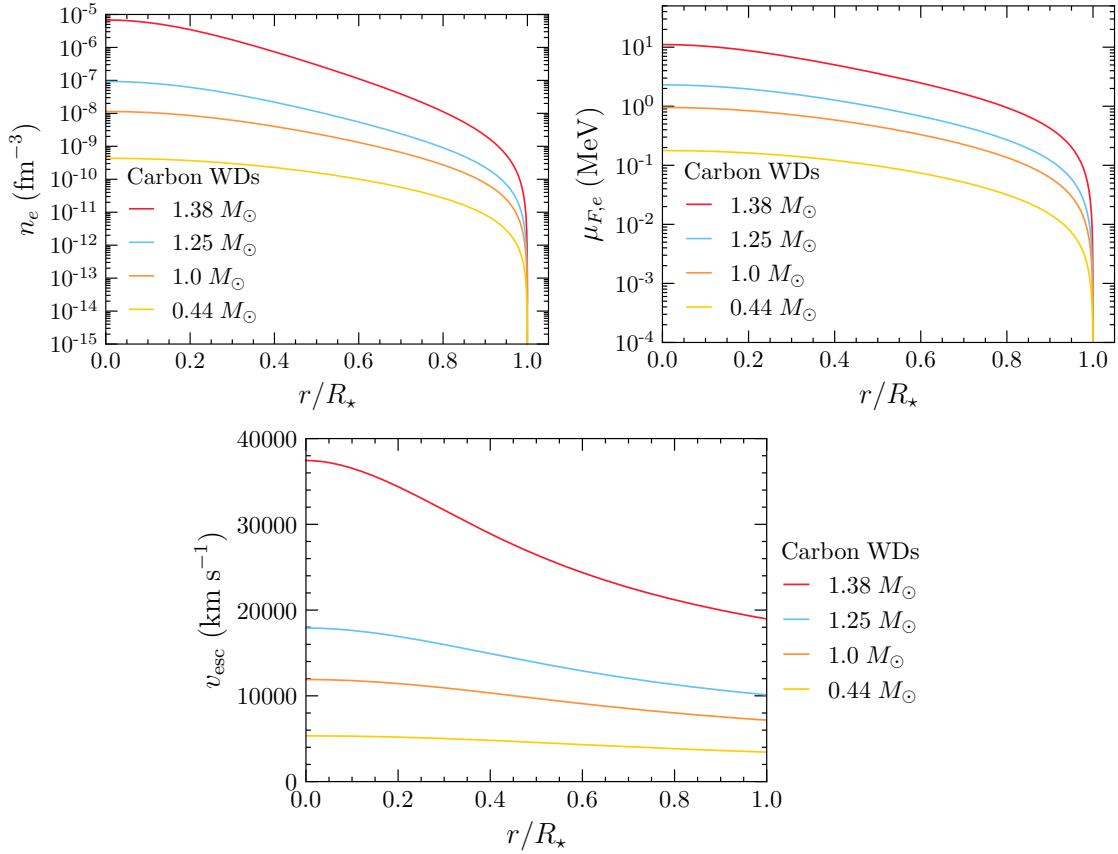


Figure 2.1: Electron number density (top left), chemical potential (top right), and escape velocity (bottom) radial profiles for the carbon WDs with FMT EoS in Table 2.1. The radial distance of each profile has been normalised to the radius of the star.

where we define the dimensionless quantities

$$t = \frac{E_e - m_e}{T_\star}, \quad (2.31)$$

$$\eta = \frac{\varepsilon_{F,e}}{T_\star}, \quad (2.32)$$

$$\beta = \frac{T_\star}{m_e}, \quad (2.33)$$

for a star at temperature T_\star . The Thomas-Fermi equilibrium condition within the WS cell is now given by

$$\varepsilon_{F,e}(r) - eV(r) = T_\star\eta(r) - eV(r) = \text{constant}, \quad (2.34)$$

with the Coulomb potential vanishing at the boundary of the cell as before. We now make the change of variables into the dimensionless quantities $\chi/r = \varepsilon_{F,e}/(\hbar c)$ and $x = x/x_{\text{WS}}$ so that the Poisson equation 2.19 becomes

$$\frac{d^2\chi}{dx^2} = -4\pi\alpha_{\text{EM}}x \left(\frac{3}{4\pi\Delta^3}\theta(x_c - x) - \frac{\sqrt{2}}{\pi^2} \left(\frac{m_e}{m_\pi} \right)^2 [F_{1/2}(\eta, \beta) + \beta F_{3/2}(\eta, \beta)] \right), \quad (2.35)$$

$$\eta(x) = \left(\frac{1}{\lambda_\pi T_\star} \right) \frac{\chi(x)}{x}, \quad (2.36)$$

with the same boundary conditions as in Eq. 2.22.

The total energy of the cell remains very similar to the zero-temperature case, with the main differences being that it gains a contribution from the thermal motion of the nucleus,

$$E_{\text{th}} = \frac{3}{2}T_\star, \quad (2.37)$$

and that the electron energy density is now given by

$$\mathcal{E}_e = m_e n_e + \frac{\sqrt{2}}{\pi^2} m_e^4 \beta^{5/2} [F_{3/2}(\eta, \beta) + \beta F_{5/2}(\eta, \beta)]. \quad (2.38)$$

The pressure of the cell will now gain contributions from the motion of the nucleus as well as the electron, such that the total pressure is

$$P_{\text{tot}} = P_N + P_e, \quad (2.39)$$

$$P_N = \frac{2}{3} \frac{E_{\text{th}}}{V_{\text{WS}}} = \frac{T_\star}{V_{\text{WS}}}, \quad (2.40)$$

$$P_e = \frac{2^{3/2}}{3\pi} m_e^4 \beta^{5/2} [F_{3/2}(\eta(x_{\text{WS}}), \beta) + \beta F_{5/2}(\eta(x_{\text{WS}}), \beta)]. \quad (2.41)$$

In Fig. 2.2 we show the Mass-Radius relations obtained from the zero temperature FMT EoS together with several finite temperature configurations. As can be seen, the deviations from the zero temperature approximation begin at rather high temperatures, $T_\star \gtrsim 10^7$ K, for masses $\lesssim 0.6M_\odot$. Additionally, we show a random selection of 20,000 WDs presented in the Gaia early data release 2 (EDR2) report [154] as the yellow-red dots. The colour of the dot represents the internal temperature of the corresponding WD. The core temperature must be determined from the observed effective surface temperature of the star², with the relation between the two depending on the composition of the WD atmosphere. To obtain the central temperature from the reported effective temperatures, we use the WD cooling sequences generated in Ref. [145]³ assuming a thin hydrogen atmosphere. In general, there is good agreement between the mass-radius relations derived from the finite temperature FMT EoS and the observed internal temperatures of the WDs.

Given the non-linear nature of the differential equations that describe the FMT EoS (both at zero and finite temperatures), solving the system is a numerically challenging task. As there are no publically available resources to help solve these systems, a significant amount of time was put into solving this problem. As such, we have outlined in Appendix ?? the method employed in numerically solving the differential equations.

2.2.2 Observational Status

The rate at which the energy of the WD core is radiated away is determined by the outer non-degenerate layers of the atmosphere. Spectroscopic observations shed light on the composition of these layers and can be used to classify WDs in terms of \sim six spectral types. Most of the observed WDs lie in the DA (hydrogen-rich) and DB (helium-rich) categories. Note that as WDs slowly cool, they undergo spectral evolution. There is a well-defined relation between their luminosity and age (cooling time) that, together with recent breakthroughs in theory and observations, allow us to estimate the age of the stars within the solar neighbourhood and to date the nearest star clusters [155–159].

Over the past few decades, WDs have been extensively observed using photometry and spectroscopy. Most of the WDs have been discovered by large area surveys, such as the Sloan Digital Sky Survey (SDSS) [160]. However, these lo-

²The effective temperature is the temperature that characterises the surface of the star. Assuming that WDs are perfect blackbody emitters, the luminosity will be $L_\gamma = 4\pi\sigma_{SB} R_\star^2 T_{\text{eff}}^4$, where σ_{SB} is the Stefan–Boltzmann constant.

³The cooling sequence data can be obtained from
<http://www.astro.umontreal.ca/bergeron/CoolingModels>.

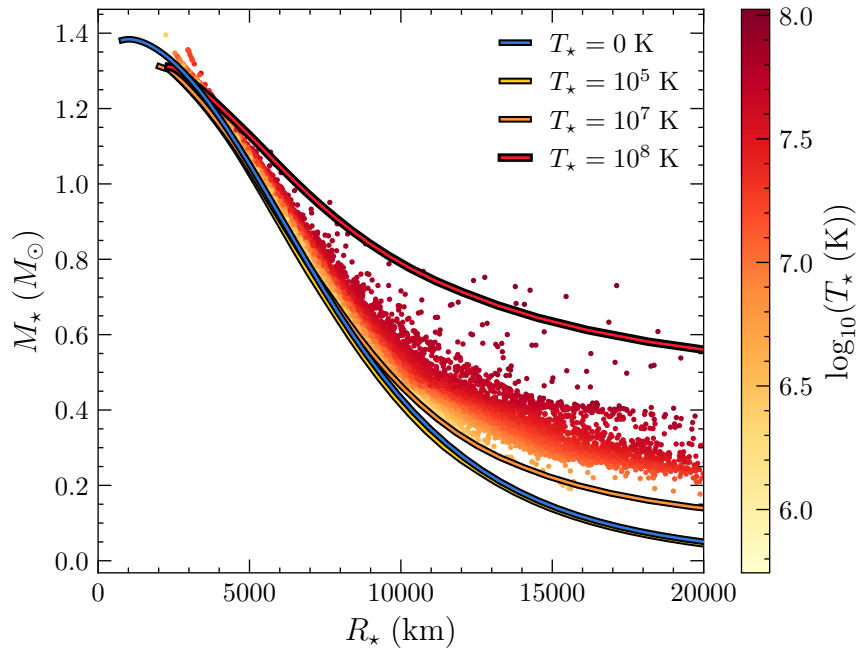


Figure 2.2: Mass-Radius relation of WDs calculated from the FMT EoS in the zero-temperature approximation (dark blue), at 10^5 K (yellow), 10^7 K (orange), and 10^8 K (red), together with observed WDs from Gaia EDR2 observations [154] (yellow-red dots). The colour of the dots represents the surface temperature of the WD inferred from cooling models [145].

cal samples are dominated by young WDs with relatively high effective temperatures ($T_{\text{eff}} \gtrsim 10^4$ K) [161–165]. Recently, the local volume sample of nearby stars within ~ 100 pc has been catalogued by the Gaia spacecraft [166, 167], an astrometric mission. New WD candidates have been identified [154], followed by dedicated spectroscopic observations [168, 169], increasing the local sample of cool WDs ($T_{\text{eff}} \lesssim 5000$ K).

On the other hand, globular clusters (GCs) are the oldest known stellar systems in the Galaxy. Among them is Messier 4 (M4), also classified as NGC 6121, which is the closest globular cluster to Earth being ~ 1.9 kpc away [170–172]. The age of M4, 11.6 Gyr, has been estimated using observations of faint cold WDs with the Hubble Space Telescope (HST) [155, 157]. This HST data, corrected for reddening and extinction, was converted into luminosities and effective temperatures in ref. [126]. From these calculations, it is possible to infer WD radii and their corresponding masses by assuming a mass-radius relation.

2.3 Neutron Stars

Being the end product of massive, $\gtrsim 8M_{\odot}$, stars, there are significantly fewer NSs than the WDs discussed above. As their name suggests, they are composed primarily of neutrons, which provide the degeneracy pressure required to prevent the gravitational collapse of the star. The internal structure of an NS is significantly more complicated than that of a WD. Broadly speaking, an NS can be divided into five main regions. We give an overview of the important features of each of these regions, and point the reader to Refs. [173–180] for more indepth discussions. Working from the outside in, these regions are:

Atmosphere

The atmosphere is an extremely thin layer of plasma that makes up less than 1% of the NS mass. However, it plays an extremely important role as the observed spectrum radiation emitted by the star must pass through this region [174, 175].

Outer Crust

The outer crust is the thin layer of ionized Iron-56 nuclei that extends down until the density reaches the neutron drip point, $\rho_{\star} = \rho_{\text{ND}} \sim 4.3 \times 10^{11} \text{ g cm}^{-3}$. This is the density at which neutrons begin to drip from the nuclei as their chemical potentials approach zero. The ionized electrons form a non-relativistic but degenerate gas,

with their chemical potentials increasing as the density increases. This leads to the “neutronisation” of the nuclei as the beta-capture of electrons by protons increases.

Inner Crust

The density within the inner crust spans the range between $\rho_{\text{ND}} \lesssim \rho_* \lesssim 0.5\rho_0$, with $\rho_0 \sim 2.8 \times 10^{14} \text{ g cm}^{-3}$ the nuclear saturation density (i.e. the density of nuclear matter) [174, 175, 181]. Here, the neutrons that have dripped from the nuclei will potentially form a superfluid. Towards the crust-core boundary, the nuclear lattice begins taking on interesting topological structures that are distinguished by the configuration of the voids in the lattice. These are known as the so-called *pasta phases* [182–184] of nuclear matter, which include 2D sheets (lasagna), cylindrical rods (spaghetti), or 3D clumps (gnocchi). Eventually, towards the crust-core interface the nuclear matter transitions into a uniform medium⁴.

Outer Core

Once densities go above $0.5\rho_0$, the nuclear clusters will dissolve into a homogenous fluid that is composed of neutrons, protons, electrons, and muons known as *npeu* matter. The relative abundances of the species, $Y_i = n_i/n_b$, are dictated by the conditions of electrical neutrality and beta-equilibrium. Charge neutrality dictates that the abundances of the charged particles obeys

$$Y_p = Y_e + Y_\mu, \quad (2.42)$$

while beta-equilibrium refers to the balance between the weak decays of neutrons and the electron/muon capture by the protons,



with $\ell = e, \mu$. Muons will begin to replace electrons in these reactions once the electron chemical potential exceeds the mass of the muon, $\mu_{F,e} \gtrsim m_\mu = 105.7 \text{ MeV}$. As neutrinos are assumed to escape the NS once produced, the relation between the chemical potential of the leptons is simply

$$\mu_{F,e} = \mu_{F,\mu}. \quad (2.45)$$

The outer core region ends once the density reaches $\rho_* \sim 2\rho_0$, and we transition into the inner core.

⁴The nuclear minestrone, if you will.

Inner Core

The densities within the inner cores of NSs extend between $2\rho_0 \lesssim \rho_* \lesssim (10 - 15)\rho_0$ and are hence a mystery to this day. As the density greatly exceeds any material that can be produced in a laboratory, the exact composition of this region is unknown and depends on the equation of state one adopts to describe it. Some of the more well-known candidates are

- A hyperonic matter component, i.e. nucleons containing a valence strange quark. These appear once the neutron chemical potential equals that of the Λ^0 hyperon, with the Ξ^- appearing once its chemical potential equals the sum of the chemical potentials of the neutrons and electrons [176, 185].
- Pion/Kaon condensates. These are Bose-Einstein condensates of pion/kaon-like excitations [186–191].
- A quark-gluon plasma comprised of deconfined u , d and s quarks and gluons [192–194].

2.3.1 Observational Status

Unlike the WDs discussed above, there are significantly fewer NS observations to constrain the EoS. However, recent years have seen significant strides in furthering our understanding of matter at super-nuclear densities, both from a theory and observational standpoint. On the theoretical side, these advances come from developments in chiral EFT allowing more detailed modelling of nuclear interactions [195–197]. The observational data has been bolstered thanks to the onset of gravitational wave astronomy due to the LIGO-VIRGO experiment [198–200] and the launch of the Neutron star Interior Composition Explorer (NICER) X-ray timing instrument.

Ultimately, what is needed to further constrain the NS EoS are more precise observations of NS masses and radii, which can be obtained from various observational techniques. NS masses have historically been much easier to measure than their radii. In particular, masses of NSs in binary systems can be precisely determined as the underlying gravitational theories are well-understood today [178, 179, 201–203]. The radii must be determined by assuming the NSs emit a blackbody spectrum, however, this method is only reliable for cool NSs where the atmospheric models are well understood [203].

The NICER experiment can provide much more precise measurements of NS radii than previous methods. This is achieved by measuring the X-ray pulse profiles of pulsars, that are sensitive to how light bends around the star. This provides information on the compactness of the star, GM_*/R_*c^2 , that can be used to determine

M_\star and R_\star given that the mass can usually be determined through other means. The heaviest NS observed to date, the millisecond pulsar PSR J0740+6620 [204, 205], had its mass determined by measuring the relativistic Shapiro time delay [206]⁵ of the radio signal, allowing the radius to be obtained once the compactness was measured [207]. Refined analyses result in a mass of $2.08 \pm 0.07 M_\odot$ [208] and a radius of $12.39^{+1.30}_{-0.98}$ km [205] or $13.71^{+2.61}_{-1.50}$ km [204] at 68% confidence levels.

Gravitational wave astronomy offers an alternative and independent determination of NS masses and radii to the electromagnetic observations above. The best candidate events for this analysis are NS binary mergers, though these are expected to be an uncommon occurrence. As the NSs inspiral toward each other, they will begin to deform due to the tidal forces they induce on one another [209]. This deformation will alter the waveform observed at the detectors, with the shift in the phase of the waveform depending on the mass ratio, $q = M_2/M_1 < 1$, the chirp mass of the system, $\mathcal{M}_{\text{chirp}} = (M_1 M_2)^{3/5}/(M_1 + M_2)^{1/5}$, and a combination of the tidal deformabilities, $\tilde{\Lambda}$. The latter refers to how susceptible the star is to deformation due to tidal forces acting upon it, with larger values corresponding to less compact objects. Comparing the observed waveform to that determined from precise numerical simulations allows constraints to be placed on these parameters, and ultimately on the masses and radii of the merging NSs.

Furthermore, the electromagnetic emission from the remnant object provides information about the maximum mass an NS can achieve. If the mass of the remnant object is too large, it will collapse into a black hole, and it is highly unlikely that a gamma-ray burst will occur. If the remnant does not immediately collapse, then its mass and how it is rotating determines whether it will be hydrodynamically stable, unstable, or metastable against gravitational collapse. A remnant that undergoes differential rotation⁶ can support heavier masses than one that is uniformly rotating. Hence, the afterglow spectrum can inform us as to how the star is rotating. Comparing the maximum mass supported by this rotation to the initial mass after inspiral yields an upper bound on the maximum NS mass achievable.

To date, the only confirmed NS-NS merger is the merger event GW170817 observed at LIGO-VIRGO in 2017 [199, 200], with the gamma-ray burst counterpart signal observed at the Fermi Gamma-ray Burst Monitor and INTEGRAL satellite [198]. These observations led to the constraint that the radius of a $1.4 M_\odot$ NS has an upper bound of $R_{1.4} < 13.3$ km [210, 211], and that the maximum NS mass must be $M_{\text{NS}}^{\text{MAX}} < 2.18 M_\odot$ [198]. These constraints on the neutron star mass-radius relation are shown as the shaded turquoise and red regions of Fig 2.3.

⁵This refers to the time it takes for light to move out of a gravitational well taking longer than the naive Newtonian prediction due to the curvature of space-time.

⁶This is when components of the star at different latitudes have different angular velocities.

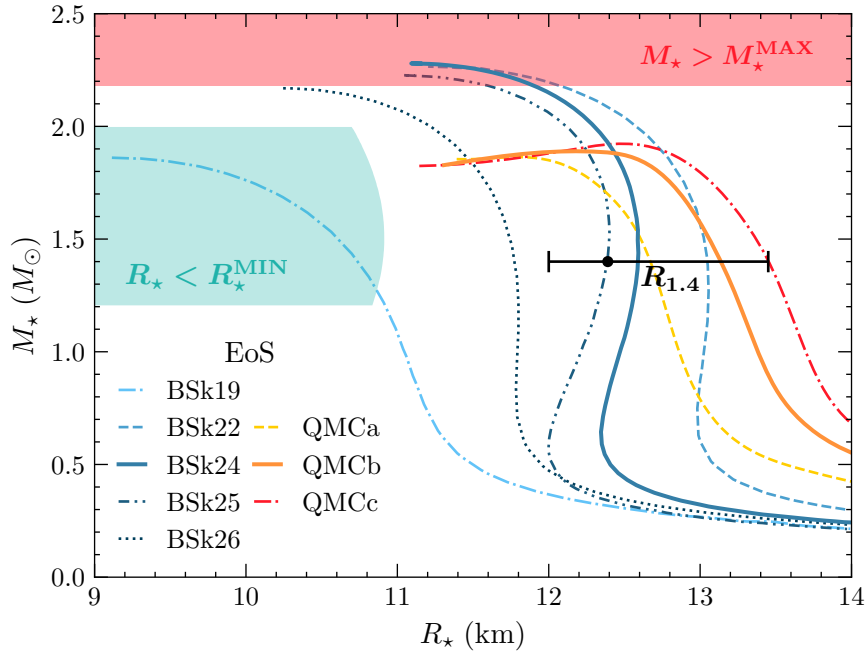


Figure 2.3: Neutron Star Mass-Radius relation predicted by the BSk (blue lines) and QMC (red lines) EoSs. Constraints obtained from the gravitational wave event GW170817 are shown as the shaded regions, with the lower bound on the radius in turquoise, and the maximum NS mass possible in red. The line band labeled $R_{1.4}$ indicates the constraints on the radius of a $1.4 M_\odot$ NS.

2.3.2 Neutron Star Equations of State

Given the scarce constraints that have been placed on the NS mass-radius relation, there are numerous equations of state in the literature that can be used to incorporate the internal structure into our calculations. In this work, we adopt two different EoSs, which we detail here.

The Brussels-Montreal EoS

The first family of EoSs adopted in this work are based on the Brussels-Montreal (BSk) energy density functionals [212–217], for cold, non-accreting NSs. In these models, the density-dependent nucleon interactions are accounted for via a mean-field approximation in either the Hartree-Fock (HF) or Hartree-Fock-Bogoliubov (HFB) formalism⁷, through effective Skyrme type forces [218, 219]. The BSk EoS family are unified EoSs, meaning they describe all the regions of the NS interior using the single effective Hamiltonian. Furthermore, the authors provide public FORTRAN subroutines that implement fits to the EoS quantities such as the pressure and density as functions of the baryon number density, allowing straightforward implementation of the EoS.

The authors provide these fits to eight configurations of the BSk EoS, labeled BSK19-26. Of these, the older BSK19-21 functionals were fitted to older atomic mass data that has since been updated in the newer models, BSk22-26. The mass-radius relation predicted by a selection of these models is shown in Fig. 2.3 by the blue lines. Missing are the BSk20 and 21 models, as they give very similar results to the 26 and 24 models respectively. The BSk19 EoS is partially ruled out from the lower bound on NS radii obtained from the electromagnetic counterpart of the GW170817 event [220], while BSk22 is ruled out from constraints on the tidal deformability from the same event [221]. Additionally, BSk22 does not support the presence of direct Urca⁸ processes in NSs described by this EoS. These processes are required to explain observations of a small population of NSs that have cooled to temperatures below those predicted by the “minimal cooling paradigm” [222, 223]. On the other hand, the BSk26 functional predicts that all stable NSs will support direct Urac processes. This goes against the current observational evidence that a majority of NSs are well modeled by the minimal cooling paradigm, ruling the EoS out. Of the remaining two models, BSk24 and 25, we choose to adopt BSk24 as it gives slightly better fits to NS mass data than that of BSk25.

We use the BSk24 EoS to generate four benchmark NSs with masses of 1, 1.5, 1.9 and $2.16 M_{\odot}$, with the central density ρ_c , stellar mass, radius, metric factor

⁷The HF method accounts for the energy associated with nucleon pairings, while the HFB method neglects this contribution.

⁸This is another name given to the reactions in Eqs. 2.43, 2.44.

EoS	BSk24-1	BSk24-2	BSk24-3	BSk24-4
ρ_c [g cm $^{-3}$]	5.94×10^{14}	7.76×10^{14}	1.04×10^{15}	1.42×10^{15}
M_\star [M_\odot]	1.000	1.500	1.900	2.160
R_\star [km]	12.215	12.593	12.419	11.965
$B(R_\star)$	0.763	0.648	0.548	0.467
$c_s(0)$ [c]	0.511	0.628	0.734	0.835

Table 2.2: Benchmark NSs, for four different configurations of the equations of state (EoS) for cold non-accreting neutron stars with Brussels–Montreal functionals BSk24 [217]. EoS configurations are determined by the central mass-energy density ρ_c .

$B(R_\star)$ and central speed of sound $c_s(0)$ in Table 2.2. Radial profiles of the baryon number density $n_b(r)$, metric factor $B(r)$, neutron chemical potential $\varepsilon_{F,n}(r)$, and neutron abundance $Y_n(r)$, are shown in Fig. 2.4.

While BSk24 and 25 lie well within current observational constraints, they are minimal models in that they only account for $npe\mu$ matter, and do not incorporate any exotic species within the NS core. This is problematic as it is highly likely that hyperonic matter will appear in the cores of NS heavier than $\sim 1.7 M_\odot$. Additionally, the Skyrme forces that describe the nuclear interaction are treated non-relativistically, while the nucleons in heavier stars can become semi-relativistic. To address these concerns, later works [224, 225] adopted the Quark-Meson Coupling (QMC) EoS.

The Quark-Meson Coupling EoS

The second EoS adopted is based on the QMC model of Refs. [226–229], in which baryons are described as bags of three valence quarks, with the bags themselves modeled by the MIT bag model [230]. The interactions among the baryons are described by the exchange of mesons between the valence non-strange quarks and are formulated within a relativistic mean-field Lagrangian. The exchange of the vector mesons acts as an overall shift to the energy of the baryons⁹. The scalar mean fields play a significantly more important role, modifying the effective mass of the baryons. The scalar (and also vector) couplings are density-dependent, leading to an effective mass of the baryons that varies throughout the NS. The density dependence of these couplings is equivalent to including repulsive three-body forces

⁹A simple analogy for this is how the force of an electron in an electromagnetic field is due to the exchange of photons, which are vector fields. The total energy of the electron is a shift relative to the free electron energy.

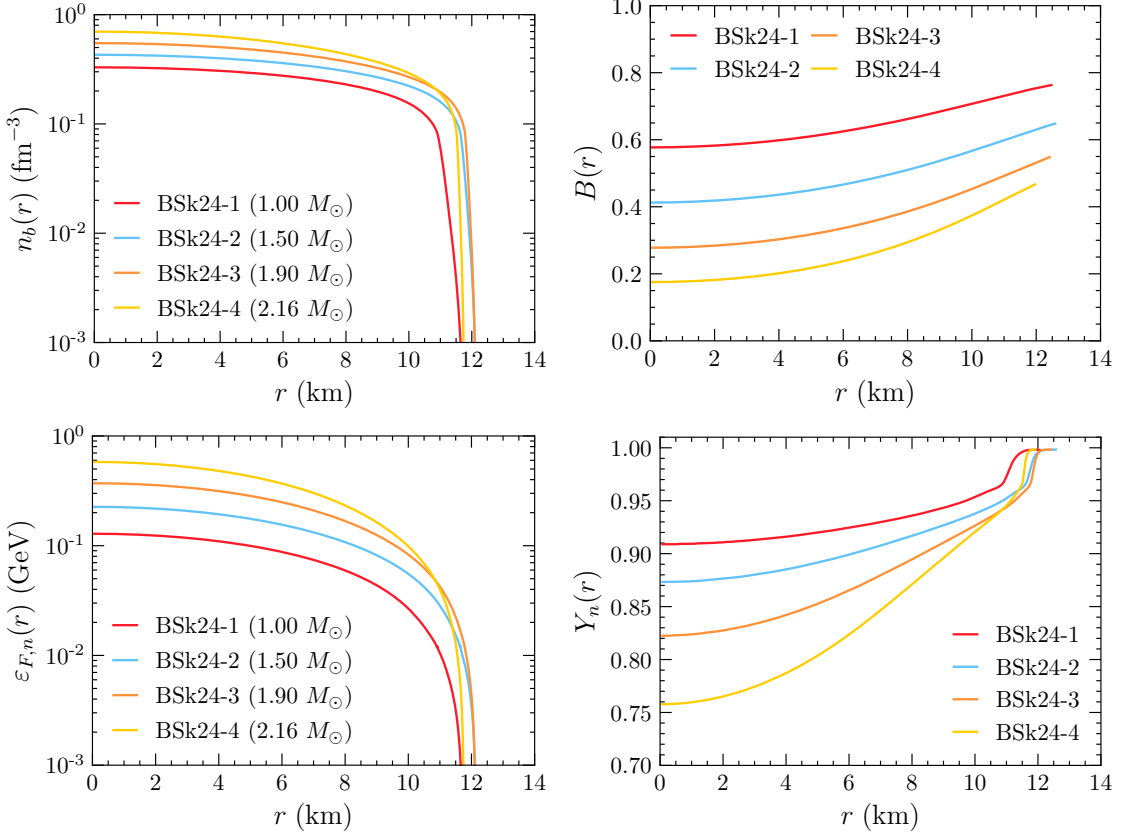


Figure 2.4: Radial profiles of the baryon number density (top left), metric factor $B(r)$ (top right), neutron chemical potential (bottom left), and neutron abundance (bottom right) for the four benchmark NS of the BSk24 EoS in Table 2.2.

EoS	QMC-1	QMC-2	QMC-3	QMC-4
$n_B^c \text{ [fm}^{-3}\text{]}$	0.325	0.447	0.540	0.872
$M_\star \text{ [M}_\odot\text{]}$	1.000	1.500	1.750	1.900
$R_\star \text{ [km]}$	13.044	12.847	12.611	12.109
$B(R_\star)$	0.772	0.653	0.588	0.535

Table 2.3: Benchmark NSs for four different configurations of the QMC equation of state. EoS configurations are determined by the central number density n_B^c .

between the baryons and arises naturally in the QMC model through the in-medium modification of the baryonic structure [231, 232]. Additional details on the energy density and couplings of the QMC model adopted in this work are given in Appendix ??.

The mass-radius relation of three different configurations of the QMC EoS, namely three different choices of the isovector coupling constant, are shown as the red lines in Fig. 2.3, obtained from Ref. [233]. Of these, QMCb (orange solid line in Fig. 2.3) lies within the constraints on the radius of a $1.4 M_\odot$ NS from GW170817, and can produce an NS of mass $1.908 \pm 0.016 M_\odot$, the currently preferred mass of PSR J1614-2230 obtained by the NANOGrav collaboration [234]¹⁰.

The QMCb EoS data was provided by the authors of Ref. [233] for use in this work and will be referred to as simply the QMC EoS from here on. From this, we calculate the internal structure of four benchmark QMC NSs, similar to the BSk models of Table 2.2, with the central baryon density replacing the central density and the speed of sound omitted. The relevant parameters are shown in Table 2.3. The top four plots in Fig. 2.5 show the radial profiles for the number densities of the neutrons and protons for each configuration on the left, with their effective masses shown on the right. The bottom two plots of the same figure show the number densities for each species within the heaviest star on the left, including leptons in dashed lines, with the effective masses for each of the baryons on the right. The replacement of high-momentum neutrons with low-momentum hyperons is clearly seen in the bottom left plot, as the neutron number density dips towards the centre of the massive star. As the densities are high enough for the charged hyperon Ξ^- to appear, the abundance of leptons decreases due to the requirement of charge neutrality, also seen in this plot.

¹⁰As mentioned above, the current heaviest NS has a mass of $2.08 \pm 0.07 M_\odot$ though the implications of this on the QMC EoS are beyond the scope of this work.

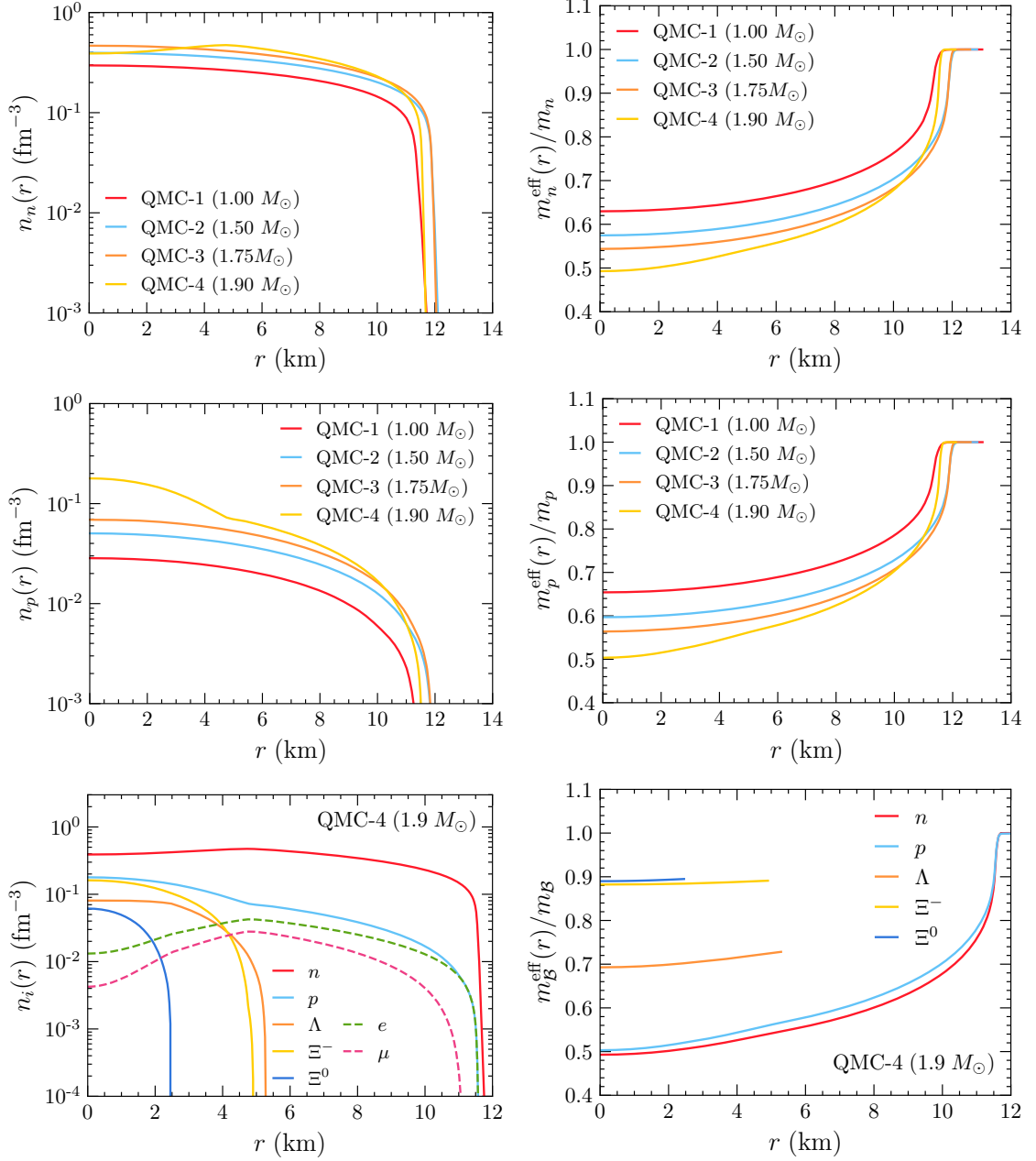


Figure 2.5: Number density profiles (left) and the ratio of the effective mass to the bare mass (right) for neutrons (top) and protons (middle) for benchmark configurations of the QMC EoS in Table 2.3. In the bottom panels, we show the same profiles for all species in the heaviest NS considered, QMC-4, which contains hyperonic matter.

3

Improved Treatment of Dark Matter Capture in Compact Objects

This chapter combines aspects of Refs. [224, 235, 236] to give a complete introduction to the formalism we have built for dark matter capture in compact objects. We begin by reviewing aspects of Gould’s formalism for capture in the Sun [97, 98]. We then build upon these results to incorporate relativistic corrections and the effects of Pauli Blocking due to scattering from a degenerate media in a self-consistent manner. Important aspects of both the interaction and capture rates are discussed, including Pauli blocking for low mass DM and the effects of multiple scattering in the high-mass regime. We then apply our results to the example DM scattering from neutron targets using the BSk24 EoS to model the neutron star.

3.1 Dark Matter Capture in the Sun

Before jumping into the capture formalism relevant to compact objects, it will serve us well to review the formalism laid out by Gould for capture in the Sun [97, 98].

To begin, we consider the flux of dark matter particles that pass through a spherical shell a large distance R from the star, where the gravitational field is negligible. For this, we need to know the distribution function of the relative velocity between the DM and the stellar constituents. The velocity distribution function will be spatially isotropic, and so for simplicity we will assume that the

DM follows a Maxwell-Boltzmann distribution function,

$$f_\infty(\tilde{u}_\chi)d\tilde{u}_\chi = 4\pi \left(\frac{3}{2\pi} \right)^{3/2} \frac{\tilde{u}_\chi^2}{v_d^2} \exp\left(-\frac{3\tilde{u}_\chi^2}{2v_d^3}\right) d\tilde{u}_\chi, \quad (3.1)$$

where \tilde{u}_χ is the DM velocity in the halo, and v_d is the DM halo velocity dispersion.

Taking into account the motion of the star through the halo and the thermal motion of the constituents, which are assumed to follow a Maxwell-Boltzmann distribution, gives the relative velocity between the DM and targets, u_χ . The distribution function for the relative velocity can be expressed as [99]

$$f_{\text{MB}}(u_\chi, T_\star)du_\chi = \frac{u_\chi}{v_\star} \sqrt{\frac{3}{2\pi(v_d^2 + 3T_\star/m_i)}} \left(e^{-\frac{3(u_\chi - v_\star)^2}{2(v_d^2 + 3T_\star/m_i)}} - e^{-\frac{3(u_\chi + v_\star)^2}{2(v_d^2 + 3T_\star/m_i)}} \right) du_\chi, \quad (3.2)$$

where v_\star is the star's velocity in the halo rest frame¹, T_\star is the temperature of the star, and m_i is the mass of the target.

Returning to the large spherical shell of radius R , given the velocity distribution function, we can obtain the flux of DM through this surface. The rate of DM particles passing through a surface element $d\tilde{A}$ with velocity between u_χ and $u_\chi + du_\chi$, with an angle to the normal of $d\tilde{A}$ between $\tilde{\theta}$ and $\tilde{\theta} + d\tilde{\theta}$ and an azimuthal angle between $\tilde{\phi}$ and $\tilde{\phi} + d\tilde{\phi}$ is given by [96]

$$\frac{dN_\chi}{dt} = \frac{\rho_\chi}{m_\chi} f_{\text{MB}}(u_\chi, T_\star) \vec{u} \cdot d\vec{\tilde{A}} du_\chi \frac{d\tilde{\Omega}}{4\pi} \quad (3.3)$$

$$= \frac{\rho_\chi}{m_\chi} f_{\text{MB}}(u_\chi, T_\star) u_\chi \cos \tilde{\theta} d\tilde{A} du_\chi \frac{d \cos \tilde{\theta} d\tilde{\phi}}{4\pi} \quad (3.4)$$

$$= \frac{1}{4} \frac{\rho_\chi}{m_\chi} f_{\text{MB}}(u_\chi, T_\star) u_\chi d\tilde{A} du_\chi d \cos^2 \tilde{\theta}, \quad (3.5)$$

where we have integrated over the azimuthal angle $\tilde{\phi}$ due to the isotropy of the system. The number density of the DM is included through the ρ_χ/m_χ factor. Integrating over the area of the sphere is trivial due to isotropy, leaving us with

$$\frac{dN_\chi}{dt} = \pi \frac{\rho_\chi}{m_\chi} f(u_\chi, T_\star) u_\chi du_\chi d \cos^2 \tilde{\theta}, \quad (3.6)$$

with the integration interval for $\cos^2 \tilde{\theta}$ being $(0, 1)$.

¹This is the frame where the DM has an average velocity of zero.

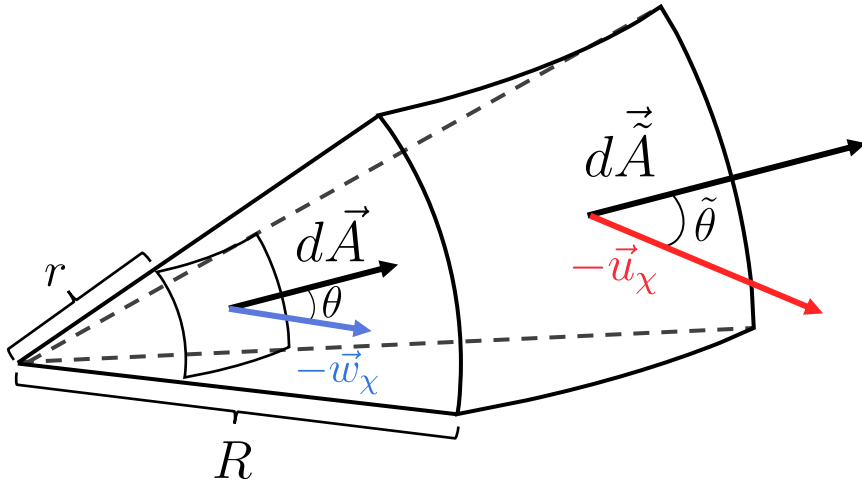


Figure 3.1: Geometry of the capture process, showing two elements of spheres with radii r close to the star

As the DM begins to infall from this large distance R to a closer distance r , the star's gravitational field will boost the velocity by the local escape velocity $v_e(r)$ such that

$$w_\chi^2(r) = u_\chi^2 + v_e^2(r), \quad (3.7)$$

$$v_e^2(r) = \frac{2GM_\star}{R_\star} + \int_r^{R_\star} \frac{GM_\star(r')}{r'^2} dr'. \quad (3.8)$$

Due to the conservation of angular momentum, we can relate the angular momentum of the DM at the two distances R and r such that

$$J_\chi = m_\chi Ru_\chi \sin \tilde{\theta} = m_\chi rw_\chi(r) \sin \theta \leq m_\chi rw_\chi(r) \equiv J_{\max}, \quad (3.9)$$

where θ is the incident angle of the DM at the closer distance r , and we have defined the maximum angular momentum J_{\max} corresponding to a linear DM trajectory.

Changing integration variables from $\cos^2 \tilde{\theta}$ to J_χ allows us to write the number of DM particles passing through the shell per unit volume as

$$\frac{dN_\chi}{dt} = 2\pi \frac{\rho_\chi}{m_\chi} \frac{f_{\text{MB}}(u_\chi, T_\star)}{u_\chi} r^2 w_\chi^2(r) \frac{J_\chi dJ_\chi}{J_{\max}^2} du_\chi. \quad (3.10)$$

The geometry of the system is shown in Fig. 3.1 for clarity.

The probability that the DM interacts with the constituents of the shell depends on the interaction rate, $\Omega(w_\chi)$, multiplied by the time spent in the shell, $dt = dr/\dot{r}$. Hence, the probability of scattering within the shell is

$$\Omega(w_\chi) \frac{dr}{\dot{r}} = 2\Omega(w_\chi) \frac{1}{w_\chi} \left(1 - \left(\frac{J_\chi}{rw_\chi}\right)^2\right)^{-1/2} \Theta(J_{\max} - J_\chi) dr, \quad (3.11)$$

where the factor of 2 is due to the DM having two opportunities to pass through the shell, once when incoming and another after turning around². The step-function is put in to ensure the angular momentum does not exceed its maximum allowed value.

For a scattered DM to be considered captured, it must lose enough energy in the collision to become gravitationally bound. The rate at which a DM particle scatters from an initial velocity w_χ to a final velocity $v < v_e(r)$ is given by [97–99]

$$\Omega^-(w_\chi) = \int_0^{v_e} R^-(w_\chi \rightarrow v) dv, \quad (3.12)$$

$$R^-(w_\chi \rightarrow v) = \int n_T(r) \frac{d\sigma_{\chi T}}{dv} |\vec{w}_\chi - \vec{u}_T| f_T(u_T) d^3 \vec{u}_T, \quad (3.13)$$

with $R^-(w_\chi \rightarrow v)$ being the differential interaction rate, n_T is the target number density, u_T is the target velocity and $f_T(u_T)$ is the corresponding distribution function, and $d\sigma_{\chi T}/dv$ is the differential cross-section. The minus superscript is used to signify that this is the down scattering rate, i.e. the rate of interactions leading to the DM losing energy.

Finally, we obtain the capture rate by multiplying Eqs. 3.10 and 3.11 and integrate over the angular momentum to give the result

$$C = \int_0^{R_*} dr 4\pi r^2 \int_0^\infty du_\chi \frac{\rho_\chi}{m_\chi} \frac{f_{\text{MB}}(u_\chi, T_*)}{u_\chi} w_\chi(r) \Omega^-(w_\chi). \quad (3.14)$$

This result is rather generic, as the choice of DM model will only dictate the form of the differential cross-section in Eq. 3.13. As written above, the distribution function for the relative velocity far from the star can be any isotropic distribution function. The MB form was chosen as it allows for a simple analytic form of the total capture rate.

²The radial velocity \dot{r} is a standard result in orbital mechanics and can be obtained from the central force Lagrangian.

3.2 Capture in Compact Objects

Having reviewed the capture process in non-relativistic stars, we can begin discussing the necessary modifications required when considering relativistic stars. In this section, we consider the two major modifications that need to be made:

- The corrections from General Relativity due to the extreme gravitational fields. This ultimately alters the flux of DM passing through the star, boosting it through gravitational focusing.
- Accounting for the relativistic and degenerate nature of the star's constituents in the interaction rate.

The former is generic to neutron stars and white dwarfs, while the latter is required for all NS constituents, but only the electrons in a WD are degenerate and relativistic. The ions of the WD are non-relativistic and non-degenerate and, hence, can the solar capture formalism can be applied in this case.

3.2.1 General Relativistic Corrections to the Capture Rate

Far from the star, the physics is the same as in the previous section. The deviations arise as the DM falls into the gravitational potential of the star. We begin by following the DM along its trajectory, moving from a distance $R \gg R_\star$ to a closer distance r . Hence, we are working in the DM rest frame and calculating the rate at which the DM passes through the shell *per unit of proper time*, τ . The proper time interval is related to the metric through

$$d\tau^2 = B(r)dt^2 - A(r)dr^2 - r^2d\Omega^2, \quad (3.15)$$

with $B(r)$ and $A(r)$ defined in Chapter 2.

Following the same arguments as in the non-relativistic case, the flux of DM passing through the shell is

$$\frac{dN_\chi}{d\tau} = 2\pi \frac{\rho_\chi}{m_\chi} \frac{f_{\text{MB}}(u_\chi)}{u_\chi} du_\chi \frac{J_\chi dJ_\chi}{m_\chi^2}, \quad (3.16)$$

which takes the same form as Eq. 3.10, with the physical difference being that this is the rate with respect to the proper time. Additionally, as we will be considering cold stars, we take the $T_\star \rightarrow 0$ limit of the DM-target relative velocity distribution, such that

$$f_{\text{MB}}(u_\chi) = \lim_{T_\star \rightarrow 0} f_{\text{MB}}(u_\chi, T_\star) \quad (3.17)$$

$$= \frac{u_\chi}{v_\star} \sqrt{\frac{3}{2\pi(v_d^2 + 3T_\star/m_i)}} \left(e^{-\frac{3(u_\chi - v_\star)^2}{2(v_d^2 + 3T_\star/m_i)}} - e^{-\frac{3(u_\chi + v_\star)^2}{2(v_d^2 + 3T_\star/m_i)}} \right), \quad (3.18)$$

The probability that DM scatters within the shell and is captured is $2\hat{\Omega}^-(r)d\tau$, where $\hat{\Omega}^-(r)$ is the interaction rate with respect to the proper time, and $d\tau$ is the proper time taken to move from coordinate r to $r + dr$. The factor of 2 once again accounts for the DM crossing the shell twice per orbit. For calculation purposes, we need to relate this to the interaction rate seen by a distant observer, $\Omega^-(r)$, that is done through

$$\hat{\Omega}^-(r)d\tau = \frac{1}{\sqrt{g_{tt}}}\Omega^-(r)d\tau = \frac{1}{\sqrt{B(r)}}\Omega^-(r)d\tau. \quad (3.19)$$

Now, the proper time that the DM spends inside a shell of thickness dr will be³

$$d\tau = \left(\frac{d\tau}{dt}\right)dt = B(r)\frac{dr}{\dot{r}} = \frac{\sqrt{B(r)}dr}{\sqrt{\frac{1}{A(r)}\left[1 - B(r)\left(1 + \frac{J_\chi^2}{m_\chi^2 r^2}\right)\right]}}. \quad (3.20)$$

The differential capture rate can then be written as

$$dC = 2\pi \frac{\rho_\chi}{m_\chi} \frac{f_{\text{MB}}(u_\chi)}{u_\chi} du_\chi \frac{dJ_\chi^2}{m_\chi^2} \frac{\Omega^-(r)\sqrt{A(r)}dr}{\sqrt{1 - B(r)\left(1 + \frac{J_\chi^2}{m_\chi^2 r^2}\right)}}. \quad (3.21)$$

As the total number of targets in the star, N_T , needs to satisfy

$$N_T = \int_0^{R_*} 4\pi r^2 n_T(r) \sqrt{A(r)} dr, \quad (3.22)$$

where $n_T(r)$ is the number density that appears in the interaction rate, we absorb the factor $\sqrt{A(r)}$ into the definition of $n_T(r)$, such that $\Omega^-(r)\sqrt{A(r)} \rightarrow \Omega^-(r)$. This is due to the number densities obtained by solving the TOV equations already account for the $\sqrt{A(r)}$ factor.

As before, we have $w_\chi^2(r) = u_\chi^2 + v_e^2(r)$, however as the escape velocity will be significantly larger than the ambient DM velocity far from the star, we can safely approximate $w_\chi^2(r) \approx v_e^2(r)$. In the relativistic case, the escape velocity can be defined as

$$v_e^2(r) = \left(\frac{dl}{d\tau}\right)^2 = A(r) \left(\frac{dr}{d\tau}\right)^2 + r^2 \left(\frac{d\phi}{d\tau}\right)^2 = 1 - B(r), \quad (3.23)$$

where dl is a length element. The large boost from the escape velocity also removes the u_χ dependence in the kinematics of the interactions and allows us to perform the integration over the initial DM velocity, yielding an overall factor of

$$\int_0^\infty \frac{f_{\text{MB}}(u_\chi)}{u_\chi} du_\chi = \frac{1}{v_*} \text{Erf}\left(\sqrt{\frac{3}{2}} \frac{v_*}{v_d}\right). \quad (3.24)$$

³See Appendix ?? for the derivation of $\dot{r} = \frac{dr}{dt}$.

To integrate over J_χ^2 , we need the maximum angular momentum the DM can achieve as it passes through the shell. This can be obtained by requiring the argument of the radical above to remain positive, giving

$$J_{\max} = \sqrt{\frac{1 - B(r)}{B(r)}} m_\chi r. \quad (3.25)$$

The factor of $1/\sqrt{B}$ arises due to the gravitational focusing of the incoming flux of DM [237].

Putting everything together, and integrating over the radius of the star, we are left with the final result for the capture rate of

$$C = \frac{4\pi}{v_\star} \frac{\rho_\chi}{m_\chi} \text{Erf} \left(\sqrt{\frac{3}{2}} \frac{v_\star}{v_d} \right) \int_0^{R_\star} r^2 \frac{\sqrt{1 - B(r)}}{B(r)} \Omega^-(r) dr. \quad (3.26)$$

All that remains is determining the form of the interaction rates for relativistic energies.

3.2.2 Geometric Limit and Threshold Cross-Section

In the previous section, we derived an expression for the capture rate assuming that the DM is captured after a single scatter, and that it only scatters once along its orbit through the NS. This first assumption is true for DM light enough to lose enough energy in this single interaction, which for nucleon targets turns out to be $m_\chi \lesssim 10^6$ GeV. The latter assumption is a statement that we are working in the optically thin regime, such that the cross-section is much less than the “threshold cross-section”, σ_{th} . The value of the threshold cross-section is defined as the cross-section for which the capture rate evaluated in the optically thin regime is equal to the geometric limit [132],

$$C_{\text{geom}} = \frac{\pi R_\star^2 (1 - B(R_\star))}{v_\star B(R_\star)} \frac{\rho_\chi}{m_\chi} \text{Erf} \left(\sqrt{\frac{3}{2}} \frac{v_\star}{v_d} \right). \quad (3.27)$$

This is the capture rate for which the entire flux of DM passing through the surface of the star is captured at the surface. Hence, it serves as an upper bound to the capture rate, with cross-sections greater than σ_{th} saturating the capture rate to this value. Note the $1/B(R_\star)$ factor in the equation above. In stars and planets where classical Newtonian mechanics can be applied, gravitational focusing would result in a factor $v_{\text{esc}}^2/v_\star = (1 - B(R_\star))/v_\star$ in Eq. 3.27, where we have used Eqs. 3.23 and 2.14. In neutron stars, on the other hand, general relativity introduces an

additional factor of $1/B(R_\star)$, which can be obtained from the derivation of the flux of DM particles accreted to a NS with a Schwarzschild metric (Eq. 3.26) [237, 238].

For scattering on neutrons, the threshold cross-section is approximately

$$\sigma_{th} = \begin{cases} \sigma_{\text{ref}} \frac{\text{GeV}}{m_\chi}, & m_\chi \lesssim 1 \text{ GeV} \quad (\text{Pauli blocking regime}), \\ \sigma_{\text{ref}}, & 1 \text{ GeV} \lesssim m_\chi \lesssim 10^6 \text{ GeV}, \\ \sigma_{\text{ref}} \frac{m_\chi}{10^6 \text{ GeV}}, & m_\chi \gtrsim 10^6 \text{ GeV} \quad (\text{Multiscattering regime}), \end{cases} \quad (3.28)$$

where we take the canonical value of

$$\sigma_{\text{ref}} \sim 1.7 \times 10^{-45} \text{ cm}^2, \quad (3.29)$$

which assumes the NS is a solid sphere such that $\sigma_{\text{ref}} \sim m_n \pi R_\star^2 / M_\star$ with m_n the neutron mass.

For scattering off other targets, Pauli blocking is relevant for $q_0^{\text{MAX}} \lesssim \mu_{\text{target}}$ while multi-scattering is relevant for $m_\chi \gtrsim q_0^{\text{MAX}} / v_\star^2$, where q_0^{MAX} is the maximum energy transferred in a collision, as will be discussed later. In addition, because the other target species have a lower abundance than neutrons, the reference cross-section, σ_{ref} , will be higher. The values of σ_{th} in Eq. 3.28, and their regions of applicability, can thus be altered appropriately for other target species of interest.

3.2.3 Interaction Rate for Relativistic Energies and Degenerate Targets

Our next goal is to write down an interaction rate suitable for describing the interactions between relativistic particles and account for the degeneracy of the target species. This will be achieved by modifying the non-relativistic interaction rate of Eq. 3.12 through the use of relativistic kinematics and the use of Lorentz invariant quantities, and the correct distribution functions for degenerate fermion targets.

As shown in Eqs. 3.12 and 3.13, the interaction rate between non-relativistic, non-degenerate species i can be expressed as

$$\Omega^-(r) = \int dv \frac{d\sigma}{dv} |\vec{w}_\chi - \vec{u}_i| n_i(r) f_{\text{MB}}(u_i) d^3 u_i. \quad (3.30)$$

First, we address the degeneracy of the targets by exchanging the Maxwell-Boltzmann distribution function for a Fermi-Dirac (FD) distribution, $f_{\text{FD}}(E_i, r)$, via the replacement

$$n_i(r) f_{\text{MB}}(u_i) d^3 u_i \rightarrow \frac{g_s}{(2\pi)^3} f_{\text{FD}}(E_i, r), \quad (3.31)$$

where $g_s = 2$ is the number of spin states of the target species, p is the 3-momentum of the incoming target, and E_i is its corresponding energy. The radial dependence of the FD distribution stems from its implicit dependence on the chemical potential of the target. Rewriting this expression in a more computationally friendly manner in terms of the relevant kinematic quantities results in

$$\frac{g_s}{(2\pi)^3} f_{\text{FD}}(E_i, r) = \frac{p E_i}{2\pi^2} f_{\text{FD}}(E_i, r) dE_i d\cos\theta_{uw}, \quad (3.32)$$

where we have expressed the angular component of the d^3p differential in terms of the angle between the incoming DM and target. This angle can be traded for the more useful quantity s , the centre of mass energy through

$$\frac{d\cos\theta_{uw}}{ds} = \frac{1}{2pp_\chi} = \frac{1}{2p\sqrt{E_\chi^2 - m_\chi^2}} = \frac{1}{2pm_\chi} \sqrt{\frac{B(r)}{1 - B(r)}}, \quad (3.33)$$

as the initial DM energy is $E_\chi = m_\chi/\sqrt{B(r)}$.

Next, we calculate the initial relative velocity, $|\vec{w}_\chi - \vec{u}_i|$, using relativistic kinematics, expressing it in terms of the Mandelstam s ,

$$|\vec{w}_\chi - \vec{u}_i| = \frac{\sqrt{s^2 - 2s(1 + \mu^2)m_i^2 + (1 - \mu^2)^2m_i^4}}{s - (1 + \mu^2)m_i^2}, \quad (3.34)$$

where $\mu = m_\chi/m_i$.

Given that it is most common to present the relativistic differential scattering cross-section $d\sigma/d\cos\theta_{\text{cm}}$ as a function of the Mandelstam variables s and t , with θ_{cm} the centre of mass frame scattering angle, we make the replacement

$$dv \frac{d\sigma}{dv} = dt \frac{d\sigma}{dt} = dt \frac{d\sigma}{d\cos\theta_{\text{cm}}} \frac{d\cos\theta_{\text{cm}}}{t}. \quad (3.35)$$

The final Jacobian factor can be expressed as

$$\frac{d\cos\theta_{\text{cm}}}{dt} = \frac{2s}{s^2 - 2s(1 + \mu^2)m_i^2 + (1 - \mu^2)^2m_i^4}, \quad (3.36)$$

for the elastic scattering we consider here.

Finally, we note that the first application of this capture formalism was for neutron targets, with the analysis completed before we had considered the additional effects from the form factors and strong interactions discussed in subSection 1.2.4. These effects will be incorporated into this formalism in a self-consistent way next chapter. The initial approach that was taken to account for the fact that we are

using realistic neutron number density profiles, despite the expression in Eq. 3.31 being for a free Fermi gas, is to introduce a correction factor as in Ref. [116],

$$\zeta(r) = \frac{n_i(r)}{n_{\text{free}}(r)}, \quad (3.37)$$

where $n_{\text{free}}(r)$ is obtained by integrating Eq. 3.32 over all phase space. In the zero-temperature approximation, the result is

$$n_{\text{free}}(r) = \frac{1}{3\pi^2} [\varepsilon_{F,i}(r)(2m_i + \varepsilon_{F,i}(r))]^{3/2}. \quad (3.38)$$

Compiling everything together leads to the final expression for the interaction rate being

$$\Omega^-(r) = \int dt dE_i ds \zeta(r) \frac{d\sigma}{d \cos \theta_{\text{cm}}} \frac{E_i}{2\pi^2 m_i} \sqrt{\frac{B(r)}{1 - B(r)}} \frac{s}{\beta(s)\gamma(s)} \times f_{\text{FD}}(E_i, r)(1 - f_{\text{FD}}(E'_i, r)), \quad (3.39)$$

where we have introduced the helper functions

$$\beta(s) = s - (m_i^2 + m_\chi^2), \quad (3.40)$$

$$\gamma(s) = \sqrt{\beta^2(s) - 4m_i^2 m_\chi^2}. \quad (3.41)$$

We have also introduced the Pauli blocking factor, $1 - f_{\text{FD}}(E'_i, r)$, to account for the phase space available to the final state target. The energy of this final state particle, E'_i , is in general a messy function of E_i , t , s , and r , and can be obtained from the kinematics of the scattering. This result is presented in Appendix ??.

The integration intervals are

$$t_{\min} = -\frac{\gamma(s)}{s}, \quad (3.42)$$

$$t_{\max} = 0, \quad (3.43)$$

$$s_{\min} = m_i^2 + m_\chi^2 + 2\frac{E_i m_\chi}{\sqrt{B(r)}} - 2m_\chi \sqrt{\frac{1 - B(r)}{B(r)}} \sqrt{E_i^2 - m_i^2}, \quad (3.44)$$

$$s_{\max} = m_i^2 + m_\chi^2 + 2\frac{E_i m_\chi}{\sqrt{B(r)}} + 2m_\chi \sqrt{\frac{1 - B(r)}{B(r)}} \sqrt{E_i^2 - m_i^2}, \quad (3.45)$$

$$E_{i,\min} = m_i, \quad (3.46)$$

$$E_{i,\max} = \frac{m_i}{\sqrt{B(r)}}. \quad (3.47)$$

As we will be dealing with NSs at low temperatures, we can take the $T_\star \rightarrow 0$ limit and replace the FD functions with step functions,

$$f_{\text{FD}}(E_i, r) \rightarrow \Theta(\varepsilon_{F,i}(r) + m_i - E_i), \quad (3.48)$$

$$1 - f_{\text{FD}}(E'_i, r) \rightarrow \Theta(E'_i - m_i - \varepsilon_{F,i}(r)). \quad (3.49)$$

The first step function can be used to further restrict the E_i integration interval to be $[m_i, m_i + \varepsilon_{F,i}(r)]$. In practice, we work with the kinetic energies of the targets rather than their total energy, as this is the quantity that directly changed in the interactions. Therefore, unless otherwise specified, we will take E_i to mean the target kinetic energy, with the integration range being $0 \leq E_i \leq \varepsilon_{F,i}$.

This expression resembles that of Ref. [116], but uses a relativistic formalism instead. In Appendix A.3, we show that Eq. 3.39 reduces to the classical expression for the interaction rate in the non-relativistic limit.

3.3 The Differential Interaction Rate

In the previous section, we have calculated the interaction rate, $\Omega^-(r)$, assuming the initial DM energy takes its pre-capture value, $E_\chi = m_\chi/B(r)$. However, we are also interested in an expression for the interaction rate valid for arbitrary DM energy. This will be required when we consider capture via multiple scatterings, and it will also be necessary to study the subsequent scattering interactions that follow capture and lead to the DM thermalising within the NS. In principle, it is possible to calculate this rate numerically by binning Ω^- , Eq. 3.39, in the energy loss, i.e. multiplying Ω^- by $\frac{1}{E_i - E_j} \Theta(E_i + E_i - E'_i) \Theta(E'_i - E_i - E_j)$ and integrating over the bin $[E_j, E_i]$. However, it is possible to derive analytic expressions for the differential rate, valid in the zero-temperature approximation. To do so, we use the definition of the scattering rate in Ref. [118, 239]

$$\begin{aligned} \Gamma^-(E_\chi) = 2 \int \frac{d^3 k'}{(2\pi)^3} \int \frac{d^3 p}{(2\pi)^3} \int \frac{d^3 p'}{(2\pi)^3} \frac{|\bar{\mathcal{M}}|^2}{(2E_\chi)(2E'_\chi)(2E_i)(2E'_i)} \\ \times (2\pi)^4 \delta^4(k_\mu + p_\mu - k'_\mu - p'_\mu) f_{\text{FD}}(E_i)(1 - f_{\text{FD}}(E'_i)), \end{aligned} \quad (3.50)$$

where $|\bar{\mathcal{M}}|^2$ is the squared matrix element, $k^\mu = (E_\chi, \vec{k})$ and $k'^\mu = (E'_\chi, \vec{k}')$ are the DM initial and final momenta, and $p^\mu = (E_i, \vec{p})$ and $p'^\mu = (E'_i, \vec{p}')$ are the target particle initial and final momenta, respectively. To see that Γ^- is indeed the same as Ω^- in Eq. 3.39, multiply and divide by $v_{\text{rel}} = |\vec{w} - \vec{u}_i|$ to reintroduce the quantum

field theoretic definition of differential cross-section,

$$d\sigma = \frac{|\mathcal{M}|^2}{2E_\chi 2E_i |\vec{w} - \vec{u}_i|} d^2\Pi_{\text{LIPS}}, \quad (3.51)$$

$$d^2\Pi_{\text{LIPS}} = \frac{1}{2E'_\chi} \frac{d^3k'}{(2\pi)^3} \frac{1}{2E'_i} \frac{d^3p'}{(2\pi)^3} (2\pi)^4 \delta^4(k_\mu + p_\mu - k'_\mu - p'_\mu), \quad (3.52)$$

$$\implies \frac{d\sigma}{d\cos\theta_{\text{cm}}} = \frac{1}{16\pi} \frac{\beta(s)}{2s\beta(s) - \gamma^2(s)} |\mathcal{M}|^2, \quad (3.53)$$

where $d^2\Pi_{\text{LIPS}}$ is the 2-body Lorentz invariant phase space.

The advantage of Eq. 3.39 is that it can be used to calculate the capture rate for any interaction given the differential cross-section. The disadvantage is that this computation has to be evaluated numerically, which can be computationally intensive. For this reason, shall now use Eq. 3.50 to derive analytic expressions that will allow us to speed up computations and, in addition, calculate the shape of the interaction rate as a function of the energy loss.

The interaction rate for $d\sigma \propto s^m t^n$ is

$$\begin{aligned} \Gamma^-(E_\chi) \propto & \sum_{n,m} \frac{(-1)^n}{128\pi^3 E_\chi k} \int_0^{E_\chi - m_\chi} dq_0 \int \frac{dt_E t_E^n}{(t_E + q_0^2)^{m+\frac{1}{2}}} \\ & \times \sum_{r=0}^m \mathcal{V}_{m,r} \sum_{j=0}^r \binom{r}{j} \varepsilon_{F,i}^{r-j} \frac{(-1)^j q_0^{j+1}}{j+1} h_j \left(\frac{E_i^{t^-} - \varepsilon_{F,i}}{q_0} \right), \end{aligned} \quad (3.54)$$

for elastic scattering with $t_E = -t = q^2 - q_0^2$, where $q_0 = E'_i - E_i$ is the DM energy loss,

$$E_i^{t^-} = - \left(m_n + \frac{q_0}{2} \right) + \sqrt{\left(m_n + \frac{q_0}{2} \right)^2 + \left(\frac{\sqrt{q^2 - q_0^2}}{2} - \frac{m_n q_0}{\sqrt{q^2 - q_0^2}} \right)^2}, \quad (3.55)$$

is the minimum energy of the neutron before the collision, obtained from kinematics, and $h_j(x)$ is a step function with a smooth transition,

$$h_j(x) = \begin{cases} 0, & x > 0 \\ (-x)^{j+1}, & -1 < x < 0 \\ 1, & x < -1 \end{cases} \quad (3.56)$$

The full derivation of this interaction rate can be found in Appendix A. Our result for Γ^- is an extension of that presented in Ref. [118], where the interaction rate was calculated only in the case of low energy and a constant matrix element. It is valid at all energy ranges. The differential interaction rate $\frac{d\Gamma}{dq_0}(E_\chi, q_0)$ is then

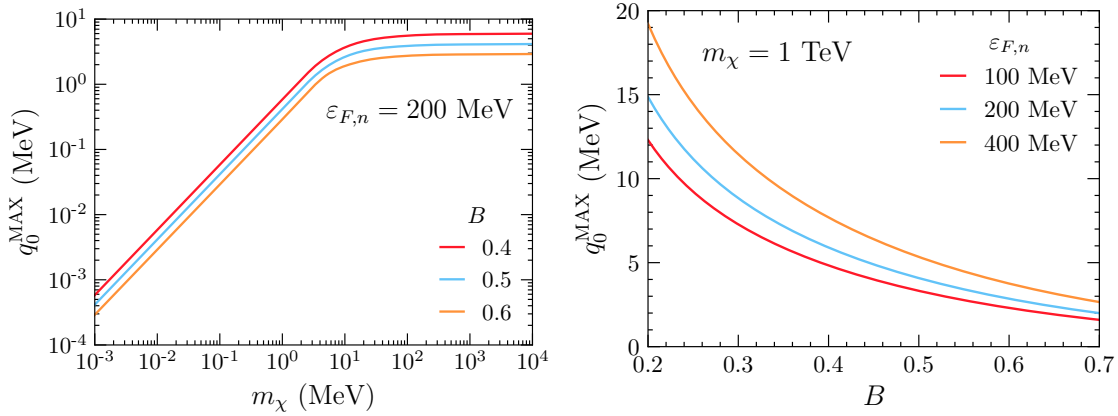


Figure 3.2: Left: q_0^{MAX} vs. m_χ for $\varepsilon_{F,n} = 200 \text{ MeV}$ and different values of B . Right: q_0^{MAX} as a function of B for different values of $\varepsilon_{F,i}$ and $m_\chi = 1 \text{ TeV}$.

just the integrand of Eq. 3.54. We will use $\frac{d\Gamma}{dq_0}$ to obtain normalised shapes for the differential interaction spectrum, while we will use Ω^- when we need the total interaction rate, such as in the capture rate.

Kinematics, and the phase space allowed by $h_j(x)$ in Eq. 3.54, determine the maximum energy that a DM particle can lose in a single scattering interaction, q_0^{MAX} . The details of how to obtain q_0^{MAX} are given in Appendix A.2.1. For DM capture, the value of q_0^{MAX} depends primarily on the DM mass, as is illustrated in the left panel of Fig. 3.2. We can see that for low m_χ , $q_0^{\text{MAX}} \propto m_\chi$, while, for $m_\chi \gg m_n$, it plateaus to values between $q_0^{\text{MAX}} \sim 3 - 6 \text{ GeV}$. Both q_0^{MAX} and $\frac{d\Gamma}{dq_0}$ also depend on $\varepsilon_{F,n}$ and B . Changing $\varepsilon_{F,n}$ has a very mild effect on the value of q_0^{MAX} (see right panel of Fig. 3.2) and on the shape of the normalised spectrum (see Fig. 3.3). On the other hand, increasing B has the main effect of reducing q_0^{MAX} (see right panel of Fig. 3.2), but only a mild effect on the shape of the profile expressed as a function of the normalised energy loss

$$q_0^{\text{norm}} = \frac{q_0}{q_0^{\text{MAX}}}. \quad (3.57)$$

We apply our results for $\frac{d\Gamma}{dq_0}$ to DM-neutron interactions, and in particular those with differential cross-sections that depend only on the transferred momentum $t = (k^\mu - k'^\mu)^2$ and not on the centre of mass energy $s = (p^\mu + k^\mu)^2$.

In Fig. 3.3 we show the normalised differential rates as a function of q_0^{norm} for the four operators D1-D4. The left-hand panels are in the limit $m_\chi \gg m_n$. We can observe that D1 has a softer spectrum, while the D2 and D4 spectra peak towards higher values of q_0 . Varying the chemical potential $\varepsilon_{F,n}$ has a very mild effect, shifting the spectrum to lower values of q_0 with increasing values of $\varepsilon_{F,n}$. Note that at small values of q_0^{norm} there is a sudden change in the slope of the

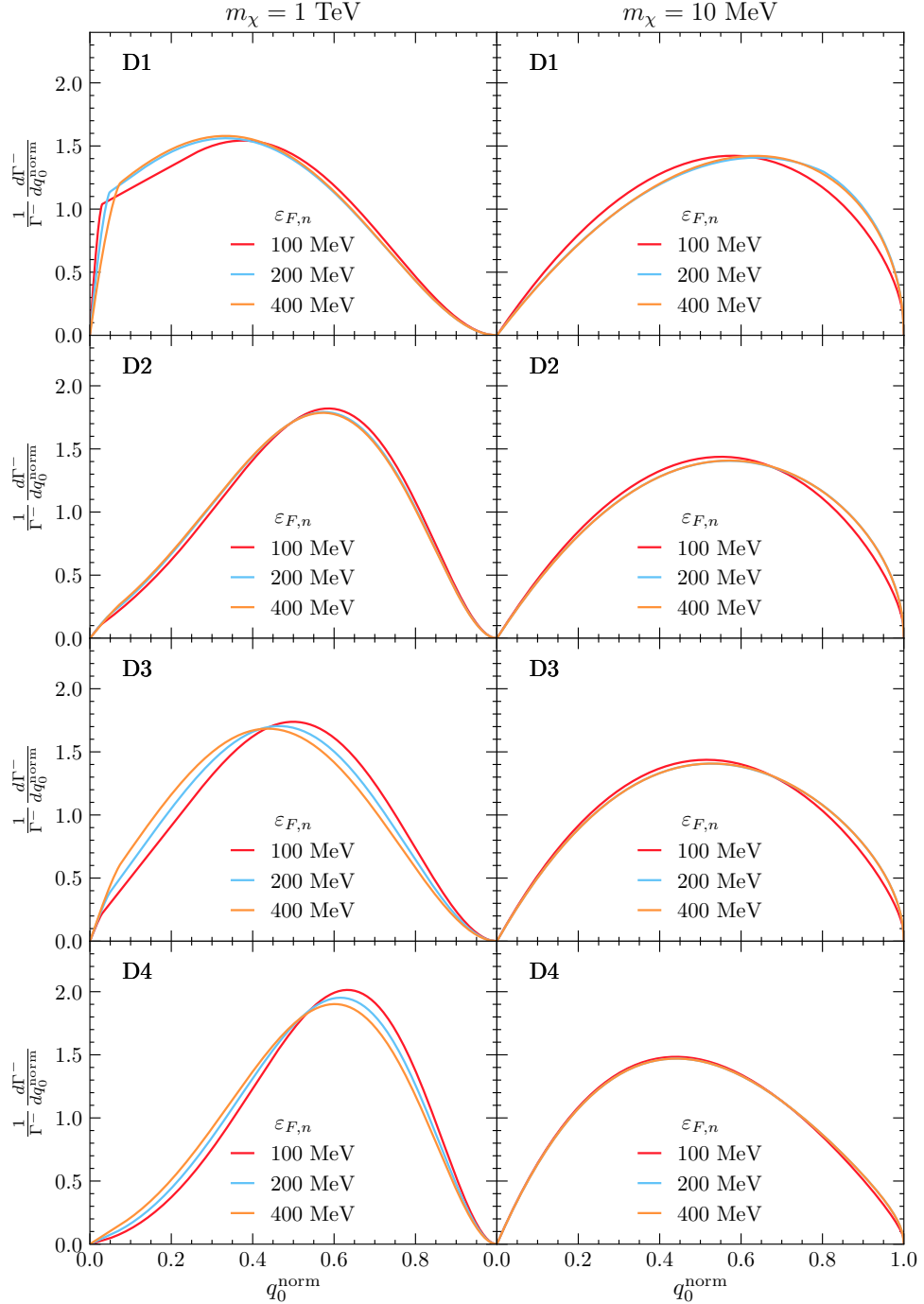


Figure 3.3: Normalised differential interaction rates $\frac{1}{\Gamma} \frac{d\Gamma}{dq_0^{\text{norm}}}$ as a function of q_0^{norm} for different values of $\varepsilon_{F,n}$, $m_\chi = 1 \text{ TeV}$ (left) and $m_\chi = 10 \text{ MeV}$ (right), $B = 0.5$ and operators D1 (first row), D2 (second row), D3 (third row) and D4 (fourth row). Profiles do not depend on m_χ in the limits $m_\chi \gg m_n$ (left) and $m_\chi \ll m_n$ (right).

normalised differential rate, which occurs for all operators but is more evident in D1 (top left panel). This is due to the zero temperature approximation, implicit in Eq. 3.54, where Heaviside functions were used to approximate FD distributions (see Appendix A.2.1); using a finite temperature would produce a smoother spectrum at small q_0^{norm} .

In the right-hand panels of Fig. 3.3, we explore the low DM mass region $m_\chi \ll m_n$. In this case, all operators give rise to similar profiles, the sole difference being that the peak of the profile is now shifted to lower q_0^{norm} for D4 in contrast to D1, with intermediate values for D2 and D3. This is a consequence of Pauli blocking, with this effect depending on the specific power of t that dominates the spectrum. Profiles with lower n ($d\sigma \propto t^n$) peak at higher q_0^{norm} (see Fig. 3.3, right panels). For D4 we have $|\bar{\mathcal{M}}|^2 \propto t^2$, while the matrix elements of D2 and D3 are linear combinations of t and t^2 , and D1 is a combination of all powers of t . Comparing the right panels of Fig. 3.3 with Fig. A.2, we observe that the lowest power of t determines the shape of the final differential interaction rate. Finally, varying $\varepsilon_{F,n}$ has a very mild effect, this time shifting the spectrum mostly to higher values of q_0 for higher $\varepsilon_{F,n}$.

The fact that the lowest power of t dictates the features of the differential interaction rate is true also for the interactions that have a dependence on s . As such, by understanding the properties of the interaction rates with $|\bar{\mathcal{M}}|^2 \propto t^n$, we can understand the rates for all the operators in Table 1.1.

3.3.1 Pauli Blocking

The DM interaction rate, Eq. 3.50, will be proportional to the number of target particles available to scatter off. Classically, this is the total number of targets within the star. However, the quantum degeneracy of the species within compact objects, due to the extreme densities, leads to a reduction in the number of available initial state target particles the DM can scatter off. To understand this, consider the $T \rightarrow 0$ approximation, in which all initial states with energies $E_i < \varepsilon_{F,i}$ are occupied. These states are known as the “Fermi sea”. In order for the DM to scatter off one of these states, it must impart enough energy to kick the target out of the Fermi sea, such that

$$E'_i = E_i + q_0 > \varepsilon_{F,i}, \quad (3.58)$$

imposing a lower limit on the energy transfer required for an interaction to take place. This effectively reduces the number of available targets to only those with kinetic energies between $\varepsilon_{F,n} - q_0$ and $\varepsilon_{F,i}$. This suppression of the initial state phase space is known as Pauli blocking (PB), and is a completely quantum phenomenon.

In this limit, we necessarily have $\Gamma^- \rightarrow 0$ for $q_0 \rightarrow 0$. It is also worth noting that Pauli blocking only affects the interaction rate when $q_0 \leq \varepsilon_{F,n}$.

To assess the impact of PB on the DM differential interaction rate, in Fig. 3.4 we compare the rate with (blue solid lines) and without (light blue dashed lines) Pauli blocking, for $B = 0.5$ and constant DM-neutron cross-section. When Pauli blocking can be neglected, the interaction rate is obtained straightforwardly from Eq. 3.50 by stripping away the $(1 - f_{\text{FD}}(E'_i))$ factor. The difference between the computations is shaded in light blue. In the top left panel, we see that the rate begins to be suppressed from PB at $q_0 \sim \varepsilon_{F,i} = 100$ MeV for a 1 GeV DM. In the top right plot, we increase the neutron chemical potential from $\varepsilon_{F,n} = 100$ MeV to $\varepsilon_{F,n} = 400$ MeV. Given that in this case $q_0^{\text{MAX}} \sim 0.4m_\chi \sim 400$ MeV, almost the whole energy range is affected by PB. The higher $\varepsilon_{F,n}$ changes the spectra (both with and without PB) such that the unsuppressed rate is no longer flat at low q_0 . The PB suppressed rate reaches a maximum at values of q_0 slightly below q_0^{MAX} , and then decreases towards 0 at lower q_0 . In the middle panels, $m_\chi = 100$ MeV, and $q_0^{\text{MAX}} \sim 40$ MeV $\ll \varepsilon_{F,n}$. In this case, it is evident that PB affects the spectrum over the full $q_0 = q_0^{\text{MAX}}$ range. In the bottom row, we set $m_\chi = 10$ MeV. As expected, for lighter DM, the effects of PB are even more pronounced.

To understand how the effect of PB varies throughout the star, we can analyse the radial profiles of the capture rates dC/dr . In Fig. 3.5 we plot the differential capture rate as a function of the NS radius, with and without Pauli blocking. We see that Pauli blocking is most significant at low DM mass, below about 1 GeV, and becomes insignificant for higher masses. Pauli blocking has a larger impact on the differential capture rate deeper into the NS interior and has a negligible effect at the surface. This is particularly apparent in the top left panel of Fig. 3.5. This is because the chemical potential is higher in the NS interior than it is near the crust, as seen in the radial $\varepsilon_{F,i}$ profile in the bottom left panel of Fig. 2.4.

3.4 Capture in the Low, Intermediate and High Mass Regimes

Having assembled all the required machinery, we are ready to explore the properties of the capture rate in the three mass regimes outlined in Eq. 3.28. Given the computational load required to evaluate Eq. 3.26 in general, we aim to provide approximations that are numerically more efficient where possible. We also discuss the high DM mass regime where multiple scatterings are required for capture, and how this is affected by Pauli blocking.

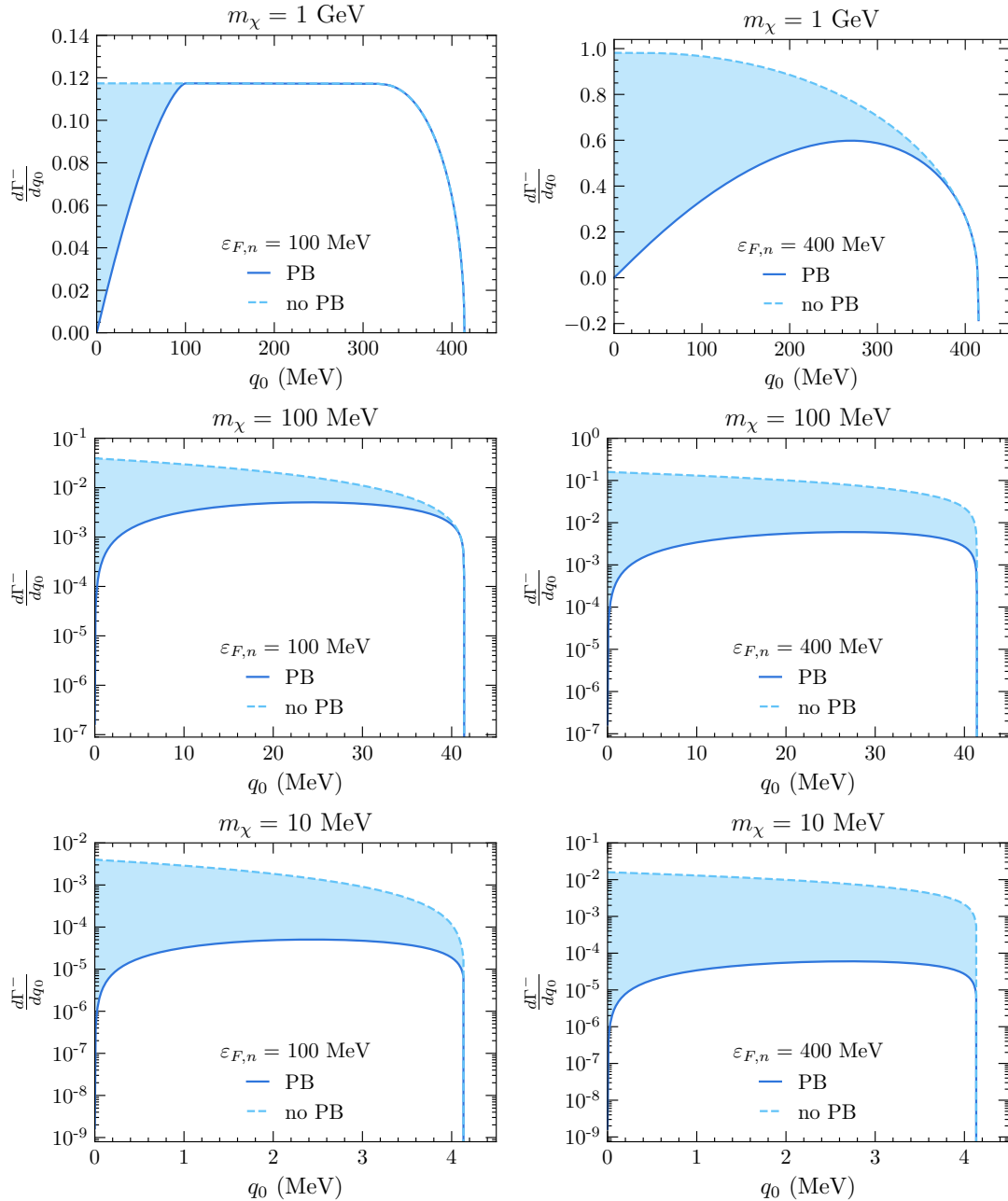


Figure 3.4: Differential interaction rates $\frac{d\Gamma}{dq_0}$ as a function of the energy loss q_0 for different values of m_χ and $\varepsilon_{F,n}$, constant cross-section and $B = 0.5$. Blue lines refer to the result that includes Pauli blocking, while the light blue dashed lines refer to the result without PB. Left column: $\varepsilon_{F,n} = 100 \text{ MeV}$, right column: $\varepsilon_{F,n} = 400 \text{ MeV}$. Top: $m_\chi = 1 \text{ GeV}$, middle: $m_\chi = 100 \text{ MeV}$, bottom: $m_\chi = 10 \text{ MeV}$.

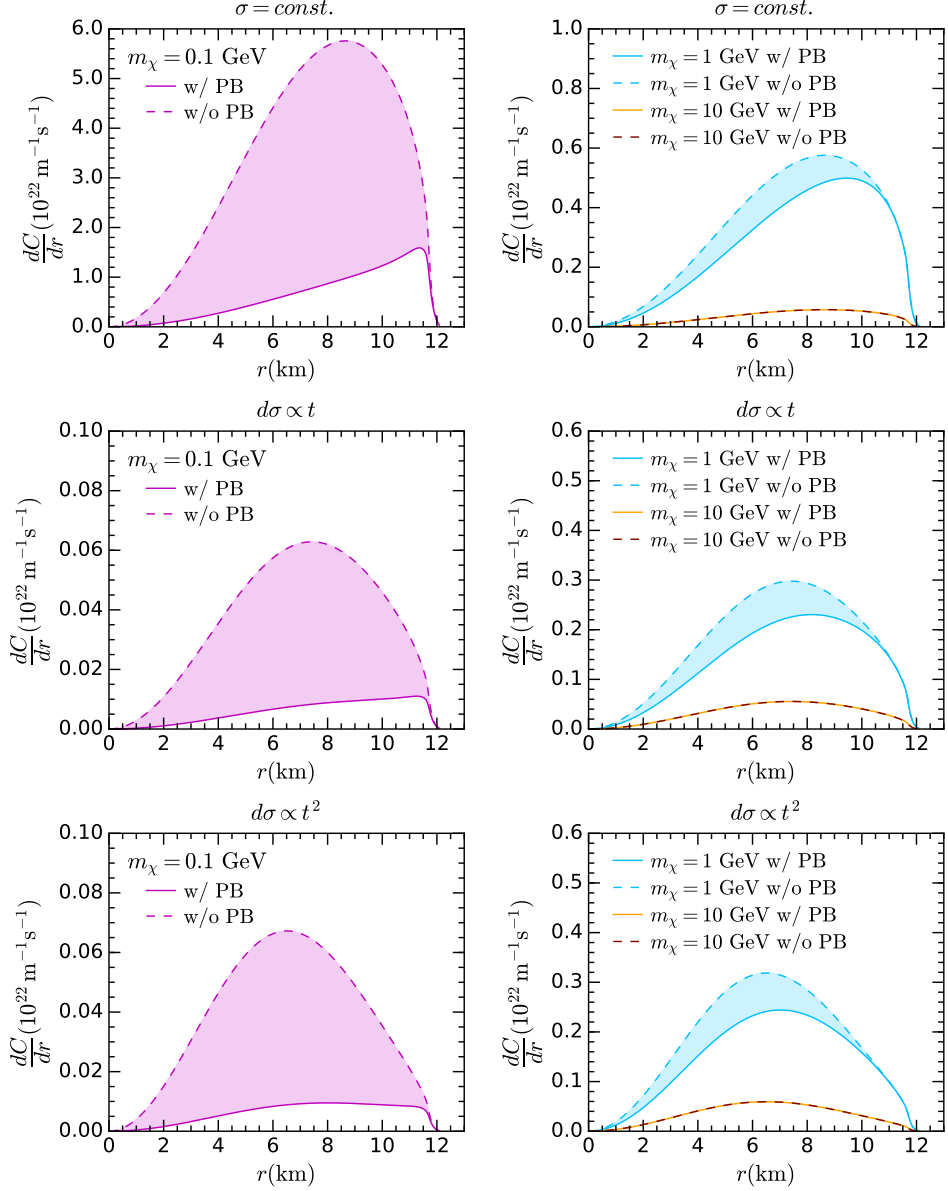


Figure 3.5: Differential capture rate as a function of the NS radius r , with (solid) and without (dashed) Pauli blocking, for the EoS benchmark BSk24-2. Top: constant cross-section, center: $d\sigma \propto t$, bottom: $d\sigma \propto t^2$.

3.4.1 Low and intermediate DM mass range

In sections 3.2 and 3.3, we have derived general expressions to numerically calculate the DM capture and interaction rates, Eqs. 3.26 and 3.39 respectively. Using these expressions, we can write the complete expression for the capture rate as a function of the differential DM-neutron cross-section

$$C = \frac{2\rho_\chi}{\pi v_\star m_\chi^2} \text{Erf} \left(\sqrt{\frac{3}{2}} \frac{v_\star}{v_d} \right) \int_0^{R_\star} dr \frac{r^2 \zeta(r)}{\sqrt{B(r)}} \int dt dE_i ds \frac{d\sigma}{d \cos \theta_{\text{cm}}} \frac{E_i s}{\beta(s) \gamma(s)} (3.59) \\ \times f_{\text{FD}}(E_i, r)(1 - f_{\text{FD}}(E'_i, r)),$$

where the functions β and γ were given in Section 3.2.3. Recall that in the limit $T \rightarrow 0$, $f_{\text{FD}}(E_i, r)$ and $1 - f_{\text{FD}}(E'_i, r)$ reduce to the step functions, $\Theta(\varepsilon_{F,i}(r) - E_i)$ and $\Theta(E'_i - \varepsilon_{F,i}(r))$, respectively.

Exchanging the differential cross-section for the squared matrix allows for easier examination of the operators in Table 1.1, and so we write the capture rate as

$$C = \frac{\rho_\chi}{8\pi^2 v_\star m_\chi^2} \text{Erf} \left(\sqrt{\frac{3}{2}} \frac{v_\star}{v_d} \right) \int_0^{R_\star} dr \frac{r^2 \zeta(r)}{\sqrt{B(r)}} \int dt dE_i ds \frac{|\bar{\mathcal{M}}|^2 E_i}{2s\beta(s) - \gamma^2(s)} \frac{s}{\gamma(s)} (3.60) \\ \times f_{\text{FD}}(E_i, r)(1 - f_{\text{FD}}(E'_i, r)).$$

This expression can be used to numerically calculate the single scatter capture rate of DM in compact objects, in the optically thin regime. In general, this must be used for low-mass DM where PB is in effect.

As discussed in Section 3.3.1, PB eventually becomes negligible for DM with masses $\gtrsim \mu_{F,i}$. Hence, between this mass and the point where multiple scattering becomes important, PB can be neglected and a simplified capture rate be obtained. For nucleon targets, this range is between $1 \text{ GeV} \lesssim m_\chi \lesssim 10^6 \text{ GeV}$, which we call the intermediate mass range.

The resulting simplified capture rate differs slightly depending on whether the matrix element depends only on t , or if it has explicit s dependence. We present the full derivations of these results in Appendix A.4 First, for $|\bar{\mathcal{M}}|^2 = at^n$, the previous expression can be simplified to

$$C \sim C_{\text{approx}} = \frac{4\pi}{v_\star} \frac{\rho_\chi}{m_\chi} \text{Erf} \left(\sqrt{\frac{3}{2}} \frac{v_\star}{v_d} \right) \int_0^{R_\star} r^2 dr n_i(r) \frac{1 - B(r)}{B(r)} \langle \sigma(r) \rangle, (3.61)$$

$$\langle \sigma(r) \rangle = \left\langle \int dt \frac{d\sigma}{dt} \right\rangle_s = \frac{a}{16\pi m_\chi^2} \frac{1}{n+1} \left(\frac{4(1 - B(r))m_\chi^2}{B(r)(1 + \mu^2)} \right)^n. (3.62)$$

For s -dependent matrix elements the result is very similar, with the only difference being that the cross-section is not averaged over s , and instead s is fixed to a

particular value as detailed in Appendix A.4. Writing the matrix element as $|\bar{\mathcal{M}}|^2 \propto \bar{g}(s)t^n$, for with g some function of s , we arrive at the result

$$C \sim C_{\text{approx},s} = \frac{4\pi}{v_\star} \frac{\rho_\chi}{m_\chi} \text{Erf} \left(\sqrt{\frac{3}{2}} \frac{v_\star}{v_d} \right) \int_0^{R_\star} r^2 dr n_i(r) \frac{1 - B(r)}{B(r)} \sigma(r), \quad (3.63)$$

$$\begin{aligned} \sigma(r) &= \int dt \frac{d\sigma}{dt} = \frac{1}{16\pi \left(m_i^2 m_\chi^2 + 2m_i m_\chi / \sqrt{B(r)} \right)} \frac{\bar{g}(s_0)}{(n+1)} \\ &\quad \times \left[\frac{4(1 - B(r))m_\chi^2}{B(r)(1 + \mu^2) + 2\sqrt{B(r)}\mu} \right]^n, \end{aligned} \quad (3.64)$$

$$s_0 = m_i^2 + m_\chi^2 + 2 \frac{E_i m_\chi}{\sqrt{B(r)}}. \quad (3.65)$$

As with the differential interaction rates, it is the t -dependence of the matrix elements that dictate the key features of the capture rate.

In Fig. 3.6, we show the capture rate as a function of the DM mass for matrix elements proportional to t^n , for $n = 0, 1, 2$ and the NS benchmark model BSk24-2. Numerical results obtained using Eq. 3.60 are shown in solid red; results using the same equation but removing the theta function that enforces Pauli blocking are depicted in light blue; and the approximation for intermediate DM masses, Eq. 3.61, in yellow. We show the geometric limit, Eq. 3.27, in blue for comparison. The capture rates were all normalised to the geometric limit at large DM mass where PB is negligible. In the same plots, we also show in brown the result obtained from using a modified version of Eq. 3.61 to include Pauli blocking. This is achieved by including the ratio between the differential the interaction rate, Γ^- , calculated with and without Pauli blocking. This comparison was done in Section 3.3.1 for various values of B and $\varepsilon_{F,n}$.

From Fig. 3.6, we can see that Eq. 3.61 is indeed a good approximation to the numerical results obtained without Pauli blocking, and can be safely used for DM masses from a few GeV up to $m_\chi \sim 10^6$ GeV, where multiple scattering becomes relevant. On the other hand, for $m_\chi \lesssim 100$ MeV the brown line is no longer a good approximation to the numerical result with Pauli blocking, as it always overestimates the capture rate by nearly an order of magnitude. Therefore, to accurately account for the effects of PB for low mass DM, the complete expression for the capture rate, Eq. 3.60 must be used and evaluated numerically.

We now compare our full numerical capture rate calculation, Eq. 3.60, with that of Ref. [116], in Fig. 3.7. The capture rates calculated in Ref. [116] correctly include the stellar structure and Pauli blocking, however, they do not account for general relativistic corrections, and the authors only considered the case of a constant cross-section, $\sigma = 10^{-45} \text{ cm}^2$. To make the comparison as fair as possible, we have

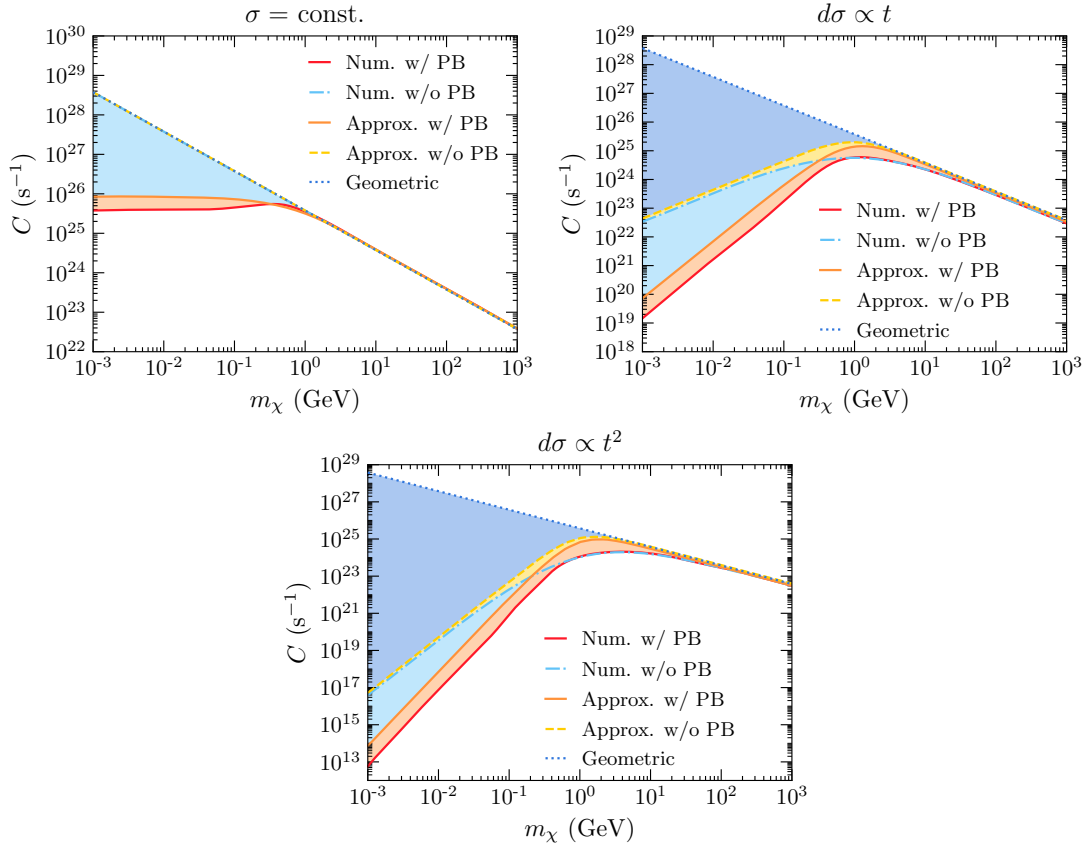


Figure 3.6: Capture rate as a function of the DM mass with cross-sections normalised to $\sigma = \sigma_{\text{ref}} \sim 1.7 \times 10^{-45} \text{ cm}^2$, for EoS BSk24-2, calculated with and without Pauli blocking. Top left: constant cross-section. Top right: $d\sigma \propto t$, bottom: $d\sigma \propto t^2$, where t is the Mandelstam variable. All rates are normalised to the geometric limit at large DM mass.

selected NS configurations that match those of Figs. 1 and 14 of Ref. [116], namely their Model A (BSk20-1): $M_\star \simeq 1.52M_\odot$, $R_\star \simeq 11.6$ km and Model D (BSk21-2): $M_\star \simeq 2.11M_\odot$ and $R_\star \simeq 12.0$ km. We denote these new benchmark models as BSk26-1 (left panel of Fig. 3.7) and BSk24-5 (right panel). Note that we were not able to use the BSk20 and BSk21 functionals, since there are no publicly available fits for the chemical potentials and particle abundances for those EoS families. However, as discussed earlier in section 2.3.2, BSk26 (BSk24) yields configurations that are almost indistinguishable from those obtained with BSk20 (BSk21) [221].

We can see in the left panel of Fig. 3.7 that in the non-Pauli suppressed region, $m_\chi \gtrsim 1$ GeV, our capture rate calculation in the optical thin limit (solid magenta) exceeds that of Ref. [116] (dot-dashed blue) by a factor of ~ 4 . When Pauli blocking is active, our capture rate calculation is about one order of magnitude higher than the classical calculation. Recall that Ref. [116] accounts for neither gravitational focusing nor relativistic kinematics. We also show in dashed light blue the approximation given in Ref. [16], which accounts for Pauli blocking with a suppression factor that depends on the neutron Fermi momentum $\sim m_\chi v_{esc}/p_{F,n}$ for $m_\chi < m_n$. Though this approximation fails to reproduce the capture rate shape due to Pauli blocking in the DM mass range [0.1 GeV, 10 GeV], it underestimates the capture rate by only a factor of 2 when the DM mass is below 0.1 GeV. Finally, we compare the geometric limit of Eq. 3.27 (solid orange) that incorporates GR effects [132] with the non-relativistic expression in Ref. [116] (dot-dashed brown). We observe that the former is $\sim 67\%$ greater than the latter, mostly due to the $1/B(R_\star)$ GR correction [237, 238]. Similar conclusions are obtained when comparing capture rate calculations for Model D of Ref. [116] (their Fig. 14) with our approach, as illustrated in the right panel of Fig. 3.7.

3.4.2 Large Mass Regime: Multiple Scattering

The capture rate expressions obtained in the previous section assume that the cross-section is small enough that the star is in the “optically thin” regime, and that a single scatter is sufficient to capture the DM. These assumptions break down if the DM-target cross-section is $\gtrsim \mathcal{O}(\sigma_{th})$, or if the DM mass exceeds $m_\chi \sim 10^6$ GeV, respectively. In this section, we focus on addressing the latter concern as we work in the optically thin regime for the remainder of this work⁴. To that end, we now explain how to modify our previous capture rate expressions to account for multiple scattering in a degenerate media⁵.

In deriving Eq. 3.59 we had assumed that the DM velocity at infinity, u_χ , can

⁴The discussion on the effect of the NS opacity in $\sigma \sim \sigma_{th}$ regime can be found in Ref. [235].

⁵For a recent discussion on multiple scattering within non-relativistic stars, or with ions in WDs, see Ref. [240].

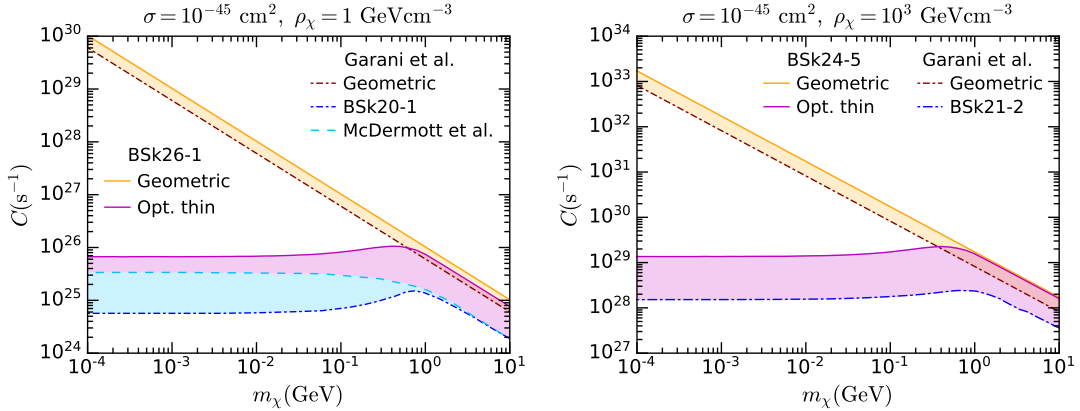


Figure 3.7: Left: Capture rate in the optically thin (magenta) and geometric (orange) limits as a function of the DM mass for constant cross-section $\sigma = 10^{-45} \text{ cm}^2$, $\rho_\chi = 1 \text{ GeV cm}^{-3}$ and BSk26 functional for $M_\star \simeq 1.52M_\odot$ and $R_\star \simeq 11.6 \text{ km}$ denoted as BSk26-1. Capture rate calculations from Ref. [116] for a NS configuration with EoS BSk20-1 [216] equivalent to BSk26-1, are shown for comparison. Right: Same as left but for $\rho_\chi = 10^3 \text{ GeV cm}^{-3}$ and the benchmark model BSk24-5 equivalent to BSk21-2 in Ref. [116]: $M_\star \simeq 2.11M_\odot$ and $R_\star \simeq 12.0 \text{ km}$.

be neglected, such that any interaction where the DM loses energy resulted in its capture. If we instead keep the leading order u_χ contribution to the total DM energy, the DM energy at infinity is

$$E_\chi^\infty \sim m_\chi \left(1 + \frac{1}{2} u_\chi^2 \right), \quad (3.66)$$

and at a distance r from the star, it gets boosted to

$$E_\chi(r) = \frac{m_\chi}{\sqrt{B(r)}} \left(1 + \frac{1}{2} u_\chi^2 \right). \quad (3.67)$$

Therefore, the amount of energy that the DM must lose to be captured is

$$E_\chi^C(r) = \frac{1}{2} u_\chi^2 \frac{m_\chi}{\sqrt{B(r)}}. \quad (3.68)$$

$$\sim 0.6 \text{ GeV} \left(\frac{u_\chi}{270 \text{ km s}^{-1}} \right)^2 \left(\frac{m_\chi}{10^6 \text{ GeV}} \right) \left(\frac{0.5}{B(r)} \right)^{1/2}. \quad (3.69)$$

Hence, DM with a mass of 10^6 GeV with an initial velocity $u_\chi = 270 \text{ km s}^{-1}$, must lose 0.6 GeV of energy for it to be captured. This is of the same order as the maximum amount of energy that can be lost in a single scatter as seen in Fig. 3.2.

Given that q_0^{MAX} plates for $m_\chi \gg m_i$, it will be highly improbable that DM heavier than $\sim 10^6$ GeV loses enough energy in a single scatter to be captured. Single scatter capture is still possible as the DM velocity at infinity is not a fixed value, rather it follows by some distribution function. Therefore, the heavy DM could have a velocity close to zero at infinity, significantly reducing the amount of energy it needs to lose.

To account for this effect, we assume that the DM particles have a speed $u_\chi \ll 1$ at infinity that follows a Maxwell-Boltzmann (MB) distribution, Eq. 3.18. We can then define the probability density function (PDF) of the energy lost by the DM using the differential interaction rate through

$$\xi(q_0, E_\chi, \varepsilon_{F,i}) = \frac{1}{\Gamma^-(E_\chi)} \frac{d\Gamma^-}{dq_0}(q_0, E_\chi, \varepsilon_{F,i}), \quad (3.70)$$

where $\frac{d\Gamma^-}{dq_0}$ is the DM differential interaction rate, calculated in Appendix 3.3. The function ξ is defined for any $q_0 \geq 0$, however, kinematics dictates that the function is non-zero only for $q_0 \leq q_0^{\text{MAX}}$. Additionally, note that ξ depends on $B(r)$ through the ratio E_χ/m_χ , and for brevity we will simply write $\xi(q_0)$.

We can define the probability of losing at least an amount of energy $q_0 = \delta q_0$ in a single collision as

$$P_1(\delta q_0) = \int_{\delta q_0}^{\infty} dx \xi(x). \quad (3.71)$$

The probability of losing at least the same amount of energy after 2 collisions will then be

$$P_2(\delta q_0) = \int_{\delta q_0}^{\infty} dy \int_0^{\infty} dx \xi(x) \xi(y-x) \quad (3.72)$$

$$= P_1(\delta q_0) + \int_{\delta q_0}^{\infty} dy \int_0^y dx \xi(x) \xi(y-x) \quad (3.73)$$

$$= P_1(\delta q_0) + \int_0^{\delta q_0} dz P_1(\delta q_0 - z) \xi(z). \quad (3.74)$$

From this, we obtain the following recursive relation for the probabilities, P_N , of losing at least $q_0 = \delta q_0$ in N scatters,

$$P_{N+1}(\delta q_0) = P_N(\delta q_0) + \int_0^{\delta q_0} dz P_N(\delta q_0 - z) \xi(z). \quad (3.75)$$

In Fig. 3.8 we show how the probability functions P_1, \dots, P_5 changes based on the t dependence of the differential cross-section. We show results for $\sigma = \text{const.}$ (top

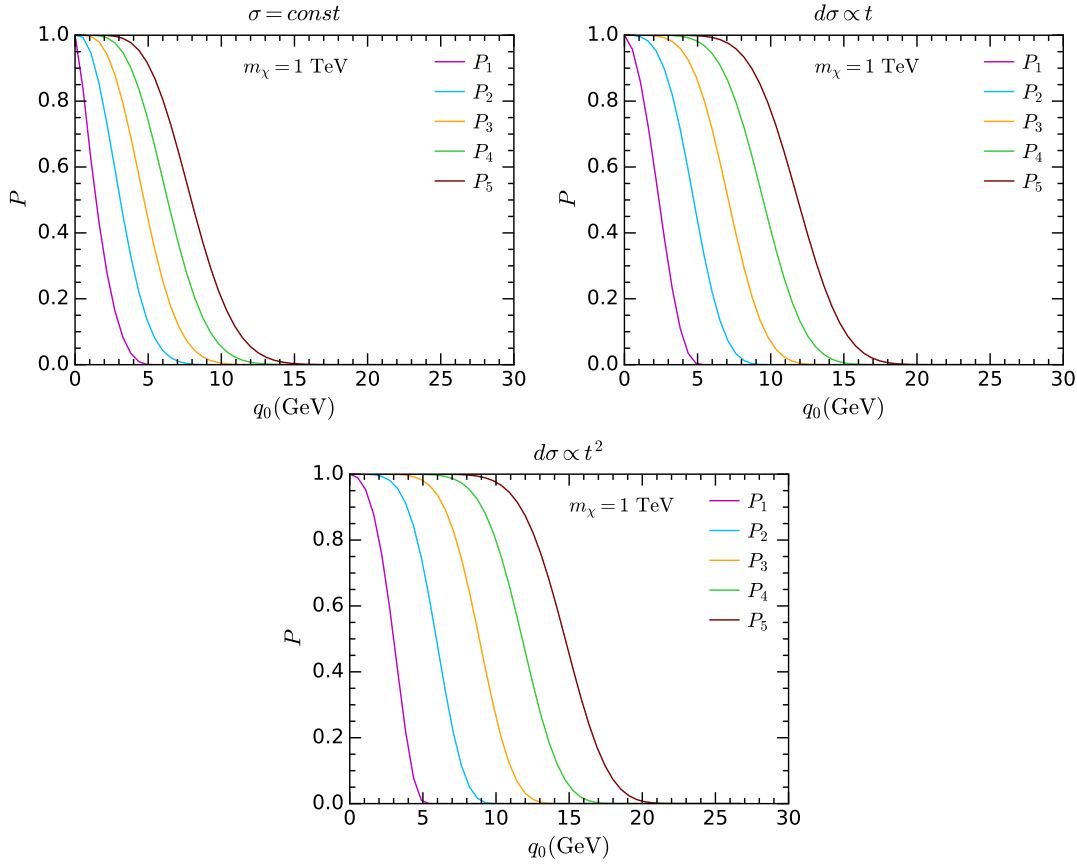


Figure 3.8: Probabilities to lose at least an amount of energy δq_0 after 1, ..., 5 scatterings, P_1, \dots, P_5 , as a function of the energy loss q_0 , assuming $B = 0.5$ and $\varepsilon_{F,n} = 400 \text{ MeV}$. Results are shown for different dependence on the cross-section on the Mandelstam variable t : constant DM-neutron cross-section (top left), $d\sigma \propto t$ (top right) and $d\sigma \propto t^2$ (bottom).

left), $d\sigma \propto t$ (top right) and $d\sigma \propto t^2$ (bottom), for fixed values of $B = 0.5$, $\varepsilon_{F,n} = 400 \text{ MeV}$.

To connect this back to the capture probability, we define the probability for a DM particle to be captured after exactly N interactions, c_N , to be $P_N(E_\chi^C) - P_{N-1}(E_\chi^C)$ averaged over the MB distribution of the initial velocity,

$$c_N(r) = \frac{1}{\int_0^\infty \frac{f_{\text{MB}}(u_\chi)}{u_\chi} du_\chi} \int_0^\infty \frac{f_{\text{MB}}(u_\chi)}{u_\chi} du_\chi \left[P_N \left(\frac{1}{2} \frac{m_\chi u_\chi^2}{\sqrt{B(r)}} \right) - P_{N-1} \left(\frac{1}{2} \frac{m_\chi u_\chi^2}{\sqrt{B(r)}} \right) \right], \quad (3.76)$$

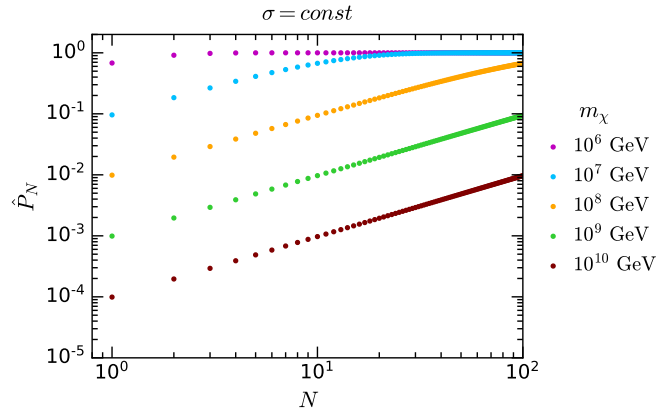


Figure 3.9: Cumulative probability \hat{P}_N for $B = 0.5$, $\varepsilon_{F,n} = 400$ MeV and for $\sigma = \text{const.}$ as a function of the number of scatterings N for several DM masses.

where c_N depends on r through the dependence of P_N on $B(r)$ and $\varepsilon_{F,n}(r)$. Note that although our results will assume a Maxwell-Boltzmann velocity distribution, it is straightforward to generalise the results to any other DM velocity distribution. The cumulative probability \hat{P}_N that a DM particle is captured after N interactions with a total energy loss $\delta q_0 = E_\chi^C$ is then

$$\hat{P}_N(r) = \sum_{i=1}^N c_i = \frac{1}{\int_0^\infty \frac{f_{\text{MB}}(u_\chi)}{u_\chi} du_\chi} \int_0^\infty \frac{f_{\text{MB}}(u_\chi)}{u_\chi} du_\chi P_N \left(\frac{1}{2} \frac{m_\chi}{\sqrt{B(r)}} u_\chi^2 \right). \quad (3.77)$$

The resulting cumulative probability is shown as a function of the number of scatterings N in Fig. 3.9, for constant cross-section and several DM masses.

The cumulative probability \hat{P}_N for the above values of $B, \varepsilon_{F,n}$ is well approximated by the function⁶

$$\hat{P}_N \sim 1 - e^{-\frac{Nm_i^*}{m_\chi}}. \quad (3.78)$$

In particular, the probability that the DM is captured in a single scatter is

$$c_1 = \hat{P}_1 \sim 1 - e^{-\frac{m_i^*}{m_\chi}}. \quad (3.79)$$

From this, we see that c_1 will begin to significantly fall below unity for $m_\chi \gtrsim m_i^*$, and hence multiple scattering will only significantly reduce the capture rate for DM masses above m_i^* .

⁶Further discussion of the multi-scattering regime, and justification of this fitting function, can be found in Appendix C of Ref. [235].

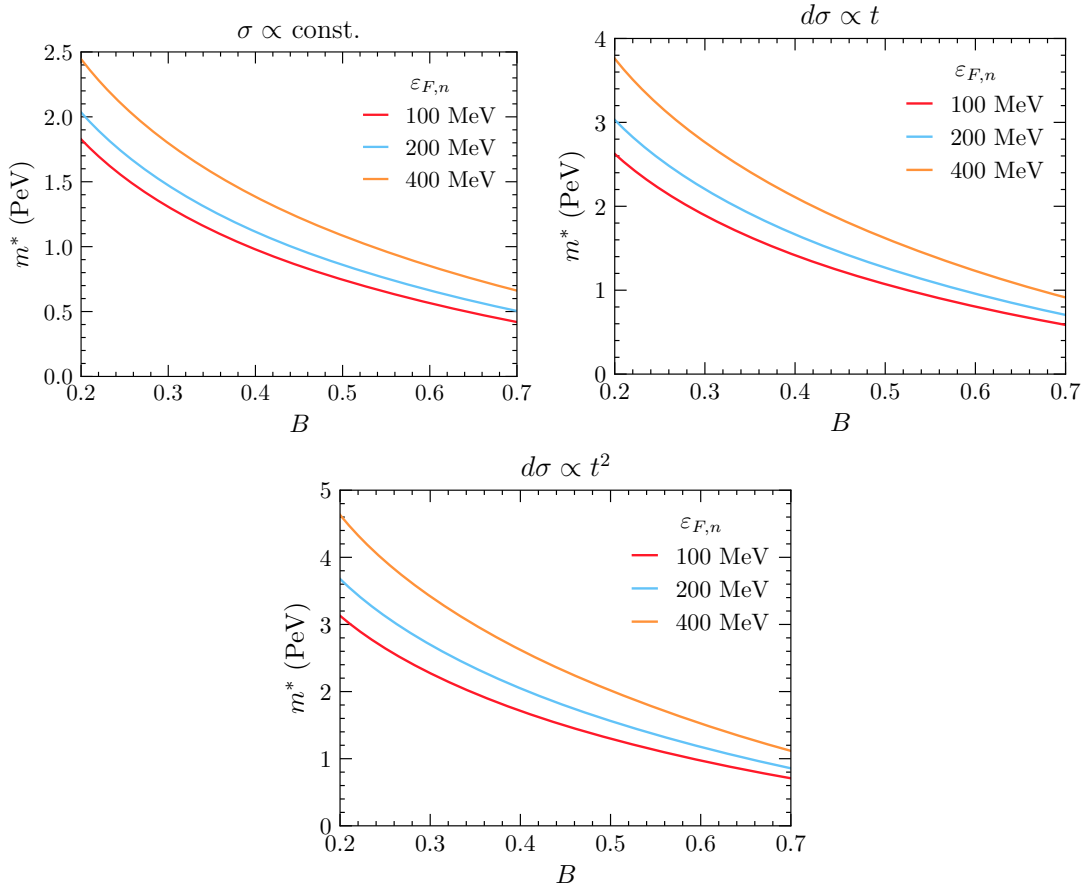


Figure 3.10: Value of m_n^* as a function of B for different values of $\varepsilon_{F,n}$, $\sigma = \text{const.}$ (top left), $d\sigma \propto t$ (top right) and $d\sigma \propto t^2$ (bottom).

To give an idea for how large the value of m_i^* will be, for neutron targets and the values $B = 0.5$ and $\varepsilon_{F,n} = 400$ MeV, we find

$$m^* = 1.08 \times 10^6 \text{ GeV}, \quad |\overline{\mathcal{M}}|^2 \propto t^0, \quad (3.80)$$

$$m^* = 1.62 \times 10^6 \text{ GeV}, \quad |\overline{\mathcal{M}}|^2 \propto t^1, \quad (3.81)$$

$$m^* = 2.01 \times 10^6 \text{ GeV}, \quad |\overline{\mathcal{M}}|^2 \propto t^2. \quad (3.82)$$

We illustrate how m_n^* varies with B and $\varepsilon_{F,n}$ in Fig. 3.10.

When the cross-section is small, $\sigma \ll \sigma_{\text{th}}$, such that we are in the optically thin regime, if the DM does not get captured in its initial scatter, then it will leave the star without interacting again. To account for this, the factor of c_1 should be included in the capture rate calculation, Eq. 3.26. However, as we have just seen, $c_1 \ll 1$ only for $m_\chi \gtrsim m_i^*$, which will always be significantly larger than the target mass and chemical potential. Therefore, multiple scattering is only important in

the regime where PB is negligible, and so a suitable approximation for the capture rate in this regime is

$$C_{\text{approx}}^* = \frac{4\pi}{v_*} \frac{\rho_\chi}{m_\chi} \text{Erf} \left(\sqrt{\frac{3}{2}} \frac{v_*}{v_d} \right) \int r^2 dr \frac{\sqrt{1 - B(r)}}{B(r)} \Omega^-(r) c_1(r), \quad (3.83)$$

with $\Omega^-(r)$ calculated as outlined in sections 3.4.1

3.5 Results

In this section, we present our results for the capture rate of fermionic DM scattering from neutrons within a NS in the zero temperature approximation. We calculate the capture rate only for scalar/pseudoscalar-scalar/pseudoscalar interactions between DM and neutrons, i.e. effective operators D1-D4 in Table 1.1, whose differential cross-sections depend only on the Mandelstam variable t and not on s . We use realistic radial profiles for the neutron number density, chemical potential, and relativistic corrections encoded in $B(r)$ as explained in Section 2.3.2, obtained from the BSk24 EoS for the configurations in Table 2.2.

To estimate the NS EoS impact on the DM capture rate computation, we numerically calculate C using the exact expression in the optically thin limit, Eq. 3.60, that properly accounts for gravitational focusing and Pauli blocking. In the optically thin regime that we are working in, the capture rate is proportional to the differential DM-neutron cross-section. Fig. 3.11 shows how this rate varies with the NS EoS for operators D1-D4 and the EoS configurations given in Table 2.2, and in turn with the NS mass and radius. The cross-section is normalised such that the capture rate in the intermediate mass range, which is unaffected by PB and multiple scattering, is equal to the geometric limit. It is worth remarking that cross-sections larger than the threshold cross-section should not be used in the optically thin limit, as this would result in capture rates larger than the geometric limit. To account for such large cross-sections, the optical depth of the NS must be accounted for as prescribed in Ref. [235]. Depending on the operator considered, going from the lightest to the heaviest NS can change the capture rate by a minimum of one order of magnitude, such as in the case of operators D1, D2 and D3 (at low DM mass), and up to 2 orders of magnitude, as in the case of operators D2 for large DM mass, and D4 in general.

At large DM mass, all operators show the same scaling with the DM mass. At $m_\chi \lesssim 1 \text{ GeV}$, a different picture arises as Pauli blocking leads to different suppressions of the capture rate for the different operators. However, we observe that the four operators give very similar results to those of Fig. 3.6, where we analysed the dependence of the capture rate on the momentum transfer t . We note that operator

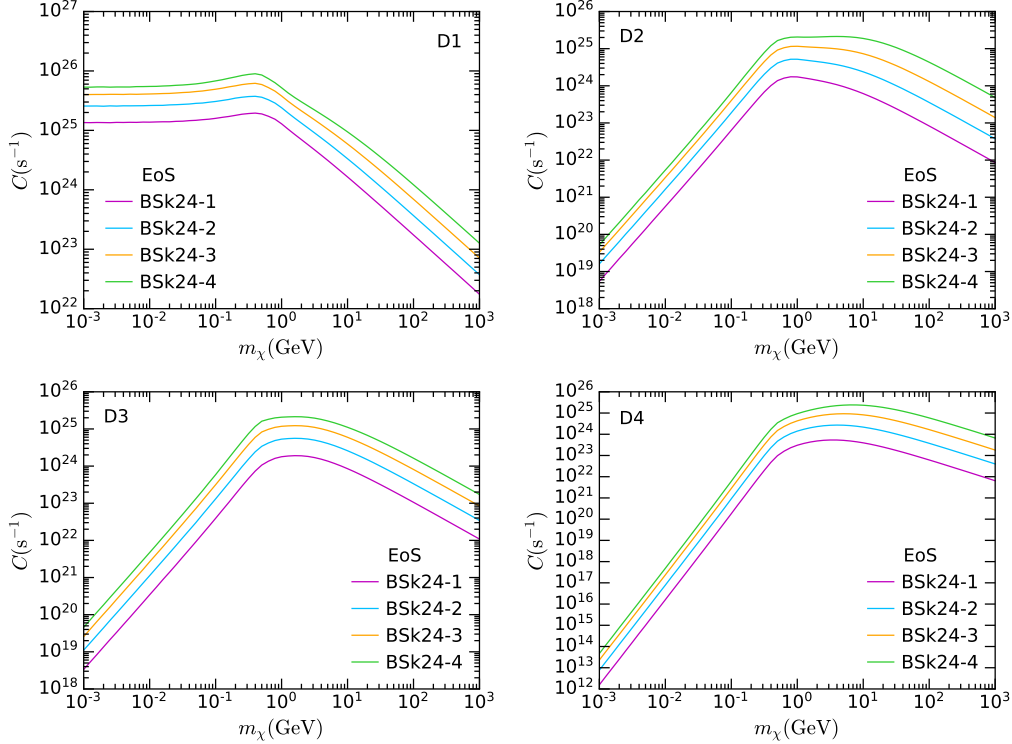


Figure 3.11: Capture rate in the optically thin limit as a function of the DM mass for $\sigma = \sigma_{\text{ref}} \sim 1.7 \times 10^{-45} \text{ cm}^2$ and the configurations of the EoS BSk24 given in Table 2.2. Rate calculated using the 4-dimensional integral in Eq. 3.60, that includes Pauli blocking but neglects the NS opacity and multiple scattering. Results are shown for the EFT operators D1 (top left), D2 (top right), D3 (bottom left) and D4 (bottom right) in Table 1.1.

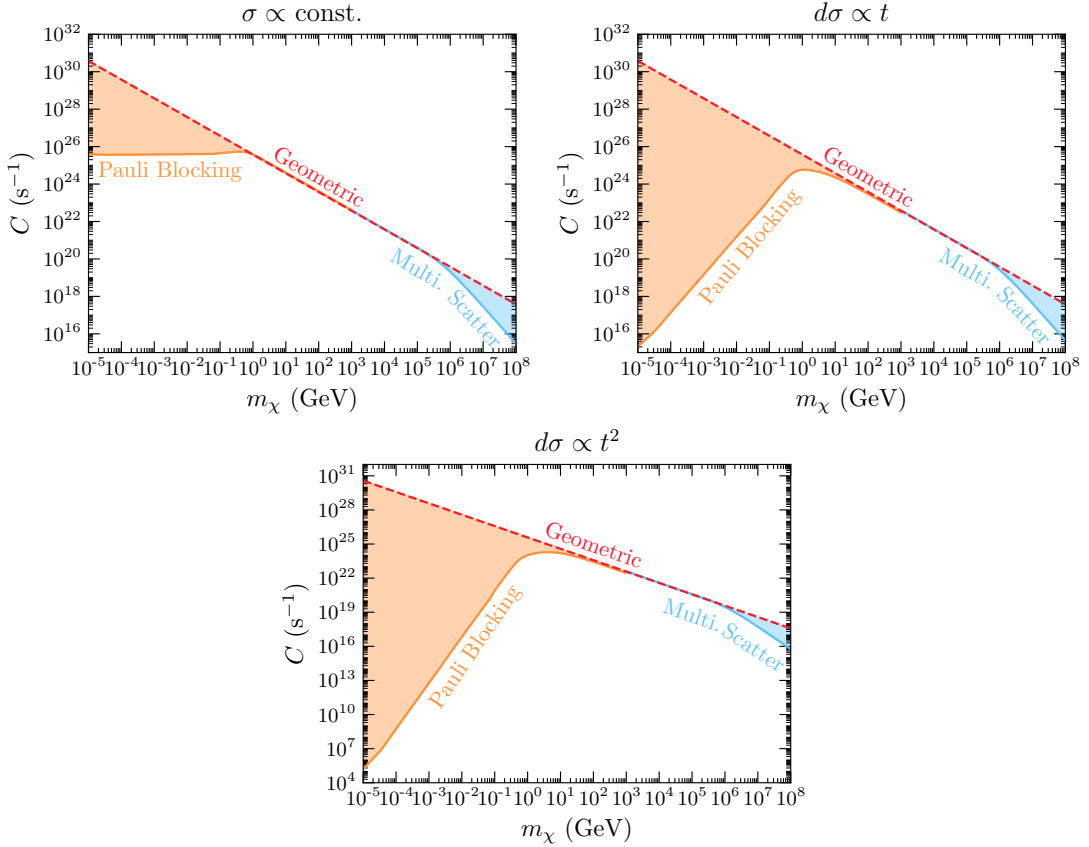


Figure 3.12: Capture rate for constant cross-section (top left), $d\sigma \propto t$ (top right) and $d\sigma \propto t^2$ (bottom), for $\sigma = \sigma_{\text{ref}} \sim 1.7 \times 10^{-45} \text{ cm}^2$ and NS EoS configuration BSk24-2. These plots extent the mass range of those in Fig. 3.6 to large DM masses.

D1, which contains in its squared matrix element a term independent of t , gives a result that is very similar to that of $\sigma = \text{const.}$ Operators D2 and D3, for which $|\bar{\mathcal{M}}|^2$ does not include terms independent of t , but rather terms proportional to t and t^2 , yield very similar results to that of $d\sigma \propto t$. Overall, we conclude that the lowest power of the transferred momentum determines the mass scaling of the capture rate at low DM mass. This result holds true for matrix elements that depend also on s .

In Fig. 3.12, we show the capture rate for a broad DM mass range, spanning 13 orders of magnitude from $m_\chi = 10 \text{ keV}$ to $m_\chi = 10^8 \text{ GeV}$, including all three of the mass regimes we have discussed in the previous sections, for $d\sigma \propto \text{const.}$ (first row), t^1 (second row) and t^2 (third row). The orange line indicates the capture rate calculated in the optically thin limit using the 4-dimensional integration in Eq. 3.59 that accounts for Pauli blocking. At large DM masses, Pauli suppression plays no

role and the capture rate approaches the geometric limit (dashed red line). We also show in Fig. 3.12 the effect of the inclusion of multiple scattering in the light blue line, which becomes relevant at $m_\chi \sim 10^6$ GeV. At $m_\chi \sim 10^5$ GeV that line matches the geometric limit as expected from the chosen value of the cross-section $\sigma = \sigma_{\text{ref}}$. At larger DM masses, $m_\chi \gtrsim 10^6$ GeV, multiple scatterings are required for the DM to be captured, hence an additional suppression factor of $1/m_\chi$ arises, as given in Eq. 3.83. Therefore, the capture rate becomes increasingly smaller than C_{geom} (light blue shaded area).

Comparing the plots for different t^n dependence, we can see that increasing the power of n has a small effect on the mass scale where the various suppressions become relevant. For example, comparing the light blue lines between the three figures, we see that the change of slope from the onset of multiple scattering moves slightly further to the right for larger n . This is a consequence of the fact that larger powers of n result in larger energy transfer (see, for example, Fig. A.2), leading to a larger capture probability c_1 and hence a larger m_i^* . However, the qualitative behaviour is the same for all choices of $d\sigma$: the suppression of the capture rate is primarily due to Pauli blocking at low mass and multiple scattering effects (i.e. a low capture probability) at large masses.

3.6 Summary

In this chapter, we have improved and extended the existing framework used to calculate the DM capture rate in the Sun to be compatible with compact objects, relaxing the simplifying assumptions that have previously been made. Specifically, we have derived exact expressions for the capture rate that correctly incorporate relativistic kinematics, gravitational focusing, Pauli blocking, and multiple-scattering effects. We also properly incorporate the internal structure of the star, consistently calculating the radial profiles of the EoS-dependent parameters and the general relativistic corrections, by solving the Tolman-Oppenheimer-Volkoff equations.

This new formalism was applied to neutron stars to highlight the features of the formalism mentioned above. Neutron stars (and compact objects in general) are composed of strongly degenerate matter, resulting in significant Pauli blocking of scattering interactions when the dark matter is light, $m_\chi \lesssim m_i$, suppressing the capture rate by several orders of magnitude. By including the radial dependence of the chemical potential in our calculations, we correctly account for Pauli suppression at any point in the star. However, note that the chemical potential is dependent on the EoS assumption.

For very large DM masses, $m_\chi \gtrsim 10^6$ GeV, the energy lost in a single collision will be insufficient for it to be captured. Hence, the DM must scatter multiple

times within an orbit to be captured, or else it simply leaves the star. To correctly compute the DM capture probability due to multiple scattering, we have derived, for the first time, an exact equation for the DM interaction rate in degenerate matter, and used that result to compute the differential capture rate as a function of the DM energy loss. This enables us to compute the cumulative probability that a DM particle is captured after multiple interactions, by averaging over the initial DM velocity distribution.

Although we have framed our results in terms of the scattering of DM from neutron targets in neutron star, it is straightforward to obtain the capture rate for DM scattering from any other degenerate species in compact objects. In the next chapter, we apply this formalism to DM scattering off the leptonic components of NSs, as well as the degenerate electrons within WDs.

4

Capture from Leptonic Species

This chapter is based on the results of Ref. [236] and on the electron capture results in Ref. [241]. We apply the formalism for capture in compact objects to leptonic targets in neutron stars and white dwarfs. In NSs, we calculate the projected sensitivities for the threshold DM-electron/muon cross-sections that could be probed in future observations. We then move to capture from the electrons in WDs, where we analyse the existing observations of the WDs in the globular cluster M4. Limits are placed on the DM-electron cross-section by requiring that the DM does not heat up the WDs above their observed temperatures through scattering and annihilation.

4.1 Capture from Leptons in Neutron Stars

Despite NSs being composed primarily of baryons (neutrons and protons in particular), they can still contain a substantial number of leptonic particles, namely electrons and, to a smaller extent, muons. For example, $1.5 M_{\odot}$ NS can contain $\sim 5 \times 10^{42}$ leptons, corresponding to a threshold cross-section $\sigma_{\ell x}^{\text{th}} \sim 10^{-43} \text{ cm}^2$, far below current direct detection bounds. This warrents a detailed study into the DM-lepton parameter space that could be explored with upcoming NSs observations.

To that end, we will consider the BSk24 EoS, with the benchmark configurations listed in Table 2.2. In Fig. 4.1 we plot the corresponding lepton profiles. As mentioned above, electrons are present in the core and the crust while muons appear at baryon number densities $n_b \simeq 0.12 \text{ fm}^{-3}$. The kink observed in the electron chemical potential marks out the transition from the core to the inner crust. The aforementioned radial profiles will be used in the following section to calculate the capture rate.

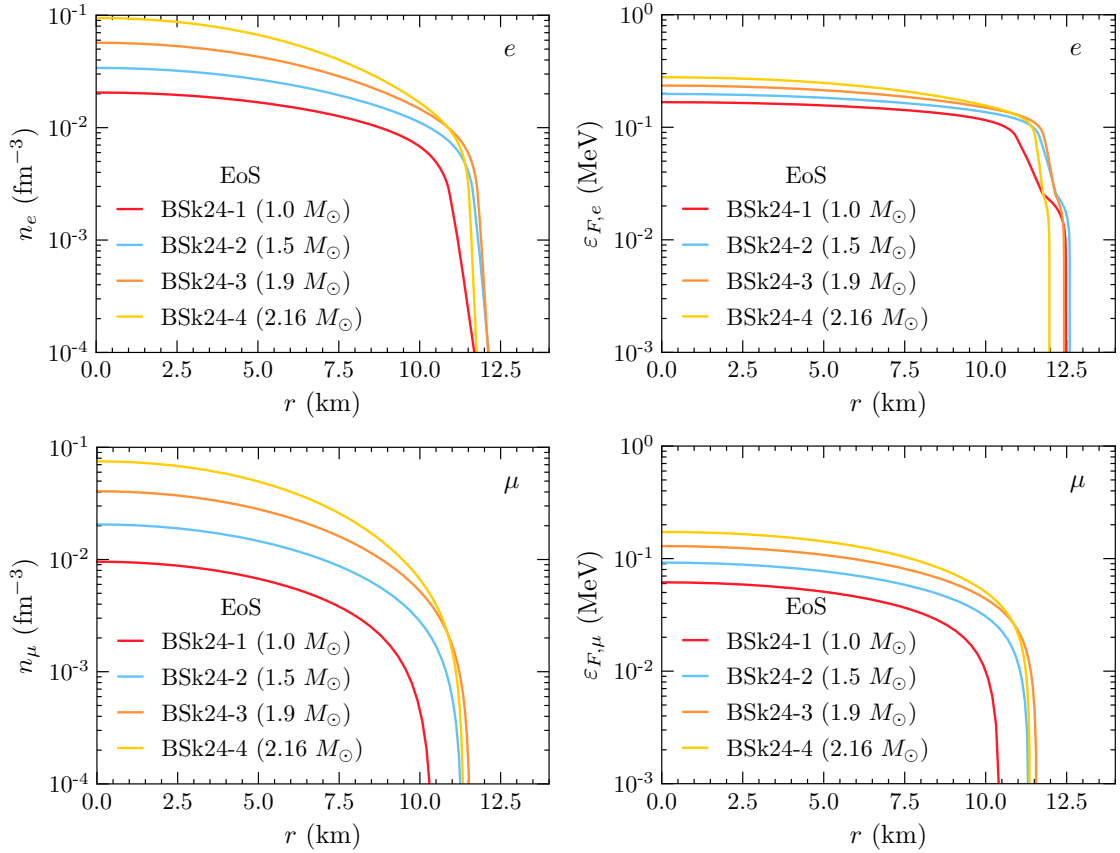


Figure 4.1: Number density profile (left) and chemical potential (right) for electrons (top) and muons (bottom) and NS configurations of the BSk24 functional in Table 2.2.

4.1.1 Capture Rate

In this section, we present results for the capture rate $C\Lambda^4$ for each of the EFT operators in Table 1.1, calculated in the optically thin limit using Eq. 3.60 for $m_\chi \lesssim m_\ell^*$ and Eq. 3.83 for $m_\chi \gtrsim m_\ell^{*1}$. Typical values of m_ℓ^* and $\sigma_{\ell\chi}^{\text{th}}$ are shown in Table 4.1 for electron and muon targets. Note that in m_ℓ^* will depend on the values of $B(r)$ and $\varepsilon_{F,\ell}(r)$, as well as the type of interaction considered.

Figs. 4.2 and 4.3 show the results for electron (light blue) and muon (magenta) targets, considering three NS benchmark models: BSk24-1 (dashed, $1M_\odot$), BSk24-2 (solid, $1.5M_\odot$) and BSk24-4 (dot-dashed, $2.16M_\odot$). In addition, we assume a nearby NS, located in the Solar neighbourhood, and thus take $\rho_\chi = 0.4 \text{ GeV cm}^{-3}$, $v_\star = 230 \text{ km s}^{-1}$ and $v_d = 270 \text{ km s}^{-1}$.

¹To numerically solve these equations we use the CUBA libraries [242, 243] linked to Mathematica [244].

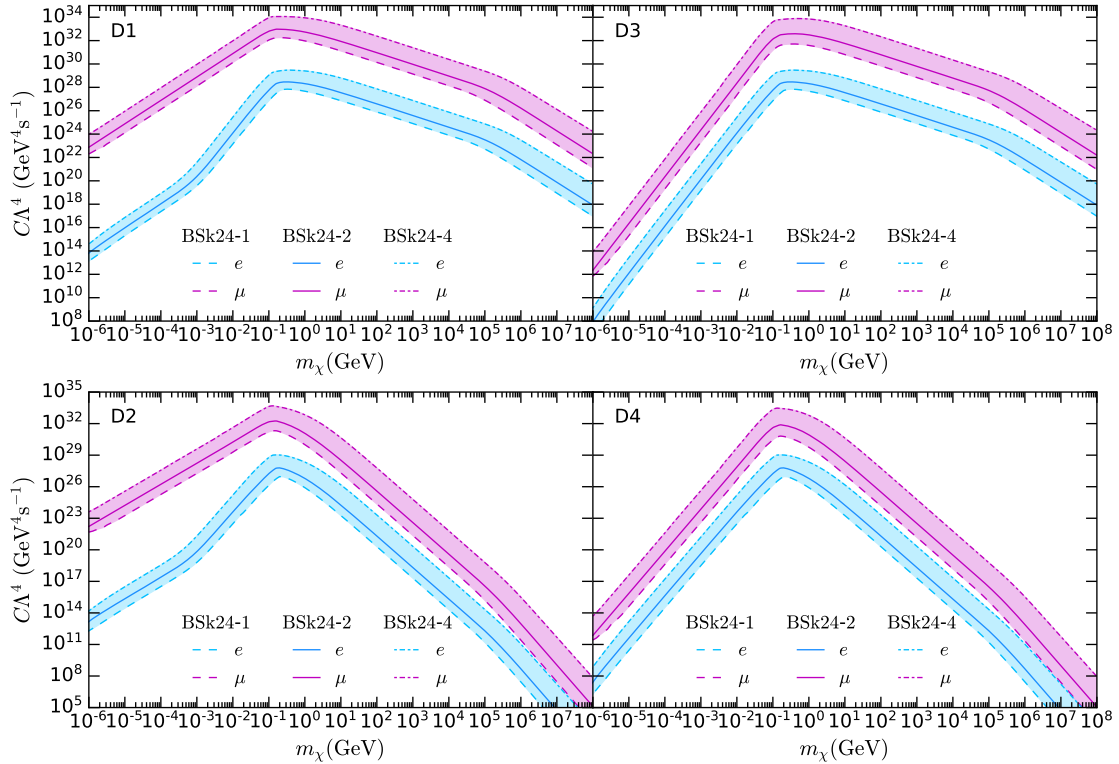


Figure 4.2: Capture rate in the optically thin limit for operators D1-D4 as a function of the DM mass m_χ for electrons (light blue) and muons (magenta) in the NS benchmark models BSk24-1 (dashed), BSk24-2 (solid) and BSk24-4 (dot-dashed). The shaded regions denote the change in the capture rate with the NS configuration for the same EoS family BSk24. All capture rates scale as Λ^{-4} . We require Λ to be sufficiently large that the capture rates are smaller than the geometric limit, C_{geom} .

Target	μ	e
$m_\ell^* \text{ (GeV)}$	$[0.3, 3] \times 10^5$	$[0.05, 1.7] \times 10^5$
$\sigma_{\ell\chi}^{\text{th}} \text{ (cm}^2)$	8×10^{-44}	3×10^{-44}

Table 4.1: Typical values of m_ℓ^* and $\sigma_{\ell\chi}^{\text{th}}$ for lepton targets. The exact value of $\sigma_{\ell\chi}^{\text{th}}$ depends on the DM mass, and the operator. We show here the simplest case of constant matrix element; other operators give similar results. The threshold cross section is approximately constant in the range $1 \text{ GeV} \lesssim m_\chi \lesssim m_\ell^*$, and takes larger values outside that range with a $1/m_\chi$ or m_χ scaling for small and large masses, respectively.

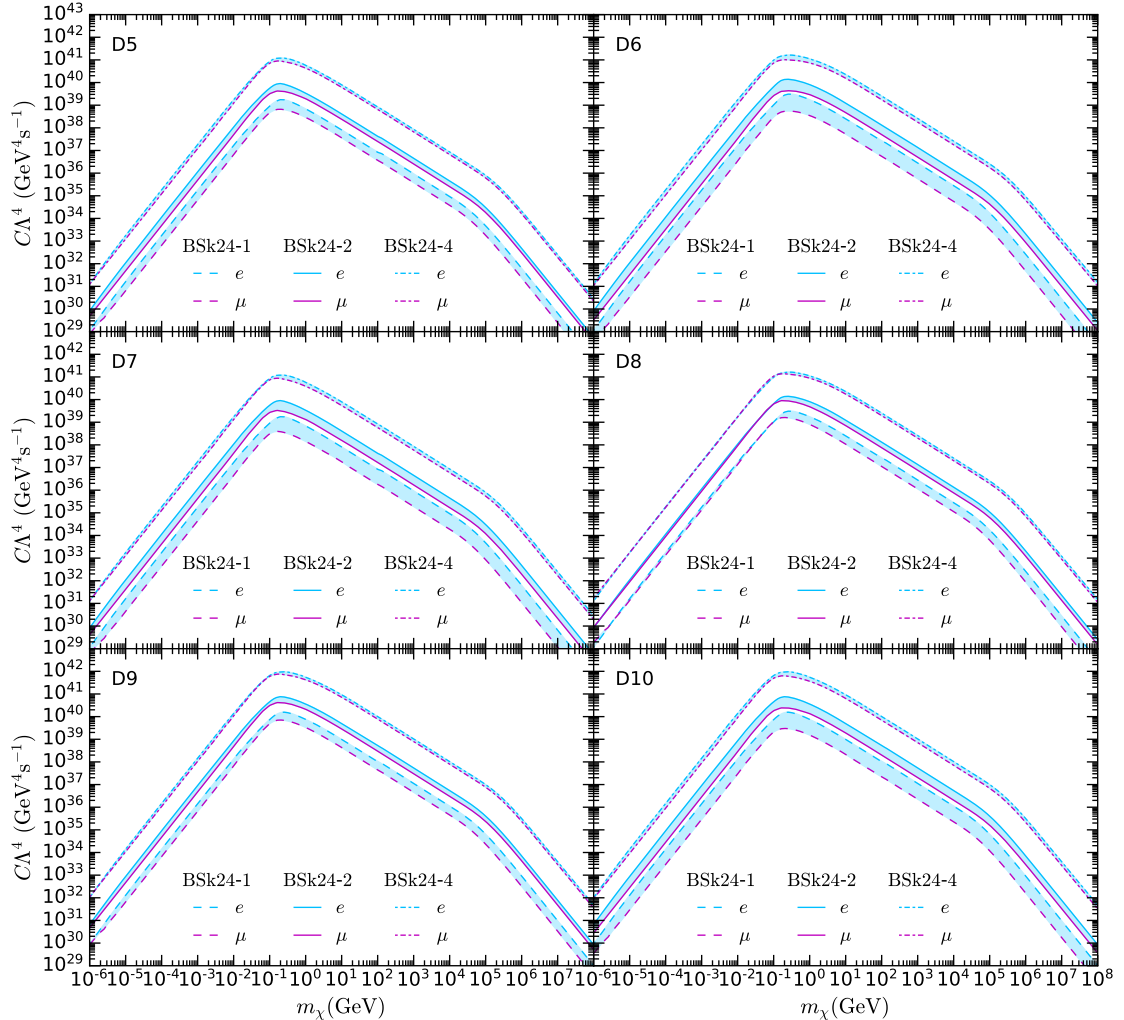


Figure 4.3: Capture rate in the optically thin limit for operators D5-D10 as a function of the DM mass m_χ for electrons (light blue) and muons (magenta) in the NS benchmark models BSk24-1 (dashed), BSk24-2 (solid) and BSk24-4 (dot-dashed). All capture rates scale as Λ^{-4} . The shaded regions depict the difference between capture by electrons and muons for the above mentioned NS models.

In these figures, we observe that the capture rate is suppressed due to Pauli blocking when $m_\chi \lesssim m_\ell$. The change of slope at $m_\chi \sim m_\ell^* \sim 10^5$ GeV, observed for both targets, is due to multiple scattering. For the operators D5-10 (Fig. 4.3), whose matrix elements depend explicitly on s , the slope of the capture rate in the three mass regimes are all very similar to one another, while for D1-D4 (Fig. 4.2), the shape of C is controlled by the power of t that dominates the interaction, which in general is the lowest power [235].

The exceptions to this are the capture rates for operators D1 and D2 with electron targets, which show a distinctive feature in the region $m_e \lesssim m_\chi \lesssim 100$ MeV that does not occur for the other operators. The capture rate for D1 and D2 is more suppressed in that particular region, similarly to D3 and D4, respectively. This is due to the form of the corresponding matrix elements together with the smallness of the electron mass. Namely, D1 and D2 are the only two operators that contain a factor $(t - 4m_\ell^2)$ in their scattering amplitudes, for electrons this means that the lowest power of t in $|\bar{\mathcal{M}}|^2$ is multiplied by m_e^2 , i.e. these terms are suppressed in the $m_e \lesssim m_\chi \lesssim 100$ MeV range. Consequently, the capture rate in that DM mass region is dominated by the unsuppressed t -terms in $|\bar{\mathcal{M}}|^2$, these being t for D1 (as for D3) and t^2 for D2 (see Table 1.1), while below m_e this additional suppression disappears and the capture rate follows the lowest power of t as was originally expected.

From Fig. 4.2, we note that for the same cutoff scale Λ , the muon contribution to the total capture rate for operators D1-D4 surpasses that of the electron by approximately 4 orders of magnitude for most of the DM mass range, and by about 8 orders of magnitude at very low mass for operators D1-D2. This is due to the large hierarchy between DM couplings to electrons and muons, which is of order $(\frac{m_\mu}{m_e})^2$. For operators D5-D10, electrons and muons will have the same strength couplings to DM (see Table 1.1). However, despite similar couplings and a lower abundance, muons are still able to capture DM at a rate comparable to electrons (see light blue regions in Fig. 4.3), thanks to their larger mass and lower chemical potential (see Fig. 4.1, right panels). This means that their interactions with DM are less Pauli suppressed, leading to a larger interaction rate. The small difference between the rates at which electron and muon are able to capture DM particles reduces for heavier NS configurations, e.g. from a factor ~ 5 (BSk24-1) to ~ 1.5 (BSk24-4) for D6 and D10; see the light blue shaded regions in Fig. 4.3. This is due to the muon abundance increasing in heavier NSs.

It is also worth noting that different EoS assumptions can lead to variations in the capture rate for electron targets of at least two orders of magnitude in the Pauli suppressed region and ~ 2.5 orders of magnitude in the large DM mass regime (compare dashed with dot-dashed light blue lines). For muons, the effect is even larger, with capture rate variations from $\sim \mathcal{O}(5 \times 10^2)$ for low DM mass to $\sim \mathcal{O}(2 \times 10^3)$ for heavy DM, when comparing the lightest and most massive NS

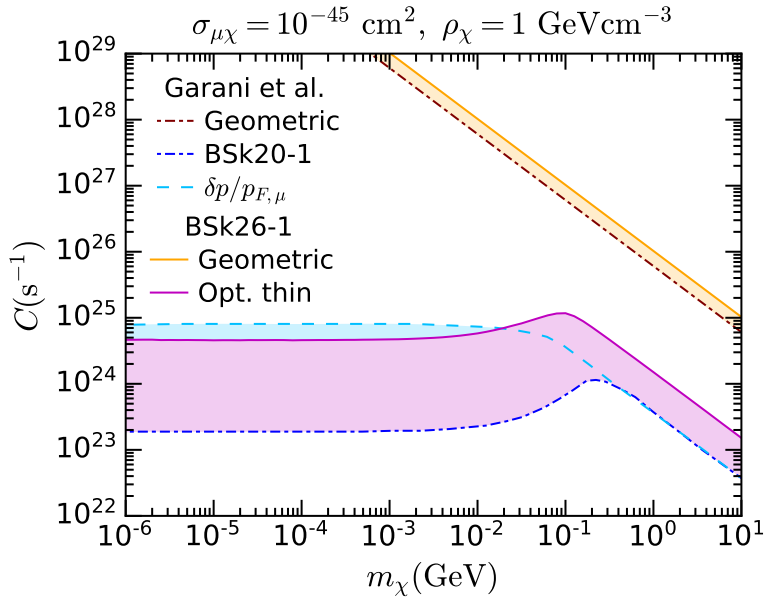


Figure 4.4: Capture rate in the optically thin limit for muon targets (magenta) and geometric (orange) limit as a function of the DM mass for constant cross-section $\sigma_{\mu\chi} = 10^{-45} \text{ cm}^2$, $\rho_\chi = 1 \text{ GeV cm}^{-3}$ and BSk26 functional for $M_\star \simeq 1.52M_\odot$ and $R_\star \simeq 11.6 \text{ km}$ denoted as BSk26-1. Capture rate calculations from Ref. [116] for a NS configuration with EoS BSk20-1 [216] equivalent to BSk26-1, are shown for comparison.

configurations of the BSk24 family. For the operators D2 and D4, these variations are even more pronounced for both electrons and muons and can reach $\sim \mathcal{O}(5 \times 10^3)$ and $\sim \mathcal{O}(5 \times 10^4)$, respectively for very large DM masses.

The DM capture rate for muon targets was calculated in Ref. [116], for constant cross-section and light DM, $m_\chi \leq 10 \text{ GeV}$. That calculation accounts for the NS internal structure and Pauli blocking, but neglects general relativity (GR) corrections and assumes that muons are non-relativistic. As outlined in Section 3.4.1, to compare our capture rate calculation with that of Ref. [116] we select a NS model that matches that of Fig. 12 of Ref. [116], namely Model A (BSk20-1): $M_\star \simeq 1.52M_\odot$, $R_\star \simeq 11.6 \text{ km}$. This new benchmark model is denoted as BSk26-1.

In Fig. 4.4, we compare both capture rate calculations for $\sigma_{\mu\chi} = 10^{-45} \text{ cm}^2$ and the same assumptions about ρ_χ , v_\star and v_d as in Ref. [116]. Comparing the geometric limit, Eq. 3.27 (solid orange), which properly accounts for gravitational focusing in NSs, with the non-relativistic computation in Ref. [116] (dot-dashed brown), we observe a $\sim 67\%$ enhancement, due to the $1/B(R_\star)$ factor that encodes GR corrections [237, 238]. In the region not affected by Pauli blocking, $m_\chi \gtrsim m_\mu$, our calculation in the optical thin limit (solid magenta) exceeds that of Ref. [116] (dot-

dashed blue) by a factor of ~ 4 , which increases as we move to the Pauli suppressed region where our computation is more than one order of magnitude higher. Unlike Ref. [116], our formalism incorporates GR corrections and made use of relativistic kinematics. We also show in dashed light blue, an estimation of the capture rate using the approximation $\delta p/p_{F,\mu} \sim m_\chi v_{esc}/p_{F,\mu}$ for $m_\chi < m_\mu$ [113], where $p_{F,\mu}$ is the muon Fermi momentum and v_{esc} is the escape velocity. This approximation overestimates the capture rate by a factor of approximately 2 in the Pauli blocked region below 10 MeV and underestimates it in the region of larger DM masses.

4.1.2 Finite Temperature Effects and Evaporation

In Section 4.1.1, we have restricted our computation of the capture rates to the DM mass range $m_\chi \in [1 \text{ keV}, 10^8 \text{ GeV}]$. While the upper limit on this mass range is somewhat arbitrary, primarily limited by the increasing numerical tax of calculating Eq. 3.83, the lower bound comes from working in the zero-temperature approximation, $T_* \rightarrow 0$. This approximation is valid for DM masses $m_\chi \gg T_*$, which for a 10^3 K star requires $m_\chi \gg 90 \text{ meV}$.

For DM masses $m_\chi \lesssim \mathcal{O}(10)T_*$, thermal effects begin to play an important role in the capture rate, significantly boosting the rate in this low mass range [116]. Consequently, the complete Fermi-Dirac distributions should be used in Eqs. 3.50 and 3.39. To illustrate the effect of the NS temperature, we show in Fig. 4.5 the ratio of the capture rate in a NS with $T_* = 10^5 \text{ K} \simeq 8.6 \text{ eV}$ to the corresponding capture rate in the $T_* \rightarrow 0$ limit, assuming scattering on electrons, the targets for which this effect is most relevant.

From this figure, we immediately notice that the ratio starts to depart from 1 at $m_\chi \sim 100 \text{ eV} \sim 10T_*$ for all operators. Operators whose matrix element depends on higher powers of the exchanged momentum t feature a larger increment in the capture rate due to finite temperature. In fact, the operator D4 ($|\bar{\mathcal{M}}|^2 \propto t^2$) receives the largest correction, followed by D2-D3 (whose $|\bar{\mathcal{M}}|^2$ is a linear combination of t^1, t^2), then D1 ($|\bar{\mathcal{M}}|^2$ is a linear combination of t^0, t^1, t^2) and finally by D5-D10 (whose $|\bar{\mathcal{M}}|^2$ include all powers of the kind $t^n s^m$).

In the very light DM regime, there is another that needs to be accounted for: evaporation. This occurs when the dark matter up-scatters to a state where the final DM kinetic energy is larger than the energy required to escape the star, and hence DM particles are expelled. Thus, as opposed to capture, evaporation drains energy from the star. To estimate the evaporation rate, we convolve the DM distribution within the star, with the interaction rate for up-scattering, $\Gamma_{\text{up}}^-(E_\chi, T_*)$, retaining the temperature dependence.

Assuming the DM distribution to be isothermal with temperature $T_\chi = T_*$, we

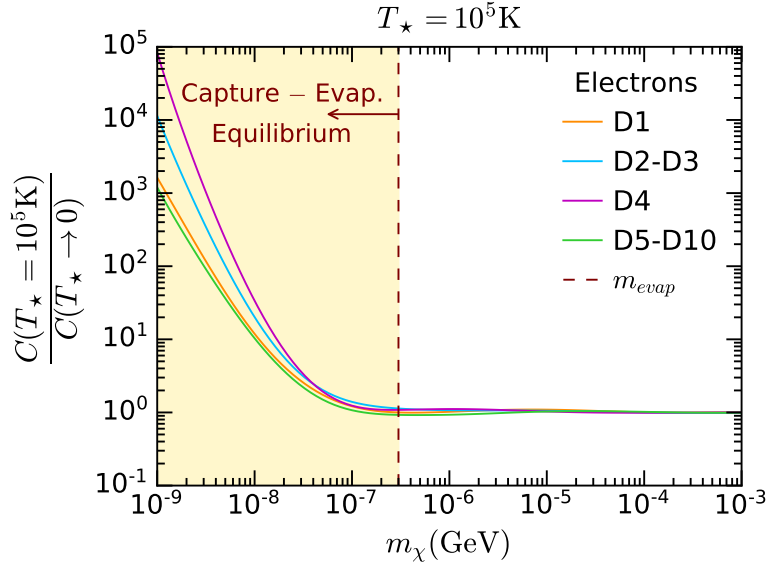


Figure 4.5: Finite temperature effects on the capture rate for electron targets, assuming the NS model BSk24-2. The DM mass range where capture and evaporation are expected to be in equilibrium is shaded in yellow. The dashed brown line corresponds to the evaporation mass.

have

$$n_\chi^{\text{iso}}(r, E_\chi) = \frac{n_c}{1 + e^{\frac{E_\chi - m_\chi \left(\frac{1}{\sqrt{B(r)}} - 1\right)}{T_*}}} \quad (4.1)$$

$$\simeq \frac{\exp \left[-\frac{E_\chi - m_\chi \left(\frac{1}{\sqrt{B(r)}} - 1\right)}{T_*} \right]}{4\pi \int_0^{R_*} dr r^2 \int_0^{m_\chi \left(\frac{1}{\sqrt{B(r)}} - 1\right)} dE_\chi \exp \left[-\frac{E_\chi - m_\chi \left(\frac{1}{\sqrt{B(r)}} - 1\right)}{T_*} \right]}, \quad (4.2)$$

where n_c is a normalisation constant such that the total number of DM particles is $N_\chi = \int d^3r \int dE_\chi n_\chi^{\text{iso}}(E_\chi, r)$. The interaction rate for up-scattering, $\Gamma_{\text{up}}^-(E_\chi, T_*)$ can be related to the down-scattering rate through

$$\frac{d\Gamma_{\text{up}}^-}{dq_0}(E_\chi, q_0, T_*) = -\frac{e^{q_0/T_*}}{1 - e^{q_0/T_*}} \frac{d\Gamma^-}{dq_0}(E_\chi, q_0), \quad q_0 < 0, \quad (4.3)$$

where $\frac{d\Gamma^-}{dq_0}$ is the differential interaction rate in the $T_* \rightarrow 0$ approximation derived in Appendix A.2.1, with the full derivation of Eq. 4.3 in Appendix A.2.2.

The evaporation rate then reads

$$E \simeq 4\pi \int_0^{R_*} dr r^2 \int_0^{m_\chi \left(\frac{1}{\sqrt{B(r)}} - 1 \right)} dE_\chi n_\chi^{\text{iso}}(r, E_\chi) \int_{-\infty}^{-q_0^{\min}} dq_0 \frac{d\Gamma_{\text{up}}^-}{dq_0}(q_0, T_*) , \quad (4.4)$$

$$q_0^{\min} = m_\chi \left(\frac{1}{\sqrt{B(r)}} - 1 \right) - E_\chi , \quad (4.5)$$

where q_0^{\min} is the minimum energy the DM needs to gain to be ejected from the star. When the DM distribution is concentrated very close to the centre of the star, this expression can be approximated by

$$E \sim \frac{m_\chi m_\ell^2 \sigma_{\ell\chi}}{4\pi^2} \left(\frac{1}{\sqrt{B(0)}} - 1 \right)^2 \exp \left[-\frac{m_\chi}{T_*} \left(\frac{1}{\sqrt{B(0)}} - 1 \right) \right] . \quad (4.6)$$

The rate at which DM particles accumulate in NSs is then given by

$$\frac{dN_\chi}{dt} = C - EN_\chi , \quad (4.7)$$

assuming that DM annihilation is negligible. The solution of this equation is

$$N_\chi(t_*) = C t_* \left(\frac{1 - e^{-Et_*}}{Et_*} \right) , \quad (4.8)$$

where t_* is the age of the NS. The term in brackets quantifies the depletion of the number of capture DM particles due to the evaporation process. This factor will be of order 1 unless $E(m_\chi) t_* \gtrsim \mathcal{O}(1)$. Therefore, we will define the evaporation mass as the DM mass for which the previous relation holds, i.e. $E(m_{\text{evap}})t_* \sim 1$. For DM masses below this threshold, $m_\chi \lesssim m_{\text{evap}}$, the capture and evaporation processes are in equilibrium with each other. In that limit, the net energy exchange in the star due to the combined effects of DM capture and evaporation would be negligible, and hence we would be unable to constrain DM interactions using the NS temperature as a probe.

Using Eq. 4.5, we find the evaporation mass to be of order $m_{\text{evap}} \sim \mathcal{O}(100T_*)$ for all scattering targets in old NSs with $t_* \sim \mathcal{O}(10 \text{ Gyr})$. For instance, for $T_* = 10^5 \text{ K}$ and electron targets, we obtain $m_{\text{evap}}^e \simeq 300 \text{ eV}$. The region in Fig. 4.5 for which capture and evaporation are in equilibrium is shaded in yellow, with the evaporation mass indicated by the dashed brown line. From this, we can see that the finite temperature effects on the capture rate become important for masses below the evaporation mass, for all operators we consider. Hence, when calculating the capture rate while aiming to constrain DM interactions, finite temperature effects can be safely neglected.

4.1.3 Results

Threshold Cross-Sections

In Section 3.2.2, we defined the threshold cross-section, $\sigma_{\ell\chi}^{\text{th}}$, as the cross-section for which the capture rate, $C(\sigma(\Lambda), m_\chi)$, calculated in the optically thin regime becomes equal to the geometric limit, C_{geom} . The threshold cross-section restricts the NS sensitivity to DM-target interactions since for $\sigma \geq \sigma_{\ell\chi}^{\text{th}}$ the capture rate saturates to the geometric limit C_{geom} .

In Fig. 4.6, we show the threshold cross-sections for lepton targets, electrons and muons, and compare them with existing direct detection limits and expected sensitivities of future experiments. The neutrino floor for electron recoil experiments for silicon targets [245] is shown as a shaded yellow region. The solid light blue and magenta lines correspond to the value of σ_{th} for electrons and muons respectively, calculated using the NS model BSk24-2 ($1.5M_\odot$), while the shaded bands in light blue and magenta denote the expected range for σ_{th} for the two different targets, obtained by varying the NS configuration along the BSk24 family. BSk24-1 ($1M_\odot$) gives the upper bound on σ_{th} and BSk24-4 ($2.16M_\odot$) the lower bound. Note that the variation in σ_{th} due to the NS EoS increases with the DM mass and for muons goes from about one order of magnitude in the low mass range, to two orders of magnitude in the multiple scattering region. For electrons, this effect is slightly less pronounced.

All the limits for existing experiments are orders of magnitude weaker than the expected NS reach, with only the future DAMIC-M [246] (dashed brown line) expected to overcome NS electron scattering sensitivity and approach that of muons, in the DM mass range $3 \text{ MeV} \lesssim m_\chi \lesssim 30 \text{ MeV}$. Moreover, NS sensitivity to DM interactions with lepton targets is expected to be well below the neutrino floor for $m_\chi \gtrsim 100 \text{ MeV}$ and, in the case of muons, even for $m_\chi \lesssim 1 \text{ MeV}$.

Note that NSs have a better sensitivity to vector-vector interactions (operator D5, see right panel) than scalar-scalar interactions (operator D1, see left panel) in the low DM regime for both leptonic targets, and especially for electrons. As discussed in Section 4.1.1, there is an additional suppression in the capture rate of scalar operators that stems from an $m_e^2 t$ term in their scattering amplitudes.

Similar threshold cross-sections can be estimated for the remaining operators. Operators with s-dependent matrix elements (D6-D10) have σ_{th} that behave like that of D5 for both electrons and muons. D2 presents the same features as D1 in the sub-GeV regime for electrons, due to the similar shape of their capture rates (see Fig. 4.2) and D3-D4 show a steeper slope in the $m_\chi \lesssim m_e$ region with respect to D1-D2, due to the capture rate dependence on higher powers of t .

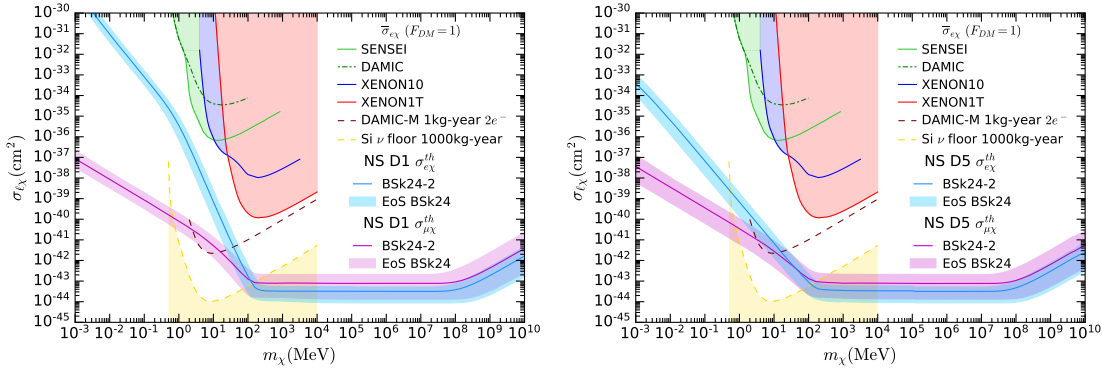


Figure 4.6: DM-lepton threshold cross-section for operators D1 (left) and D5 (right) for the EoS BSk24. The solid blue (electron) and magenta (muon) lines represent σ_{th} , are computed assuming the NS model BSk24-2, while the shaded bands represent the expected range due to variation of the EoS. For comparison, we show leading electron recoil bounds for heavy mediators from SENSEI [247], DAMIC [248], XENON10 [249], XENON1T [250], projected sensitivities from DAMIC-M [246] as well as the neutrino floor for silicon detectors [245].

Comparison with Literature

We now compare our calculations for the capture rates and resulting reach in the EFT cutoff Λ for operators D1 and D5 to those presented in Refs. [133, 251]². The formalism in Refs. [133, 251] is valid for relativistic and non-relativistic targets in a broad mass range, however, several simplifying assumptions were made that are accounted for in our results. Namely, they do not account for the DM velocity distribution far from the star, nor do they incorporate the internal structure of the NS. Instead, constant chemical potentials and particle abundances that have been averaged over the core volume are used. These quantities correspond to the NS model BSk24-2 and were calculated in Ref. [135].

In the top panels of Figs. 4.7 and 4.8, we compare the reach in Λ for DM-lepton scattering cross-sections in Refs. [133, 251] with the cutoff scale we obtain for the maximum capture rate, $C(\Lambda, m_\chi) = C_{\text{geom}}$. Our results differ the most for electron targets in the Pauli suppressed region by a factor of ~ 2.5 , and we find Pauli blocking is active at a slightly lighter DM mass. This arises from our use of the full radial profiles for the NS input parameters, and that light DM particles whose interactions are subject to Pauli blocking are captured closer to the surface [235]. The discrepancy is reduced to a factor of ~ 1.25 in the intermediate mass region and there is almost no difference in the large mass regime. For muons, we find a Λ that is, on average, a factor ~ 1.33 greater than that of Refs. [133, 251] along the

²Note that the Yukawa couplings for scalar and pseudoscalar operators in Refs. [133, 251] are embedded into the cutoff scale Λ .

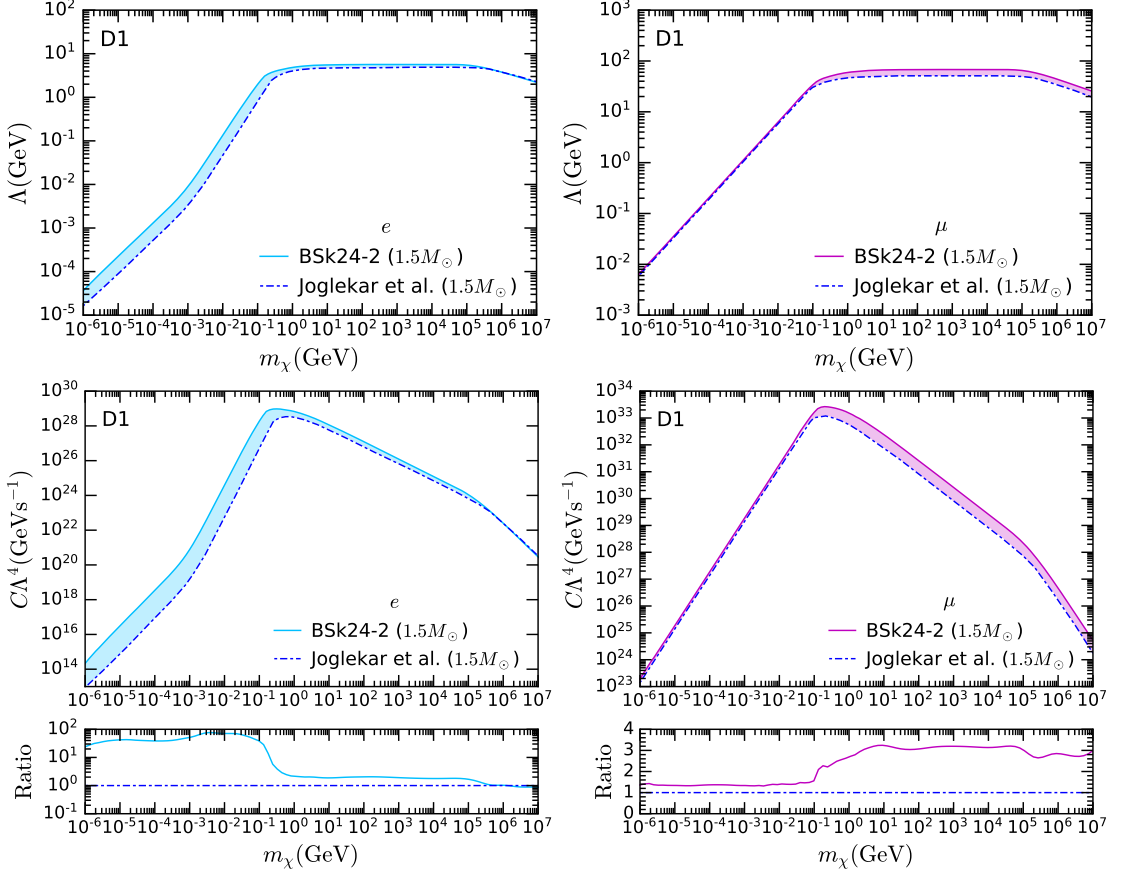


Figure 4.7: Comparison of the reach in Λ for D1 with the approach of Ref. [251]. The shaded regions denote the difference in Λ (top) and $C\Lambda^4$ (middle) between the two approaches and their ratio is shown in the bottom panels.

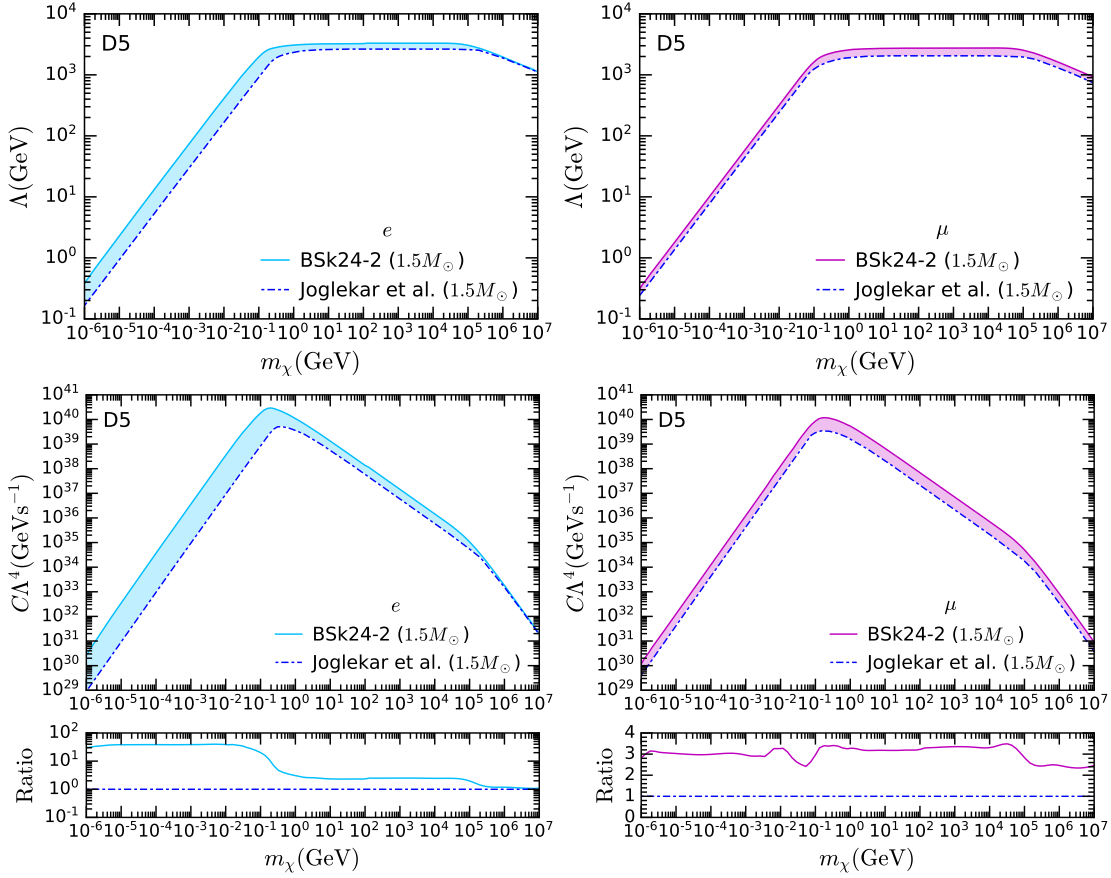


Figure 4.8: Same as Fig. 4.7 but for the vector operator D5.

whole DM mass range for D5, and is in almost perfect agreement in the $m_\chi \lesssim m_\mu$ region for D1.

In the middle panels of Figs. 4.7 and 4.8 we show how these small differences in the two approaches translate to differences in the capture rate, comparing $C\Lambda^4 = \Lambda^4 C_{\text{geom}}$ obtained with the two formalisms. Since the geometric limit of the capture rate is not defined in Refs. [133, 251], we use a definition similar to Eq. 3.27 that is compliant with the assumptions made by these authors. For electron scattering, we see that the formalism that does not account for the NS internal structure underestimates the capture rate in the region affected by Pauli blocking by a factor ~ 40 (bottom LH panels of Figs. 4.7 and 4.8). This difference is slightly larger in the region where the Pauli suppression is stronger, becoming almost a factor of ~ 100 for D1 in the range $m_e \lesssim m_\chi \lesssim 100$ MeV. For muons, the difference between the two approaches is less pronounced, with a maximum ratio of ~ 3.5 for both operators.

4.2 Capture from Electrons in White Dwarfs

We now turn our attention to DM capture in white dwarfs, where the degenerate electrons preventing these stars from gravitational collapse are a perfect candidate for the capture formalism we have constructed. Not only are the electrons extremely degenerate, with chemical potentials $\varepsilon_{F,e} \gg m_e$ in some stars, but they can also be ultra-relativistic. As the gravitational fields of WDs are significantly weaker than those of NSs, the incoming DM does not get boosted to relativistic velocities in this case. This leads to the scattering interactions taking place in an interesting kinematic regime, as we are dealing with non-relativistic DM scattering off ultra-relativistic electrons.

4.2.1 Capture Rates

Single scattering

The kinematics involved in treating the scattering of non-relativistic DM off ultra-relativistic electrons requires a few modifications to the interaction rate derived in Section 3.2.3, Eq. 3.39. We also reintroduce the dependence of the capture rate on the DM-target relative velocity distribution, $f_{\text{MB}}(u_\chi)$, one might be interested in departures from the standard MB speed distribution. The generalised expression for the capture rate without integrating over the DM velocity u_χ is

$$C = 4\pi \frac{\rho_\chi}{m_\chi} \int_0^\infty \frac{f_{\text{MB}}(u_\chi) du_\chi}{u_\chi} \int_0^{R_*} \eta(r) r^2 \frac{\sqrt{1 - B(r)}}{B(r)} \Omega^-(r) dr, \quad (4.9)$$

where interaction rate between DM and the electron targets is given by [235, 236]

$$\begin{aligned} \Omega^-(r) = & \frac{\zeta(r)}{32\pi^3} \int dt dE_e ds \frac{|\bar{\mathcal{M}}_{e\chi}|^2}{2s\beta(s) - \gamma^2(s)} \frac{E_e}{m_\chi} \sqrt{\frac{B(r)}{1 - B(r)}} \frac{s}{\gamma(s)} \Theta(E'_e - E_e) \\ & \times f_{\text{FD}}(E_e, r)(1 - f_{\text{FD}}(E'_e, r)) \Theta\left(E_e \sqrt{\frac{1 - B(r)}{E_e^2 - m_e^2}} - \frac{s_{\max} + s_{\min} - 2s}{s_{\max} - s_{\min}}\right), \end{aligned} \quad (4.10)$$

$$\beta(s) = s - (m_e^2 + m_\chi^2), \quad (4.11)$$

$$\gamma(s) = \sqrt{\beta^2(s) - 4m_e^2 m_\chi^2}, \quad (4.12)$$

where E_e and E'_e are the target electron initial and final energies, respectively. The correction factor $\zeta(r) = \frac{n_e(r)}{n_{\text{free}}(r)}$ accounts for the fact we are using realistic profiles for the electron number density $n_e(r)$ and the chemical potential $\varepsilon_{F,e}(r)$, while the

interaction rate is defined in the free Fermi gas approximation [116, 235, 252]. The definition of $n_{\text{free}}(r)$ can be found in Ref. [235]. The integration intervals in Eq. 4.10 are

$$t_{\max} = 0, \quad (4.13)$$

$$t_{\min} = -\frac{\gamma^2(s)}{s}, \quad (4.14)$$

$$s_{\min} = m_e^2 + m_\chi^2 + 2 \frac{E_e m_\chi}{\sqrt{B(r)}} - 2 \sqrt{\frac{1 - B(r)}{B(r)}} m_\chi \sqrt{E_e^2 - m_e^2}, \quad (4.15)$$

$$s_{\max} = m_e^2 + m_\chi^2 + 2 \frac{E_e m_\chi}{\sqrt{B(r)}} + 2 \sqrt{\frac{1 - B(r)}{B(r)}} m_\chi \sqrt{E_e^2 - m_e^2}, \quad (4.16)$$

$$E_{e,\min} = m_e, \quad (4.17)$$

while $E_{e,\max}$ should be set to $E_{e,\max} = m_e + \varepsilon_{F,e}$ in the $T_\star \rightarrow 0$ limit, or left free otherwise.

We have introduced two additional Θ functions in Eq. 4.10 when compared to Refs. [235, 236]. The first Θ function ensures that we count only scatterings that are kinematically allowed, in this case requiring that the collision is head-on. We explain the details of the derivation of this phase space constraint in Appendix A.5. The second Heaviside function enforces that the DM loses energy, which is required for finite temperature calculations. In the zero temperature limit, on the other hand, the FD distributions can themselves be approximated by Θ functions. Therefore, the initial states occupy all the lower energy levels, and scattering can proceed only if the target acquires enough energy to be ejected from the Fermi Sea. Specifically, the inequalities enforced are

$$E_e \leq m_e + \varepsilon_{F,e}, \quad (4.18)$$

$$E'_e > m_e + \varepsilon_{F,e}. \quad (4.19)$$

It is also worth noting that when computing the capture rate while keeping the leading order terms in the initial DM energy, i.e. setting $E_\chi = m_\chi(1/\sqrt{B(r)} + u_\chi^2/2)$ in the interaction rate, we find that there is no significant effect compared to setting $u_\chi \rightarrow 0$ and using Eq. 3.26 instead. This can be understood by noting that the halo velocities are of order $u_\chi^2 \sim 10^{-6}$, while the escape velocity is $v_{\text{esc}}^2 = 1 - B(r) \sim 10^{-3}$, and so the corrections are expected to be only of order $u_\chi^2/v_e^2 \sim 10^{-3}$. It is worth noting that in the case of scattering of the ions in WDs the $u_\chi \rightarrow 0$ approximation is less justifiable, discussed in Ref. [241].

Multiple Scattering

In the optically thin limit, and for DM masses larger than a certain threshold denoted m_e^* , the single scatter capture probability is no longer ~ 1 . In this regime, multiple collisions are required for the DM particles to lose sufficient energy to be captured. In the $T_\star \rightarrow 0$ limit, one can use the multiple scattering approach outlined in Section 3.4.2, which involves inserting the capture probability $c_1(r)$ in Eq. 4.10 instead of the $\Theta(E'_e - E_e)$ term, with

$$c_1(r) = 1 - e^{-\frac{m_e^*(r)}{m_\chi}} \sim \frac{m_e^*(r)}{m_\chi}. \quad (4.20)$$

Since the DM energy loss for scattering on electrons is much larger than the WD core temperature, as is the case for DM scattering in neutron stars, we can calculate m_e^* using the same method as for NS in the previous chapter. We assume a MB velocity distribution for the DM velocities in M4, with $v_\star = 20 \text{ km s}^{-1}$, $v_d = 8 \text{ km s}^{-1}$. Taking a WD of mass $M_\star = 1.38M_\odot$, a constant matrix element, $B = 0.995$ and $\varepsilon_{F,e} = 8 \text{ MeV}$, we find a typical value of

$$m_e^* \simeq 10^5 \text{ GeV}. \quad (4.21)$$

Capture Rates for Electron Scattering

We are now ready to calculate the capture rate for the operators in Table 1.1, for DM-electron interactions with $\Lambda_f = \Lambda_e$, $\mu = m_\chi/m_e$ and the coefficients c_N^I , $I = S, P, V, A, T$ set to 1. In Fig. 4.9, we present our results for $C\Lambda_e^4$ in the zero temperature and optically thin limits for carbon WDs with $M_\star = 0.49M_\odot$ (top panels) and $M_\star = 1.38M_\odot$ (bottom panels). In both WDs, Pauli blocking strongly suppresses the capture rate in the light mass regime, $m_\chi \lesssim 100 \text{ MeV}$. Above this mass range, Pauli suppression persists but remains minimal.

The change of slope in the Pauli suppressed region for operators D1 and D2 is due to their matrix elements containing a factor $(t - 4m_e^2)$, which introduces an additional suppression due to the smallness of the electron mass in the $m_e \lesssim m_\chi \lesssim 100 \text{ MeV}$ interval [236]. This was also present in the NS case discussed in the previous section. Then, a transition between the Pauli blocked and the unsuppressed capture rate is observed for all the operators, which is immediately noticeable in the case of the light WD, where we observe a valley in the $100 \text{ MeV} \lesssim m_\chi \lesssim 1 \text{ GeV}$ mass range. In the heavy WD, this transition region extends up to $\sim 10 \text{ GeV}$ and is more evident for operators D5-D10. The region at which multiple scattering becomes relevant also depends on the star configuration. It occurs at $m_\chi \gtrsim 1 \text{ TeV}$ for the light WD, and at around $m_\chi \gtrsim 10^5 \text{ GeV}$ for the heavy WD, observed as a change of slope in the capture rate at around those masses.

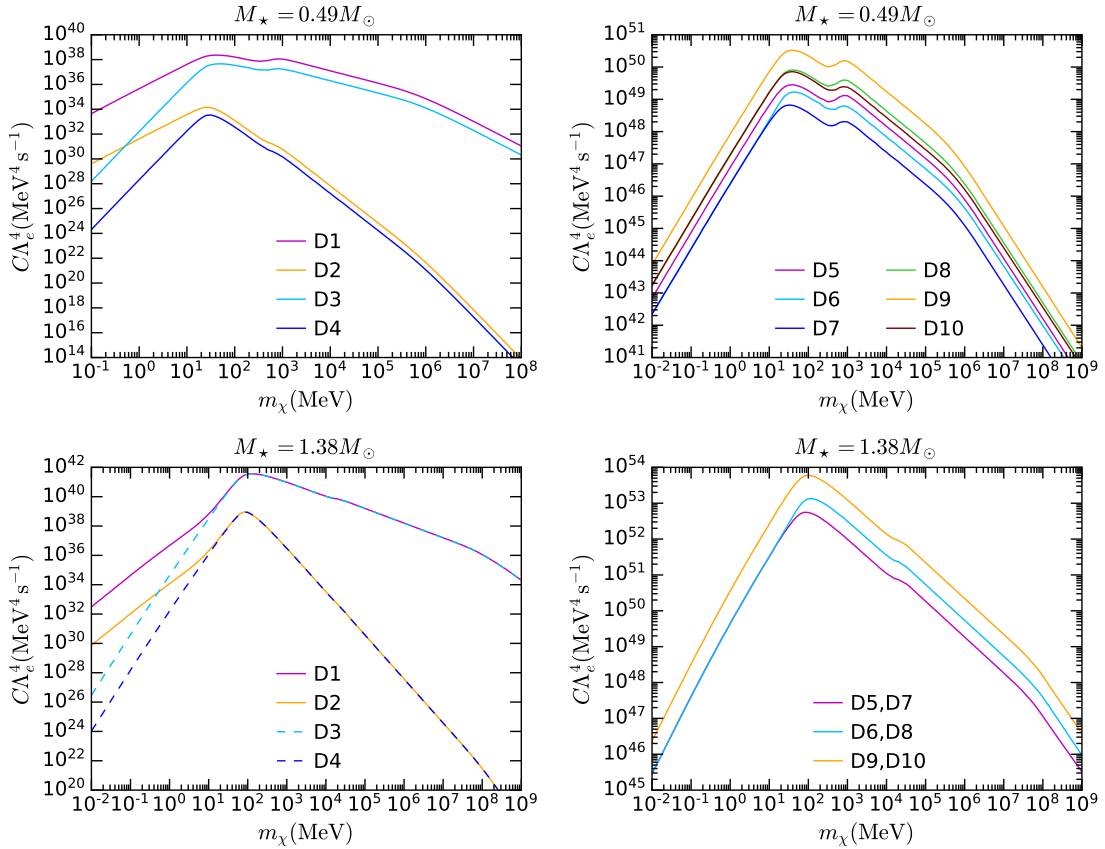


Figure 4.9: Capture rate for scattering on electrons, in the optically thin limit, as a function of the DM mass for the lightest (WD₁, top panels) and heaviest (WD₄, bottom panels) carbon WDs in Table ??.

It is worth remarking that, in contrast to the light WD, the heavy WD features an electron chemical potential more than one order magnitude higher, and that the electrons here are ultra-relativistic. As a result, the capture rate curves for WD₄ exhibit similar features to those observed in neutron stars where electrons are degenerate and ultra-relativistic [236]. In addition, since the electrons in the heavy WD are relativistic, the scattering amplitudes are dominated by terms of the form $t^n s^m$ in the large DM mass regime, while terms proportional to m_e^2 are suppressed (see Table 1.1). This results in very similar capture rates for operators D1 and D3, D2 and D4, D5 and D7, D6 and D8, D9 and D10.

Finally, we note that the capture rate due to scattering on electrons would scarcely be affected by a different chemical composition, such as He or O.

4.2.2 Finite Temperature Effects and Evaporation

As was observed in the case of DM scattering off electrons in NSs, accounting for the finite temperature of the star can have a large impact when the dark matter mass is low. There are two main effects to consider. First, there is a boost in the capture and interaction rates as there is a greater volume of phase space for the interactions to take place in. This is due to the DM energy loss, q_0 , being bounded from above such that $q_0^{\text{MAX}} \lesssim 3 \text{ MeV}$ at zero temperature, and so only the outer shell of the Fermi sphere contributes to the capture rate. In comparison, non-zero T_\star allows deeper shells of the Fermi sphere to contribute, substantially increasing the capture rate. Calculating the capture rate for finite T_\star is achieved by using the full form of the Fermi-Dirac distributions in Eq. 4.10, instead of approximating them with Θ -functions, and removing the upper limit on the E_e integration interval.

Second, evaporation of the captured DM becomes possible due to scattering off the thermal electrons. Again, this is relevant for low-mass DM. For these finite temperature effects to be relevant in DM capture, they need to come into effect at DM masses above the evaporation mass of the WD [116, 236]. To estimate the evaporation rate, we use the full expression obtained in Section 4.1.2 for neutron stars, reiterated here for electrons in WDs

$$E \sim \frac{m_\chi m_e^2 \sigma_{e\chi}}{4\pi^2} \left(\frac{1}{\sqrt{B(0)}} - 1 \right)^2 \exp \left[-\frac{m_\chi}{T_\star} \left(\frac{1}{\sqrt{B(0)}} - 1 \right) \right], \quad (4.22)$$

when the accreted DM is confined close to the centre of the star. Note that the evaporation rate is driven by the ratio m_χ/T_\star , and as such is enhanced for light DM.

In Fig. 4.10, we plot the ratio of the capture rate for $T_\star = 10^5 \text{ K}$ to the zero temperature approximation for the same WDs as in Fig. 4.9. Operators that depend

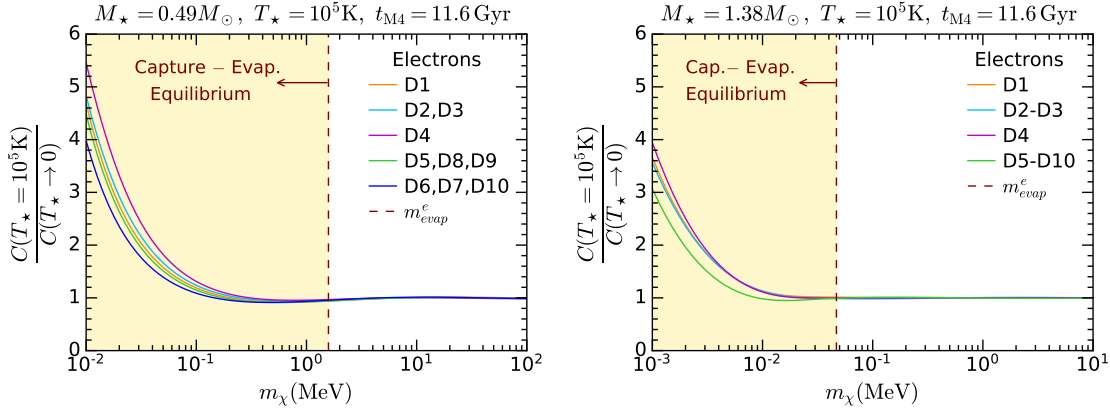


Figure 4.10: Finite temperature effects on the capture rate in the case of scattering on electron targets, for two WDs in the globular cluster M4, namely WD₁ (left) and WD₄ (right) in Table 2.1. The DM mass range where capture and evaporation are expected to be in equilibrium is shaded in yellow. The dashed brown line corresponds to the evaporation mass.

only on powers of the exchanged momentum t , namely D1-D4, are the most affected by finite temperature corrections, followed by operators that contain in their matrix elements linear terms of the form $t^n s^m$, i.e., D5-D10. As can be noticed, the DM mass range at which these effects become relevant depends on the specific WD configuration and similar to the NS case is always below the evaporation mass for electron scattering m_{evap}^e (dashed brown lines). We find that the evaporation mass for carbon WDs with $T_\star = 10^5$ K ranges from $m_{\text{evap}}^e \sim 50$ keV ($M_\star = 1.38 M_\odot$, right panel) to $m_{\text{evap}}^e \sim 1.5$ MeV ($M_\star = 0.49 M_\odot$, left panel). The evaporation mass is larger in warmer WDs, e.g. $T_\star = 10^6$ K, with an increase of one order of magnitude in T_\star resulting in a similar rise in m_{evap}^e .

4.2.3 DM Induced Heating of WDs in GC M4

In this section, we calculate bounds on the cutoff scale of the dimension 6 EFT operators that describe DM interactions with electrons in WDs. To that end, we use the observed luminosity of the faintest WDs in the globular cluster M4 [126, 157], together with the estimations for ρ_χ , v_\star and v_d derived in Ref. [126]. We compute the capture rate in the optically thin limit, assuming that the WDs are made of ¹²C. Even though colder WDs have been recently observed by the Gaia mission [154], no significant bounds can be derived from this data due to the low DM density in the solar neighbourhood.

Once captured, the gravitationally bound DM will continue to scatter with

the WD constituents until they reach thermal equilibrium. We have checked the thermalisation timescales for scattering on electrons, using the method described in Ref. [118]. We find that the longest time required for the DM to thermalize is $\sim 10^5$ yrs for any of the operators of interest.

Following thermalisation, the DM can self-annihilate in the WD interior. The number of DM particles present in the WD core therefore evolves as

$$\frac{dN_\chi}{dt} = C - AN_\chi^2, \quad (4.23)$$

where the coefficient A is related to the annihilation rate through

$$\Gamma_{\text{ann}} = \frac{1}{2}AN_\chi^2, \quad (4.24)$$

and we have assumed that evaporation is negligible, i.e., $m_\chi \geq m_{\text{evap}}$. The annihilation coefficients can be calculated from the thermally averaged annihilation cross-sections for each operator that can be found in Ref. [253]. To calculate these cross-sections, we only consider DM annihilating to SM leptons at tree level, as there is no a priori reason to expect similar scale DM couplings to quarks, nor for them to be related in any specific way. In principle one would have two cutoff scales for DM coupling to the quark and lepton sectors respectively, with the details depending on the UV physics. This means that when computing bounds on Λ_e for interactions with electrons, no assumptions were made regarding the strength of DM-quark interactions. Instead, loop-induced effective couplings to quarks were calculated similarly to Refs. [135, 254]. Importantly, note that below the electron mass annihilation to neutrinos, or loop-induced annihilation to photons (non-zero only for some operators) are the only allowed annihilation channels.

If the capture and annihilation processes are in equilibrium, then $\Gamma_{\text{ann}} = C/2$ and the DM contribution to the star luminosity is $L_\chi = m_\chi C(m_\chi, \Lambda_f)$. The time in which this equilibrium is reached is determined by the steady state solution of Eq. 4.23, and is given by

$$\tau_{\text{eq}} = \frac{1}{\sqrt{CA}}. \quad (4.25)$$

We can then set the EFT cutoff Λ_e to the values obtained from the WD luminosity (see paragraph below) to calculate the corresponding equilibrium times, and hence verify that capture-annihilation equilibrium is met.

To estimate the limits on the cutoff scale Λ_e for DM interactions with electrons, we compare the luminosity due to DM with the WD observed luminosities L_γ . In Fig. 4.11, we illustrate how we have performed this calculation. The observed luminosity of the WDs in M4 is shown in the $L_\gamma - M_\star$ plane³, where we have

³Actually, there are more WDs observed in the globular cluster M4 than those shown in Fig. 4.11. We have given preference to the faintest WDs.

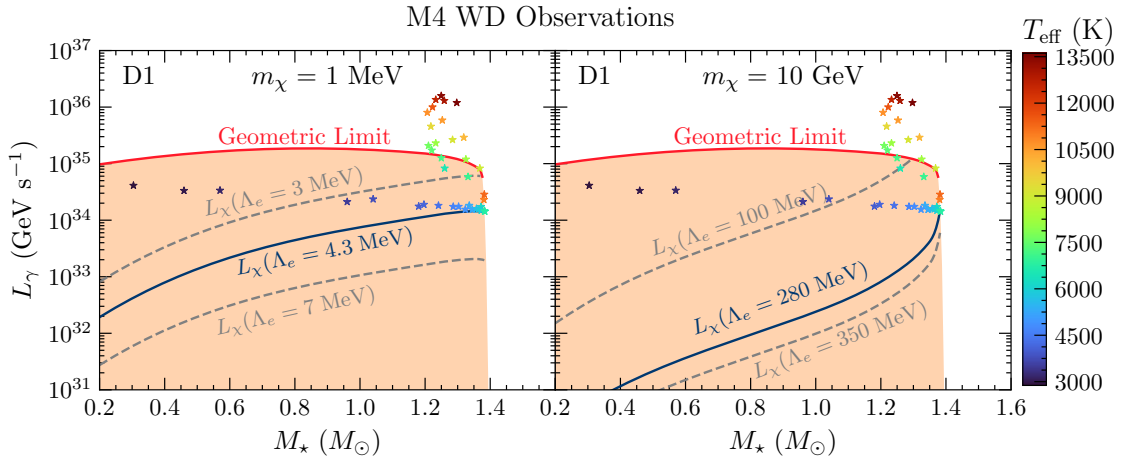


Figure 4.11: WDs observed in the globular cluster M4 and DM contribution to the star luminosity L_χ for different values of the cutoff scale Λ_e and m_χ for D1. The red lines correspond to the maximum achievable L_χ for electron targets, obtained in the geometric limit. The blue lines represent the minimum value of Λ_e that is consistent with the WD observations.

used the effective temperature to infer the radius of every star. Since, there are no independent measures of the mass of the WDs in M4, and we require radial profiles of the target number density, electron Fermi energy and escape velocity to compute capture and evaporation rates, we have solved the TOV equations coupled with the FMT EoS for carbon WDs to calculate M_\star .⁴ We also show the DM luminosity for different values of Λ_q for $m_\chi = 100$ MeV (left) and $m_\chi = 10$ GeV (right), calculated using different WD configurations.

As can be seen, the WD with $M_\star \simeq 1.38 M_\odot$ is the star that imposes a lowest bound on Λ_q (solid blue line), since L_γ should be at least equal to the expected contribution from DM for all the observed WDs. In other words, if the luminosity due to DM capture and annihilation is at most equal to the observed luminosity of the faintest and heaviest WD in M4 ($M_\star \simeq 1.38 M_\odot$), there will be no tension between these observations and DM-induced heating of the WDs. While the results in Fig. 4.11 assume WDs of a pure carbon composition, we have checked that a pure He composition for stars of $M_\star \lesssim 0.5 M_\odot$ does significantly not alter the bounds on Λ_e . Note that the lower bounds are always well below the DM luminosity for maximal capture (geometric limit, see red lines). Lower values of Λ_e (dashed grey lines) would be in tension with the lowest luminosity WDs.

⁴The mass and radius obtained using this method are in good agreement with recent observations within 2 kpc retrieved from the Montreal White Dwarf Database [255], which contains more than 32000 WDs identified by Gaia DR2 [256] and EDR3 [167], and spectroscopy measurements from surveys including SDSS DR12 and 2MASS. See Fig. 2.2 for the comparison.

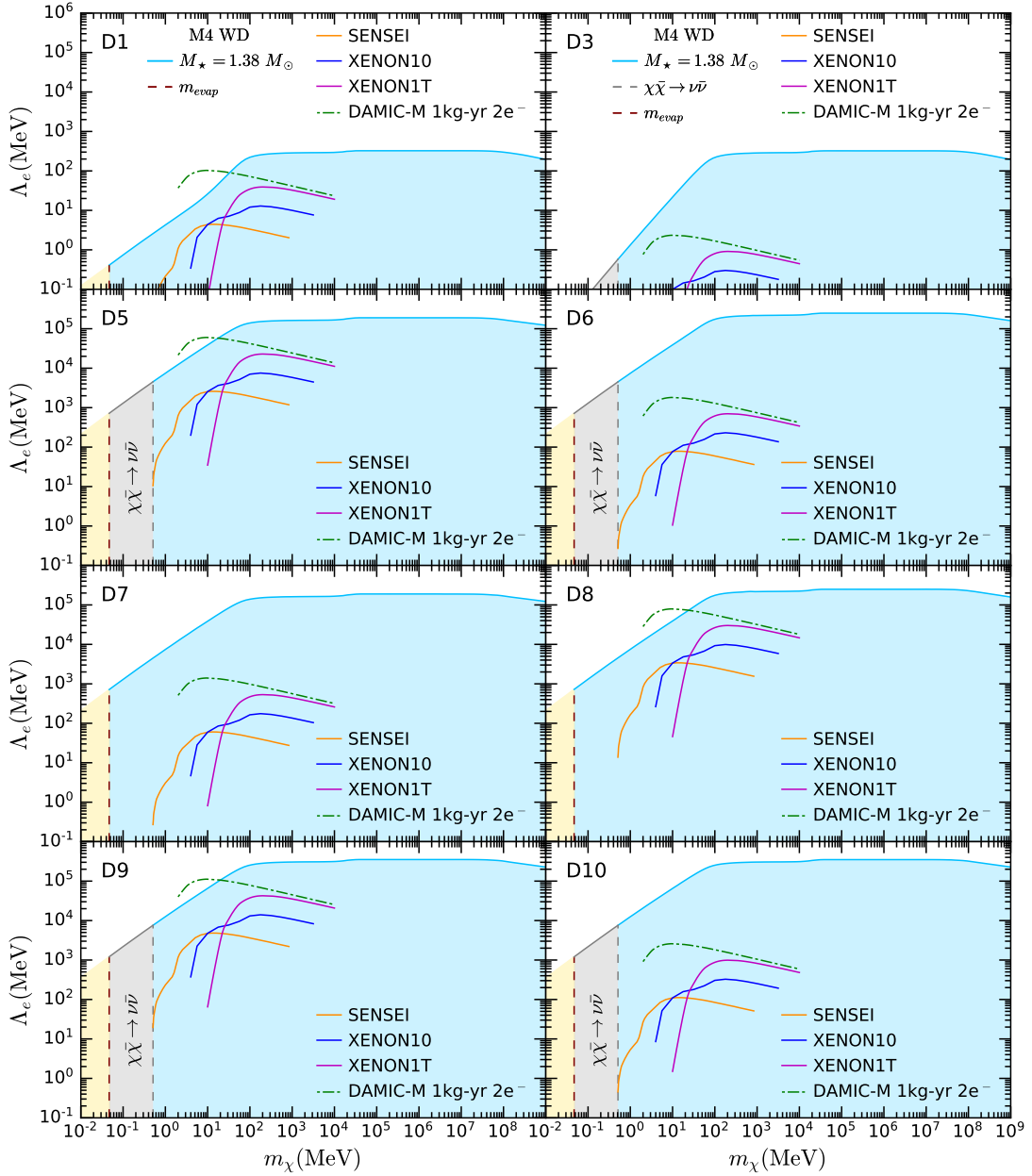


Figure 4.12: Limits on Λ_e for DM interactions with electrons for the same WD obtained with the lowest luminosity and heaviest WD in the globular cluster M4, assuming $\rho_\chi = 798 \text{ GeV cm}^{-3}$ (contracted halo) [126] and $T_\star = 10^5 \text{ K}$. The region where capture and evaporation (for $T_\star = 10^5 \text{ K}$) are expected to be in equilibrium is shaded in yellow, and the region where DM annihilates to neutrinos that escape the WD is shaded in grey. For comparison, we show upper bounds from the leading electron recoil experiments for heavy mediators from SENSEI [247]/DAMIC [248], Xenon10 [249], Xenon1T [250] and the projected sensitivity for DAMIC-M [246].

In Fig. 4.12, we show the limits on the cutoff scale Λ_e , in the case where DM is captured solely by collisions with the degenerate electrons. The shaded blue regions are the excluded parameters. For operators D1-D4, for which the squared matrix elements depend exclusively on the transferred momentum t , the DM-electron couplings is proportional to the tiny electron Yukawa coupling. This reduces the capture rate in such a way that for operator D4, the bounds on Λ_e lie entirely in the $\Lambda_e \lesssim m_\chi$ region, and for D2 only a small corner of the allowed parameter space surpasses this threshold. Given these low limits on the EFT cutoff scale Λ_e , such that an EFT description would not be valid, we do not plot results for D4 or D2.

For the remaining operators, especially D5-D10, there is a much larger region of parameter space where the limits on Λ_e are such that an EFT description would be valid. In all cases, the lower limits on Λ_e , obtained using the WD with $M_\star = 1.38M_\odot$ in M4, outperform the leading bounds from electron recoil experiments by at least \sim an order of magnitude. In most cases, they even outshine the projected sensitivity for the future experiment DAMIC-M (with the exceptions being D1, D5, D8 and D9 in the region below $m_\chi \lesssim 10$ MeV – see dot-dashed green lines). DM scattering on electrons is heavily hampered by Pauli blocking for $m_\chi \lesssim 100$ MeV.

The reach in the light DM mass regime is restricted by the evaporation mass for operators D1, D7, and D8 (see yellow region) and the electron mass for D3, D5, D6, D9 and D10 (see region shaded in grey) where DM annihilation to neutrinos is either the only final state allowed or the dominant channel. Despite those limitations, we conclude that constraints from the observed luminosity of cold faint WDs in old globular clusters that have been able to retain their initial DM content in the innermost region of the cluster, can potentially exclude larger regions of the parameter space than direct detection, particularly in the sub-GeV region. This is especially relevant for leptophilic DM models.

Finally, in Fig. 4.13, we conservatively compare the bound on the scattering cross-section of the vector-vector operator D5 obtained from WDs in M4, with the limits from electron recoil experiments. Even though the WD constraint is not able to probe the region where neutrino coherent scattering is expected to hamper the sensitivity of silicon detectors or extend down below the electron mass, it would certainly surpass current DD bounds by orders of magnitude in σ_{ex} . It would even surpass the projected sensitivity for DAMIC-M, especially in the sub-MeV regime where no projections have been made⁵, despite the reduced WD sensitivity in this region due to Pauli blocking.

⁵In the sub-MeV DM mass regime, modest limits on the DM-electron scattering cross-section can be obtained by considering DM upscattered by cosmic rays. See, e.g. Refs. [257–259].

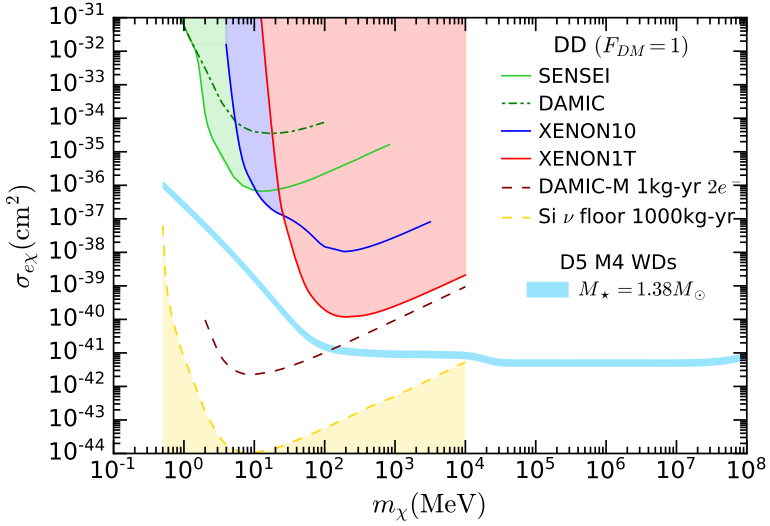


Figure 4.13: Upper bounds on the DM-electron scattering cross-section for D5. The light blue band represents the limit from the WD observations in M4. The width of this band denotes the uncertainty in the DM density in M4 [126]. For comparison, we show leading electron recoil bounds for heavy mediators from SENSEI [247], DAMIC [248], Xenon10 [249], Xenon1T [250], the projected sensitivity for DAMIC-M [246], and the neutrino floor for silicon detectors [245].

4.3 Summary

In this chapter, we have applied the formalism for dark matter capture in compact objects discussed in Chapter 3 to leptonic targets. Namely, we looked at DM scattering from electrons and muons in NSs, as well as electrons in WDs.

In the NS case, we saw that capture from muon targets was qualitatively similar to the neutron target case of Section 3.5. On the other hand, capture from electrons for a subset of the EFT operators exhibits interesting behaviour in the low DM mass regime due to their ultrarelativistic nature. We then projected the sensitivity on the DM-lepton scattering cross-section, $\sigma_{e\chi}^{\text{th}}$, a future observation of an old, cold NS may be able to achieve, comparing these results to current and upcoming direct detection experiments. This indicated that NSs have the potential to probe regions of this parameter space orders of magnitude below current constraints.

In terms of the electrons in WDs, we took advantage of the existing catalogue of WD observations in globular cluster M4 to explore the impact of DM heating in these stars. We find that requiring that the luminosity induced by the kinetic and annihilation heating from the captured DM not exceed the observed luminosities of the WDs, we can constrain the DM-electron scattering cross-section over a wide DM mass range. In fact, despite the considerable suppression from Pauli blocking, limits

from DM heating are shown to exceed direct detection constraints and probe deep into the neutrino floor. We note that these limits are dependent on M4 containing dark matter, and whether this is true is still debated in the literature.

We now move on from scattering off point-like objects to consider capture from baryons in NSs. Here, we will need to account for both their finite size correctly treat them as a strongly interacting medium.

5

Capture on Baryonics in Neutron Stars

This chapter is based on the papers [224, 252], where we incorporate two important effects that are important when considering dark matter capture from baryons in neutron stars. As the momentum transfers involved in the scattering events leading to capture are large, one must account for the internal structure of the baryon. In addition, the high densities of neutron star matter require us to take into account the strong interactions experienced amongst the baryons. We discuss how to properly incorporate both of these effects into the capture formalism presented in this thesis in a self-consistent manner, and discuss their effects on the capture and interaction rates as well as on the threshold cross-sections that a future NS observation would be sensitive to.

5.1 Baryon Structure and Strong Interactions

5.1.1 Baryon Effective Masses

At the extremely high densities found in the interiors of neutron stars, the strong interactions amongst the baryons render the free Fermi gas approximation used in Chapter 3 to model the scattering targets invalid. To account for these interactions in a self-consistent way, they should be included in the Lagrangian used to model the nucleon-rich matter. This is often achieved by including effective Skyrme forces, or through a relativistic mean field theory.

The QMC EoS, described in Section 2.3.2, adopts the latter approach. The forces mediated by the Lorentz scalars induce an effective mass for the baryons different from their vacuum value, such that $m_i^{\text{eff}} \leq m_i$. In this model, the single

particle energy for a baryon with momentum \vec{p}_i can be expressed as

$$E_i(p_i) = \sqrt{p_i^2 + [m_i^{\text{eff}}(n_b)]^2} + U_i(n_b), \quad (5.1)$$

where $U_i(n_b)$ is the potential induced by the Lorentz vector forces, which depends on the baryon number density. This expression resembles the dispersion relation for a particle of mass m_i^{eff} under the influence of an external force with corresponding potential U_i . Hence, the single-particle energy spectrum of the interacting baryons must be expressed in terms of m_i^{eff} rather than the mass in vacuum, and it is this mass that will enter into the kinematics of the scattering processes.

Accounting for the strong interactions in this way leads to several modifications to the results obtained in Chapter 3. Firstly, all appearances of the bare mass m_i are replaced by m_i^{eff} in all the results. This will lead to non-trivial modifications of the capture and interaction rates throughout the star as the mass of the target will decrease deeper into the star (see right panels of Fig. 2.5).

In addition, the Fermi energies, $\varepsilon_{F,i} = \mu_{F,i} - m_i$, are now calculated according to

$$\varepsilon_{F,i}(r) = \sqrt{[p_{F,i}(n_i)]^2 + [m_i^{\text{eff}}(r)]^2} - m_i^{\text{eff}}(r), \quad (5.2)$$

where $p_{F,i}$ is the Fermi momentum of species i . This becomes the input to the Fermi-Dirac distributions for the capture and interaction rates. In doing this, the number density evaluated in the free Fermi gas approximation, Eq. 3.38, becomes equal to the true number density, $n_i(r)$, provided by solving the EoS alongside the TOV equations. To see this, substitute Eq. 5.2 into Eq. 3.38 and make the replacement $m_i \rightarrow m_i^{\text{eff}}$ to get

$$n_{\text{free}}(\varepsilon_{F,i}(r), m_i^{\text{eff}}(r)) = \frac{1}{3\pi^2} [\varepsilon_{F,i}(r)(2m_i^{\text{eff}} + \varepsilon_{F,i}(r))]^{3/2} \quad (5.3)$$

$$= \frac{(p_{F,i}(r)^2 + [m_i^{\text{eff}}]^2)^{3/2}}{3\pi^2} \quad (5.4)$$

$$= \frac{p_{F,i}^3}{3\pi^2} \quad (5.5)$$

$$= n_i(r) \quad (5.6)$$

for a Fermi gas, interacting or otherwise. As such, the correction factor used to correct for usign realistic profiles for the target is now $\zeta(r) = 1$.

In Fig. 5.1 we show the values of the Fermi energies for neutrons (left panel) and protons (right panel). The dashed lines are the radial profiles used in the free Fermi gas approximation and the solid lines correspond to the calculation outlined above for the effective mass approach. We immediately notice that the profiles for the free Fermi gas approximation are steeper, having larger values in the core and

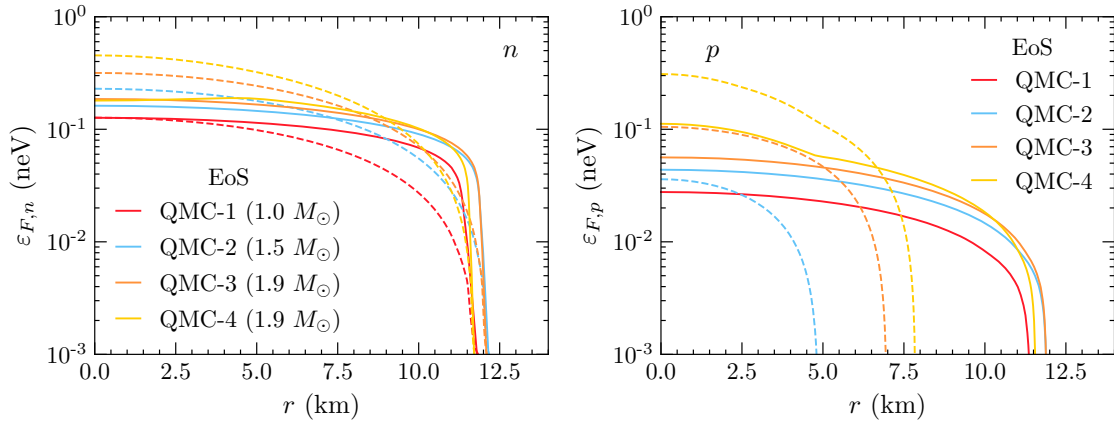


Figure 5.1: Radial profiles of the Fermi energy for neutrons (left) and protons (right). Results are shown for the free Fermi gas (dashed) and interacting baryon (solid) approaches, for the benchmark NS configurations of Table 2.3.

decreasing more rapidly towards the surface, while those obtained with the effective mass approach are quite flat, especially in the core, and go to zero only very close to the surface.

The difference between these two calculations is significantly more prominent for protons. Specifically, in the free Fermi gas approach, we find that protons are non-degenerate in the outer regions of the core and, for light NS configurations such as QMC-1, are non-degenerate throughout the whole star.¹ In contrast, protons are degenerate throughout the entire star in the interacting baryon treatment. As we shall see, these different Fermi energies will have important consequences when calculating DM capture and interaction rates, especially for proton targets.

5.1.2 Momentum Dependence of Hadronic Form Factors

In the preceding chapters, we had regarded the target as a point-like particle that the DM scattered off, which is perfectly valid for the leptonic species. Baryons, on the other hand, are composite particles made of three valence quarks and hence have a finite size. When the momentum transfer exceeds the inverse Compton wavelength of the baryon, $\sim 1/\lambda_B \sim m_B$, the internal structure begins to be probed, and we must account for their finite size.

As discussed in Section 1.2.4, this is achieved by reintroducing the momentum

¹Not shown in Fig. 5.1 because of the logarithmic scale.

dependence in the hadronic form factors,

$$c_{\mathcal{B}}^I(t) = c_{\mathcal{B}}^I(0)F^2(t), \quad I \in \{S, P, V, A, T\}, \quad (5.7)$$

$$F(t) = \frac{1}{(1 - t/Q_0^2)^2}, \quad (5.8)$$

where t is the Mandelstam variable, Q_0 is an energy scale taken to be 0.9 GeV, and $c_{\mathcal{B}}^I(0)$ are the form factors evaluated at zero momentum transfer, with their values given in Appendix B. This factor is included in the matrix elements of the operators in Table 1.1, and as such modifies the analytic result for the interaction rate derived in Section 3.3 for matrix elements $|\overline{\mathcal{M}}|^2 \propto t^n s^m$ to become

$$\begin{aligned} \Gamma^-(E_\chi) \propto & \frac{(-1)^n}{128\pi^3 E_\chi k} \int_0^{E_\chi - m_\chi} dq_0 \int dt_E \frac{t_E^n}{(t_E + q_0^2)^{m+\frac{1}{2}}} \frac{1}{(1 + t_E/Q_0^2)^4} \\ & \times \sum_{r=0}^m \mathcal{V}_{m,r} \sum_{j=0}^r \binom{r}{j} \varepsilon_{F,i}^{r-j} \frac{(-1)^j q_0^{j+1}}{j+1} h_j \left(\frac{E_i^{t^-} - \varepsilon_{F,i}}{q_0} \right), \end{aligned} \quad (5.9)$$

where $E_i^{t^-}$ and $h_j(x)$ are given in Eqs. 3.55 and 3.56 respectively.

The main effect of these form factors is the suppression of high momentum transfer interactions. This will also increase the DM mass range over which Pauli blocking is expected to be active. We can see these effects by examining the kinematically allowed regions of phase space together with the differential interaction rate profiles.

In Fig. 5.2, we show how Pauli blocking affects the integration domain of Eq. 5.9, which is controlled by the smoothed step function $h_0(x)$, for some representative choices of DM mass and the benchmark values $\varepsilon_{F,n} = 0.4$ GeV and $B = 0.5$. The region where $h_0(x) = 0$ is not kinematically allowed and hence not shown in Fig. 5.2. The light blue area represents the region that is not affected by Pauli blocking (PB), i.e. $h_0(x) = -x$, while the dark blue shaded area indicates the PB region, where $h_0(x) = 1$. We observe that for light DM masses such as $m_\chi = 0.1$ GeV (top left panel), the whole domain lies in the PB region. For $m_\chi = 1$ GeV (top right panel), there is a tiny slice of the domain that is not Pauli suppressed. The picture changes dramatically when the DM mass is increased to $m_\chi = 10$ GeV (bottom left panel), where almost the whole integration domain is unaffected by PB. Increasing the DM mass even further, e.g., up to $m_\chi = 1$ TeV (bottom right panel) does not result in much further change to the shape of the domain, demonstrating that the transition between the PB and non-PB regimes occurs between $m_\chi \sim 1$ GeV and $m_\chi \sim 10$ GeV.

In Fig. 5.3 we show the normalised differential interaction rates for operators D1-D4 as a function of the energy loss q_0 , calculated with (orange) and without (light blue) momentum dependent couplings, for neutron targets and $m_\chi = 1$ TeV. In all

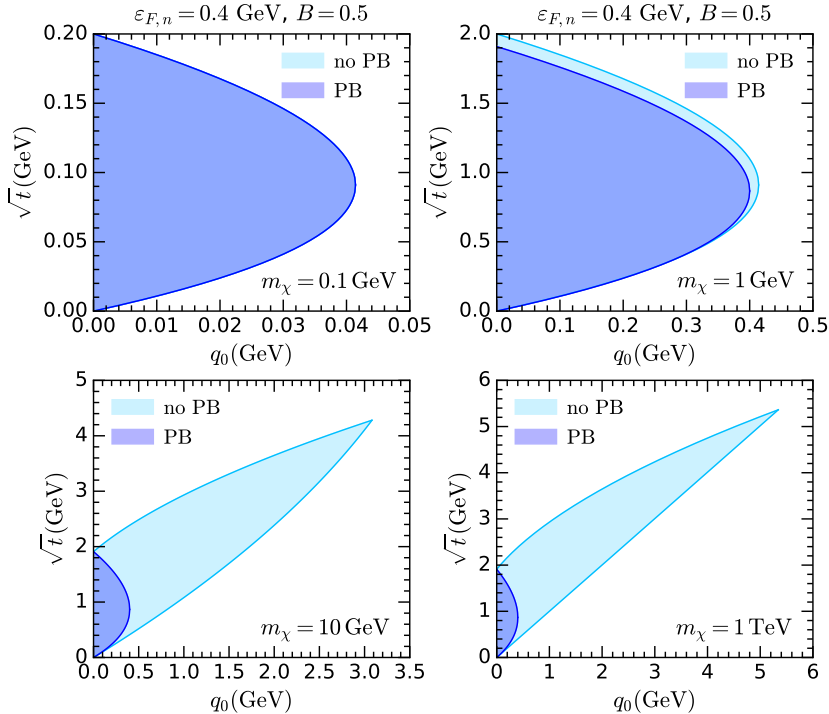


Figure 5.2: Integration domain for the interaction rate, for different choices of DM mass, assuming $B = 0.5$ and $\varepsilon_{F,n} = 0.4 \text{ GeV}$. The kinematically allowed region is shaded in light blue and the Pauli suppressed region (PB) in dark blue.

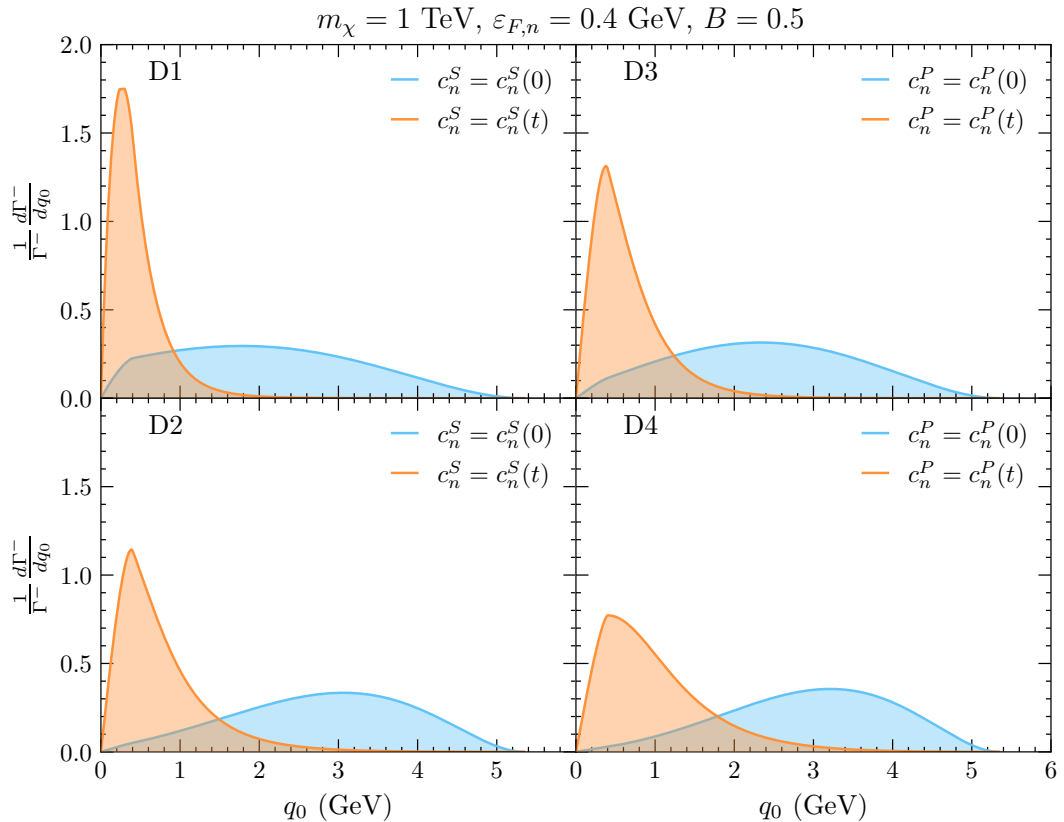


Figure 5.3: Normalised differential DM-neutron interaction rate as a function of the DM energy loss, q_0 , for the operators D1 (top left), D3 (top right), D2 (bottom left) and D4 (bottom right). The light blue lines denote the interaction rate calculated using constant neutron form factors $c_n^S(0)$, $c_n^P(0)$, while the orange lines correspond to that for momentum-dependent couplings $c_n^S(t)$, $c_n^P(t)$. We have set $m_\chi = 1$ TeV, $B = 0.5$, $\varepsilon_{F,n} = 0.4$ GeV.

cases, we observe that the inclusion of t -dependent hadronic matrix elements shifts the peak of the spectrum towards lower energy transfers, q_0 . Thus, the inclusion of $c_i^I(t)$ in Eq. 5.9 suppresses DM-neutron interactions at large momentum transfers. Replacing the target mass with the corresponding effective mass $m_i^{\text{eff}} \leq m_i$ also shifts the average energy transfer to lower energies. When both effects are present, a lighter target mass reduces the suppression arising from t -dependent form factors.

Asside: Deep Inelastic Scattering

Given that the momentum transfer in the DM-nucleon scattering process is sufficiently large that we cannot treat the nucleons as point particles (up to ~ 10 GeV in the cores of the heaviest NSs), one may wonder if there are sizable contributions from Deep Inelastic Scattering (DIS). To that end, we examine the contribution from DIS to the total DM-neutron scattering cross-section.

The kinematics of DIS of dark matter in NSs is not similar to any case that has previously been treated in the literature, at least not to our knowledge. In contrast to DIS of neutrinos and boosted DM, we are interested in much larger DM masses and relatively lower energies. Specifically, $E_\chi/m_\chi = 1/\sqrt{B}$, where B is the time component of the Schwarzschild metric, which falls in the range $[\sim 0.2, \sim 0.75]$. Therefore, we have $E_\chi \lesssim 2m_\chi$. Following ref. [260], we derive the DIS cross-section in NSs for the operators in Table 1.1.

The parton level differential cross-section is given by

$$\frac{d\hat{\sigma}}{d\hat{t}} = \frac{\hat{s}}{8\pi\hat{\gamma}^2} \frac{\hat{s} - (m_\chi^2 + x^2 m_n^2)}{\hat{s}^2 - (m_\chi^2 - x^2 m_n^2)^2} |\overline{\mathcal{M}}(\hat{s}, \hat{t}, m_i = xm_n)|^2, \quad (5.10)$$

where $\hat{\gamma} = \gamma(\hat{s}, m_\chi, xm_n)$, $\hat{t} = -Q^2$ is the squared 4-momentum transfer, $\hat{s} = (1-x)(m_\chi^2 - xm_n^2) + xs$, $|\overline{\mathcal{M}}|^2$ is defined at the parton level with couplings $g_i = g_q$, and x is the fraction of the nucleon momentum (P) carried by the parton, $p = xP$. We define y , the fractional energy lost by the DM in the nucleon rest frame [260]

$$y = \frac{2q \cdot P}{2k \cdot P} = \frac{-\hat{t}}{\hat{s} - m_\chi^2 - x^2 m_n^2}, \quad (5.11)$$

and obtain

$$dQ^2 = (\hat{s} - m_\chi^2 - x^2 m_n^2) dy = x(s - m_\chi^2 - m_n^2) dy. \quad (5.12)$$

We then use the parton distribution functions (PDFs), f_i , to obtain the nucleon level differential DIS cross-section

$$\frac{d^2\sigma}{dx dy} = (\hat{s} - m_\chi^2 - x^2 m_n^2) \frac{\hat{s}}{8\pi\hat{\gamma}^2} \frac{\hat{s} - (m_\chi^2 + x^2 m_n^2)}{\hat{s}^2 - (m_\chi^2 - x^2 m_n^2)^2} \sum_i f_i(x, Q^2) |\overline{\mathcal{M}}(\hat{s}, \hat{t}, xm_n)|^2. \quad (5.13)$$

The integration bounds for the DIS cross-section are generically $0 < x < 1$ and $0 < y < y_{max}$, where y_{max} is set by imposing $\cos \theta \leq 1$, and in general $y_{max} \neq 1$ [260]. The value of y_{max} is set by

$$y_{max} = \frac{-\hat{t}_{min}}{\hat{s} - m_\chi^2 - x^2 m_n^2} = \frac{(\hat{s} - m_\chi^2 - x^2 m_n^2)^2 - 4x^2 m_\chi^2 m_n^2}{\hat{s}(\hat{s} - m_\chi^2 - x^2 m_n^2)}. \quad (5.14)$$

The capture rate requires integrating the differential cross-section over \hat{s} , which must be done at the parton level, i.e., before integrating over x . We perform this integration over the centre of mass energy by following the same procedure performed for capture in the intermediate mass regime outlined in Section 3.4.1. The differential capture rate will then scale as

$$\frac{dC}{dr} \propto \int_0^1 dx \int_{\hat{s}_0 - \delta\hat{s}}^{\hat{s}_0 + \delta\hat{s}} d\hat{s} \int_0^{y_{max}} dy \frac{d^2\sigma}{dx dy} \Theta(Q^2 - 1 \text{ GeV}^2), \quad (5.15)$$

where the step function enforces the momentum transfer to be above the 1 GeV threshold where the PDFs are reliable, and

$$\hat{s}_0 = m_\chi^2 + 2xE_n E_\chi, \quad (5.16)$$

$$\delta\hat{s} = 2xm_\chi \sqrt{E_n^2 - m_n^2} \sqrt{\frac{1 - B(r)}{B(r)}}, \quad (5.17)$$

$$E_n \simeq m_n + \mu_{F,n}. \quad (5.18)$$

We numerically evaluate the DIS cross-section using the MSTW2008 NLO PDFs [261].

In Fig. ??, we show the ratios of the elastic (EL) and deep inelastic scattering (DIS) cross-sections to the total cross-section (TOT=DIS+EL), as a function of the radial coordinate r for the NS QMC-4, neutron targets and $m_\chi = 10^6 \text{ GeV}$. We consider two scenarios: the free Fermi gas approach and the interactive baryon approach characterised by m_n^{eff} . The radial coordinate determines the value of B , the Fermi energy of the target, and m_n^{eff} .

In both the m_n^{eff} and free Fermi gas approaches, the DIS contribution (light blue and green lines, respectively) increases towards the centre of the star, where B takes lower values and hence the DM kinetic energy is higher. The ratio $\sigma^{\text{DIS}}/\sigma^{\text{TOT}}$ is smaller in the m_n^{eff} approach, compared to the free Fermi gas approach, due to a smaller neutron effective mass. In the correct interactive baryon approach, the ratio of the DIS contribution (light blue lines) to the total cross-section is at most $\mathcal{O}(40\%)$ at the centre of the star for D8, $\mathcal{O}(20\%)$ for D7, D9-D10, and much lower for the remaining operators.

As a result, for most operators, the elastic cross-section provides a very good approximation to the total cross-section (compare magenta with dashed blue lines). Note that these cross-sections are weighted by $r^2 dr$ in the capture rate calculation

of Eq. 3.26 (i.e. weighted by volume) which further reduces the importance of the DIS contribution.

It is worth noting that we have neglected the effect of Pauli blocking on the DIS cross-section. In deep inelastic scattering, one must have a baryon in the final state and with a nucleon target this is almost always a nucleon. As shown in both theoretical calculations [262] and direct experimental studies [263], this nucleon has low momentum in the laboratory frame, typically 300 MeV or less. Such nucleons will be totally Pauli blocked in the core of a NS, and hence the deep inelastic cross-section drastically reduced. As a result, the contribution of the deep inelastic process to the capture rate will have a negligible effect on our conclusions.

We performed a similar calculation for hyperon targets and found that as for neutrons, the DIS contribution to the total cross-section is more important for operators D7-D10 in the absence of Pauli blocking of the fragmented baryonic final states. For D8 and Ξ^- targets, the DIS cross-section can even surpass the elastic scattering contribution (including form factors) and reach $\sim 60\%$ of the total cross-section at the centre of the star. Ξ^- provides the largest hyperonic contribution to the capture rate, however, this (elastic scattering) contribution is already more than one order of magnitude lower than that of neutrons for D7-D10. Even if Pauli blocking does not suppress the DIS final states, the contribution of the deep inelastic process to the capture of DM is negligible, since it would enhance the capture rate by scattering on Ξ^- at most by a factor of ~ 2 .

In addition to DIS, there may, in principle, be a contribution from the excitation of baryon resonances. However, the resonance excitation cross-section is also expected to be suppressed. In NSs, the mass of the Δ baryon, which gives the largest contribution to this cross-section, increases with the baryon number density by between ~ 100 and 300 MeV [264]. This will suppress the resonance excitation cross-section significantly. Therefore, we consider only elastic collisions.

5.1.3 Modifications to the Capture Rate

Low and Intermediate Mass Regime

We now incorporate the effects discussed above into the expressions for the capture rates derived in Chapter 3. In the low mass regime, where Pauli blocking is relevant, the modifications are minor, and we simply replace $m_i \rightarrow m_i^{\text{eff}}$ in Eqs. 3.26 and 3.39 and set $\zeta(r) = 1$, as the form factors are incorporated in the matrix elements. We

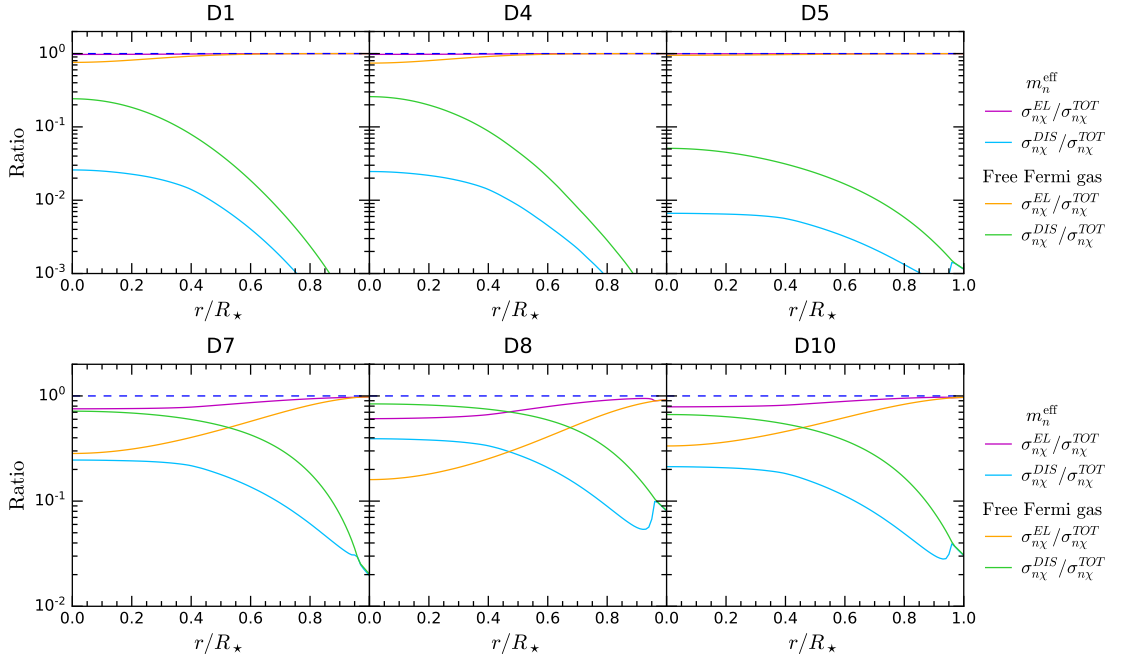


Figure 5.4: Ratios of the elastic (EL) and deep inelastic scattering (DIS) cross-sections to the total cross-section ($TOT = EL + DIS$) as a function of the NS radius, for neutron targets in the NS QMC-4 and six of the dimension-6 EFT operators. We have taken $m_\chi = 10^6$ GeV, and shown the comparison for both the interacting baryon and free Fermi gas approaches. Momentum-dependent form factors have been included in the elastic calculations.

write these explicitly here for clarity,

$$C = \frac{4\pi}{v_\star} \frac{\rho_\chi}{m_\chi} \operatorname{Erf} \left(\sqrt{\frac{3}{2}} \frac{v_\star}{v_d} \right) \int_0^{R_\star} r^2 \frac{\sqrt{1 - B(r)}}{B(r)} \Omega^-(r) dr, \quad (5.19)$$

$$\begin{aligned} \Omega^-(r) &= \frac{1}{32\pi^3} \int dt dE_i ds \frac{|\bar{\mathcal{M}}(s, t, m_i^{\text{eff}})|^2}{\beta(s, m_i^{\text{eff}})\gamma(s, m_i^{\text{eff}})} \frac{E_i s}{m_\chi} \sqrt{\frac{B(r)}{1 - B(r)}} \\ &\quad \times f_{\text{FD}}(E_i, r) (1 - f_{\text{FD}}(E'_i, r)), \end{aligned} \quad (5.20)$$

where we have made the m_i^{eff} dependence of the β and γ functions of Eqs. 3.40 and 3.41 explicit.

In the intermediate mass range, where Pauli blocking no longer suppresses the capture rate, we derived the simplified expression Eq. 3.63 valid for matrix elements of the form $|\bar{\mathcal{M}}|^2 \propto \bar{g}(s)t^n$, with $\bar{g}(s)$ some function of the centre of the mass energy, and $n = 0, 1, 2$. While including the effective masses is simple, the inclusion of the momentum-dependent form factors, Eq. 5.8, complicates the integration over the momentum transfer t . Fortunately, we can still write down an analytic expression for the capture rate in this regime, for matrix elements $|\bar{\mathcal{M}}|^2 \propto \bar{g}(s)t^n F^2(t)$, this being

$$\begin{aligned} C_{\text{appox.}} &= \frac{1}{v_\star} \frac{\rho_\chi}{m_\chi} \operatorname{Erf} \left(\sqrt{\frac{3}{2}} \frac{v_\star}{v_d} \right) \int_0^{R_\star} dr r^2 n_i^2(r) \frac{\bar{g}(s_0)}{n+1} [2m_i^{\text{eff}}]^{2n} \\ &\quad \times \left[\frac{1 - B(r)}{B(r)} \right]^{n+1} \mathcal{F}_n(|t_{\min}|), \end{aligned} \quad (5.21)$$

with s_0 given in Eq. 3.65, and the functions $\mathcal{F}_n(|t_{\min}|)$ are given by

$$\mathcal{F}_n(x) = \frac{\int_0^x dt t^n F^2(t)}{\int_0^x dt t^n}, \quad (5.22)$$

$$\mathcal{F}_0(x) = \frac{Q_0^2}{x + Q_0^2}, \quad (5.23)$$

$$\mathcal{F}_1(x) = 2 \frac{Q_0^2}{x^2} \left[\log \left(1 + \frac{x}{Q_0^2} \right) - \frac{x}{x + Q_0^2} \right], \quad (5.24)$$

$$\mathcal{F}_2(x) = 6 \frac{Q_0^3}{x^3} \left[-\log \left(1 + \frac{x}{Q_0^2} \right) + \frac{x(x + 2Q_0^2)}{2Q_0(x + Q_0^2)}, \right] \quad (5.25)$$

$$|t_{\min}| = \frac{\gamma^2(s, m_i^{\text{eff}})}{s} \approx \frac{4m_\chi^2(1 - B(r))}{B(r)(1 + \mu^2) + 2\mu\sqrt{B(r)}}. \quad (5.26)$$

Note that the \mathcal{F}_n are decreasing functions of both n and $|t_{\min}|$, and hence are decreasing functions of the target mass.

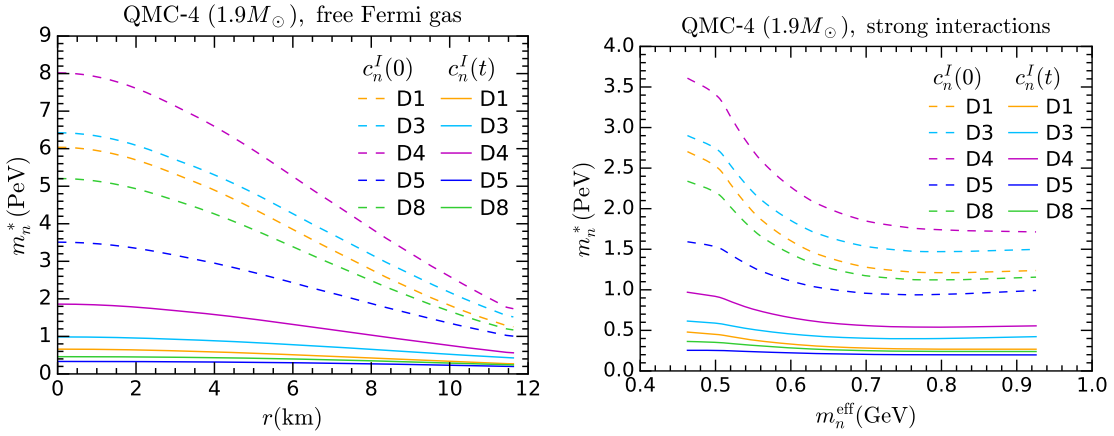


Figure 5.5: Radial profiles of m_n^* in the free Fermi gas approach (left) and m_n^* as a function of the neutron effective mass (right) in the interacting baryon approach, for selected operators. We assume the NS configuration QMC-4 ($1.9M_{\odot}$). In both cases, m_n^* has been calculated using neutron couplings at zero momentum transfer (dashed lines) and including the dependence on t (solid lines).

Large Mass Regime

As discussed in Section 3.4.2, the probability that a DM particle with a mass greater than the threshold value m_i^* loses enough energy in a single scatter such that it becomes captured becomes less than 1. The precise value of m_i^* depends both on the species the DM scatters with, and the nature of this interaction. This reduced capture probability is accounted for by including the factor $c_1(r)$, Eq. 3.79, in the expression for the capture rate Eq. 5.21 for $m_\chi \gg m_i$.

Note that c_1 depends on $\varepsilon_{F,i}(r)$, $B(r)$ and m_i through the interaction rate Γ^- . Aside from B , m_i^* depends only on 2 quantities that have dimension of energy: the mass of the target m_i and its Fermi energy $\varepsilon_{F,i}$. Interestingly, if one rescales both m_i and $\varepsilon_{F,i}$ by the same factor, the resulting m_i^* will just acquire this factor. This means that for baryon couplings at zero momentum transfer, we can calculate m_i^* for a generic target mass m_i^{eff} by rescaling the values obtained in the free Fermi gas approximation in the following way:

$$m_i^*(m_i^{\text{eff}}, \varepsilon_{F,i}) = \frac{m_i^{\text{eff}}}{m_i} m_i^*(m_i, \varepsilon_{F,i} \frac{m_i}{m_i^{\text{eff}}}). \quad (5.27)$$

However, when including the dependence of the baryon couplings on the transferred momentum an additional energy scale comes into play, namely Q_0 . Unfortunately, it is not possible to rescale the m_i^* values obtained with $c_i^I(0)$ to obtain the correct value required when using $c_i^I(t)$.

In the left panel of Fig. 5.5, we show radial profiles of m_n^* for five representative

operators in the case of a QMC-4 NS. These profiles have been calculated in the free Fermi gas approximation (i.e. the neutron mass remains constant throughout the star) both with (solid lines) and without (dashed lines) including the momentum-dependent neutron form factors $c_n^I(t)$. The profiles illustrate the variation of m_n^* with $B(r)$ and $\varepsilon_{F,n}(r)$ in the stellar interior. Note that m_n^* also depends on the DM velocity distribution, which we have taken to be Maxwell-Boltzmann. We can see that the inclusion of t -dependent neutron couplings lowers m_n^* by a factor of $\sim 1.2 - 4.5$, with D4 and D3 being less affected. This is because of the suppression of large energy transfers when introducing $c_i^I(t)$ (as illustrated in Fig. 5.3) which results in less energy being lost by the DM particle per collision. A lower value of m_n^* means that multiple scattering is relevant at smaller DM masses than those expected with $c_i^I(0)$.

In the interactive baryon approach, m_n^* is also a function of $m_n^{\text{eff}}(r)$, as plotted in the right hand panel of Fig. 5.5. The values of $B(r)$, $\varepsilon_{F,n}(r)$, and $m_n^{\text{eff}}(r)$ used in the right-hand panel are those corresponding to the appropriate radial coordinate within the NS as in the left-hand panel. In this case, when including the dependence on the transferred momentum (solid lines), m_n^* is reduced by a factor of $\sim 1.2 - 2.5$ compared the result obtained with hadronic matrix elements at zero momentum transfer (dashed lines). Thus, multiple scattering is relevant at an even lower DM mass in the complete approach that accounts both for strong interactions and t -dependent nucleon couplings. The remaining operators show a similar behaviour to those presented in Fig. 5.5.

5.2 Capture Rate Results

In this section, we present our results for the capture rate, for each EFT operator in Table 1.1 and every baryonic species in the QMC family. The rates have been calculated in the optically thin limit using Eq. 5.19 for $m_\chi \lesssim m_i^*$ and with same equation but including the capture probability $c_1(r)$ in the interaction rate for $m_\chi \gtrsim m_i^*$ wherever the target is degenerate, and Eq. 5.21 in the non-degenerate regime². We compute the capture rate for each target species individually as these can be summed to obtain the total capture rate. Since we shall always work in the optically thin limit (i.e., where the probability for more than one scattering interaction per DM orbit is very low) this procedure is a good approximation, even in the multi-scattering mass region. We assume a NS located in the Solar neighbourhood, thus $\rho_\chi = 0.4 \text{ GeV cm}^{-3}$, $v_\star = 230 \text{ km s}^{-1}$ and $v_d = 270 \text{ km s}^{-1}$.

²We have numerically evaluated these equations using the CUBA libraries [242, 243] linked to Mathematica [244].

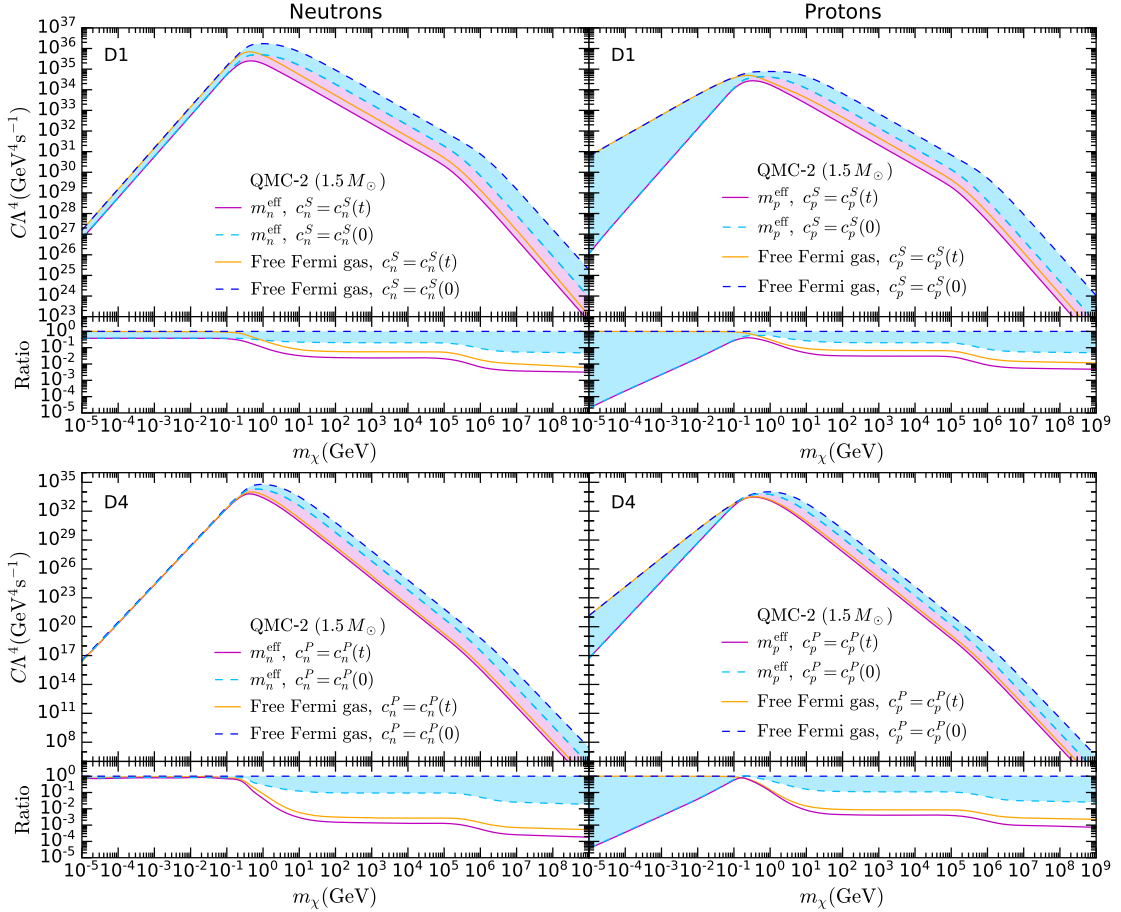


Figure 5.6: Capture rate in the optically thin limit for the operators D1 (top) and D4 (bottom) as a function of the DM mass m_χ for neutron (left) and proton (right) targets, for a QMC-2 NS configuration. We compare the free Fermi gas approach with constant nucleon couplings (dashed blue) and momentum-dependent couplings (solid orange), and the interacting nucleon approach for constant couplings (dashed light blue) and momentum-dependent couplings (solid magenta). Note that these rates scale as Λ^{-4} . The ratio of the capture rate compared to that for the free Fermi gas approximation for point-like targets (dashed dark blue, as computed in Chapter 3) is shown in the lower panels.

5.2.1 Nucleons

To illustrate the effect of accounting for strong interactions and the momentum dependence of the nucleon couplings, we show in Figs. 5.6 and 5.7 the capture rate for four representative operators, D1, D4, D5, and D8, for a QMC-2 NS configuration ($1.5M_\odot$). Note that in these figures we have not assumed a value of Λ , i.e.

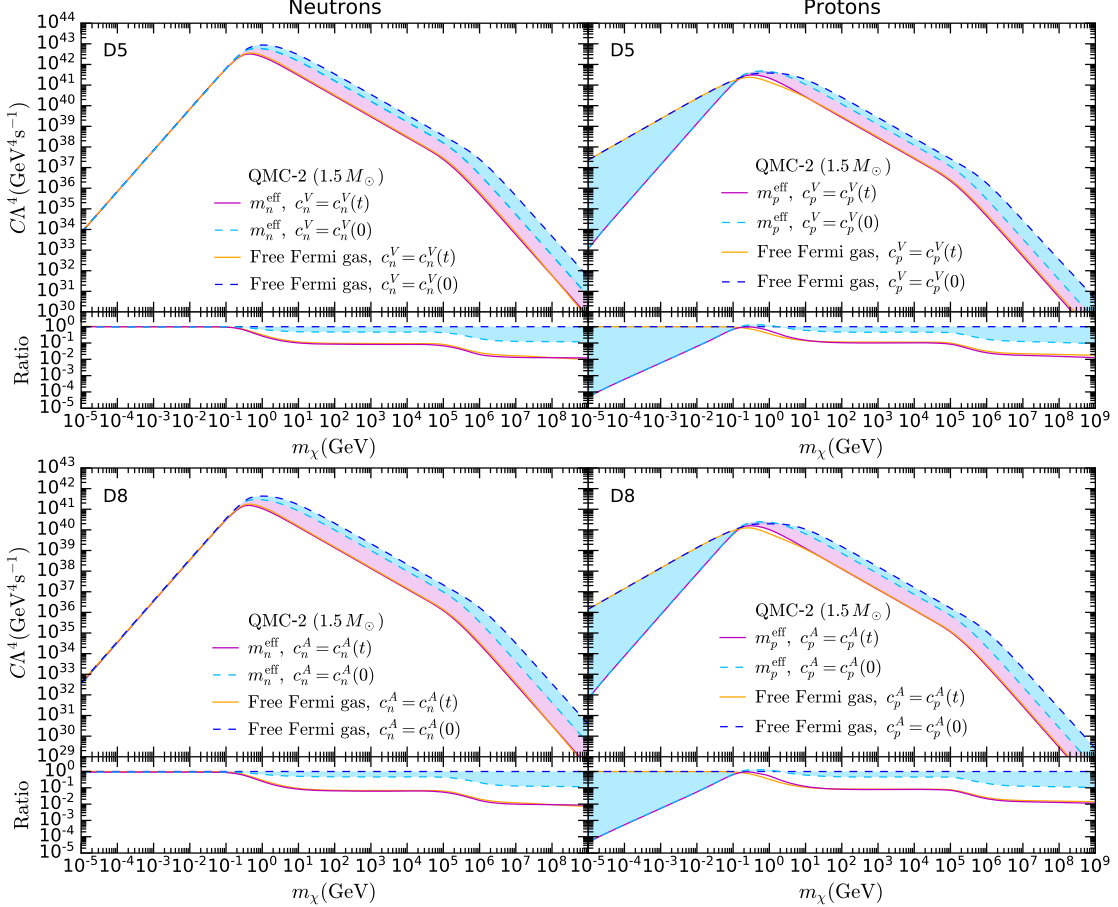


Figure 5.7: Capture rate in the optically thin limit for the operators D5 (top) and D8 (bottom) as a function of the DM mass m_χ for neutron (left) and proton (right) targets, using the free Fermi gas approach with constant nucleon couplings (dashed blue) and momentum-dependent couplings (solid orange), and the interacting nucleon approach for constant couplings (dashed light blue) and momentum-dependent couplings (solid magenta), for a QMC-2 NS configuration. Note that these rates scale as Λ^{-4} . The ratio of the capture rate compared that for the free Fermi gas approximation for point-like targets (dashed dark blue) is shown in the lower panels.

we plot $C\Lambda^4$. Results are shown for the free Fermi gas approximation with constant nucleon couplings (dashed dark blue) and momentum dependent form factors (orange), and for the interacting baryon framework with (magenta) and without (dashed light blue) t -dependent nucleon couplings.

For neutron targets in the free Fermi gas approach, we find that including momentum-dependent form factors in the scattering cross-section does not affect the capture rate for DM masses $m_\chi \lesssim 0.2 \text{ GeV}$, since the energy scale at which this effect comes into play is $Q_0 \sim 1 \text{ GeV}$. For $m_\chi \gtrsim 1 \text{ GeV}$, the ratio of the calculation that accounts for t -dependent neutron couplings compared to that obtained with constant hadronic matrix elements is $\mathcal{O}(10^{-2})$ for D4 in the large DM mass range; for the remaining operators the suppression exceeds one order of magnitude.

The fact that this effect is stronger for operators whose matrix elements are a function of larger powers of t , such as D4, can be seen from Eq. 5.21, where we note that \mathcal{F}_n is a decreasing function of n . We also note that the suppression caused by the form factors is stronger in the multiple scattering regime, $m_\chi \gtrsim m_n^*$, because the values of m_n^* become lower when t -dependent neutron couplings are introduced (see Fig. 5.5, left panel). As mentioned above, this is a consequence of the form factors imposing a cutoff on the size of the momentum transfer in the capture process, hence lowering the average DM energy loss per scattering. It is worth remarking that the suppression caused by the momentum dependence of the form factors is even more pronounced in heavier NSs where higher momentum transfers are possible [252].

Similar conclusions are obtained for DM capture associated with scattering from protons (right panels), where the suppression of the capture rate is slightly smaller than that for neutrons. As previously stated, we have taken $Q_0 = 0.9 \text{ GeV}$ as a conservative choice; smaller values of Q_0 will result in a stronger suppression of the capture rate.

We now turn to the effect of strong interactions on the capture process. For $m_\chi \lesssim 0.2 \text{ GeV}$, the DM mass range where Pauli blocking is in effect, the capture rate due to DM-neutron scattering is almost identical for the free Fermi gas (dashed dark blue) and interacting baryon (dashed light blue) approaches, for operators D3–D10. This is because capture occurs very close to the NS surface. Operators D1 and D2 suffer a relatively small overall rescaling, because their interaction rates scale with the neutron mass, in this case $(m_n^{\text{eff}})^2$.

For protons, however, there is a significant difference in the capture rate in the low DM mass range. In the free Fermi gas approach, protons are degenerate only in the innermost region of the NS core, with the exact extent of that region dependent on the NS configuration (see Fig. 5.1, dashed lines). For the particular NS model QMC-2, proton targets are affected by Pauli blocking only within a radius of $\sim 4 \text{ km}$ from the NS centre. Consequently, in the free Fermi gas approach (dashed dark blue) the capture rate for scattering on protons is not Pauli suppressed at low DM

mass, in contrast to that for neutrons; see the different slope of the capture rates at $m_\chi \lesssim m_p$. As a result, capture on proton targets surpasses the contribution of the dominant species, neutrons, in the free Fermi gas approximation and light DM mass regime.

However, in the interacting baryon approach, protons are degenerate over a much wider region of the stellar interior (see Fig. 5.1, solid lines). Therefore, the more accurate interacting baryon approach leads to much greater Pauli suppression of the capture rate for scattering on protons. Indeed, the proton contribution to the total capture rate is lower than that of neutrons in most cases. In the case of a QMC-2 NS configuration, the sole exception is for the operator D4. Therefore, the ratio of capture rates for the free Fermi gas and interacting baryon approaches is largest for the scattering of light DM on protons, and exceeds 4 orders of magnitude at $m_\chi = 10 \text{ keV}$, for all operators.

For DM masses above $m_\chi \sim m_n$, the capture rate in the interacting baryon framework and with constant nucleon couplings is lower by up to one order of magnitude compared to that for the free Fermi gas approach, for both neutron and proton targets for operators D1-4. For the remaining operators, the suppression reaches the $\sim 30\%$ level in the large DM mass region. Note that the capture rate depends on the DM-target reduced mass, which for $m_\chi \gg m_i$ is approximately target mass. Furthermore, in this mass regime, DM capture can occur deep inside the star, where $m_i^{\text{eff}} < m_i$, hence the capture rate is suppressed by a lower target mass.

Introducing momentum-dependent form factors in the interacting baryon approach (magenta lines) results in a similar reduction of the capture rate to that of the ideal Fermi gas formalism (orange lines), especially for operators D5-D10. For operators D1-D4, the capture rate is lowered by ~ 3 orders of magnitude in the multiple scattering regime for both neutron and proton targets.

It is worth noting that the combined effect of using the interacting baryon approach and including momentum-dependent form factors is smaller than the product of the two individual effects. This is because the form factor suppression \mathcal{F}_n in Eq. 5.21 is a decreasing function of the target mass, which can reach values as small as $m_n^{\text{eff}} \sim 0.5m_n$ for nucleon targets, thereby resulting in a weaker reduction of the capture rate when compared to the free Fermi gas approach.

Hyperons

In Figs. ?? and ??, we show the capture rates $C\Lambda^4$ for all the baryon targets in the benchmark NS QMC-4, calculated using the interactive baryon framework with momentum dependent DM couplings for all the baryonic species. As outlined in section ??, the NS configuration QMC-4 contains Λ^0 , Ξ^- and Ξ^0 hyperons in the

inner core. The orange line represents the sum of the capture rate due to scattering on all of the hyperonic species. Their individual contributions are determined by their abundance in the NS core (see Fig. ??, bottom left panel) and hence Ξ^- and Λ^0 give sizeable contributions to the capture rate while that of Ξ^0 is negligible.

For operators D1 and D5-D10, scattering on neutrons (magenta) clearly dominates the total capture rate (dashed dark blue) throughout the whole DM mass range considered here, as expected, followed by protons (light blue) and hyperons. For D3 and D4, proton targets provide the largest contribution to the capture rate in the Pauli blocked region $m_\chi \lesssim 0.2$ GeV. This occurs because of the interplay of two facts. First, the proton Fermi energy is lower than that of neutrons close to the surface (see Fig. ??, solid lines). In fact, the proton contribution to the total capture rate is largest in the light DM mass regime for all operators. Second, operators whose matrix elements are a function of larger powers of t (such as D3 and D4) are more greatly affected by Pauli blocking, i.e., the neutron contribution is more suppressed for these operators.

For D3 and D4, the capture rates due to scattering on the three species, neutrons, protons and hyperons, are all of similar magnitude when $m_\chi \gtrsim 0.2$ GeV. In fact, hyperons surpass the neutron contribution for D4, especially in the multiple scattering regime. Recall that hyperon effective masses are much larger than the nucleon masses in the inner core (see Fig. ??, bottom right panel). Thus, despite being under-abundant, their contribution to the capture rate is enhanced by a larger DM-target reduced mass and by the D4 matrix element being $|\bar{\mathcal{M}}|^2 \propto t^2$ ($n = 2$ in Eq. ??). For D2-D4, the capture rates due to scattering on neutrons and hyperons are almost identical for $m_\chi \lesssim 0.1$ GeV, with hyperons once again surpassing neutrons in the particular case of D4. This occurs because the depth of the Fermi sea of hyperons is much lower than that of the neutrons in the NS core, thus leading to less Pauli blocking.

In addition, we have compared these results with those for a NS configuration of very similar compactness to that of QMC-4, but obtained with a QMC model that does not contain hyperons. We have found that the total capture rate due to DM interactions with baryons for operators D2-D4 is actually enhanced by the presence of hyperonic matter in the NS core. For D3 and D4, this enhancement reaches a factor of ~ 2 and ~ 3 , respectively.

5.3 Threshold Cross-Sections for Nucleon Scattering

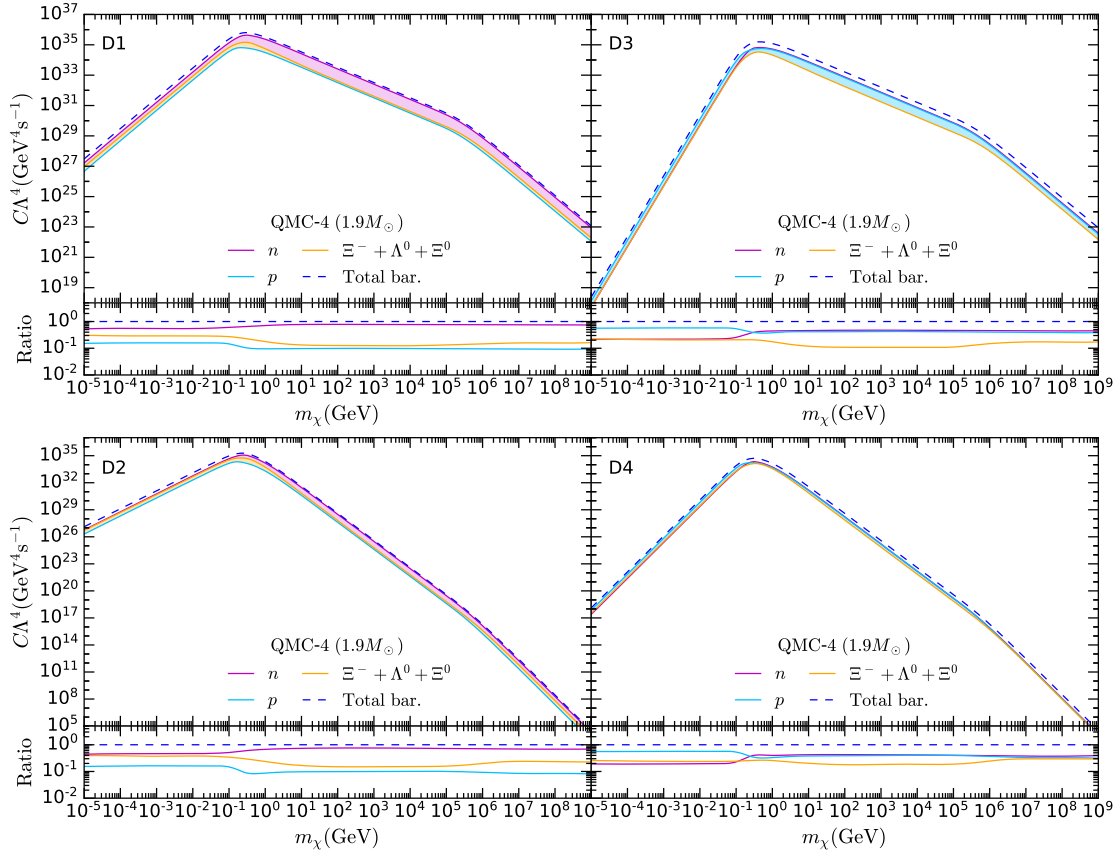


Figure 5.8: Capture rate in the optically thin limit for operators D1-D4 as a function of the DM mass m_χ for nucleons and exotic targets in the NS benchmark configuration QMC-4 ($1.9M_\odot$). All capture rates were calculated using the complete approach that accounts for strong interactions and momentum dependent form factors for baryons. Note that these rates scale as Λ^{-4} . The lower panels show the contribution of each baryonic species to the total capture rate associated with DM interactions with baryons (dashed blue line).

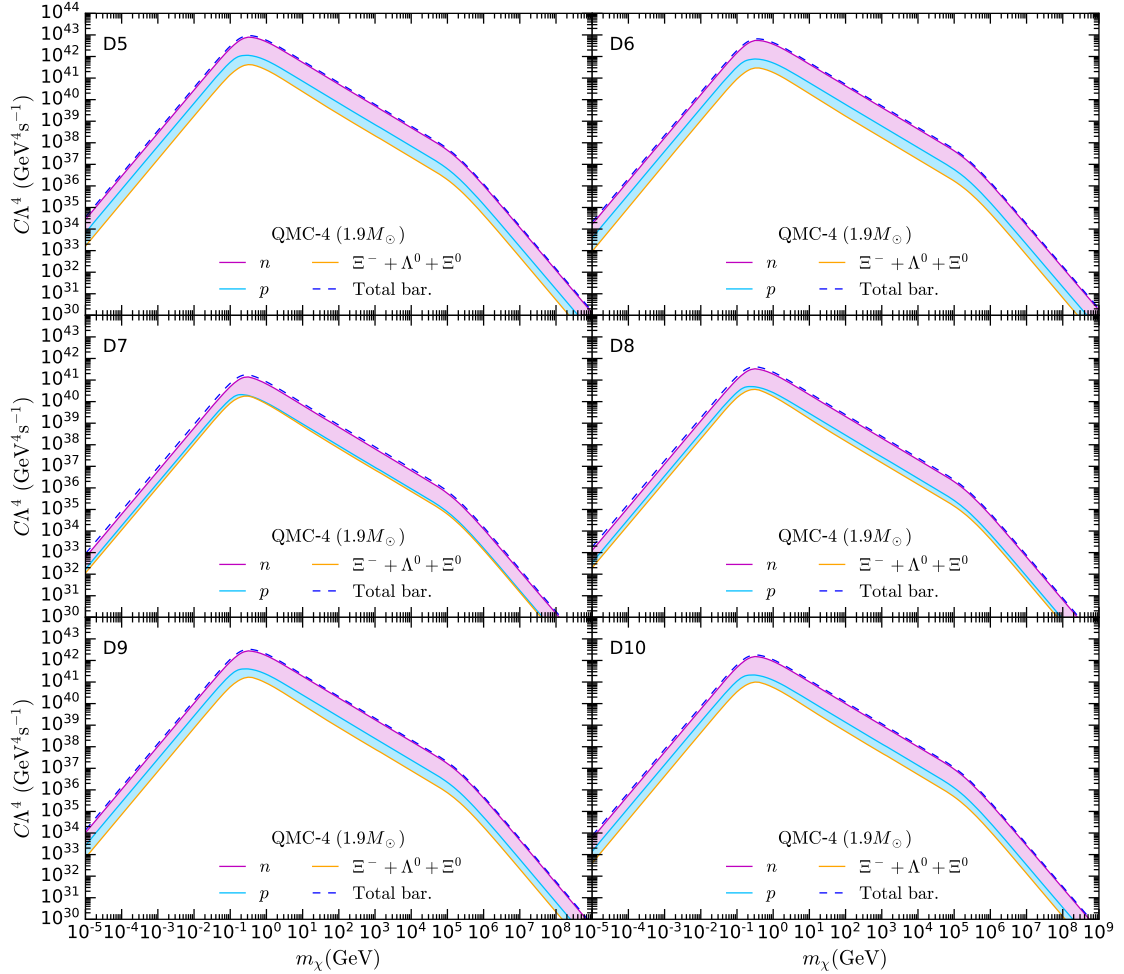


Figure 5.9: Capture rate in the optically thin limit for operators D5-D10 as a function of the DM mass m_χ for nucleons and exotic targets in the NS benchmark configuration QMC-4 ($1.9M_\odot$). All capture rates were calculated using the complete approach that accounts for strong interactions and momentum dependent form factors for baryons. Note that these rates scale as Λ^{-4} .

A

Dark Matter Interaction Rates

A.1 General Interaction Rates for Scattering within a Degenerate Media

The most general form of the interaction rate, following Ref. [118], can be written in terms of the spin-averaged squared matrix element, $|\bar{\mathcal{M}}|^2$, as

$$\Gamma = \int \frac{d^3 k'}{(2\pi)^3} \frac{1}{(2E_\chi)(2E'_\chi)(2m_i)(2m_i)} \Theta(E'_\chi - m_\chi) \Theta(\pm q_0) S(q_0, q), \quad (\text{A.1})$$

$$S(q_0, q) = 2 \int \frac{d^3 p}{(2\pi)^3} \int \frac{d^3 p'}{(2\pi)^3} \frac{m_i^2}{E_i E'_i} |\bar{\mathcal{M}}|^2 (2\pi)^4 \delta^4(k_\mu + p_\mu - k'_\mu - p'_\mu) \\ \times f_{\text{FD}}(E_i)(1 - f_{\text{FD}}(E'_i)) \Theta(E_i - m_i) \Theta(E'_i - m_i), \quad (\text{A.2})$$

where $S(q_0, q)$ is the target response function that depends on the energy and momentum transfers, q_0 and q respectively. E_χ and E_i are the DM and target initial energies, with k and p their respective momenta. Primed variables represent final state quantities.

The δ -function can be used to perform the $d^3 p'$ integrations, leaving

$$S(q_0, q) = \frac{1}{2\pi^2} \int d^3 p \frac{m_i^2}{E_i E'_i} |\bar{\mathcal{M}}|^2 \delta(q_0 + E_i - E'_i) f_{\text{FD}}(E_i)(1 - f_{\text{FD}}(E'_i)) \\ \times \Theta(E_i - m_i) \Theta(E'_i - m_i). \quad (\text{A.3})$$

After this, the final state target energy is fixed to

$$E'_i(E_i, q, \theta) = \sqrt{m_i^2 + (\vec{p} + \vec{q})^2} \quad (\text{A.4})$$

$$= \sqrt{E_i^2 + q^2 + 2qp \cos \theta} > m_i, \quad \forall p, q, \theta, |\cos \theta| < 1, \quad (\text{A.5})$$

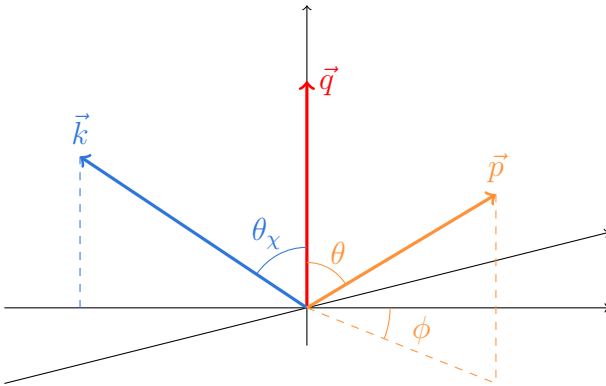


Figure A.1: Schematic of kinematics for dark matter interacting with a target in the frame of the star. We set the momentum transfer to lie along the z -axis with the initial momenta defined relative to it.

where θ is the angle between the target initial momentum and the transferred momentum, \vec{q} , that is defined below. To perform the remaining integrals, we write $d^3p = pE_idE_i d\cos\theta d\phi$. The kinematics of this interaction are depicted in Fig. A.1, where the incoming momenta are defined relative to the momentum transfer that is set to lie along the z -axis. In doing so, we must account for the fact that in this frame we cannot assume all three of the vectors are coplanar, and assign the additional azimuthal angle ϕ to the target momentum.

In general, the squared matrix elements we are interested in can be expressed as polynomials in the Mandelstam variables s and t , such that

$$|\overline{\mathcal{M}}|^2 = \sum_{n,m} \alpha_{n,m} t^n s^m. \quad (\text{A.6})$$

Writing $s = m_\chi^2 + m_i^2 + 2E_\chi E_i - 2\vec{p} \cdot \vec{k}$, the quantity $\vec{k} \cdot \vec{p}$ is obtained by analysing the kinematics of the interaction. From the diagram in Fig. A.1, we can write the initial momenta as

$$\vec{k} = (k \sin \theta_\chi, 0, k \cos \theta_\chi), \quad (\text{A.7})$$

$$\vec{p} = (p \sin \theta \cos \phi, p \sin \theta \sin \phi, p \cos \theta). \quad (\text{A.8})$$

The angles can then be expressed in terms of the other kinematic quantities by

noting that

$$E'_\chi = \sqrt{m_\chi^2 + (\vec{k} - \vec{q})}, \quad (\text{A.9})$$

$$\implies (E_\chi - q_0)^2 = m_\chi^2 + (k^2 + q^2 - 2kq \cos \theta_\chi) \quad (\text{A.10})$$

$$\implies \cos \theta_\chi = \frac{q^2 - q_0^2 + 2E_\chi q_0}{2q \sqrt{E_\chi^2 - m_\chi^2}}, \quad (\text{A.11})$$

$$E'_i = \sqrt{m_i^2 + (\vec{p} + \vec{q})}, \quad (\text{A.12})$$

$$(\text{A.13})$$

for the dark matter angle, and

$$\implies (E_i + q_0)^2 = m_i^2 + (p^2 + q^2 + 2pq \cos \theta) \quad (\text{A.14})$$

$$\implies \cos \theta = \frac{q_0^2 - q^2 + 2E_i q_0}{2q \sqrt{E_i^2 - m_i^2}} \quad (\text{A.15})$$

for the target angle. These result in

$$\vec{k} \cdot \vec{p} = kp \sin \theta_\chi \sin \theta \cos \phi + kp \cos \theta_\chi \cos \theta \quad (\text{A.16})$$

$$\begin{aligned} &= kp \left[\sqrt{1 - \frac{(q^2 - q_0^2 + 2E_\chi q_0)^2}{4q^2(E_\chi^2 - m_\chi^2)}} \sqrt{1 - \frac{(q_0^2 - q^2 + 2E_i q_0)^2}{4q^2(E_i^2 - m_i^2)}} \cos \phi \right. \\ &\quad \left. + \frac{(q^2 - q_0^2 + 2E_\chi q_0)(q_0^2 - q^2 + 2E_i q_0)}{4q^2 \sqrt{E_\chi^2 - m_\chi^2} \sqrt{E_i^2 - m_i^2}} \right] \end{aligned} \quad (\text{A.17})$$

$$\begin{aligned} &= \frac{(q^2 - q_0^2 + 2E_\chi q_0)(q_0^2 - q^2 + 2E_i q_0)}{4q^2} \\ &\quad + \sqrt{E_\chi^2 - m_\chi^2 - \frac{(q^2 - q_0^2 + 2E_\chi q_0)^2}{4q^2}} \sqrt{E_i^2 - m_i^2 - \frac{(q_0^2 - q^2 + 2E_i q_0)^2}{4q^2}} \cos \phi. \end{aligned} \quad (\text{A.18})$$

This makes explicit that s is now a function of the azimuthal angle ϕ .

We then use the remaining delta function to integrate over θ , giving rise to a step function $\Theta(1 - \cos^2 \theta(q, q_0, E_i))$, leaving the

$$S(q_0, q) = \alpha t^n \frac{m_i^2}{2\pi^2 q} \int dE_i d\phi s^m f_{\text{FD}}(E_i) (1 - f_{\text{FD}}(E_i + q_0)) \Theta(E_i) \Theta(1 - \cos^2 \theta). \quad (\text{A.19})$$

It will be more convenient to work with the kinetic energies of the targets rather than their total energies, as we are only interested in elastic scattering. From here on out, E_i will refer to the kinetic energy of the target, i.e. $E_i \rightarrow E_i + m_i$.

This is compensated by using the Fermi kinetic energy in the FD distributions, $\varepsilon_{F,i} = \mu_{F,i} - m_i$.

The ϕ integrals can be easily computed for a given power of s , in general resulting in a messy function of the kinematic variables. However, we know that they will always be a polynomial of degree m , and so to make this explicit while keeping things as tidy as possible, we define the polynomials $\mathcal{U}_m(q^2, q_0, E_\chi, E_i)$ as

$$\mathcal{U}_m = \frac{q^{2m}}{2\pi} \int_0^{2\pi} d\phi s^m = \sum_r \mathcal{V}_{m,r} E_i^r \quad (\text{A.20})$$

where the coefficients of the polynomial, $\mathcal{V}_{m,r}$, are functions of q^2, q_0 , and E_χ . The response function is then

$$S(q_0, q) = \alpha t^n \frac{m_i^2}{\pi q} \int dE_i f_{\text{FD}}(E_i) (1 - f_{\text{FD}}(E_i + q_0)) \frac{\mathcal{U}_m}{q^{2m}} \Theta(E_i) \Theta(1 - \cos^2 \theta). \quad (\text{A.21})$$

Therefore, the integrals we are interested in computing are over the FD distributions, which we call

$$\mathcal{F}_r(E_i, q_0) = \int dE_i E_i^r f_{\text{FD}}(E_i) (1 - f_{\text{FD}}(E_i + q_0)). \quad (\text{A.22})$$

To proceed, make the change to the dimensionless variables

$$x = \frac{E_i - \varepsilon_{F,i}}{T_\star}, \quad z = \frac{q_0}{T_\star}, \quad (\text{A.23})$$

which we can use to write

$$\mathcal{F}_r(E_i, q_0) = T_\star \int dx (\varepsilon_{F,i} + T_\star x)^r f_{\text{FD}}(x) f_{\text{FD}}(-x - z) \quad (\text{A.24})$$

$$= T_\star \int dx \sum_{j=0}^r \binom{r}{j} T_\star^j x^j \varepsilon_{F,i}^{r-j} f_{\text{FD}}(x) f_{\text{FD}}(-x - z) \quad (\text{A.25})$$

$$= \sum_{j=0}^r T_\star^{j+1} \binom{r}{j} \varepsilon_{F,i}^{r-j} \int dx x^j f_{\text{FD}}(x) f_{\text{FD}}(-x - z) \quad (\text{A.26})$$

$$= \sum_{j=0}^r \binom{r}{j} \varepsilon_{F,i}^{r-j} \int dE_i (E_i - \varepsilon_{F,i})^j f_{\text{FD}}(E_i) f_{\text{FD}}(-E_i - q_0) \quad (\text{A.27})$$

$$= \sum_{j=0}^r \binom{r}{j} \varepsilon_{F,i}^{r-j} (-1)^j \frac{q_0^{j+1}}{j+1} g_j \left(\frac{E_i - \varepsilon_{F,i}}{q_0} \right), \quad \text{for } T_\star \rightarrow 0, \quad (\text{A.28})$$

where the final line holds in the zero-temperature approximation in which the FD distributions become Θ -functions, allowing the integrals to be expressed in terms of the function

$$g_j(x) = \begin{cases} 1, & x > 0 \\ 1 - (-x)^{j+1}, & -1 < x < 0 \\ 0, & x < -1 \end{cases} \quad (\text{A.29})$$

The integration range for E_i is obtained from the two Θ -functions. There are two cases to be considered, $t < 0$ and $t > 0$. In the former case, the range become $E_i^{t^-} < E_i < \infty$ and for the latter $0 < E_i < E_i^{t^+}$. These integration bounds are obtained from Eq. A.15, by settting $\cos \theta = 1$, and are given by

$$E_i^{t^-} = -\left(m_i + \frac{q_0}{2}\right) + \sqrt{\left(m_i + \frac{q_0}{2}\right)^2 + \left(\frac{\sqrt{q^2 - q_0^2}}{2} - \frac{m_i q_0}{\sqrt{q^2 - q_0^2}}\right)^2} \quad (\text{A.30})$$

$$E_i^{t^+} = -\left(m_i + \frac{q_0}{2}\right) + \sqrt{\left(m_i + \frac{q_0}{2}\right)^2 - \left(\frac{\sqrt{q_0^2 - q^2}}{2} + \frac{m_i q_0}{\sqrt{q_0^2 - q^2}}\right)^2}. \quad (\text{A.31})$$

These are both the same root of Eq. A.15, but with an interchange of $t \leftrightarrow -t$. We denote the response function for $t < 0$ as S^- and for $t > 0$ as S^+ . For S^- we have

$$S_m^- = \alpha t^n \frac{m_i^2}{\pi q^{2m+1}} \sum_{r=0}^m \mathcal{V}_{m,r} \int_{E_i^{t^-}}^{\infty} dE_i E_i^r f_{\text{FD}}(E_i) (1 - f_{\text{FD}}(E_i + q_0)) \quad (\text{A.32})$$

$$= \alpha t^n \frac{m_i^2}{\pi q^{2m+1}} \sum_{r=0}^m \mathcal{V}_{m,r} \sum_{j=0}^r \binom{r}{j} \varepsilon_{F,i}^{r-j} \int_{E_i^{t^-}}^{\infty} dE_i (E_i - \varepsilon_{F,i})^j f_{\text{FD}}(E_i) f_{\text{FD}}(-E_i - q_0) \quad (\text{A.33})$$

$$= \alpha t^n \frac{m_i^2}{\pi q^{2m+1}} \sum_{r=0}^m \mathcal{V}_{m,r} \sum_{j=0}^r \binom{r}{j} \varepsilon_{F,i}^{r-j} \frac{(-1)^j q_0^{j+1}}{j+1} \left[1 - g_j \left(\frac{E_i^{t^-} - \varepsilon_{F,i}}{q_0} \right) \right] \quad (\text{A.34})$$

$$= \alpha t^n \frac{m_i^2}{\pi q^{2m+1}} \sum_{r=0}^m \mathcal{V}_{m,r} \sum_{j=0}^r \binom{r}{j} \varepsilon_{F,i}^{r-j} \frac{(-1)^j q_0^{j+1}}{j+1} h_j \left(\frac{E_i^{t^-} - \varepsilon_{F,i}}{q_0} \right), \quad (\text{A.35})$$

while for S^+ the logic is

$$S_m^+ = \alpha t^n \frac{m_i^2}{\pi q^{2m+1}} \sum_{r=0}^m \mathcal{V}_{m,r} \int_0^{E_i^{t^+}} dE_i E_i^r f_{\text{FD}}(E_i) (1 - f_{\text{FD}}(E_i + q_0)) \quad (\text{A.36})$$

$$= \alpha t^n \frac{m_i^2}{\pi q^{2m+1}} \sum_{r=0}^m \mathcal{V}_{m,r} \sum_{j=0}^r \binom{r}{j} \varepsilon_{F,i}^{r-j} \int_0^{E_i^{t^+}} dE_i (E_i - \varepsilon_{F,i})^j f_{\text{FD}}(E_i) f_{\text{FD}}(-E_i - q_0) \quad (\text{A.37})$$

$$= \alpha t^n \frac{m_i^2}{\pi q^{2m+1}} \sum_{r=0}^m \mathcal{V}_{m,r} \sum_{j=0}^r \binom{r}{j} \varepsilon_{F,i}^{r-j} \frac{(-1)^j q_0^{j+1}}{j+1} \left[g_j \left(\frac{E_i^{t^+} - \varepsilon_{F,i}}{q_0} \right) - g_j \left(\frac{-\varepsilon_{F,i}}{q_0} \right) \right] \quad (\text{A.38})$$

$$= -\alpha t^n \frac{m_i^2}{\pi q^{2m+1}} \sum_{r=0}^m \mathcal{V}_{m,r} \sum_{j=0}^r \binom{r}{j} \varepsilon_{F,i}^{r-j} \frac{(-1)^j q_0^{j+1}}{j+1} h_j \left(\frac{E_i^{t^+} - \varepsilon_{F,i}}{q_0} \right) \quad \text{for } q_0 < 0, \quad (\text{A.39})$$

with

$$h_j(x) = \begin{cases} 0, & x > 0 \\ (-x)^{j+1}, & -1 < x < 0 \\ 1, & x < -1 \end{cases} \quad (\text{A.40})$$

The final step of the S^+ calculation holds only for up-scattering of the DM, i.e. $q_0 < 0$.

For matrix elements that are polynomials in s and t , the full response function is simply the sum of the n and m , giving

$$S^- = \sum_{n,m} \alpha_{n,m} t^n \frac{m_i^2}{\pi q^{2m+1}} \sum_{r=0}^m \mathcal{V}_{m,r} \sum_{j=0}^r \binom{r}{j} \varepsilon_{F,i}^{r-j} \frac{(-1)^j q_0^{j+1}}{j+1} h_j \left(\frac{E_i^{t^-} - \varepsilon_{F,i}}{q_0} \right) \quad (\text{A.41})$$

$$S^+ = - \sum_{n,m} \alpha_{n,m} t^n \frac{m_i^2}{\pi q^{2m+1}} \sum_{r=0}^m \mathcal{V}_{m,r} \sum_{j=0}^r \binom{r}{j} \varepsilon_{F,i}^{r-j} \frac{(-1)^j q_0^{j+1}}{j+1} h_j \left(\frac{E_i^{t^+} - \varepsilon_{F,i}}{q_0} \right) \quad (\text{A.42})$$

A.2 Elsatic Scattering

A.2.1 Down-scattering Rate

Returning to the scattering rate, we first look at the case of down-scattering, where the DM loses energy, $q_0 > 0$. In this case, the interaction rate is given by

$$\begin{aligned} \Gamma^-(E_\chi) = & \int \frac{d \cos \theta_\chi k'^2 dk'}{64\pi^3 E_\chi E'_\chi} \Theta(E_\chi - q_0 - m_\chi) \Theta(q_0) \sum_{n,m} \frac{\alpha_{n,m} t^n}{q^{2m+1}} \\ & \times \sum_{r=0}^m \mathcal{V}_{m,r} \sum_{j=0}^r \binom{r}{j} \varepsilon_{F,i}^{r-j} \frac{(-1)^j q_0^{j+1}}{j+1} h_j \left(\frac{E_i^{t^-} - \varepsilon_{F,i}}{q_0} \right) \end{aligned} \quad (\text{A.43})$$

Change variables to q_0 and q through

$$q_0 = E_\chi - \sqrt{k'^2 + m_\chi^2}, \quad (\text{A.44})$$

$$q^2 = k^2 + k'^2 - 2kk' \cos \theta_\chi, \quad (\text{A.45})$$

$$\implies dk' d \cos \theta_\chi = \frac{E'_\chi q}{kk'^2} dq_0 dq \quad (\text{A.46})$$

To further simplify the notation we introduce $t_E = -t = q^2 - q_0^2$, $dq = dt_E/(2q)$, and exchange the q -integral for

$$\implies dk' d \cos \theta_\chi = \frac{E'_\chi}{2kk'^2} dq_0 dt_E, \quad (\text{A.47})$$

giving the interaction rate as

$$\begin{aligned} \Gamma^-(E_\chi) = & \frac{1}{128\pi^3 E_\chi k} \int_0^{E_\chi - m_\chi} dq_0 \int dt_E \sum_{n,m} \frac{\alpha_{n,m} (-1)^n t_E^n}{(t_E + q_0^2)^{m+\frac{1}{2}}} \\ & \times \sum_{r=0}^m \mathcal{V}_{m,r} \sum_{j=0}^r \binom{r}{j} \varepsilon_{F,i}^{r-j} \frac{(-1)^j q_0^{j+1}}{j+1} h_j \left(\frac{E_i^{t^-} - \varepsilon_{F,i}}{q_0} \right) \end{aligned} \quad (\text{A.48})$$

$$\begin{aligned} = & \sum_{n,m} \frac{(-1)^n \alpha_{n,m}}{128\pi^3 E_\chi k} \int_0^{E_\chi - m_\chi} dq_0 \int \frac{dt_E t_E^n}{(t_E + q_0^2)^{m+\frac{1}{2}}} \\ & \times \sum_{r=0}^m \mathcal{V}_{m,r} \sum_{j=0}^r \binom{r}{j} \varepsilon_{F,i}^{r-j} \frac{(-1)^j q_0^{j+1}}{j+1} h_j \left(\frac{E_i^{t^-} - \varepsilon_{F,i}}{q_0} \right). \end{aligned} \quad (\text{A.49})$$

There are then two main cases to consider; when $h_j(x)$ is unity or when it is not. We denote the t_E integrand in the former case as f_1 and f_2 for the latter, given explicitly as

$$f_1^{(m,n)}(t_E) = \frac{t_E^n}{(t_E + q_0^2)^{m+\frac{1}{2}}} \sum_{r=0}^m \mathcal{V}_{m,r} \sum_{j=0}^r \binom{r}{j} \varepsilon_{F,i}^{r-j} \frac{(-1)^j q_0^{j+1}}{j+1}, \quad (\text{A.50})$$

$$f_2^{(m,n)}(t_E) = \frac{-t_E^n}{(t_E + q_0^2)^{m+\frac{1}{2}}} \sum_{r=0}^m \mathcal{V}_{m,r} \sum_{j=0}^r \binom{r}{j} \varepsilon_{F,i}^{r-j} \frac{1}{j+1} \left(E_i^{t^-} - \varepsilon_{F,i} \right)^{j+1}, \quad (\text{A.51})$$

where we suppress the explicit dependence on the other variables for brevity. We encode the integrals over t_E within an operator

$$\begin{aligned} \mathcal{I}_{n,m}(f^{(m,n)}(t), t_1^+, t_2^+, t_1^-, t_2^-) &= \sum_{i=1,2} \sum_{j=1,2} \left(F^{(m,n)}(t_i^+) - F^{(m,n)}(t_j^-) \right) \\ &\quad \times \Theta(t_{3-i}^+ - t_i^+) \Theta(t_i^+ - t_j^-) \Theta(t_j^- - t_{3-j}^-), \end{aligned} \quad (\text{A.52})$$

$$F^{(m,n)}(t) = \int dt f^{(m,n)}(t). \quad (\text{A.53})$$

The full interaction rate is then written as

$$\begin{aligned} \Gamma^-(E_\chi) &= \sum_{n,m} \frac{(-1)^n \alpha_{n,m}}{128\pi^3 E_\chi k} \int_0^{E_\chi - m_\chi} dq_0 \\ &\quad \times \left[\mathcal{I}_{n,m} \left(f_1^{(m,n)}(t), t_E^+, t_{\mu^-}^+, t_E^-, t_{\mu^-}^- \right) \Theta(\varepsilon_{F,i} - q_0) \right. \\ &\quad + \mathcal{I}_{n,m} \left(f_2^{(m,n)}(t), t_E^+, t_{\mu^+}^+, t_E^-, t_{\mu^+}^- \right) \Theta(\varepsilon_{F,i} - q_0) \\ &\quad + \mathcal{I}_{n,m} \left(f_2^{(m,n)}(t), t_E^+, t_{\mu^-}^-, t_E^-, t_{\mu^+}^- \right) \Theta(\varepsilon_{F,i} - q_0) \\ &\quad \left. + \mathcal{I}_{n,m} \left(f_2^{(m,n)}(t), t_E^+, t_{\mu^+}^+, t_E^-, t_{\mu^+}^- \right) \Theta(q_0 - \varepsilon_{F,i}) \right], \end{aligned} \quad (\text{A.54})$$

where the t_E integration limits are

$$t_E^\pm = 2 \left[E_\chi(E_\chi - q_0) - m_\chi^2 \pm k \sqrt{(E_\chi - q_0)^2 - m_\chi^2} \right], \quad (\text{A.55})$$

$$\begin{aligned} t_{\mu^+}^\pm &= 2 [\varepsilon_{F,i}(\varepsilon_{F,i} + q_0) + m_i(2\varepsilon_{F,i} + q_0) \\ &\quad \pm \sqrt{(\varepsilon_{F,i}(\varepsilon_{F,i} + q_0) + m_i(2\varepsilon_{F,i} + q_0))^2 - m_i^2 q_0^2}], \end{aligned} \quad (\text{A.56})$$

$$\begin{aligned} t_{\mu^-}^\pm &= 2 [\varepsilon_{F,i}(\varepsilon_{F,i} - q_0) + m_i(2\varepsilon_{F,i} - q_0) \\ &\quad \pm \sqrt{(\varepsilon_{F,i}(\varepsilon_{F,i} - q_0) + m_i(2\varepsilon_{F,i} - q_0))^2 - m_i^2 q_0^2}], \end{aligned} \quad (\text{A.57})$$

All interaction rate spectra will have an endpoint at $q_0 = q_0^{\text{MAX}}$, the maximum amount of energy that can be lost in a single interaction. The value of q_0^{MAX} is shown in the left panel of Fig. 3.2 as a function of B in the case of large DM mass ($m_\chi = 1 \text{ TeV}$), for several values of $\varepsilon_{F,n}$. The endpoint can be found as the minimum between the DM kinetic energy and the root of one of the following two equations

$$t_E^- = t_{\mu^+}^+, \quad (\text{A.58})$$

$$t_E^+ = t_{\mu^+}^-. \quad (\text{A.59})$$

Only one of these equations will have a positive root for a given choice of m_χ , $\varepsilon_{F,n}$ and E_χ . For $m_\chi \gg m_i$, the second equation never has a solution, and the solution of the first equation is always much lower than the kinetic energy. This results in the value of q_0^{MAX} becoming independent of m_χ in this mass range.

The shape of the differential interaction rate depends very weakly on m_χ and B for $m_\chi \gg m_i$ and $m_\chi \ll m_i$, as seen by plotting it as a function of $q_0^{\text{norm}} = q_0/q_0^{\text{MAX}}$. Therefore, we use as a reference $m_\chi = 1 \text{ TeV}$ (left) and $m_\chi = 10 \text{ MeV}$ (right), $B = 0.5$, and show the normalised differential interaction rates in Fig. A.2 for $n = 0, 1, 2$, and neutron targets. We observe in the left panels that for $n = 0$ interaction rates are flat (or peaked, depending on $\varepsilon_{F,n}$) at low energy and suppressed at high energies, while for $n = 1, 2$ the profiles become peaked at higher and higher energies. Conversely, for $m_\chi = 10 \text{ MeV}$ the peak of the spectrum is shifted to lower energies with increasing power of t ($d\sigma \propto t^n$).

A.2.2 Up-scattering Rate

We now treat the case of $q_0 < 0$, applicable to up scattering and evaporation. Focusing on s -independent matrix elements for the moment, the response function is

$$S_{\text{up}}^-(q_0, q) = \frac{m_i^2}{\pi q} \int_{E_i^{t-}}^{\infty} f_{\text{FD}}(E_i) (1 - f_{\text{FD}}(E_i - |q_0|)) \quad (\text{A.60})$$

and evaluate the integral, now with $q_0 < 0$. If we attempt to take the $T_* \rightarrow 0$ limit as before, we find that there is no overlap of the FD distributions and the result vanishes. Instead, we keep the leading order thermal corrections, i.e. terms of order $e^{-|q_0|/T_*}$. The result is

$$\mathcal{F}_0(E_i, -|q_0|) = \frac{T_* e^{-|q_0|/T_*}}{1 - e^{-|q_0|/T_*}} [\log(1 + e^{(E_i - \varepsilon_{F,i})/T_*}) - \log(1 + e^{(E_i - |q_0| - \varepsilon_{F,i})/T_*})], \quad (\text{A.61})$$

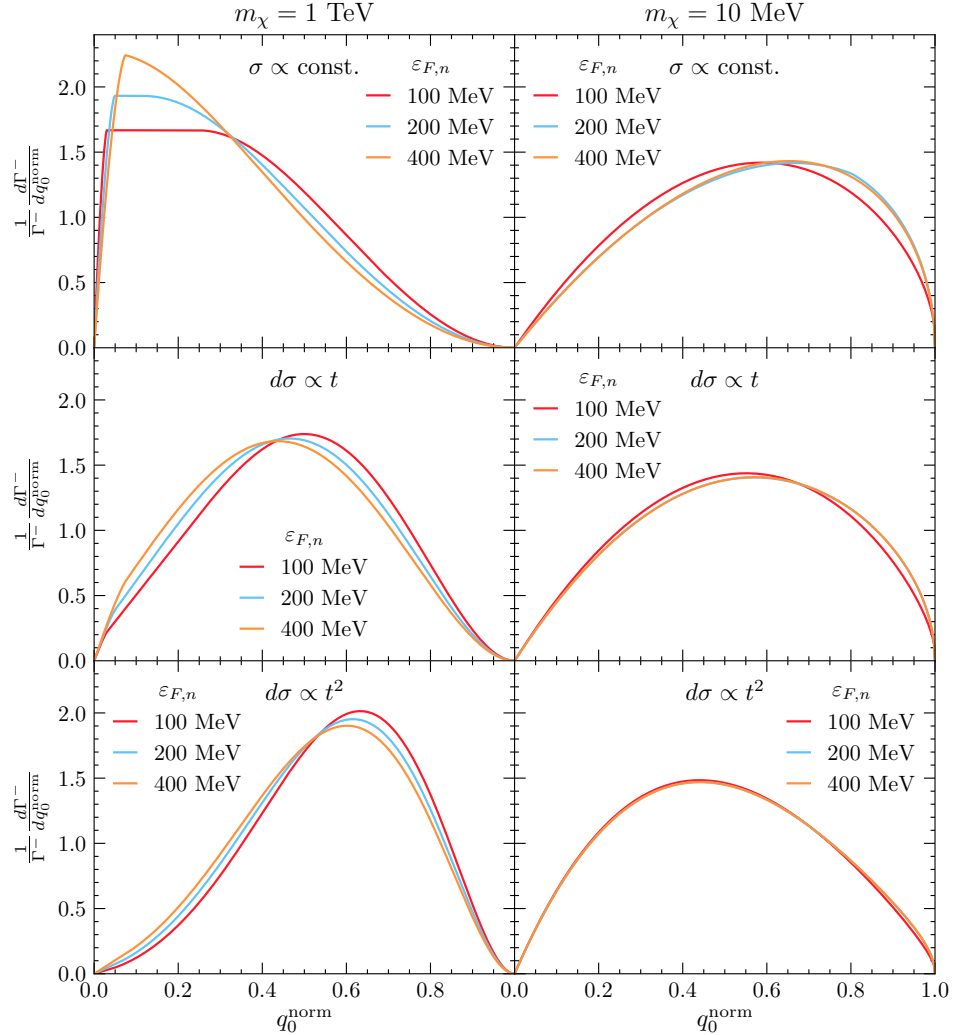


Figure A.2: Normalised differential interaction rates, $\frac{1}{\Gamma} \frac{d\Gamma^-}{dq_0^{\text{norm}}}$, as a function of q_0^{norm} for different values of $\varepsilon_{F,n}$, with $m_\chi = 1 \text{ TeV}$ (left panels) $m_\chi = 10 \text{ MeV}$ (right panels) and $B = 0.5$. Top row: $n = 0$, middle row: $n = 1$, bottom row: $n = 2$.

where after taking $T_\star \rightarrow 0$ we recognise three regions of interest

$$\lim_{T_\star \rightarrow 0} T_\star \mathcal{F}_0(E_i, -|q_0|) = \begin{cases} \frac{|q_0| e^{-|q_0|/T_\star}}{1 - e^{-|q_0|/T_\star}}, & E_i > \varepsilon_{F,i} + |q_0| \\ \frac{(E_i - \varepsilon_{F,i}) e^{-|q_0|/T_\star}}{1 - e^{-|q_0|/T_\star}}, & \varepsilon_{F,i} + |q_0| > E_i > \varepsilon_{F,i} \\ 0, & \varepsilon_{F,i} > E_i \end{cases}, \quad (\text{A.62})$$

and we can write this as

$$\lim_{T_\star \rightarrow 0} T_\star \mathcal{F}_0(E_i, -|q_0|) = \frac{|q_0| e^{-|q_0|/T_\star}}{1 - e^{-|q_0|/T_\star}} h_0\left(\frac{\varepsilon_{F,i} - E_i}{q_0}\right). \quad (\text{A.63})$$

The response function for upscattering is then

$$S_{\text{up}}^-(q_0, q) = \frac{m_i^2 q_0}{\pi q} \frac{e^{-|q_0|/T_\star}}{e^{-|q_0|/T_\star} - 1} \left[1 - h_0\left(\frac{E_i^{t^-} - \varepsilon_{F,i}}{q_0}\right) \right] \quad (\text{A.64})$$

$$= \frac{m_i^2 q_0}{\pi q} \frac{e^{-|q_0|/T_\star}}{e^{-|q_0|/T_\star} - 1} g_0\left(\frac{\varepsilon_{F,i} - E_i^{t^-}}{q_0}\right), \quad (\text{A.65})$$

leading to the corresponding up-scattering rate being

$$\Gamma_{\text{up}}^-(E_\chi) = \int \frac{k'^2 d \cos \theta dk'}{64\pi^2 m_i^2 E_\chi E'_\chi} |\bar{\mathcal{M}}|^2 \Theta(E_\chi + |q_0| - m_\chi) \Theta(q_0) S_{\text{up}}^-(q_0, q) \quad (\text{A.66})$$

$$= \frac{(-1)^n \alpha}{128\pi^3 E_\chi k} \int_{-\infty}^0 dq_0 \frac{q_0 e^{q_0/T_\star}}{e^{q_0/T_\star} - 1} \int dt_E \frac{t_E^n}{\sqrt{t_E - |q_0|^2}} g_0\left(\frac{\varepsilon_{F,i} - E_i^{t^-}}{q_0}\right) \quad (\text{A.67})$$

where we have substituted $|\bar{\mathcal{M}}|^2 = \alpha t^n$ as the matrix element. Typically, we expect to be in the regime where $g_0 = 1$, and so the differential up-scattering rate is related result for down-scattering through

$$\frac{d\Gamma_{\text{up}}^-}{dq_0} = \frac{e^{-|q_0|/T_\star}}{e^{-|q_0|/T_\star} - 1} \frac{d\Gamma_{\text{down}}^-}{dq_0} \quad (\text{A.68})$$

This result applies generally to all matrix elements, not just the ones $\propto t^n$. The result can be derived from the principle of detailed balance, and hence is true for all interactions we consider. To calculate the total interaction rate, the t_E integrations can be performed in the same manner as in the previous section, with the q_0 integration bounds being $(-\infty, 0)$.

A.3 Non-degenerate weak field limit

When setting up the centre of mass energy interval in Section 3.3, we have set the DM energy to 0 at infinity. This means that when taking the classical non-relativistic limit, the interaction rate would approach

$$\Omega^-(r) \rightarrow n_i(r)v_{\text{esc}}(r)\sigma, \quad (\text{A.69})$$

in the simple case of a constant cross-section. Taking Eq. 3.39, one can first strip out the Pauli blocking term $(1 - f_{\text{FD}})$, and then the integration in t and s can be performed analytically. Taking the limit $u_i \rightarrow 0$, $E_i = m_i/\sqrt{1 - u_i^2}$, and then the weak field approximation $B(r) \rightarrow 1 - v_{\text{esc}}^2(r)$, for a constant cross-section $\frac{d\sigma}{d\cos\theta_{\text{cm}}} = \frac{\sigma}{2}$, we find

$$\Omega^-(r) \rightarrow m_i^2 \frac{\sigma}{2} \frac{2u_i v_{\text{esc}}(r) f_{\text{FD}}(E_i, r)}{\pi^2} dE_i \quad (\text{A.70})$$

$$= m_i^3 \frac{\sigma}{2} \frac{2u_i v_{\text{esc}}(r) f_{\text{FD}}(E_i, r)}{\pi^2} u_i du_i \quad (\text{A.71})$$

$$= m_i^3 \frac{\sigma}{2} \frac{v_{\text{esc}}(r) f_{\text{FD}}(E_i, r)}{2\pi^3} d^3 u_i \quad (\text{A.72})$$

$$= \frac{\sigma}{2} \frac{v_{\text{esc}}(r) f_{\text{FD}}(E_i, r)}{2\pi^3} d^3 p. \quad (\text{A.73})$$

Cases with $\sigma \propto t^n$ give similar results. Recall that

$$\frac{2f_{\text{FD}}(E_i)}{(2\pi)^3} d^3 p, \quad (\text{A.74})$$

is the number density of neutron states. Then, following expression in 3.31 we substitute it with the classical number density $n_i(r)$, to obtain the expected classical limit given by Eq. A.69.

A.4 Intermediate DM mass range

The interaction rate in Eq. 3.39 can be rewritten in terms of the DM momentum p_χ , such that

$$\begin{aligned} \Omega^-(r) &= \frac{\zeta(r)}{32\pi^3} \int dt dE_i ds |\bar{M}|^2 \frac{E_i}{2s\beta(s) - \gamma^2(s)} \frac{1}{p_\chi} \frac{s}{\gamma(s)} \\ &\quad \times f_{\text{FD}}(E_i, r)(1 - f_{\text{FD}}(E'_i, r)), \end{aligned} \quad (\text{A.75})$$

where we have also used Eq. 3.51. We first consider the case where the squared matrix element depends only on t , i.e. $|\bar{M}|^2 \propto t^n$, we can straightforwardly perform the integral over t ,

$$\Omega^-(r) = \frac{\zeta(r)}{32\pi^3} \int dE_i ds \bar{g}(s) \frac{E_i \gamma(s)}{2s\beta(s) - \gamma^2(s)} \frac{1}{n+1} \frac{1}{p_\chi} \left(\frac{\gamma^2(s)}{s} \right)^n \times f_{\text{FD}}(E_i, r)(1 - f_{\text{FD}}(E'_i, r)). \quad (\text{A.76})$$

We now assume that either $\mu \gg 1$ or $\mu \ll 1$. In both cases, the integration range for s shrinks to $[s_0 - \delta s, s_0 + \delta s]$, with $\delta s \ll s_0$, and the following simplifications can be made;

$$s_0 = m_i^2 + m_\chi^2 + 2 \frac{E_i m_\chi}{\sqrt{B(r)}} = m_i^2 + m_\chi^2 + 2 E_i E_\chi, \quad (\text{A.77})$$

$$\delta s = 2 \sqrt{\frac{1 - B(r)}{B(r)}} m_\chi \sqrt{E_i^2 - m_i^2} = 2 p_\chi \sqrt{E_i^2 - m_i^2}, \quad (\text{A.78})$$

$$\frac{\gamma(s)}{2s\beta(s) - \gamma^2(s)} \rightarrow \frac{\sqrt{1 - B(r)}}{2(m_i^2 + m_\chi^2)} = \frac{p_\chi}{2E_\chi(m_i^2 + m_\chi^2)}, \quad (\text{A.79})$$

$$\frac{\gamma^2(s)}{s} \rightarrow \frac{4(1 - B(r))m_\chi^2}{B(r)(1 + \mu^2)} = \frac{4p_\chi^2}{1 + \mu^2}. \quad (\text{A.80})$$

If $g(s)$ is regular in s_0 , we can estimate the integral in s to be $2\delta s$, approximating the integrand as being constant in that range, which gives

$$\Omega^-(r) \sim \zeta(r) \frac{1}{16\pi^3} \frac{\sqrt{E_\chi^2 - m_\chi^2}}{E_\chi(m_i^2 + m_\chi^2)} \frac{\left[\frac{4(E_\chi^2 - m_\chi^2)}{1 + \mu^2} \right]^n}{n+1} \int dE_i E_i \sqrt{E_i^2 - m_i^2} \times f_{\text{FD}}(E_i, r)(1 - f_{\text{FD}}(E'_i, r)). \quad (\text{A.81})$$

To perform the integral in E_i , we have to potentially deal with Pauli blocking. However, for $\mu \gg 1$, Pauli blocking is not effective and we can drop the $1 - f_{\text{FD}}$ term to obtain

$$\int_{m_i}^{m_i + \varepsilon_{F,i}(r)} dE_i E_i \sqrt{E_i^2 - m_i^2} f_{\text{FD}}(E_i, r) = \frac{[\varepsilon_{F,i}(r)(2m_i + \varepsilon_{F,i}(r))]^{3/2}}{3} \quad (\text{A.82})$$

$$= \pi^2 n_{\text{free}}(r). \quad (\text{A.83})$$

This, together with $\zeta(r)$, result in an overall factor of $\pi^2 n_i(r)$, leaving

$$\Omega^-(r) \sim \frac{n_i(r)}{16\pi} \frac{\sqrt{E_\chi^2 - m_\chi^2}}{m_\chi^2 E_\chi} \frac{1}{n+1} \left[\frac{4(1 - B(r))m_\chi^2}{B(r)(1 + \mu^2)} \right]^n, \quad (\text{A.84})$$

and the capture rate reads,

$$C \sim \frac{1}{4v_\star} \frac{\rho_\chi}{m_\chi^3} \text{Erf} \left(\sqrt{\frac{3}{2}} \frac{v_\star}{v_d} \right) \int_0^{R_\star} r^2 dr n_i(r) \frac{1 - B(r)}{B(r)} \frac{1}{n+1} \times \left[\frac{4(1 - B(r))m_\chi^2}{B(r)(1 + \mu^2)} \right]^n. \quad (\text{A.85})$$

We can now rewrite these expressions in terms of the cross-section which has been averaged over s ,

$$\langle \sigma(r) \rangle = \left\langle \int dt \frac{d\sigma}{dt} \right\rangle_s \quad (\text{A.86})$$

$$= \frac{1}{2\delta s} \int_{s_0 - \delta s}^{s_0 + \delta s} ds \int dt \frac{d\sigma}{dt} \quad (\text{A.87})$$

$$= \frac{1}{64\pi m_i^2 m_\chi^2} \frac{B(r)}{(1 - B(r))} \int dt t^n \quad (\text{A.88})$$

$$= \frac{1}{64\pi m_i^2 m_\chi^2} \frac{B(r)}{(1 - B(r))} \frac{1}{(n+1)} \left[\frac{4(1 - B(r))m_\chi^2}{B(r)(1 + \mu^2)} \right]^{n+1} \quad (\text{A.89})$$

$$= \frac{1}{16\pi (m_i^2 + m_\chi^2)} \frac{1}{(n+1)} \left[\frac{4(1 - B(r))m_\chi^2}{B(r)(1 + \mu^2)} \right]^n, \quad (\text{A.90})$$

which leads to,

$$\Omega^-(r) \sim n_i(r) \langle \sigma(r) \rangle \frac{\sqrt{E_\chi^2 - m_\chi^2}}{E_\chi}, \quad (\text{A.91})$$

$$C \sim \frac{4\pi}{v_\star} \frac{\rho_\chi}{m_\chi} \text{Erf} \left(\sqrt{\frac{3}{2}} \frac{v_\star}{v_d} \right) \int_0^{R_\star} r^2 dr n_i(r) \frac{1 - B(r)}{B(r)} \langle \sigma(r) \rangle. \quad (\text{A.92})$$

From Eq. A.92, we can identify the typical $1/m_\chi$ scaling of the capture rate. This equation also looks very similar to the non-relativistic case, with $1 - B(r)$ playing the role of the escape velocity, $v_{\text{esc}}^2(r)$, and $1/B(r)$ being a relativistic correction.

Turning to the case of s -dependent matrix elements, $|\bar{\mathcal{M}}|^2 = g(s)t^n$ for \bar{g} some function of s , the result is fairly similar. The main difference is that we must keep all terms in m_i and m_χ , leading to the new substitutions

$$\frac{\gamma(s)}{s^2 - [m_i^2 - m_\chi^2]^2} \sim \frac{\sqrt{1 - B(r)}}{2 \left(m_i^2 + m_\chi^2 + 2m_i m_\chi / \sqrt{B(r)} \right)}, \quad (\text{A.93})$$

$$\frac{\gamma^2(s)}{s} \rightarrow \frac{4(1 - B(r))m_\chi^2}{B(r)(1 + \mu^2) + 2\sqrt{B(r)}\mu}. \quad (\text{A.94})$$

Now when we take the limit as $\varepsilon_{F,n} \rightarrow 0$, the integrand over s can be approximated as a δ -function, resulting in s being fixed to the value of s_0 . As such, we no longer need to average the cross-section over s . The results are

$$\Omega^-(r) \sim \frac{n_i(r)}{16\pi} \frac{\sqrt{E_\chi^2 - m_\chi^2}}{E_\chi (m_i^2 + m_\chi^2 + 2m_i E_\chi)} \frac{\bar{g}(s_0)}{n+1} \left[\frac{4(1-B(r))m_\chi^2}{B(r)(1+\mu^2) + 2\sqrt{B(r)}\mu} \right]^n. \quad (\text{A.95})$$

$$C \sim C_{\text{approx},s} = \frac{4\pi}{v_\star} \frac{\rho_\chi}{m_\chi} \text{Erf} \left(\sqrt{\frac{3}{2}} \frac{v_\star}{v_d} \right) \int_0^{R_\star} r^2 dr n_i(r) \frac{1-B(r)}{B(r)} \sigma(r), \quad (\text{A.96})$$

$$\sigma(r) = \int dt \frac{d\sigma}{dt} = \frac{1}{16\pi (m_i^2 m_\chi^2 + 2m_i m_\chi / \sqrt{B(r)})} \frac{\bar{g}(s_0)}{(n+1)} \times \left[\frac{4(1-B(r))m_\chi^2}{B(r)(1+\mu^2) + 2\sqrt{B(r)}\mu} \right]^n. \quad (\text{A.97})$$

A.5 Kinematic phase space for DM-electron scattering

When deriving the interaction rate in the context of DM capture in NSs, we assumed that all the target phase space was available to scatter with DM. This is not necessarily true if the target is highly degenerate or if gravity is not particularly strong, like in NSs. In fact, for the scattering to occur, both the DM and target momenta should be in the inbound direction in the centre of mass frame. This is true in the whole phase space only when the following condition is satisfied

$$\frac{1}{\sqrt{B(r)}} > \frac{\varepsilon_{F,e}}{m_e}. \quad (\text{A.98})$$

To clarify this point, we first derive this constraint using non-relativistic kinematics. The DM particle of mass m_χ has an initial speed

$$v_{\text{esc}} = \sqrt{1 - B}, \quad (\text{A.99})$$

while the target has a mass m_e and an energy

$$E_e = m_e + b\varepsilon_{F,e} = m_e \left(1 + b \frac{\varepsilon_{F,e}}{m_e} \right), \quad b \in [0, 1]. \quad (\text{A.100})$$

Using non-relativistic kinematics, the speed of the target is

$$v_e = \sqrt{2b \frac{\varepsilon_{F,e}}{m_e}}. \quad (\text{A.101})$$

The centre of mass velocity is defined as

$$\vec{v}_{com} = \frac{1}{m_\chi + m_e} (m_\chi \vec{v}_{esc} + m_e \vec{v}_e), \quad (\text{A.102})$$

so the DM speed in the CoM frame is $\vec{v}'_\chi = \vec{v}_{esc} - \vec{v}_{com}$. To ensure that the DM and the target are not moving away from each other, the following condition should hold, $\vec{v}'_\chi \cdot \vec{v}_{esc} > 0$, i.e., the component of the DM velocity in the CoM frame is always parallel to the initial speed in the star frame. This condition leads to

$$\cos \theta < \sqrt{\frac{1-B}{2b(\varepsilon_{F,e}/m_e)}}, \quad (\text{A.103})$$

where θ is the angle between the DM and the target speed in the star frame. If $\varepsilon_{F,e}/m_e \gg 1-B$, the condition reduces to

$$\cos \theta < 0, \quad (\text{A.104})$$

meaning that the collision is head-on only.

Repeating the same exercise with relativistic kinematics, the variable whose parameter space is modified by the above mentioned condition is the centre of mass energy s ,

$$s = m_\chi^2 + m_e^2 + \frac{2m_e m_\chi}{\sqrt{B}} \left(1 + b \frac{\varepsilon_{F,e}}{m_e} - a \sqrt{1-B} \sqrt{2b \frac{\varepsilon_{F,e}}{m_e} + b^2 \frac{\varepsilon_{F,e}^2}{m_e^2}} \right), \quad a \in [-1, 1], \quad (\text{A.105})$$

and the new condition becomes

$$a = \frac{s_{\max} + s_{\min} - 2s}{s_{\max} - s_{\min}} < \left(1 + b \frac{\varepsilon_{F,e}}{m_e} \right) \sqrt{\frac{1-B}{2b \frac{\varepsilon_{F,e}}{m_e} + b^2 \frac{\varepsilon_{F,e}^2}{m_e^2}}} = E_e \sqrt{\frac{1-B}{E_e^2 - m_e^2}}. \quad (\text{A.106})$$

With the exception of the heaviest WDs, we have $\varepsilon_{F,e}/m_e \lesssim 1$. Then, with $1-B \sim 10^{-3}$, we can check that expanding Eq. A.106 leads to Eq. A.103 and that $a \lesssim 0$. This implies that approximately half of the phase space is not available for scattering. (For electrons in NSs we instead have $\varepsilon_{F,e}/m_e \gg 1$, and hence this does not occur.)

Taking the ultra-relativistic limit for electrons, Eq. A.106 reduces to

$$a < \sqrt{1-B}. \quad (\text{A.107})$$

This restriction of the available phase space results in variations of the order of $\mathcal{O}(10\%)$ for both the interaction and capture rates.

A.6 Interaction Rate for Low Energies

Need to consider the case where $T_\chi = E_\chi - m_\chi < \mu_F$, with $0 < q_0 < T_\chi < \varepsilon_{F,i}$. Then the t_E integration limits follow the hierarchy; $t_{\mu^+}^+ \sim t_{\mu^-}^+ \geq t_{\mu^-}^- \sim t_{\mu^+}^- \gtrsim 0$, and $t_{\mu^-}^+ \gg t_E^+ \geq t_E^- \gg t_{\mu^-}^-$. Then the only term in A.54 that remains is the first term, and only the $i = j = 1$ term contributes, leaving

$$\Gamma^-(E_\chi) = \sum_{n,m} \frac{(-1)^n \alpha_{n,m}}{128\pi^3 E_\chi k} \int_0^{E_\chi - m_\chi} dq_0 \int_{t_E^-}^{t_E^+} dt_E f_1^{(m,n)}(t_E) \quad (\text{A.108})$$

At first order in q_0 and K_χ , we have the following approximations

$$E_\chi \approx m_\chi \quad (\text{A.109})$$

$$k \approx \sqrt{2m_\chi T_\chi} \quad (\text{A.110})$$

$$t_E^\pm \approx 4m_\chi T_\chi \left[1 - \frac{q_0}{2K_\chi} \pm \sqrt{1 - \frac{q_0}{K_\chi}} \right] \quad (\text{A.111})$$

$$\Gamma^- \approx \sum_{n,m} \frac{(-1)^n \alpha_{n,m}}{128\sqrt{2}\pi^3 m_\chi^{3/2} K_\chi^{1/2}} \int_0^{K_\chi} dq_0 \int_{t_E^-}^{t_E^+} dt_E f_1^{(m,n)}(t_E) \quad (\text{A.112})$$

For single term matrix elements such that $|\bar{\mathcal{M}}|^2 = \alpha_{n,m}(-t)^n s^m$, the corresponding $\Gamma_{n,m}^-$ are

$$\Gamma_{0,0}^- = \frac{\alpha_{0,0}}{120\pi^3 m_\chi} K_\chi^2 \quad (\text{A.113})$$

$$\Gamma_{1,0}^- = \frac{2\alpha_{1,0}}{105\pi^3} K_\chi^3 \quad (\text{A.114})$$

$$\Gamma_{2,0}^- = \frac{4\alpha_{2,0} m_\chi}{63\pi^3} K_\chi^4 \quad (\text{A.115})$$

$$\Gamma_{0,1}^- = \frac{\alpha_{0,1}((m_i + m_\chi)^2 + 2m_\chi \varepsilon_{F,i})}{120\pi^3} K_\chi^2 \quad (\text{A.116})$$

$$\Gamma_{1,1}^- = \frac{2\alpha_{1,1}((m_i + m_\chi)^2 + 2m_\chi \varepsilon_{F,i})}{105\pi^3} K_\chi^3 \quad (\text{A.117})$$

$$\Gamma_{0,2}^- = \frac{\alpha_{0,2}((m_i + m_\chi)^2 + 2m_\chi \varepsilon_{F,i})^2}{120\pi^3} K_\chi^2 \quad (\text{A.118})$$

The $\alpha_{n,m}$ can be obtained at some reference point, taken to be the surface of the NS, from the differential cross-section,

$$\frac{d\sigma}{d \cos \theta_{\text{cm}}} = \frac{\alpha_{n,m}(-t)^n s^m}{32\pi(m_i + m_\chi)^2} \quad (\text{A.119})$$

which gives

$$\sigma_{0,0} = \frac{\alpha_{0,0}}{16\pi(m_i + m_\chi)^2} \quad (\text{A.120})$$

$$\sigma_{1,0} = \frac{\alpha_{1,0}}{32\pi(m_i + m_\chi)^2} t_{\max} \quad (\text{A.121})$$

$$\sigma_{2,0} = \frac{1}{3} \frac{\alpha_{2,0}}{16\pi(m_i + m_\chi)^2} t_{\max}^2 \quad (\text{A.122})$$

$$\sigma_{0,1} = \frac{\alpha_{0,1}}{16\pi(m_i + m_\chi)^2} s \quad (\text{A.123})$$

$$\sigma_{1,1} = \frac{\alpha_{1,1}}{32\pi(m_i + m_\chi)^2} t_{\max} s \quad (\text{A.124})$$

$$\sigma_{0,2} = \frac{\alpha_{0,2}}{16\pi(m_i + m_\chi)^2} s^2 \quad (\text{A.125})$$

where I have used

$$t = -\frac{t_{\max}}{2}(1 - \cos \theta_{\text{cm}}) \quad (\text{A.126})$$

$$t_{\max} \sim \frac{4m_i^2 m_\chi^2}{(m_i^2 + m_\chi^2)} \frac{1 - B(R_\star)}{B(R_\star)} \quad (\text{A.127})$$

$$s \sim m_i^2 + m_\chi^2 + \frac{2m_\chi(m_i + \varepsilon_{F,i})}{\sqrt{B(R_\star)}} \quad (\text{A.128})$$

$$\sim (m_i + m_\chi)^2 \quad (\text{A.129})$$

Again introducing the correction

$$\zeta = \frac{n_i}{n_{\text{free}}} \sim \frac{3\pi^2}{(2m_i \varepsilon_{F,i})^{3/2}} n_i \quad (\text{A.130})$$

Then the interaction rates can be expressed with respect to the surface of the star

as

$$\Gamma_{0,0}^-(K_\chi) = \frac{\sqrt{2}}{10} \frac{(1+\mu)^2}{\mu} \frac{m_i}{(m_i \varepsilon_{F,i})^{3/2}} \sigma_{surf} n_i K_\chi^2 \quad (\text{A.131})$$

$$\Gamma_{1,0}^-(K_\chi) = \frac{4\sqrt{2}}{35} \frac{(1+\mu)^2(1+\mu^2)}{\mu^2} \frac{1}{(m_i \varepsilon_{F,i})^{3/2}} \frac{B(R_\star)}{(1-B(R_\star))} \sigma_{surf} n_i K_\chi^3 \quad (\text{A.132})$$

$$\Gamma_{2,0}^-(K_\chi) = \frac{\sqrt{2}}{7} \frac{(1+\mu)^2(1+\mu^2)^2}{\mu^3} \frac{1}{m_i(m_i \varepsilon_{F,i})^{3/2}} \left(\frac{B(R_\star)}{(1-B(R_\star))} \right)^2 \sigma_{surf} n_i K_\chi^4 \quad (\text{A.133})$$

$$\Gamma_{0,1}^-(K_\chi) = \frac{\sqrt{2}}{10} \frac{(m_i(1+\mu)^2 + 2\mu\varepsilon_{F,i})}{\mu(m_i \varepsilon_{F,i})^{3/2}} \sigma_{surf} n_i K_\chi^2 \quad (\text{A.134})$$

$$\Gamma_{1,1}^-(K_\chi) = \frac{4\sqrt{2}}{35} \frac{(m_i(1+\mu)^2 + 2\mu\varepsilon_{F,i})(1+\mu^2)}{\mu^2 m_i(m_i \varepsilon_{F,i})^{3/2}} \frac{B(R_\star)}{(1-B(R_\star))} \sigma_{surf} n_i K_\chi^3 \quad (\text{A.135})$$

$$\Gamma_{0,2}^-(K_\chi) = \frac{\sqrt{2}}{10} \frac{(m_i(\mu+1)^2 + 2\mu\varepsilon_{F,i})^2}{\mu(\mu+1)^2 m_i(m_i \varepsilon_{F,i})^{3/2}} \sigma_{surf} n_i K_\chi^2 \quad (\text{A.136})$$

The average energy loss per collision is given by

$$\langle \Delta T \rangle = \frac{1}{\Gamma^-} \int_0^{K_\chi} dq_0 q_0 \frac{d\Gamma^-}{dq_0} \quad (\text{A.137})$$

which gives the results

$$\langle \Delta T^{0,0} \rangle = \frac{4}{7} K_\chi \sim \langle \Delta T^{0,1} \rangle \sim \langle \Delta T^{0,2} \rangle \quad (\text{A.138})$$

$$\langle \Delta T^{1,0} \rangle = \frac{5}{9} K_\chi \sim \langle \Delta T^{1,1} \rangle \quad (\text{A.139})$$

$$\langle \Delta T^{2,0} \rangle = \frac{28}{55} K_\chi \quad (\text{A.140})$$

The DM will reach thermal equilibrium with the targets when $K_\chi = T_\star$. There are two stages to this process; one where the interactions are not affected by Pauli blocking which takes N_1 collisions, and the next N_2 collisions where Pauli blocking is in effect. The time it takes for thermalisation to occur is given by the sum of the average times between collisions

$$t_{\text{therm}} = \sum_{n=0}^{N_2} \frac{1}{\Gamma^-(T_n)} \sim \sum_{n=N_1}^{N_2} \frac{1}{\Gamma^-(T_n)} \quad (\text{A.141})$$

where T_n is the DM kinetic energy after n collisions. If Pauli blocking is in effect for the entire process, then T_n is related to the initial kinetic energy, T_0 through

$$T_n = T_0 \left(1 - \frac{\Delta T}{T} \right)^n. \quad (\text{A.142})$$

This result implies the following relation;

$$\frac{T_N}{T_0} = \frac{T_{eq}}{T_0} = \left(1 - \frac{\Delta T}{T}\right)^N \quad (\text{A.143})$$

Then for interaction rates which follow $\Gamma^- \propto (K_\chi)^p$, we have that

$$t_{\text{therm}} \propto \sum_{n=N_1}^{N_2} (T_n)^{-p} \quad (\text{A.144})$$

$$= \frac{1}{T_{N_1}^p} \sum_{n=N_1}^{N_2} \left(\left(1 - \frac{\Delta T}{T}\right)^{-p} \right)^n \quad (\text{A.145})$$

$$= \frac{1}{T_{N_1}^p} \frac{(1 - \Delta T/T)^{p(1-N_1)} - (1 - \Delta T/T)^{-pN_2}}{-1 + (1 - \Delta T/T)^p} \quad (\text{A.146})$$

$$\sim \frac{1}{T_{N_1}^p} \frac{(1 - \Delta T/T)^{-pN_2}}{1 - (1 - \Delta T/T)^p} \quad \text{for } N_2 > N_1 \quad (\text{A.147})$$

$$= \frac{1}{T_{N_1}^p} \left(\frac{T_{eq}}{T_{N_1}} \right)^{-p} \frac{1}{1 - (1 - \Delta T/T)^p} \quad (\text{A.148})$$

$$= \frac{1}{T_{eq}^p} \frac{1}{1 - (1 - \Delta T/T)^p} \quad (\text{A.149})$$

B

Hadronic matrix elements for scattering operators

This appendix provides the hadronic matrix elements required for computing the dark matter-baryon couplings given in Eqs. ??-??, for both nucleons and hyperons.

B.1 Nucleons

The values of the hadronic matrix elements for neutrons and protons used in this paper are listed in Table ???. The values of $\Delta_q^{(p)}$ (and similarly for $\delta_q^{(p)}$) are obtained using isospin symmetry:

$$\Delta_u^N = \Delta_d^{N^\star}, \quad \Delta_s^N = \Delta_s^{N^\star}, \quad (\text{B.1})$$

where N^\star is the nucleon obtained interchanging $u \iff d$ quarks.

q	$f_{T_q}^{(n)} [265]$	$f_{T_q}^{(p)} [265]$	$\Delta_q^{(n)}$	$\delta_q^{(n)} [265]$
u	0.0110	0.0153	-0.319 [266]	-0.230
d	0.0273	0.0191	0.787 [266]	0.840
s	0.0447	0.0447	-0.040 [267]	-0.046

Table B.1: Hadronic matrix elements for neutrons and protons.

B.2 Hyperons

To calculate the $f_{T_q}^{(\mathcal{B})}$ couplings for hyperons, we use the baryonic sigma terms from ref. [268], listed in Table B.2, in the following way

$$f_{T_{u,d}}^{(\mathcal{B})} = \frac{\sigma_{l\mathcal{B}}}{m_{\mathcal{B}}} \frac{m_{u,d}}{m_u + m_d}, \quad (\text{B.2})$$

$$f_{T_s}^{(\mathcal{B})} = \frac{\sigma_s}{m_{\mathcal{B}}}, \quad (\text{B.3})$$

where the first relation assumes

$$\frac{\sigma_u^{\mathcal{B}}}{m_u} = \frac{\sigma_d^{\mathcal{B}}}{m_d}. \quad (\text{B.4})$$

In addition, we assume

$$\sigma_u^{\mathcal{B}} = \sigma_d^{\mathcal{B}*}, \quad \sigma_s^{\mathcal{B}} = \sigma_s^{\mathcal{B}*}. \quad (\text{B.5})$$

For the dimension 6 operators where $c_q \propto m_q$, the nucleon couplings depend only on the following sum of the $f_{T_q}^{(\mathcal{B})}$ values

$$\sum_{q=u,d,s} f_{T_q}^{(\mathcal{B})} = \frac{\sigma_{l\mathcal{B}} + \sigma_s}{m_{\mathcal{B}}}, \quad (\text{B.6})$$

and hence exact values for the individual $f_{T_q}^{(\mathcal{B})}$ are unnecessary. The axial vector [268, 269] and tensor [270] couplings are listed in Table B.2.

\mathcal{B}	$\sigma_{l\mathcal{B}}$ (MeV)	σ_s (MeV)	Δ_u	Δ_d	Δ_s	δ_u	δ_d	δ_s
Λ^0	32 ± 4	176 ± 19	0	0	0.59	0	0	0.47
Ξ^0	13 ± 10	334 ± 21	-0.38	0	1.03	-0.22	0	0.9
Ξ^-	13 ± 10	334 ± 21	0	-0.38	1.03	0	-0.22	0.9

Table B.2: Sigma commutators for scalar interactions for each hyperon \mathcal{B} (first and second column). Spin matrix elements for axial vector [268, 269] and tensor interactions are given in the remaining columns. Tensor couplings for Ξ are taken from ref. [270], while those for Λ^0 are our estimates.